Exoplanet Meteorology: Characterizing the Atmospheres of Directly Imaged Sub-Stellar Objects

by

Abhijith Rajan

A Dissertation Presented in Partial Fulfillment
of the Requirements for the Degree
Doctor of Philosophy

Approved April 2017 by the
Graduate Supervisory Committee:

Jennifer Patience, Co-Chair
Patrick Young, Co-Chair
Paul Scowen
Nathaniel Butler
Evgenya Shkolnik

ARIZONA STATE UNIVERSITY

May 2017

ABSTRACT

The field of exoplanet science has matured over the past two decades with over 3500 confirmed exoplanets. However, many fundamental questions regarding the composition, and formation mechanism remain unanswered. Atmospheres are a window into the properties of a planet, and spectroscopic studies can help resolve many of these questions. For the first part of my dissertation, I participated in two studies of the atmospheres of brown dwarfs to search for weather variations. To understand the evolution of weather on brown dwarfs we conducted a multi-epoch study monitoring four cool brown dwarfs to search for photometric variability. These cool brown dwarfs are predicted to have salt and sulfide clouds condensing in their upper atmosphere and we detected one high amplitude variable. Combining observations for all T5 and later brown dwarfs we note a possible correlation between variability and cloud opacity.

For the second half of my thesis, I focused on characterizing the atmospheres of directly imaged exoplanets. In the first study *Hubble Space Telescope* data on HR8799, in wavelengths unobservable from the ground, provide constraints on the presence of clouds in the outer planets. Next, I present research done in collaboration with the Gemini Planet Imager Exoplanet Survey (GPIES) team including an exploration of the instrument contrast against environmental parameters, and an examination of the environment of the planet in the HD 106906 system. By analyzing archival *HST* data and examining the near-infrared colors of HD 106906b, we conclude that the companion shows weak evidence of a circumplanetary dust disk or cloud. Finally, I measure the properties of the low mass directly imaged planet 51 Eridani b. We combined published J, H spectra with updated L_P photometry, new $K1$, $K2$ spectra, and M_S photometry. The new data confirms that the planet has redder than similar

spectral type objects, which might be due to the planet still transitioning from to L-to-T. Model atmospheres indicate a cooler effective temperature best fit by a patchy cloud atmosphere making 51 Eri b an excellent candidate for future variability studies with the *James Webb Space Telescope*.

To my wife, Divya: Thank you for your love and unconditional support.

To my parents, and my brother: Thank you for enabling me to pursue my dreams

ACKNOWLEDGMENTS

As a fan of sci-fi I have always dreamt of exploring the Universe and solving its mysteries and I wanted to be an astronaut and a rocket scientist to achieve this dream. It wasn't until many years later while in doing my engineering that I read about SETI and downloaded the SETI@HOME software. The idea that my tiny machine in a corner of India could be searching for signs of intelligent life completely changed my life. That was when I knew that I would become an astronomer. That moment was more than a decade ago and I have followed a windy path to reach this point and I am glad that I persevered.

I have been fortunate in my career to have met many incredible people who were willing to guide and support me even when at times I didn't believe in myself. I would like to thank Patrick and Steve for their incredible support these last two years and Jenny for all the wonderful science and research opportunities she made possible. To Rémi, Travis and Laurent for being my friends and mentors. To my wonderful group mates Kim, Joanna and Rob without whom those many proposal writing nights would have been impossible. My office mates Caleb and Kay who patiently listened to me whine and complain even when I know they'd rather have been out having a drink. To Heather, Alli, and Julie for making my years in Tempe so much more fun and for watching *Archer* while I was working. Thanks to the entire GPIES team for their incredible support and to Bruce for letting me work at Stanford this last year. To the wonderful people in the SESE administration office, you have been incredibly nice to me even when I bungled my forms and forgot deadlines.

This is for my father who taught me to follow my dreams and my mother who motivated me to persevere on in the face of failure. They made me the person I am today and to them I owe everything. To my brother with whom I spent many nights

dreaming about exploring the uncharted cosmos. And in the words of Walt Whitman "I am to see to it that I do not lose you", my wife, the best part of my everyday.

TABLE OF CONTENTS

LIST OF TABLES

LIST OF FIGURES

Figure Page

Figure Page

Chapter 1

INTRODUCTION

1.1 Brown Dwarfs

Brown dwarfs are the link between the lowest mass stars and giant exoplanets. These substellar objects have masses ranging from $\sim$75 M_{Jup} to a few Jupiter masses and are the tail end of the star formation process, a regime wherein they are considered to form in a manner similar to stars (Chabrier *et al.*, 2000). The existence of brown dwarfs was independently theorized in the 1960s by two different groups, Kumar (1963b,a) and Hayashi and Nakano (1963). They concluded that the hydrogen-burning main sequence limit for Population I stars ranges between 0.07 to 0.075 $M_{\odot}$. Recent work on measuring dynamical masses for brown dwarfs confirms that the brown dwarf upper mass limit appears to be 70 M_{Jup} (Dupuy and Liu, 2017). Objects with mass lower than this limit will not have hydrogen burning occurring in their core, and will contract to have an electron-degenerate core, preventing the object from collapsing further. Kumar (1963b) originally called these new objects "black" dwarfs; however, Jill Tarter renamed them as "brown" dwarfs (Tarter, 1975) since the term black dwarfs is already used to refer to extremely cool and faint white dwarfs.

As the upper limit for brown dwarfs is determined by the hydrogen burning limit, objects with mass high enough to fuse hydrogen in their cores are classified as stars, and objects with lower masses are classified as brown dwarfs. The lower limit, i.e., the distinction between the most massive planets and the least massive brown dwarfs is poorly understood at this time. A suggested boundary is a mass of 13 M_{Jup}, which is

based on the lower limit for objects to have deuterium burning in their cores (Burrows *et al.*, 1997). Objects with masses lower than this limit are typically referred to as giant planets (Burrows *et al.*, 2001). A separate classification scheme is based on the formation mechanism, i.e., free floating brown dwarfs are objects that form in a manner similar to stars and when orbiting a star they have similar composition as the star while giant planets form in stellar disk typically with higher metallicity than the star (Chabrier *et al.*, 2014). However, while this classification scheme is more physically motivated, distinguishing between the two formation mechanisms is difficult. Measurements of the star to planet C/O ratio have been suggested as a distinguishing feature whereby objects with super-stellar C/O ratio would form via core accretion while similar C/O ratio would be due to gravitational instability (Öberg *et al.*, 2011). Brown dwarfs and imaged planets have similar atmospheric properties, where as they cool condensates form in their atmosphere initially resulting in clouds of iron and silicates in L-dwarfs, before being replaced by salt and sulfide clouds in T-dwarfs and ammonia and water clouds in Y-dwarfs (Burrows *et al.*, 1997; Morley *et al.*, 2012, 2014). However, the atmospheres of low mass imaged planets are not identical to brown dwarfs where imaged planets tend to have redder infrared colors compared to similar temperature brown dwarfs most likely caused by greater cloud opacity (Barman *et al.*, 2011; Marley *et al.*, 2012).

1.1.1 Discovery and Classification

It took 25 years before the theoretical predictions of the existence of brown dwarfs were confirmed with the detection of a faint companion to the white dwarf GD 165 (Becklin and Zuckerman, 1988). The companion was detected as part of a large near

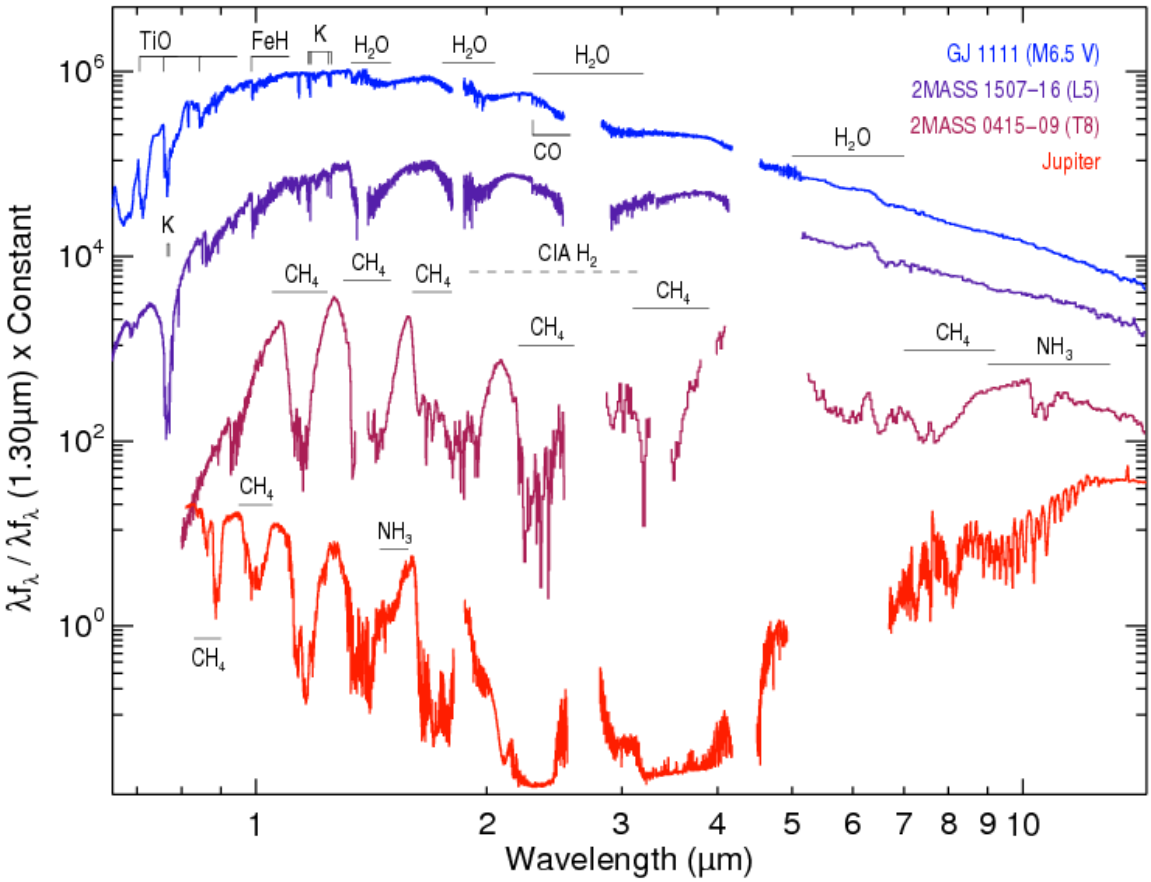

Figure 1. Brown dwarf spectral sequence going from late Ms through to giant planets. The spectra plotted above shows the evolution of brown dwarfs as their atmospheres cool. Late M brown dwarfs are the warmest and have few molecular absorption features. The cooler L-dwarfs show deeper absorption features and in the T-dwarfs we see large portions of the spectral energy distribution carved out by methane gas in the atmosphere. Late T and Y dwarfs have spectral features similar to Jupiters atmosphere even though the planet is much cooler. Permission to reproduce figure granted by M. Cushing and M. Marley.

infrared (IR) survey of 200 nearby white dwarfs, and was found to have an effective temperature of ∼2100 K. However, it was the detection of Gl 229B (Nakajima *et al.*, 1995; Oppenheimer *et al.*, 1995) that heralded the age of brown discovery. The brown dwarf companion to the late-type dwarf GL 229 was confirmed as the first bona fide detection of a brown dwarf, in which a methane signature in the spectrum and the

low luminosity indicated that it had a low effective temperature (<1000 K). With the advent of the Two Micron All Sky Survey (2MASS, Skrutskie *et al.*, 2006a) and the Deep Near-Infrared Survey (DENIS, Epchtein *et al.*, 1999), astronomers were able to scan the entire sky and compare optical data, taken with surveys like the Sloan Digital Sky Survey (SDSS, York *et al.*, 2000), to the near IR, enabling a search for point sources with extremely red near IR colors and without clear optical counterparts. Kirkpatrick *et al.* (1997) and Delfosse *et al.* (1997) were amongst the first to present candidate brown dwarfs detected within studies using the 2MASS and DENIS surveys.

The early detections were late M-types and cooler with spectral features matching GD 165B, confirming beyond a doubt the brown dwarf nature of the white dwarf companion. Following these early results, brown dwarfs similar to Gl 229B were also detected using data from SDSS and 2MASS (Strauss *et al.*, 1999; Burgasser *et al.*, 1999; Tsvetanov *et al.*, 2000). Finally, with the detection of three cool brown dwarfs using SDSS, Leggett *et al.* (2000) presented for the first time a clear spectral series of brown dwarfs spanning temperatures from ∼2000 K to ∼900 K (see Figure 1). These objects included an elusive type of brown dwarfs spanning cooler temperatures which would come to be known as "L-T" transition objects. Brown dwarfs like the first discovery of GD 165B are classified as "L"-type. The "L" spectral type is defined using optical spectra covering 650 – 1000 nm, a region which includes several absorption features: weakening signatures of TiO and VO, and signatures of metal hydride, alkali and H_2O that strengthen from late M through the L spectral range. In contrast, brown dwarfs like Gl 229B were classified as "T"-type. The classification scheme proposed originally by Burgasser *et al.* (2002) and Geballe *et al.* (2002) and later unified in Burgasser *et al.* (2006b), utilized near infrared spectra spanning JHK near

IR-bands and focused on the strength of the H_2O and CH_4 absorption features in this wavelength range to differentiate between different sub-classes.

Over the next decade, astronomers discovered over a thousand brown dwarfs. However, a large difference still existed between the coolest known brown dwarfs and Jupiter in our solar system. Additionally, none of the objects detected showed spectral signatures of ammonia that is common in the atmosphere of Jupiter. One of the primary science goals of the Wide-field Infrared Survey Explorer (WISE, Wright *et al.*, 2010a) space telescope, an all-sky survey telescope studying the sky in the mid IR, was to look for the coolest brown dwarfs using purpose-built filters, specifically the $W1$ (3.4μm) and $W2$ (4.6μm) filters. Cushing *et al.* (2011) presented six brown dwarfs that had similar J and H band peaks and two that demonstrated tentative absorption features attributed to NH_3 that were classified as a new spectral type, the "Y"-type brown dwarfs. The new spectral type is defined based on a range of spectral and photometric features exhibited by these brown dwarfs (Cushing *et al.*, 2011; Kirkpatrick *et al.*, 2012), including a narrowing of the J-band spectral morphology attributed to absorption by NH_3 and a reversal of the near IR color trend whereby the $J - H$ colors of Y-dwarfs appear to be reddened compared to mid and late-T dwarfs.

1.1.2 Brown Dwarf Atmospheres

Understanding the characteristics of a brown dwarf requires an understanding of its atmosphere. The atmosphere provides a window into the properties of the object, and despite being a tiny fraction of the object total mass, it controls the thermal evolution of the brown dwarf. A spectrum of the brown dwarf is a measurement of its atmosphere. Contained in it are the signatures of the various molecules that are present, the surface

gravity, and the effective temperature. The relatively cool temperatures of brown dwarfs results in the formation of molecules in their atmospheres. These condense to form clouds that have a strong effect on the emergent flux of the object. One of the earliest non-gray models for brown dwarf atmospheres was proposed by Burrows *et al.* (1997), wherein they presented model atmospheres for objects down to ∼100K and presented the effects of absorption by molecules such as H_2O, H_2, and CH_4 on the spectra of these cool brown dwarfs.

There exist a variety of atmospheric models that use different methods of solving for the emergent spectra. These include models by Lunine *et al.* (1989); Allard *et al.* (2001a); Ackerman and Marley (2001a); Tsuji (2002); Marley *et al.* (2002); Burrows *et al.* (2006); Helling and Woitke (2006); Barman *et al.* (2011). An assumption that is common between the different groups is stratification of the atmosphere into multiple layers to solve for the local gas temperature (Helling and Casewell, 2014). In this case, the atmosphere is a radiative layer surrounding a deep convective interior assumed to be in local thermal equilibrium. There is conservation of flux which is represented by the effective temperature at the boundary of the atmosphere. The layers are typically assumed to be in chemical equilibrium, to permit the calculation of the opacity of the medium due to the different constituents. The pressure in each layer is calculated assuming hydrostatic equilibrium. The molecules in brown dwarf atmospheres condense to form clouds which have a large impact on the emergent flux. A major differentiator amongst the different available models lies in their treatment of clouds. In the next section, we discuss brown dwarf clouds and the observational techniques used to study weather on brown dwarfs.

1.1.2.1 Clouds on Brown Dwarfs

As mentioned earlier, measurements of brown dwarf atmospheres provide insights into a wide range of brown dwarf parameters, including but not limited to: the temperature-pressure profile, surface gravity, metallicity and chemical composition. In the atmospheres of both brown dwarfs and planets, the condensing molecules include iron and silicates in the warmer L-dwarf atmospheres, to alkali salts and sulfides in T-dwarfs, to water and ammonia in Y-dwarfs. Clouds are expected to form as a natural consequence of the cool temperatures on brown dwarfs, where the atmosphere condenses to form seed particles that continue to grow through chemical reactions with the surrounding atmosphere to form solid sub-micron to micron-sized particles.

Clouds affect the atmosphere of the object in a number of ways. For example, the process of condensation modifies the local abundance of the gas phase, which needs to be accounted for when computing the different opacity sources in a given layer. Furthermore, clouds act to increase the opacity of the atmosphere, which can have significant effects on self-luminous objects like brown dwarfs. In a cloudy brown dwarf, the emergent flux is from the top of the clouds, whereas in the cloud-free brown dwarf the flux will emerge from much deeper in the atmosphere where the primary opacity source is the gas medium. Therefore, at wavelengths where the cloud opacity is highest, in cloud-free objects we are peering deeper into the atmosphere and thus consequently into hotter layers of the atmosphere. This makes cloud-free objects brighter than cloudy brown dwarfs at the same wavelength range. However, at wavelength ranges where the atmosphere is dominated by the gas opacity, cloudy brown dwarfs are brighter than cloud-free brown dwarfs at the same effective temperature. This is due

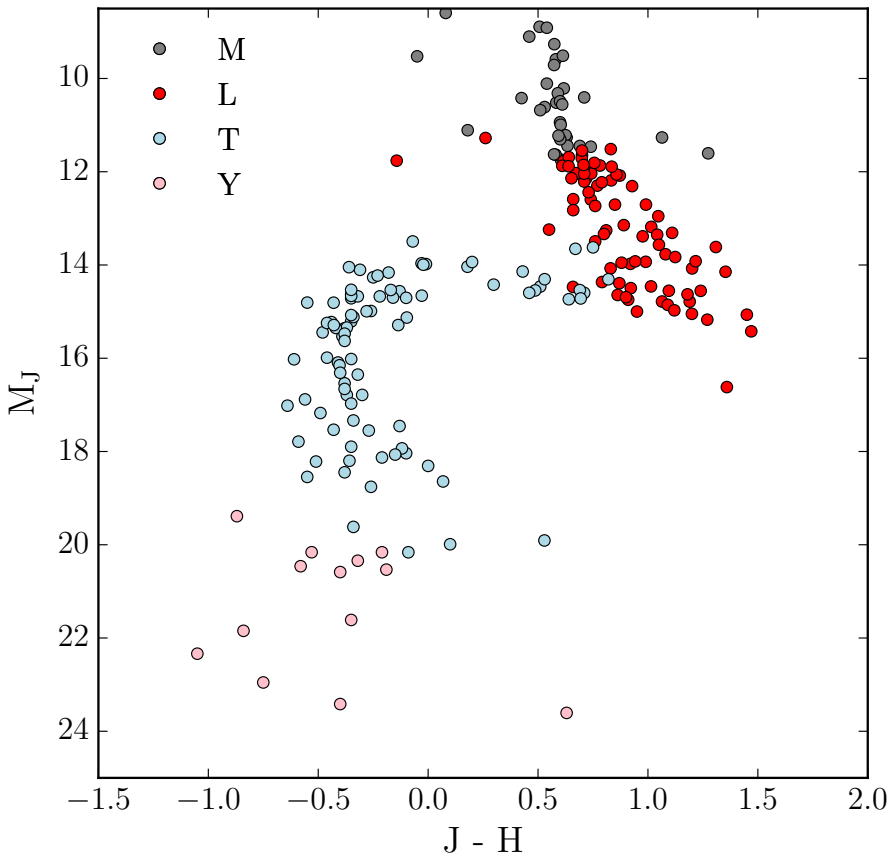

Figure 2. The J vs $J-H$ brown dwarf color magnitude diagram. The photometry for the field M-dwarfs (gray), L-dwarfs (red), T-dwarfs (light blue) and Y-dwarfs (pink) comes from the compilation of Dupuy and Liu (2012a); Dupuy and Kraus (2013); Liu *et al.* (2016).

to the effect of clouds increasing the overall atmospheric opacity and thus increasing the temperature-pressure profile.

Plotted in Figure 2 is a brown dwarf color-magnitude diagram (CMD) indicating the positions of the late-M, L, T and Y brown dwarfs. In a departure from the typical CMD for stars, the brown dwarf CMD reflects the unusual property of all objects having approximately the same radii. Therefore, for brown dwarfs, the brightness plotted on the Y-axis of the figure is a direct proxy for the effective temperature of the objects, where the objects on the top are the warmest brown dwarfs, approaching

temperatures of stars, while those at the bottom are the coolest, comparable to solar system giant planets. Clouds are suspected to play a large role in the distribution of brown dwarfs on the CMD, where the near IR colors are predicted to be affected significantly by the opacity of the clouds in the atmosphere. In the L-dwarf sequence, the colors become progressively redder from early to late type due to the enhanced presence of condensate particles and thus higher opacity clouds. As brown dwarfs transition from L to T, there is a sharp change in the brown dwarf colors, where the colors switch from red to blue at an almost constant effective temperature of $\sim$1400 K. This change is predicted to be caused by the decreasing cloud opacity (Golimowski *et al.*, 2004). Other parameters such as the surface gravity, and metallicity are also expected to increase the color within each spectral type.

The L-T transition region has been defined as starting at L7 and continues until T4 (Golimowski *et al.*, 2004), and a variety of solutions have been proposed to explain the transition. The most widely accepted explanation involves the idea of holes in the clouds (Ackerman and Marley, 2001a; Burgasser *et al.*, 2003), which reduce the opacity in the atmosphere. These holes permit flux to emerge from the deeper, hotter layers thereby causing a brightening on the brown dwarf in the wavelength regions most affected by cloud opacity, i.e., H and K. Cloud free models are extremely successful at reproducing the spectra of early to mid-T dwarfs (Saumon *et al.*, 2012), however as shown in Morley *et al.* (2012), as brown dwarfs cool through the T-dwarf sequence the colors of these objects start to become redder again. This has been explained by the emergence of a new cloud-deck, one composed of salt and sulfide clouds at lower atmospheric pressures and hence higher in the atmosphere. Clouds are also expected to play a major role in Y-dwarfs (Morley *et al.*, 2014), where H_2O and NH_3 clouds form in the photosphere, similar to the clouds on Jupiter. Another model recently proposed

by Tremblin *et al.* (2016) does not require the presence of clouds in the atmosphere to explain the reddening of the L and T dwarfs or the L-T transition features seen in the CMD. Instead, their model proposes that these features can be explained by chemical instability due to the slow reaction rates of the CO/CH_4 and N_2/NH_3. These chemically-driven instabilities generate turbulent energy transportation from deeper in the atmosphere, thereby explaining the near IR color reddening. The removal of the chemical instability, once the reactions complete, cause the colors to transition to blue. This theory is an exciting proposal that could redefine the way atmospheres are explained; however, it struggles to reproduce brown dwarf variability which is easily explained by patchy clouds.

1.1.2.2 Brown dwarf variability studies

Brown dwarf variability has been an active field of research since the first time-domain study of four brown dwarfs at optical wavelengths by Tinney and Tolley (1999), where they found signs of optical variability in a late-M brown dwarf. The most widely accepted explanation for brown dwarf variability is a heterogeneous cloud cover where the variability is measured on the rotational timescales.

The majority of the original brown dwarf variability studies focused on L-dwarfs and were conducted in the red optical (typically I-band) using time series photometry (Bailer-Jones and Mundt, 1999, 2001; Martín *et al.*, 2001; Clarke *et al.*, 2002b,a; Gelino *et al.*, 2002; Koen, 2003, 2004, 2005; Maiti *et al.*, 2005; Maiti, 2007; Rockenfeller *et al.*, 2006; Koen, 2013a; Heinze *et al.*, 2015). Variability searches focusing on later type brown dwarfs tended to be performed in the near IR, where these later type objects are more luminous, enabling high precision photometry and detections of small amplitude

variations (Artigau *et al.*, 2003a; Bailer-Jones and Lamm, 2003; Enoch *et al.*, 2003; Koen *et al.*, 2004, 2005a; Morales-Calderón *et al.*, 2006; Clarke *et al.*, 2008a). The early searches for variability tended to focus on a few brown dwarfs and found 1–2% variability to be common across the observed targets with very different sensitivities to variation. The discovery of two large amplitude variables, SIMP 0136 (Artigau *et al.*, 2009a), and 2M 2139 (Radigan *et al.*, 2012a), both of which fall in the L-T transition, generated increased interest in variability searches. This renewed interest became focused specifically in the transition region where clouds are expected to have holes in them. A near IR survey by Radigan *et al.* (2014a) that surveyed 57 brown dwarfs spanning mid-L to late-T type brown dwarfs found that large amplitude variability, defined as >2%, was limited to L-T transition brown dwarfs. The first Brown dwarf Atmosphere Monitoring survey (BAM-I; Wilson *et al.*, 2014), published contemporaneously with a similar sample size of 69 brown dwarfs spanning early-L to late-T spectral types, found a different result where both the amplitude and frequency of variability were statistically similar through the entire brown dwarf sequence. Further details of the BAM-I study are presented in the next section. Both of these studies were undertaken with ground based telescopes, and since that time, two large brown dwarf surveys have also been published by Buenzli *et al.* (2014a); Metchev *et al.* (2015) that spanned the L – T spectral range. These surveys found results both in agreement with the BAM-I study, where variability is not a feature of any single spectral bin and with Radigan *et al.* (2014a) where the amplitude of variability was highest at the L-T transition.

1.1.2.3 The Brown dwarf Atmosphere Monitoring program

The Brown dwarf Atmosphere Monitoring program comprises two separate studies aimed at understanding the atmospheric dynamics of brown dwarfs spanning L, T, and Y spectral types. The first paper, BAM-I, focused on understanding the occurrence of variability in brown dwarf atmospheres across the full L-T spectral sequence. Variability in brown dwarf atmospheres is expected to be largest at the z', Y, and J bands where the emergent spectrum is coming from deeper in the atmosphere. BAM-I was specifically chosen to be conducted in the J_s-band (1.16-1.32 μm), where the authors chose to maximize both the chance of detecting variability while ensuring high signal to noise monitoring of the targets, given that brown dwarfs become progressively fainter the bluer the wavelength of observation. The monitoring campaign of 69 field brown dwarfs was conducted using the SofI instrument on the 3.5 m New Technology Telescope (NTT). The monitored targets are shown in Figure 3 where the BAM-I sample is plotted on top of the known brown dwarfs in gray and the orange corresponds to detected variables. The objects observed as part of the BAM-I program spanned the full L- and T-spectral sequence in an unbiased manner sampling in and out of the L-T transition, using the list at the Brown Dwarf Archive (dwarfarchives.org). Based on the previous literature, the L-T transition was chosen to include all brown dwarfs with spectral types between L7 and T4.

One of the important results to come out of the BAM-I data, in addition to the detection of new brown dwarf variables, was an examination of the question of persistence of variability over multiple epochs. The variable brown dwarf SIM0136 had previously shown variable amplitudes ranging from flat photometry to amplitudes in excess of 9% over epochs separated by a few months. If the assumption of storm

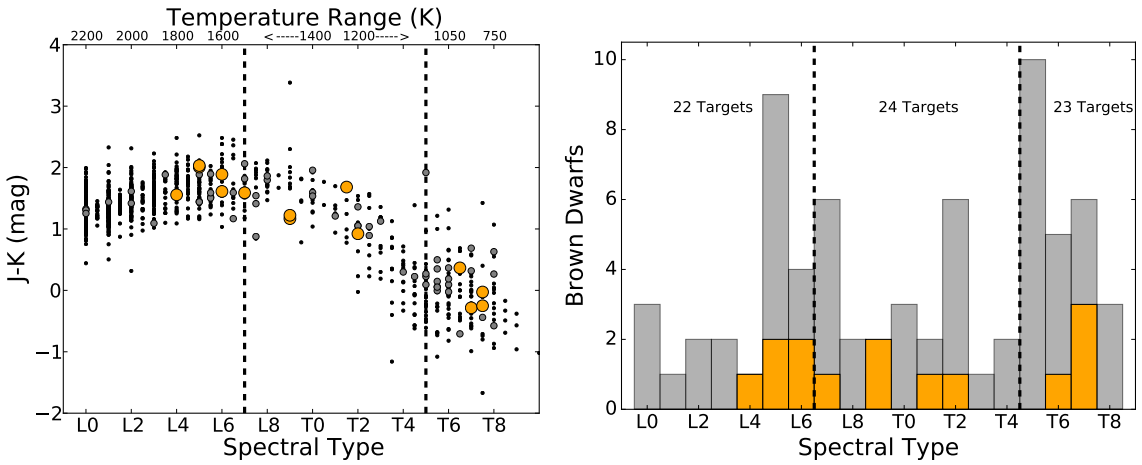

Figure 3. (left) Color vs spectral type plot showing the entire L through T spectral range with the BAM-I sample shown with gray circles and the variables detected as part of the with orange circles. (right) Histogram of the BAM-I brown dwarf sample monitored for variability in the survey (in gray) along with the detected variables (in orange). The histogram also shows the unbiased nature of the BAM-I sample, monitoring equal numbers of L, L-T transition, and T-dwarfs.

features causing the variability is correct, then the changing variability suggests a dynamic atmosphere with changing storm features. We used the BAM-I sample, a subset of which (34 objects) had been previously monitored for variability to try and understand whether the BAM-I targets showed signs of similar changing variability. Table 1 from the BAM-I study summarizes the observations related to persistence of variability and has been included here. The table shows that nearly 40% of the objects that had been previously monitored switched from variable to constant or vice versa suggesting that single epoch variability studies might be underestimating the true brown dwarf variability fraction. Additionally, it suggests that truly understanding the atmospheres of these objects requires careful multi-epoch monitoring to study the evolution of the atmosphere and the typical evolution timescale required for objects to transition from quiescent to active. The topic of variability persistence is discussed in greater detail in the next chapter, the BAM-II study.

Table 1. Summary of Persistence Results

Total targets with 2 epochs	34
Variable at 2 epochs	6
Constant at 2 epochs	15
Switch between variable and constant	13

1.2 Exoplanets

The field of exoplanet science has grown immensely since the discovery of 51 Peg b, the first planet discovered to be orbiting a sun-like star (Mayor and Queloz, 1995). In the 20 years since this event, there have many new exoplanet discoveries with over 3500 confirmed exoplanets currently, with the majority having been detected by the *Kepler* spacecraft (Borucki, 2016), a telescope which has revolutionized our understanding of exoplanet architecture. The known exoplanet population has been detected by a range of methods, primarily through transits, radial velocity, direct imaging and microlensing. Other methods such as astrometry and transit timing variation have also been used to search for planets, however, the current yields from these methods are small. The diverse exoplanet population is shown in Figure 4. Highlighted in the figure are the different methods used to detect exoplanets, each of which is sensitive to a different orbital separation and mass and thus these methods are highly complementary in nature. The different detection methods of transit, radial velocity and microlensing are described in greater detail below, while direct imaging is discussed in the following section.

Radial Velocity: The first exoplanet discovered, 51 Peg b, was detected through the radial velocity technique. An exoplanet orbiting a star will cause the center of mass to shift away from the center of the star, inducing a wobble in the star as the planet rotates around it. Through Doppler spectroscopy, we can measure the shift

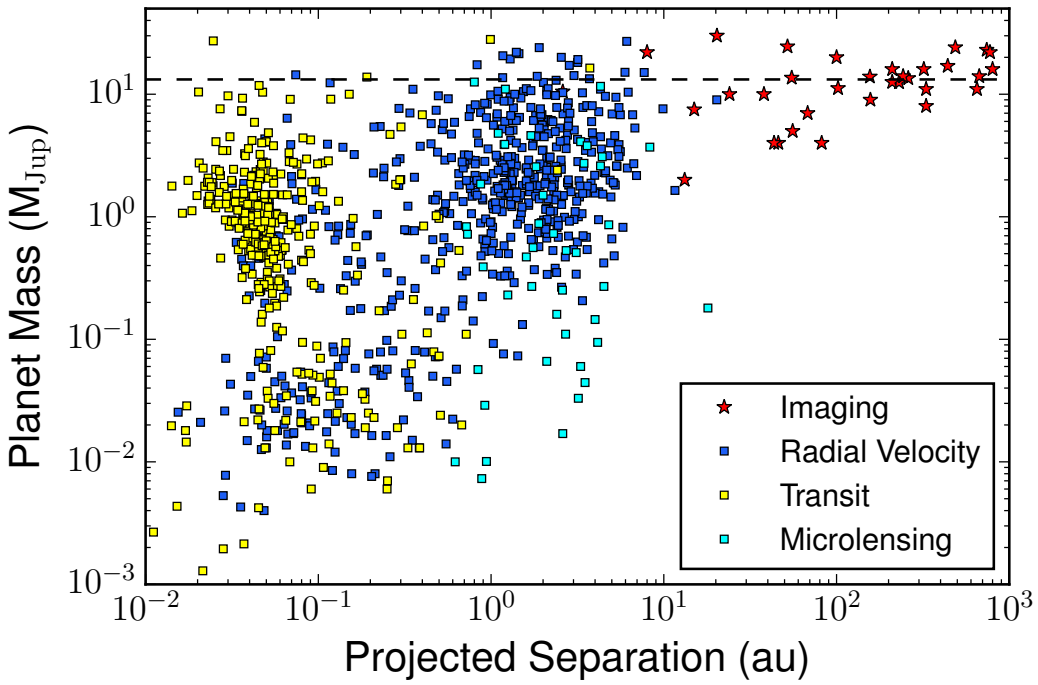

Figure 4. Ensemble of confirmed planets and their mass period relation. The planets detected by the four primary exoplanet detection techniques are highlighted in the figure. The dotted line indicates the 13 M_{Jup}, planet-brown dwarf, mass limit. Data for this figure is taken from the NASA Exoplanet Archive.

induced by the orbiting companion to estimate the period and eccentricity and thereby the minimum mass of the object. Since this method does not permit a measurement of the inclination of the orbit, we cannot derive the true mass of the companion. Radial velocity surveys typically target older main sequence stars since stellar activity can both mimic and drown out the effects of a planet. This method is very sensitive to higher mass planets which have larger radial velocities in excess of 50 m/s for a Jupiter at 0.1 AU. Detecting earth mass planets around solar type stars at 1 AU is significantly more challenging requiring $\lesssim$10 cm/s precision.

Transit: The transit method of detecting exoplanets depends measuring the drop in flux of a star as a planet orbiting it passes in front of the disk, with respect to the observer. Transiting planets are detected by monitoring a multitude of stars to look

for periodic dips in their fluxes. By measuring the drop in flux and prior knowledge of the stellar radius, we can estimate the radius of the planet. The first planet detected by the transit technique was HD 209458b by Charbonneau *et al.* (2000). The group went on to detect the presence of sodium in the atmosphere of the same planet, making it the first exoplanet to have its atmosphere characterized (Charbonneau *et al.*, 2002). The *Kepler* space telescope made use of high precision time-series photometry to detect planets via the transit technique. Since transit signals are a function of both the stellar and planet radius, it is significantly harder to find an earth-size planet around a sun-like star compared to a planet of similar radius around an M-dwarf. This fact has been used to great success to detect some of the smallest exoplanets yet, including the recent remarkable discovery of seven earth-sized planets around the low mass star, TRAPPIST-1 (Gillon *et al.*, 2017).

The transit technique is one of only two methods that permit a careful study of the exoplanet atmosphere. Measuring the depth of the planet transit in front of the star or the decrease in flux as it goes behind it permits recovery of either the "transmission" (Charbonneau *et al.*, 2002; Sing *et al.*, 2011) or "emission" (Charbonneau *et al.*, 2008) spectra of the exoplanet. By modeling these spectra we can extract interesting planet parameters including the molecular composition of the atmosphere and/or the global wind profile of the planet (Knutson *et al.*, 2007). Combining the transit method with either radial velocity or transit timing variations permits a measurement of the true mass of the planet. Knowledge of both the mass and radius allows us to estimate the bulk density of the planet and the bulk composition which is vital in the search for habitable planets. The transit technique is most suited to finding short period planets due to the stringent inclination requirements for a system to transit.

Microlensing: The technique of microlensing depends on the lensing of a back-

ground star by a foreground star with a planet (Gaudi, 2012). The greatest strength of this method is its sensitivity to low mass planets at separations greater than the "snow line" and free floating planets. Unlike planets detected via most other detection methods, planets detected by microlensing are not amenable to follow-up characterization. However, unlike the other techniques, microlensing has the potential to provide valuable statistical information on planets inaccessible to other planet finding methods permitting a more complete understanding of planet populations. Microlensing is one of the main focus for an upcoming mission in the next generation of space telescopes, the *Wide Field Infrared Survey Telescope (WFIRST)*.

1.3 Direct Imaging of Exoplanets

The exoplanet detection techniques discussed in the previous section are all indirect methods, since the planet signal is inferred by studying the effect of the planet on either the parent star in transit and radial velocity or the background star in microlensing. Direct imaging of exoplanets is the only technique where the flux from the planet is detected and studied directly. To detect planet flux, most instruments make use of a combination of an adaptive optics (AO) system which corrects aberrations in the incoming stellar light caused by atmospheric turbulence and a coronagraph to block the light of the star while allowing the light of any companion through. Since the flux detected is emitted from the planet, direct imaging is one of only two planet detection techniques (the other being the transit technique) that permits a direct exploration of the atmospheric properties of the exoplanet through spectrophotometry.

The field of direct imaging of substellar companions had its first indisputable detection of a brown dwarf companion orbiting an M-star with the discovery of

Gl 229 B (Nakajima *et al.*, 1995; Oppenheimer *et al.*, 1995). It took nearly a decade since that discovery before the next set of discoveries occurred with the detection of 2M1207 b (Chauvin *et al.*, 2004, 2005a), which is a planetary mass companion orbiting an early L-type brown dwarf, and AB Pic B (Chauvin *et al.*, 2005b), a brown dwarf companion to a K-dwarf. The early direct detections of brown dwarfs and exoplanets were limited to very low contrast objects, i.e., bright companions orbiting faint primary objects. Unlike stars, exoplanets are hottest at the time of their formation and cool monotonically from that point (Burrows *et al.*, 1997), ($L_{\rm bol} \propto t^{-5/4} M^{5/2}$; Stevenson, 1991), where t is time and M is mass. This means that a Jupiter mass planet at 5 Gyr around a sun-like star has a contrast of $\sim 10^{-9}$, which in practice is extremely difficult to achieve with ground-based AO systems. This is the biggest limitation of direct imaging surveys, and to circumvent this issue, most direct imaging surveys focus on searching for companions around young stars since planets are bright when they are young. Planets at few to tens of millions of years have more favorable planet-to-star contrasts. Currently direct imaging is most effective at finding planets of Jovian mass and greater orbiting young stars at orbital separations greater than 5 – 10 AU, making it very complementary to both transit and radial velocity planets.

1.3.1 Brown Dwarfs and Imaged Planets

As mentioned earlier in this chapter, brown dwarfs masses start all the way from the tail end of the star formation process and extend below the 13 $M_{\rm Jup}$ planetary mass limit. Oppenheimer *et al.* (2000) tackle the question of providing an observational method for distinguishing between brown dwarfs and planets and define planets as objects which never undergo any nuclear fusion throughout their evolution. By this

definition, any object lower than ∼13 MJup can be defined as a planet, since brown dwarfs with mass greater than this limit fuse deuterium in their cores (Burrows *et al.*, 1997). However, the discovery of free floating companions such as PSO J318 (Liu *et al.*, 2013) makes this definition questionable, since the formation mechanism of free floating planets is uncertain. Indeed, they may have formed via molecular cloud collapse, making them more akin to brown dwarfs.

Brown dwarfs share many observational similarities with giant exoplanets and as shown in Figure 5, both brown dwarfs and imaged exoplanets occupy the same space in the CMD. While they have similar atmospheres, they are not identical. Imaged planets typically have redder near IR colors when compared to field brown dwarfs of the same spectral type. This has been attributed to the greater presence of clouds in the atmospheres of the imaged planets. Studies such as those by Allers and Liu (2013); Faherty *et al.* (2016) within the last five years have demonstrated that the near IR color spread observed for L-dwarfs and very possibly extending to T-dwarfs can be attributed to youth and lower surface gravity. And, similarly to imaged planets, the redder colors in their atmospheres are most likely caused by greater condensates in atmospheres forming clouds.

1.3.2 Exoplanet Formation

The properties of a planetary system originate from the mode and environment of formation, and other environmental aspects such as the interaction with the circumstellar disk and other bodies in the system. To estimate the mass of a directly imaged companion, observations of the planet are compared with planet formation and evolutionary model predictions since currently there are no direct estimates for

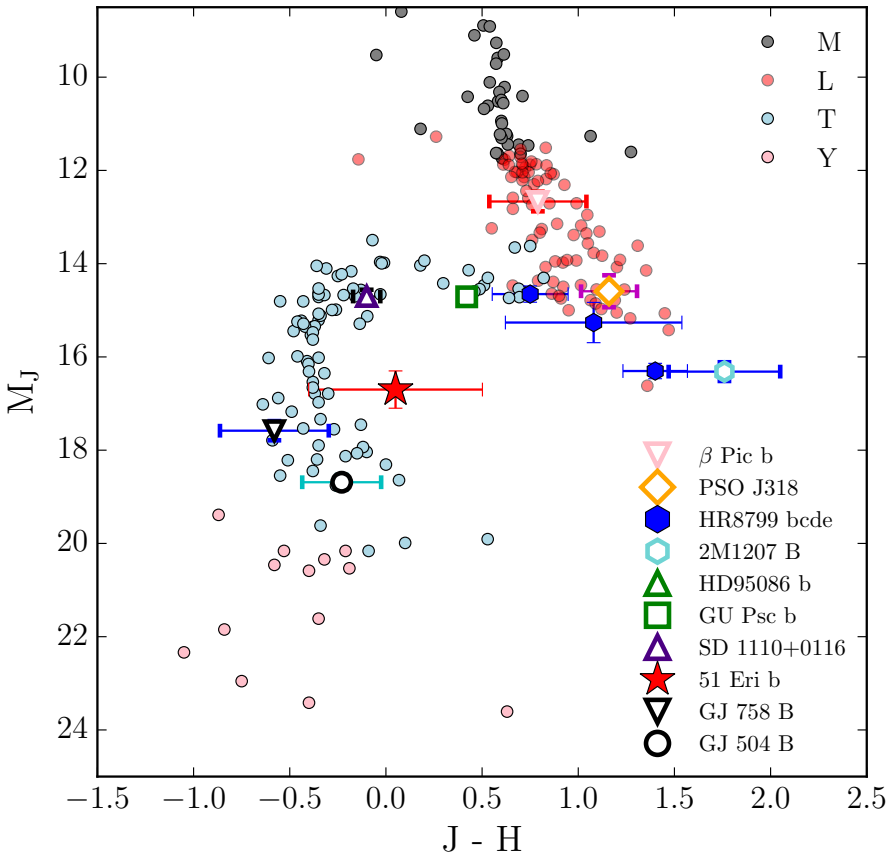

Figure 5. The J vs $J-H$ color magnitude diagram showing both brown dwarfs and imaged exoplanets. Similar to Figure 2 with directly imaged planets included. The imaged planets follow a similar and possibly redder evolutionary track to brown dwarfs. The photometry for the directly imaged planets and young brown dwarfs were taken from Lagrange *et al.* (2009); Liu *et al.* (2013); Marois *et al.* (2010b); Chauvin *et al.* (2005a); Rameau *et al.* (2013a); Naud *et al.* (2014); Leggett *et al.* (2007); Janson *et al.* (2011b); Kuzuhara *et al.* (2013).

the true mass of the companions. There are two primary models of planet formation: (1) the solar system giant planets such as Jupiter and Saturn are expected to have formed via core accretion (Mizuno, 1980; Pollack *et al.*, 1996), a pathway which is expected to be the dominant method of planet formation in the inner 10 AU, and (2) gravitational collapse via disk instability (Cameron, 1978; Boss, 1997), which might be the mechanism of planet formation at separations from 10 – 100 AU (Rafikov, 2007, 2011).

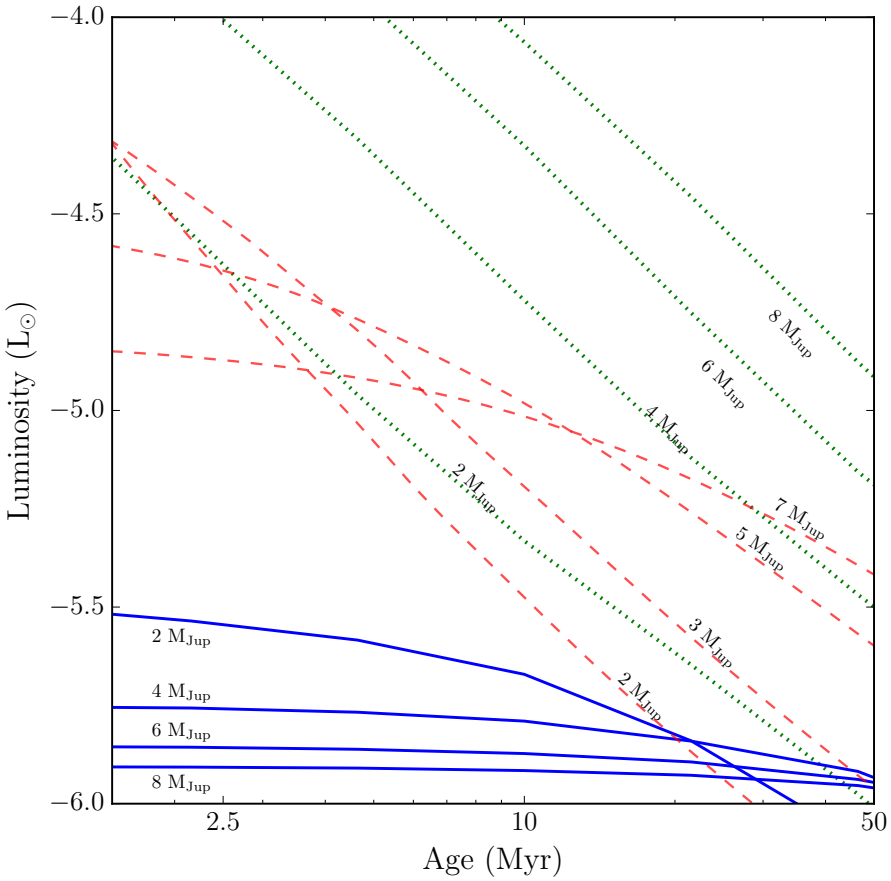

Figure 6. Predictions of the variation of bolometric luminosity as a function of age for three different evolutionary tracks. The three models plotted are hot (green dotted) and cold (blue solid) start models (Marley *et al.*, 2007; Fortney *et al.*, 2008) and a single set of warm start models (red dashed) with an initial core mass of 22 $M_{\oplus}$ (Mordasini, 2013).

Core Accretion: The fundamental idea behind the core accretion model is the formation of a solid core, which is thought to range between a few to $\sim$10 $M_\oplus$. This is accomplished through the accretion of small dust grains from the (extra)solar nebula to form planetesimals, which will grow until the protoplanets' feeding zones are depleted. During this phase, the gas accretion rate is significantly lower compared to the accretion of solids. Early models of core accretion suffered from the so-called "meter barrier", where particles smaller than 1 meter fall into the star within a few hundred years (Youdin, 2010). The meter barrier can be circumvented by streaming instabilities which destabilize the relative motion between gas and particles resulting in an increase in the density of particles leading to the formation of large planetesimals (Youdin and Goodman, 2005; Johansen and Youdin, 2007). Once the solid and gas masses approximately equal ($\sim$10 $M_\oplus$), a runaway gas accretion phase occurs where the core accretes hydrogen and helium from its surrounding to form an atmosphere, which continues to grow until the stellar gas disk dissipates. During the process of the gas accretion, a shock forms as the gas falls from the radius of the Hill sphere to the surface of the planet (Hubickyj *et al.*, 2005). Due to this accretion shock, the in-falling gas radiates away much of its gravitational potential energy. Planets that form by this process are labeled as "cold start" planets where the initial entropy is low (Marley *et al.*, 2007). The canonical model of core accretion, where km-sized planetesimals collide to form the core requires several million years to form the planet (Pollack *et al.*, 1996), however the accretion of smaller cm-sized particles or "pebbles" coupled to the gas can form gas giant planets at a range of separations before the dissipation of the gas disk (Lambrechts and Johansen, 2012).

Gravitational Instability: The second mode of giant planet formation requires the fragmentation of the protoplanetary disk to form planets directly. For disk

instability to occur, the Toomre Q-criterion (Toomre, 1964), $Q = c_s\kappa/\pi G\Sigma$, must approach unity. In this relation, c_s is the speed of sound, κ is the epicyclic frequency, and Σ is the surface density of the disk. In addition, the cooling timescale for the disk must be less than or equal to the orbital timescale to ensure fragmentation (Rafikov, 2007). Numerical simulations have shown that as the size of the protoplanetary disk increases, there is a corresponding increase in the number of "clumps" that can form (Boley, 2009; Boss, 2011). Here for stars with mass between 1–2 $M_\odot$, gravitational instability is able to produce clumps at radii of 30–100 AU, required to explain wide orbit, directly imaged giant planets, e.g., HR8799 bcd (Marois *et al.*, 2008) and HD95086 b (Rameau *et al.*, 2013a). In contrast to the core-accretion mode of planet formation, planets formed by gravitational instability are expected to retain much of the initial entropy of the gas leading to these planets being called "hot start" (Burrows *et al.*, 1997).

An intermediate class of formation models has been proposed over the last five years, called "warm start" models (Spiegel and Burrows, 2012; Mordasini, 2013). These models propose a family of solutions existing between the hot and cold start extreme cases. By neither assuming that the initial accretion shock in core accretion is a 100% efficient process, nor that planets formed via gravitational instability retain all of the initial entropy, these warm start models focus on exploring the range of initial entropies with which the planets might form when taking into account non-ideal accretion shock scenarios.

Plotted in Figure 6 are model predictions for the evolution of the luminosity of planets from the three different evolutionary models, namely hot and cold start models from Marley *et al.* (2007); Fortney *et al.* (2008) and warm start luminosity for a set of planets with core mass of 22 $M_\oplus$ (Mordasini, 2013). It is immediately obvious

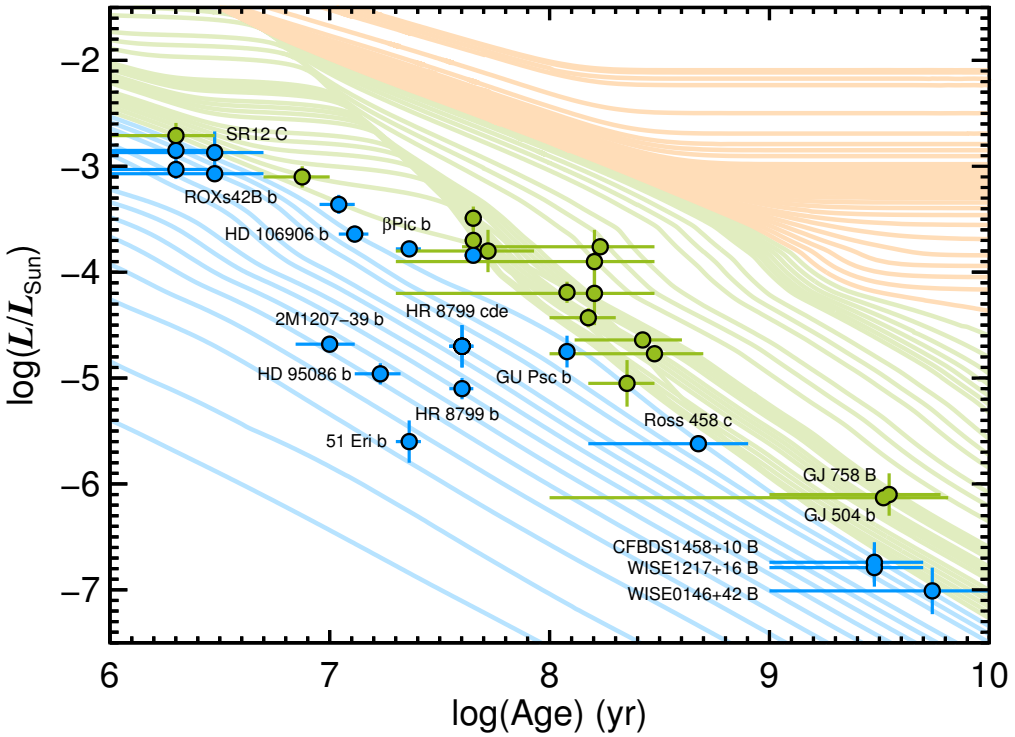

Figure 7. Bolometric luminosity for the sample of brown dwarf (green) and planetary mass (blue) objects with measured ages. Also shown in the figure are hot start models from (Burrows *et al.*, 1997), where the colors of the line indicate different mass ranges; orange, green, and blue tracks denote masses >80 M_{Jup}, 14–80 M_{Jup}, and <14 M_{Jup}. Permission to reproduce figure granted by B. Bowler.

from the plots that all three models predict very different luminosities for planets at young ages but converge as the planets get older, at ages $\gtrsim$ 50 Myr. Thus for directly imaged planets with ages $\lesssim$50 Myr, at least those that have well-constrained ages and reliable mass estimates, the measured bolometric luminosity of the planet can help distinguish the formation mechanism.

Figure 7 shows the sample of brown dwarfs and imaged planetary mass companions that have reliable age and luminosity measurements from Bowler (2016). All of the tracks plotted in the figure are from the hot start evolutionary models of Burrows

et al. (1997), i.e., the objects that formed via gravitational instability. As can be seen from location of the objects and the overlap with the evolutionary tracks, all of the currently known companions are best fit by the hot start models. As I show in Chapter 5, the low mass planet 51 Eridani b is the first imaged companion truly consistent with both hot and cold start evolutionary model tracks.

1.3.3 Characterizing planets

The process of characterizing planets starts with the collection of relevant data on the system. Broadly, the observations can be categorized into three types (Madhusudhan *et al.*, 2014), observations of the planets mass and radius via radial velocities, transits, orbit monitoring or astrometry, the atmosphere through spectroscopy either transit transmission/emission spectra or directly imaged spectra, and a precise understanding of the stellar properties including the spectral shape, effective temperature, radius, abundance. I focus on the direct imaging aspect of planet characterization in the rest of this section. The challenges of collecting data via direct imaging are elaborated in the following section, here we describe the typical data available and the methods applied to recover the properties of directly imaged planets.

The directly imaged planets currently known are young, with masses larger than Jupiter, since planets are brightest when they are young, and at separations of 10–100 AU. For most of these companions, the process of observations and characterization involves either astrometric monitoring to measure their orbit as well as to derive dynamical masses (Nielsen *et al.*, 2014; Pueyo *et al.*, 2015; Nielsen *et al.*, 2016) or obtaining the spectra and photometry of the companions across 1–5μm for atmosphere characterization (Marois *et al.*, 2008, 2010a; Currie *et al.*, 2011a). The method of

retrieving planet parameters involves the comparison of the data to pre-computed model grids (Marois *et al.*, 2008; Konopacky *et al.*, 2013; Rice *et al.*, 2015). However, even the best model fits struggle to match the complete spectral energy distribution of the planet and require ad hoc linear combinations of different models or arbitrarily small radii (Barman *et al.*, 2011; Marley *et al.*, 2012). By comparison, atmosphere retrievals of the planet properties have been used successfully to reproduce transiting exoplanet and brown dwarf atmospheres (Kreidberg *et al.*, 2014; Line *et al.*, 2014; Todorov *et al.*, 2015). A caveat though is that the best fits can often be achieved by making completely unphysical assumptions. A different approach to understanding the atmosphere of imaged planet is via the technique of polarimetric imaging, where the polarized light, if observed, can provide valuable information regarding the structure of the clouds in the planet photosphere (Jensen-Clem *et al.*, 2016) as well as the period of rotation. Doppler imaging via high resolution spectroscopy can be used to generate a 2D map of the planet surface and estimate the rotational period (Snellen *et al.*, 2014; Crossfield, 2014). Atmospheric variability can also permit an exploration of the rotational period while multi-wavelength monitoring probes the atmospheric structure (Apai *et al.*, 2016).

1.4 Surveys Searching for Imaged Planets, Past and Present

The search for imaged substellar companions has been an on-going pursuit for over 30 years, with surveys conducted using an array of different instruments and methods. These methods include: infrared photometry/imaging (Zuckerman and Becklin, 1987; Skrutskie *et al.*, 1989), infrared speckle interferometry (Henry and McCarthy, 1990), HST imaging (Sartoretti *et al.*, 1998; Brandner *et al.*, 2000; Schroeder *et al.*, 2000;

Lowrance *et al.*, 2005; Luhman *et al.*, 2005), speckle imaging of young stars (Neuhäuser *et al.*, 2003), and surveys with new adaptive optics instrumentation (Nakajima *et al.*, 1994; Macintosh *et al.*, 2001; Oppenheimer *et al.*, 2001; Chauvin *et al.*, 2003; McCarthy and Zuckerman, 2004; Carson *et al.*, 2005; Nakajima *et al.*, 2005; Tanner *et al.*, 2007). These early surveys discovered several brown dwarfs and planetary mass candidates, e.g., the aforementioned GD 165 (Becklin and Zuckerman, 1988), Gl 229B (Nakajima *et al.*, 1995), and 2M1207b (Chauvin *et al.*, 2004). While these early surveys provided valuable scientific discoveries, they were typically conducted on non-optimal instrumentation that was not designed to find substellar companions. These surveys laid the groundwork for the next generation of adaptive optics instrumentation and software innovations that have become standard in direct imaging surveys.

1.4.1 Understanding adaptive optics and coronagraphs for high contrast imaging

The primary obstacle to directly imaging companions is the residual starlight that obstructs the region of interest closest to the star, at orbital separations corresponding to planets. This can occur due to the scattering of light through the telescope or, the more challenging issue, which is the blurring of the incoming wavefront of light due to Earth's turbulent refractive atmosphere. For an ideal point spread function (PSF) of a star, described by an Airy function, the regions close to the star which are of greatest scientific interest, few λ/D, have stellar flux with contrasts ranging between $10^{-4} - 10^{-5}$. A typical Jovian mass companion around a young star will have a contrast $\sim 10^{-6}$, and imaging an evolved Jupiter would require contrasts better than $\sim 10^{-9}$. Typical telescopes are non-ideal systems and tiny imperfections in the optics will have detrimental effects on the final science image. In addition, the uncorrected

atmospheric wavefront will also result in an imperfect PSF. These imperfections result in what is known as "speckle noise", where speckles are copies of the stellar PSF that arise from the aberrations in the incoming wavefront. Speckles do not follow Poisson statistics and are correlated sources of noise, and thus long exposures do not average over the speckles to provide a gain in SNR (Soummer *et al.*, 2007). Additionally, the speckles are not constant in time, are bright (being several orders of magnitude brighter than the companions), and are affected by instrumental variations and atmospheric

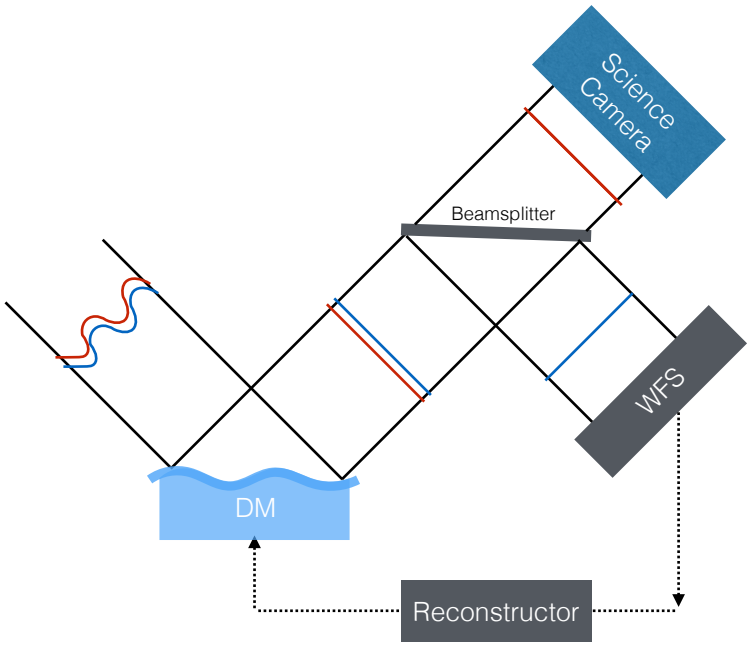

Figure 8. Simplified diagram showing the principle of an Adaptive Optics system. The aberrant wavefront enters the telescope from the left, and is corrected by the deformable mirror. This beam is split into its optical and near IR counterparts with the near IR light continuing to the science camera, while the optical beam is fed to a wavefront sensor and the reconstructor that command the DM.

The goal of the adaptive optics system is to generate a diffraction-limited PSF with a high Strehl ratio. The Strehl ratio is defined as the ratio between the peak of the PSF flux compared to the peak of an ideal PSF. In typical astronomical data without adaptive optics, the Strehl ratio is $< 1\%$ (Oppenheimer and Hinkley, 2009). The adaptive optics systems can be broken down into three parts, shown in Figure 8, (1) *Wavefront sensing*: component used to measure the shape of the incoming wavefront. The Shack-Hartmann optical instrument is one example of a wavefront sensor (WFS), where an array of lenslets produces an array of spots of light corresponding to reimaged starlight across the telescope pupil. The centroids of these spots can be used to estimate the slope of the wavefront in that region. (2) *Wavefront reconstruction*: This is the step of calculating the wavefront error, which is then applied to correct the aberration estimated by the WFS. (3) *Deformable mirror (DM)*: This is the device used to correct the incoming wavefront. Typically a DM is a series of actuators covered by a thin optical surface that deforms under the influence of the actuators. Adaptive optics systems built by the University of Arizona have pioneered the adaptive secondary technology, which replaces the telescope secondary mirror with deformable secondary mirrors that can correct the incoming wavefront without requiring additional optical elements. Other forms of DMs are piezo DMs which have smaller actuator stroke, of the order of $\sim 10\mu$m, than adaptive secondaries but are much smaller in size. And the final form of DMs are micro-electrical-mechanical systems (MEMs) devices, which are the smallest devices of the three and manufactured using standard semiconductor fabrication techniques. However, currently these can only provide $\sim 2\mu$m of stroke.

Suppression of the stellar PSF is typically done with the use of an occulting disk known as a coronagraph and here I describe the application of the classic

Lyot coronagraph that has been optimized for high contrast imaging (Lyot, 1939; Sivaramakrishnan *et al.*, 2001). In the simplest case shown in Figure 9, the Lyot coronagraph uses two masks to remove the stellar flux while still permitting light from an off-axis companion through to the science camera. The first mask, placed in the focal plane of the telescope, is an opaque disk used to suppress the core of the stellar PSF. However, starlight diffracts around this mask to form two bright rings and thus it is necessary to add a second stage in the pupil plane, called the Lyot stop, to block these signatures of diffracted light. This two-stage coronagraph can suppress $\sim 99\%$ of the stellar core while leaving the companion flux mostly unaffected.

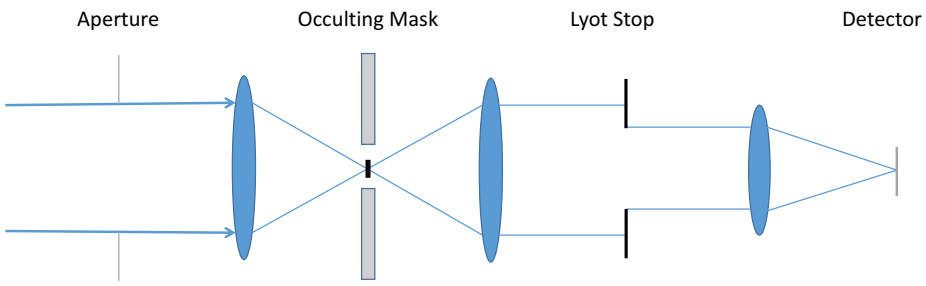

Figure 9. A schematic of a classic Lyot coronagraph assuming a non-aberrated wavefront. Adapted from Sivaramakrishnan *et al.* (2001).

As stated above, a combination of the adaptive optics system with a coronagraph can correct the incoming wavefront and significantly suppress the stellar core. However, even with the implementation of these systems the final science data will have residual speckles caused by any uncorrected residual wavefront error, either due to changes in the telescope optics or rapidly varying atmospheric turbulence. It is therefore

necessary to model and subtract the stellar PSF in post-processing of the data. The speckles caused by telescope optics, called "quasi-static" speckles, can be dealt with by a technique known as "Angular Differential Imaging" (ADI; Marois *et al.*, 2006a) where the telescope derotator is turned off to let the astronomical field of view rotate while the telescope and all other systems are held steady during the observations. Combining the images taken in the ADI mode permits the generation of a reference PSF from the science data itself. The technique is similar to "roll deconvolution" which has been applied to space telescopes (Walter and Weigelt, 1985; Schneider *et al.*, 2003) to generate reference PSFs. An additional processing technique is known as "spectral differential imaging" (SDI), where the correlation of speckles as a function of wavelength is utilized to subtract the speckle background to search for planets. Advanced algorithms such as as the Linear Optimized Combination of Images (LOCI, Lafrenière *et al.*, 2007) and Karhunen-Loève Image Projection (KLIP, Soummer *et al.*, 2012; Amara and Quanz, 2012) aim to make use of the rotating reference stack of images to generate the most ideal reference frame aimed at maximizing the SNR of a companion. However, each of the post-processing techniques described above will result in some self-subtraction of the planet flux. Thus, it is critical to quantify the effects of self-subtraction when extracting accurate photometry or spectroscopy.

1.4.2 Previous High-Contrast Imaging Surveys

The list of the surveys that can be classified as the the first generation of large exoplanet imaging surveys is presented in Table 2. These surveys utilized adaptive optics cameras that were purpose built to detect exoplanet companions. In combination with the instrumentation, these surveys typically targeted young stars, where

the planet-to-star contrasts are more favorable. Furthermore, these were some of the first studies that made use of the advanced post-processing techniques previously mentioned. These studies were significantly successful in the detection of faint sub-stellar companions at tens to hundreds of AU, including the directly imaged systems HR8799 bcde (Marois *et al.*, 2008, 2010b), β Pic b (Lagrange *et al.*, 2009), HD95086 b (Rameau *et al.*, 2013a), GJ504 b (Kuzuhara *et al.*, 2013), FW Tau, ROXs 12, and ROXs 42B (Kraus *et al.*, 2014), and HD106906 b (Bailey *et al.*, 2014).

The limited number of detections (and null results) from the previous generation of imaging surveys has led to the conclusion that there are very few massive planets at wide separations. Lafrenière *et al.* (2007) found that at the 95% confidence level (CL), <28% of FGKM stars host planets with mass 0.5–13 M_{Jup} between 10–25 AU, <13% for 25–50 AU, and <9% for 50–250 AU. A recent study by Vigan *et al.* (2017) compiling the results of 11 studies to examine the sub-stellar (0.5–75 M_{Jup}) companion frequency using 199 stars, finds that less than 0.75–5.7% of stars have companions within 20–300 AU at the 68% CL.

1.4.3 State of field today

Over the past several years, the second generation of adaptive optics instruments have come online at a range of different telescopes. These instruments are designed with adaptive optics systems that have thousands of actuators compared to the hundreds of actuators used in the previous generations. The adaptive optics systems are designed to provide $<$ 100nm RMS wavefront error compared to $>$ 300nm previously. Additional design improvements include: coronagraphs optimized for smaller inner working angles,

Table 2. First generation exoplanet imaging surveys. Adapted from Chauvin *et al.* (2015)

Reference	Telescope	Instr.	Mode	Filter	FoV	#	SpT	Age
Biller *et al.* (2007)	VLT	NaCo	SDI	H	5×5	45	GKM	$\lesssim$300
	MMT		SDI	H	5×5	–	–	–
Lafrenière *et al.* (2007)	Gemini-N	NIRI	ADI	H	22×22	85	–	10–5000
Apai *et al.* (2008)	VLT	NaCo	SDI	H	3×3	8	FG	12–500
Chauvin *et al.* (2010)	VLT	NaCo	Cor-I	H, K	28×28	88	BAFGKM	$\lesssim$100
Heinze *et al.* (2010)	MMT	Clio	ADI	L, M	15.5×12.4	54	FGK	100–5000
Janson *et al.* (2011a)	Gemini-N	NIRI	ADI	H, K	22×22	15	BA	20–700
Vigan *et al.* (2012)	Gemini-N	NIRI	ADI	H, K	22×22	42	AF	10–400
	VLT	NaCo	ADI	H, K	14×14	–	–	–
Delorme *et al.* (2012)	VLT	NaCo	ADI	L	28×28	16	M	$\lesssim$200
Rameau *et al.* (2013b)	VLT	NaCo	ADI	L	28×28	59	AF	$\lesssim$200
Yamamoto *et al.* (2013)	Subaru	HiCIAO	ADI	H, K	20×20	20	FG	125±8
Biller *et al.* (2013)	Gemini-S	NICI	Cor-ASDI	H	18×18	80	BAFGKM	$\lesssim$200
Nielsen *et al.* (2013)	Gemini-S	NICI	Cor-ASDI	H	18×18	70	BA	50–500
Wahhaj *et al.* (2013)	Gemini-S	NICI	Cor-ASDI	H	18×18	57	AFGKM	∼100
Janson *et al.* (2013)	Subaru	HiCIAO	ADI	H	20×20	50	AFGKM	$\lesssim$1000
Brandt *et al.* (2014)	Subaru	HiCIAO	ADI	H	20×20	63	AFGKM	$\lesssim$500
Bowler *et al.* (2015)	Keck	NIRC2	ADI	H, K_S	10.2×10.2	78	M	20–620
	Subaru	HiCIAO	ADI	H, K_S	20×20	–	–	–
Chauvin *et al.* (2015)	VLT	NaCo	ADI	H	14×14	86	BAFGK	10–1700
Meshkat *et al.* (2015)	VLT	NaCo	ADI	L	14×14	13	AF	23–125
Galicher *et al.* (2016)	Gemini-N	NIRI	ADI	H, K	22×22	292	BAFGKM	∼120
	Gemini-S	NICI	ADI	H	18×18	80	BAFGKM	$\lesssim$200
	Keck	NIRC2	ADI	H, K	10×10	–	–	–

Cor-I: coronagraphic imaging; SDI: simultaneous differential imaging; ADI: angular differential imaging; ASDI: angular and spectral differential imaging

optical designs emphasizing PSF stability, and high spatial-resolution integral field spectrographs to permit both detection and characterization with the same system.

A range of surveys are either currently on-going with these instruments or have recently been completed. These are presented below,

- Project 1640 (P1640; PI: R. Oppenheimer): P1640 was the first of the next generation high order adaptive optics ("extreme AO") systems to become operational. The instrument was installed on the 200 inch Hale Telescope at Palomar Observatory and as has become standard for many of the new extreme AO instruments, it was coupled with a lenslet-based integral field spectrograph as its primary science camera, operating in the Y, J and H bands (Hinkley *et al.*, 2011). The Palomar AO system (PALM-3000) uses a 3388-actuator DM as a tweeter in conjunction with an existing 241-actuator mirror that acts as a woofer to provide tip-tilt and larger stroke correction. Both P1640 and the Gemini Planet Imager described below make use of a apodized-pupil Lyot coronagraph (Soummer *et al.*, 2011b). The P1640 survey has produced several results, including the astrometric and photometric characterization of the planets in the HR8799 system (Oppenheimer *et al.*, 2013; Pueyo *et al.*, 2015).
- LBTI Exozodi Exoplanet Common Hunt (LEECH; PI: A. Skemer): The Large Binocular Telescope (LBT) in Arizona has a pair of twin 8.4m telescopes. The adaptive optics system uses two individual adaptive secondary mirrors each with 672 actuators and a high-order pyramid wavefront sensor to correct the incoming wavefront with measured Strehl ratios as high as 80% (Esposito *et al.*, 2011; Bailey *et al.*, 2014). The LEECH survey is a recently completed 50$\sim$70 night search for exoplanets using the Large Binocular Telescope mid-infrared camera (LMIRCam) on LBT. Unlike most of the new surveys, LEECH aims to

search for companions around an older sample of stars, including the ∼500 Myr Ursa Majoris moving group. This is made possible because older, hence cooler, planets have more favorable planet-to-star contrasts at L-band than at H-band. LMIRCam on LBT has been used to great effect to characterize faint companions including the HR8799 planets (Skemer *et al.*, 2012), and GJ 504 b (Skemer *et al.*, 2016). A recent upgrade to the instrument added the Arizona Lenslets for Exoplanet Spectroscopy (ALES Skemer *et al.*, 2015). This instrument is an integral field spectrograph designed to take low-resolution (R∼20) spectra from ∼2.8–4.2μm.

- Gemini Planet Imager Exoplanet Survey (GPIES; PI: B. Macintosh): The Gemini Planet Imager is an extreme AO system on the 8m Gemini South telescope (Macintosh *et al.*, 2014). The Gemini Planet Imager Exoplanet Survey is a 890 hr search for exoplanets around young (10–300 Myr), nearby ($\lesssim$100 pc) stars. Both the instrument and the survey are described in much greater detail in Chapter 4.
- SpHere INfrared survEy (SHINE; PI: J. Beuzit): The Spectro-Polarimetric High-contrast Exoplanet REsearch (SPHERE) camera is an extreme AO system on the Very Large Telescope (VLT) in Chile (Beuzit *et al.*, 2008). Similar to GPI and P1640, SPHERE also has a near IR integral field spectrograph providing low resolution spectra (R∼30–50) from 0.95–1.65μm. SPHERE also has two other instruments: IRDIS (Infrared Dual-band Imager and Spectrograph), which provides near-IR dual-band differential imaging, polarimetry, or long-slit spectroscopy, and ZIMPOL (Zurich IMaging POLarimeter), which provides visible-light polarimetry. The SPHERE AO system has a 41×41 actuator DM and a Shack-Hartmann wavefront sensor using a low read-noise EMCCD that

allows it to provide AO corrections for fainter stars. The exoplanet survey, SHINE, will obtain deep contrasts on ∼400–600 stars over 200 nights to search for close companions. The survey simultaneously observes with the integral field unit and IRDIS in dual band imaging mode to obtain a spectrum in a small field of view ($1.8'' \times 1.8''$), as well as deeper imaging to look for companions further out in the IRDIS field (square $11'$ FoV).

1.5 Structure of this thesis

In Chapter 2, I present the results of our second Brown dwarf Atmosphere Monitoring (BAM-II) survey, where we conducted a multiple epoch study to monitor three late T- and one Y-dwarf to search for photometric variability in near IR. These cool brown dwarfs are predicted to have salt and sulfide clouds condensing in their upper atmospheres. We combine the different BAM studies with previous multi-epoch observations of cool brown dwarfs to explore correlations between variability and the near-infrared colors of brown dwarfs. Chapter 3 focuses on results from a *Hubble Space Telescope* program to characterize the atmospheres of the known directly imaged planetary system HR8799. These data enable new measurements of the planet in wavelengths unobservable from the ground. Chapters 4 and 5 present research done in collaboration with the Gemini Planet Imager Exoplanet Survey (GPIES) team, including an exploration of the instrument contrast against a range of environmental and data parameters to better calibrate instrument performance. Text from Kalas *et al.* (2015a) has been included with the explicit permission of the first author. Included from the paper, is an analysis of archival *HST* data in the optical and published near-IR colors of the planetary mass companion HD 106906b to search for

evidence that the companion interacted with the debris disk of the primary in the past. From these analyses, we conclude that the companion shows weak evidence of a circumplanetary dust disk or cloud that might have been captured from the primary. Finally, I present spectroscopic characterization of the low mass directly imaged planet 51 Eridani b. For this analysis we combined published J and H band spectra with updated L_P photometry, new $K1$ and $K2$ spectra, and M_S photometry to present the spectral energy distribution of the planet spanning 1–5 μm. By fitting the planet to an extensive set of atmosphere models, we are able to refine the planetary parameters and discuss possible formation mechanisms. In Chapter 6, I discuss future steps in the field of brown dwarf and imaged exoplanet atmosphere characterization.

Chapter 2

THE BROWN-DWARF ATMOSPHERE MONITORING (BAM) PROJECT II: MULTI-EPOCH MONITORING OF EXTREMELY COOL BROWN DWARFS

2.1 Introduction

Ultracool dwarfs, spanning the L, T, and recently discovered Y dwarf (Kirkpatrick *et al.*, 1999; Cushing *et al.*, 2011) spectral types, provide a link between the coolest stars, giant planets in our Solar System, and exoplanets. Without sufficient mass for nuclear fusion (e.g Hayashi and Nakano, 1963), brown dwarfs cool monotonically over time, causing changes in the chemical and physical processes responsible for sculpting the emergent spectra of their atmospheres. The formation and dissipation of dusty condensate clouds are key components of theoretical models developed to explain the fluxes and spectral features of brown dwarfs (e.g Allard *et al.*, 2001a; Marley *et al.*, 2002; Burrows *et al.*, 2006; Helling and Woitke, 2006). Early T dwarf atmospheric models predicted that once the clouds from the L/T transition sink below the photosphere, the subsequent T-sequence should remain cloud-free (Marley *et al.*, 2002). T-dwarfs however, appear to deviate from the expected cloud-free atmosphere colour as they cool (Figure 10; blue curve) and become progressively redder. This phenomenon can be best explained by the formation of sulfide and alkali salt clouds as the brown dwarf cools (Lodders and Fegley, 2006; Visscher *et al.*, 2006; Morley *et al.*, 2012). With a three-dimensional treatment of the atmospheric dynamics, recent models have suggested that large-scale temperature variations may be present near the photospheres of brown dwarfs and that these regions with different temperatures

may result in light curve variability (Showman and Kaspi, 2013; Robinson and Marley, 2014). Zhang and Showman (2014) also discuss how atmospheric turbulence and the resulting vortices and/or zonal jets can lead to photometric variability up to several percent over a wide range of timescales.

Photometric monitoring of brown dwarfs provides a method to search for evidence and evolution of cloud features, storms, or activity that cause surface brightness differences (e.g. Koen *et al.*, 2005b; Artigau *et al.*, 2009b; Buenzli *et al.*, 2014b; Radigan *et al.*, 2014b; Wilson *et al.*, 2014). The strength, persistence, and wavelength dependence of the variations reveal the underlying atmospheric processes of cloud formation, dissipation, and dynamics of the atmospheres (e.g. Showman and Kaspi, 2013; Zhang and Showman, 2014). Over the past several years, we have conducted a large-scale photometric variability survey of brown dwarfs – the Brown dwarf Atmosphere Monitoring (BAM) program. The initial BAM study (Wilson *et al.*, 2014) covered 69 targets spanning the L0-T8 sequence, and detected multiple late-T variables. In this paper, we present the results of the second component of the BAM project that is designed to search for photometric variability over several epochs in four ultracool brown dwarfs at or near the T/Y spectral boundary. The properties of the sample of T/Y dwarfs are summarised in Section 2. The near-infrared imaging observations are described in Section 3. In Section 4, the data reduction and analysis required to construct the light curves is detailed. Results for each target are given in Section 5, followed by the discussion in Section 6 that includes a comparison with samples of higher temperature L and T brown dwarfs and theoretical models of cool atmospheres.

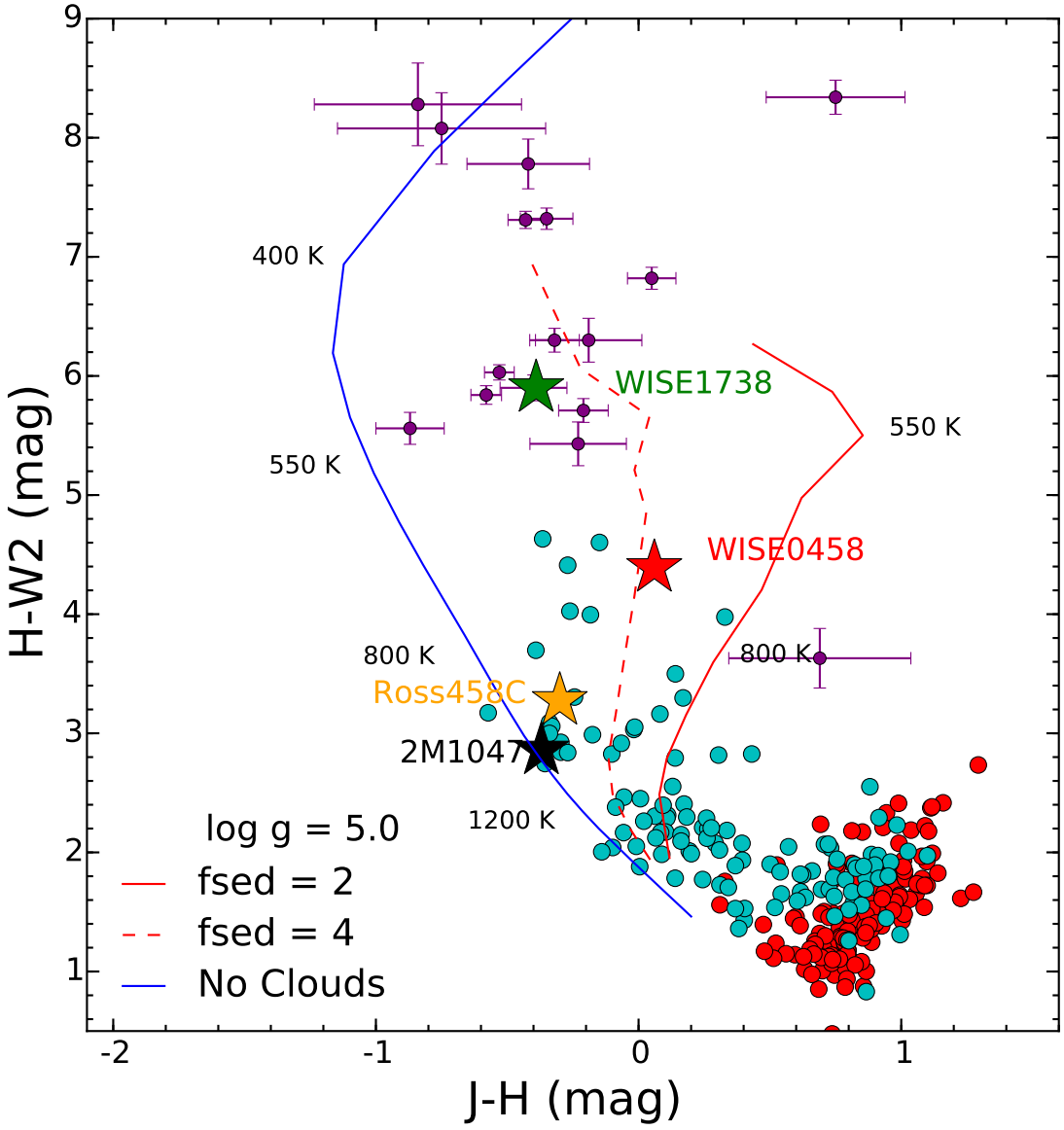

Figure 10. The L (red points), T (cyan points), and Y (purple points) brown dwarf sequence on an MKO J, H and $W2$ ($WISE$ 4.6μm) colour-colour diagram. The blue solid line represents a cloudless atmosphere showing the change in photometric colour with temperature (Saumon *et al.*, 2012). The dashed red line and solid red line represent atmosphere models with an increasing cloud opacity from Morley *et al.* (2012). Magnitudes for the L, T & Y dwarfs are from Dupuy and Liu (2012a); Kirkpatrick *et al.* (2012); Leggett *et al.* (2015). Details of the full sample are given in Table 3.

Table 3. Target list

Target	RA	Dec	J_{MKO} (mag)	SpT	Temperature (K)	Distance (pc)	References
2MASSW J1047539+212423	10:47:53.8	+21:24:23	15.46	T6.5	∼900	10.6	1, 2, 3
Ross 458C	13:00:41.7	+12:21:14	16.71	T8	∼650	11.7	4, 5, 6
WISEP J045853.89+643452.9AB	04:58:53.9	+64:34:51.9	17.47	T8.5[a]	$\sim 600^{a}$	14	7, 6
WISEP J173835.53+273258.9	17:38:35.52	+27:32:58.9	20.05	Y0	430^{+50}_{-40}	9.8	11, 9, 6

a: assigned value is for the binary and not the individual components.

References: [1] Burgasser *et al.* (1999), [2] Burgasser *et al.* (2002), [3] Vrba *et al.* (2004), [4] Goldman *et al.* (2010), [5] Burgasser *et al.* (2010), [6] Dupuy and Kraus (2013), [7] Mainzer *et al.* (2011), [8] Delorme *et al.* (2010), [9] Cushing *et al.* (2011), [10] Liu *et al.* (2011) [11] Leggett *et al.* (2013)

2.2 The BAM-II sample

The sample for this pilot study consists of four ultracool field brown dwarfs which span the late-T to early-Y spectral types (see Figure 10). Table 3 reports the target names, coordinates, *J*-band magnitudes, spectral types, effective temperatures and distances. The targets were discovered as part of large-scale surveys with 2MASS (Burgasser *et al.*, 1999), UKIDSS (Goldman *et al.*, 2010), and *WISE* (Cushing *et al.*, 2011). For this initial study, the targets include objects with a range of properties, including youth (West *et al.*, 2008), radio emission (Route and Wolszczan, 2012; Williams *et al.*, 2013), and binarity (Burgasser *et al.*, 2012).

The colour-colour diagram using near-infrared (J, H) and $WISE$ $(W2)$ filters in Figure 10 shows the variation in colours across the T and Y spectral types. Over-plotted is the clear atmosphere track from Saumon *et al.* (2012) and theoretical models of brown dwarf atmospheres that include the effects of emergent sulfide clouds in the photosphere from Morley *et al.* (2012). Clouds with different values of the parameter $f_{\rm sed}$ have different cloud properties; low $f_{\rm sed}$ indicates smaller grain sizes and higher optical depth. Assuming that these clouds are patchy, we may expect to see more

variability for the objects with colours consistent with more optically thick (low $f_{\rm sed}$) clouds. Our targets span a range of colours and model tracks, ranging from completely cloud-free (blue line), to low $f_{\rm sed}$ (solid red line) atmospheres with optically thick clouds, smaller grains, and larger vertical extent.

2.2.1 2MASSW J1047539+212423

The brown dwarf 2MASSW J1047539+212423 (2M1047) was identified with multi-epoch 2MASS images and classified as a T6.5 dwarf with Keck near-IR spectroscopy (Burgasser *et al.*, 1999, 2002). Using a parallax-based distance of 10.3 pc an effective temperature of ∼900 K was inferred (Vrba *et al.*, 2004). 2M1047 is notable for measurement of radio variability, with bursts measured at a frequency of 4.75 GHz (Route and Wolszczan, 2012), and quasi-quiescent emission at 5.8 GHz (Williams *et al.*, 2013), making it the coolest brown dwarf with measured radio emission. Highly circularly polarised radio bursts lasting ∼100 s were detected in three of the fifteen observations with Arecibo each with a cadence of 0.1 s over ∼2 h. The radio observations were carried out over the course of one year, indicating a persistent source (Route and Wolszczan, 2012). The quasi-quiescent emission was of longer duration (∼40 min), but also two orders of magnitude fainter than the radio bursts. The target was monitored for variability in the J and H bands by Artigau *et al.* (2003b) but did not exhibit any signs of variation. No contemporaneous optical or near-infrared photometric observations were recorded during either of the radio campaigns.

2.2.2 Ross 458C

Ross 458C is the 102 arcsec common proper motion substellar companion to the stellar binary Ross 458AB (Goldman *et al.*, 2010), composed of two M-stars with a projected separation of ∼5 au (Heintz, 1994). The companion was detected in the UKIRT Infrared Deep Sky Survey (UKIDSS; Lawrence *et al.*, 2007) and broad-band/methane filter photometry identified Ross 458 C as a late-T dwarf (Goldman *et al.*, 2010). Subsequent near-infrared spectroscopy determined a spectral type of T8 and effective temperature of ∼650 K (Burgasser *et al.*, 2010). Similar assessments are reported in Burningham *et al.* (2011) and Cushing *et al.* (2011). The distance to the Ross 458 system is $11.7^{+0.21}_{-0.20}$ pc (Dupuy and Kraus, 2013). The stellar pair in the system provides a means to estimate the age through measurements of stellar activity. The age for a field brown dwarf is hard to constrain. Based on the strength of Hα emission, the level of variability (West *et al.*, 2008) and space motion (Montes *et al.*, 2001) of Ross 458AB, the age of the system has been estimated at <1 Gyr (e.g. Burgasser *et al.*, 2010; Burningham *et al.*, 2011). Given the youth of the system, Ross 458C is predicted to be very low mass (5-20 M_{Jup}; Burningham *et al.*, 2011), which overlaps with planetary mass regime. Ross 458C is therefore a benchmark object for the investigation of both brown dwarf and exoplanet atmospheres.

The atmosphere of Ross 458C measured by Burgasser *et al.* (2010) with near-IR spectroscopy reveals evidence of low surface gravity and the authors were able to better fit the near-infrared spectrum with a cloudy atmosphere compared to cloudless. Burgasser *et al.* (2010) initially proposed the clouds in the atmosphere to be the reemergence of iron and silicate clouds, but more recently Morley *et al.* (2012) showed that models including salt and sulfide clouds fits the data better. Models incorporating

both sulfide clouds and non-equilibrium chemistry have not yet been applied to the observational data.

2.2.3 WISEP J045853.89+643452.9AB

WISEP J045853.89+643452.9AB (WISE0458) was the first ultracool brown dwarf discovered by the Wide-field Infrared Survey Explorer satellite (*WISE*; Wright *et al.*, 2010a) in its search for the coldest brown dwarfs in the solar neighborhood (Mainzer *et al.*, 2011). Comparison of the medium resolution near-infrared spectrum of WISE0458 with a grid of cloudless models suggested a very cool effective temperature of ∼600 K (Mainzer *et al.*, 2011). High angular resolution imaging with the Keck laser guide star AO system revealed that the system has a binary companion at a separation of ∼0.”5 and with a magnitude difference of ∼1 mag (Gelino *et al.*, 2011). Recent parallax measurements estimated the objects distance to be 14^{+5}_{-3} pc (Dupuy and Kraus, 2013). AO-assisted spatially resolved spectroscopy confirmed both objects are very late T dwarfs near the T/Y boundary; from the resolved spectra, the primary spectral type is T8.5 and the secondary spectral type is T9.5 (Burgasser *et al.*, 2012). We do not resolve the individual components in this study.

2.2.4 WISEP J173835.53+273258.9

The final target, WISEP J173835.53+273258.9 (WISE1738), is among the first Y dwarfs detected by the *WISE* satellite (Cushing *et al.*, 2011) and is still only one of 18 known Y dwarfs (Kirkpatrick *et al.*, 2012; Leggett *et al.*, 2015). With a spectral classification of Y0 and an effective temperature of 430^{+50}_{-40} K (Dupuy and Kraus,

2013), this object is one of the coldest brown dwarfs discovered. WISE1738 has been selected as the spectral standard for the Y0 class (Kirkpatrick *et al.*, 2012). At these low temperatures water clouds are expected to form (Burrows *et al.*, 2003), potentially leading to variability in the emergent flux. Interestingly, WISE1738 might show long period photometric variability. The object was originally measured to have a J-band magnitude of 19.51 ± 0.08 mag in Kirkpatrick *et al.* (2012), which was subsequently measured to be 20.05 ± 0.09 mag in the recent Leggett *et al.* (2013) study. We adopt the latter magnitude for the purposes of this study. The Leggett *et al.* (2013) study does note the inconsistency in the original Kirkpatrick *et al.* (2012) photometry and suggests that the difference could be due to corrupted Palomar WIRC data. We adopt the Leggett *et al.* (2013) magnitude for the purposes of this study.

2.3 Observations and Data Reduction

This pilot study to monitor brown dwarfs at the T and Y dwarf boundary was initiated at the MMT observatory, with the first epoch of data for each of the four targets being obtained there. Follow-up observations were taken at three different observatories including the Canada-France-Hawaii Telescope (CFHT), UK Infrared Telescope (UKIRT), and the New Technology Telescope (NTT). The details for each of the targets is provided in the observing log presented in Table 4.

2.3.1 MMT

Observations of the entire target dataset were taken with the SAO Widefield InfraRed Camera (SWIRC; Brown *et al.*, 2008) at the 6.5 m MMT Observatory

in Arizona, on the 12th and 13th of March 2012. The camera has an engineering grade 2048 × 2048 HAWAII-2 HgCdTe array, with a plate scale of 0.15 arcsec pixel^{-1}, corresponding to an on-sky field-of-view of 5.12 × 5.12 arcmin. We employed the J-band filter on SWIRC, which closely matches the Mauna Kea Observatory (MKO) J-band filter (Tokunaga and Vacca, 2005). This filter was selected since the largest amplitude variations in known brown dwarf variables occur in the J-band (Artigau *et al.*, 2009b; Radigan *et al.*, 2012b). The observing strategy involved maintaining the target on a single pixel over an ∼20 min timescale with a four-point dither pattern for the purpose of sky subtraction; this sequence was repeated over a ∼1 – 4 hour time period, as summarized in Table 4. All of the raw images were calibrated using median combined darks and flat-field images. The exposure times ranged from 10s to 60s, depending on the target brightness, and the per-frame overhead for the detector was ∼5 s. The SWIRC detector has a scattered light artifact in the lower-left quadrant of the detector which was removed by using a high-pass filter. The SWIRC H2RG-detector is linear to within 0.1 per cent up to 40000 DN and the exposure times were set to ensure that the target brown dwarfs were maintained well below the levels approaching the non-linear regime of the detector. Additionally, comparison stars with peak fluxes greater than 40000 DN were rejected from the analysis.

2.3.2 CFHT

We obtained ∼3 h of data on the T8.5 binary brown dwarf WISE0458 using the Wide-field InfraRed Camera (WIRCAM; Puget *et al.*, 2004) on the 3.5 m Canada France Hawaii Telescope (CFHT). With a plate scale of 0.3 arcsec pixel^{-1}, corresponding to an on-sky field-of-view of 20 × 20 arcmin, there were several tens of

Table 4. Observing log

Target	Telescope	Date	Δt (h)	t_{exp} (s)	Seeing[a] (arcsec)
2M1047	MMT	2012-03-12T04:12:25	1.0	30	0.6
	MMT	2012-03-12T09:37:52	1.9	30	0.8
	NTT	2014-05-15T23:16:45	2.8	10	0.8
Ross 458C	MMT	2012-03-12T07:34:24	1.5	30, 60	0.9
	UKIRT	2014-04-23T07:02:54	2.5	10	0.9
	NTT	2014-05-16T23:42:38	5.3	20, 40	0.9
	NTT	2014-05-20T04:18:56	5.1	40, 50, 70, 90	0.9
WISE0458	MMT	2012-03-13T02:49:59	3.7	45	1.0
	CFHT	2014-03-21T05:50:09	2.7	60	1.0
WISE1738	MMT	2012-03-13T10:04:48	2.3	60	0.8

a: We report the median seeing for each target.

similar-brightness reference stars within the field of each target for the differential photometry calculation. The observations were carried out in a queue-based observing mode in J-band with a median seeing of $\sim 1''$ through most the sequence. The images were obtained in a staring mode, at a 60 s cadence. Per-frame overhead for the detector was ∼6.5 s. The data was dark and flat field calibrated using the 'I'iwi automatic data pipeline from CFHT. The data was then sky subtracted in similar manner as described above, using a median filter (where the stars were first masked) to generate individual sky frames. The CFHT detector is linear to better than a per cent up to 5000 DN. The target and all the reference stars were exposed to less than this limit. Comparison stars brighter than 5000 DN were rejected in the analysis.

2.3.3 UKIRT

The second epoch on Ross 458C was obtained on 23 April 2014 using the Wide-Field infrared Camera (WFCAM; Casali *et al.*, 2007), an infrared wide-field camera on the 3.8 m UK Infrared Telescope (UKIRT). WFCAM has four 2048x2048 array detectors with a pixel scale of 0.4 arcsec pixel^{-1}, corresponding to an on-sky field-of-view of 0.21×0.21 degrees. The observations were carried out with the MKO J-band filter, with seeing of ~ 0.9 arcsec during the sequence. A five-point dither pattern was used, with each individual image having an exposure time of 10 s. Per-frame overhead for the detector was $\sim$1.3 s. The data were calibrated, and the different dithers were combined using the a dedicated pipeline developed by the Cambridge Astronomy Survey Unit (Irwin, 2008). The WFCAM detectors are linear to better than a per cent within 40000 DN and care was taken to ensure that neither the target nor the reference stars used in the reduction were approaching this limit.

2.3.4 NTT

2M1047 and Ross 458C were observed between the 15th and 23rd of May 2014 with Son of ISAAC (SofI; Moorwood *et al.*, 1998) mounted on the 3.6 m NTT (New Technology Telescope). The observations utilized the wide-field imaging mode of SofI, with a plate scale of 0.28 arcsec pixel^{-1}, corresponding to an on-sky field-of-view of 4.92×4.92 arcmin. Per-frame overhead for the detector was $\sim$7.5 s. The NTT detector is linear to >1.5 per cent when objects have less than 10000 DN peak flux. The observations were all obtained using the $J_{\rm s}$ filter, with a two-point AB-AB nodding pattern based on recommendations from the instrument scientist. The flux of the

target, and reference stars within the field, was kept below 10,000 DN to minimise the effects from the detector non-linearity. To limit systematics in the data we used a two-point nod which permitted an accurate estimate of the sky background for the targets. For each object, data reduction consisting of correcting for the dark current and division by a flat field and sky subtraction were applied.

2.4 Light Curve Generation and Identification of Variability

We performed aperture photometry on the calibrated and aligned images from each of the observatories, using the `APPHOT` package in IRAF[1]. For each of the targets in our study we computed the aperture photometry for a range of aperture sizes ranging from radii of 0.6 – 2.0 times the full width half maximum (FWHM), and found that an aperture of 1.0 × FWHM provided the highest signal-to-noise ratio (SNR) across the full sample. Data taken during periods of poor conditions were not included in the analysis; the frame selection caused the gap between epoch 1 and 2 from 2M1047 and limited the W1738 observation period. A catalogue of all the stars in the field of view was generated, which typically included $10 \sim 50$ stars, from which the 15 reference stars most similar in brightness to the target were selected. We chose the similar brightness stars over the brightest stars for two reasons: to limit non-linearity effects, and to ensure that non-astrophysical variations due to weather were more accurately duplicated by the references. The limited field-of-view of the different detectors meant that there were not any objects of the same late-T spectral types to be used as references.

[1]IRAF is distributed by the National Optical Astronomy Observatories, which are operated by the Association of Universities for Research in Astronomy, Inc., under cooperative agreement with the National Science Foundation.

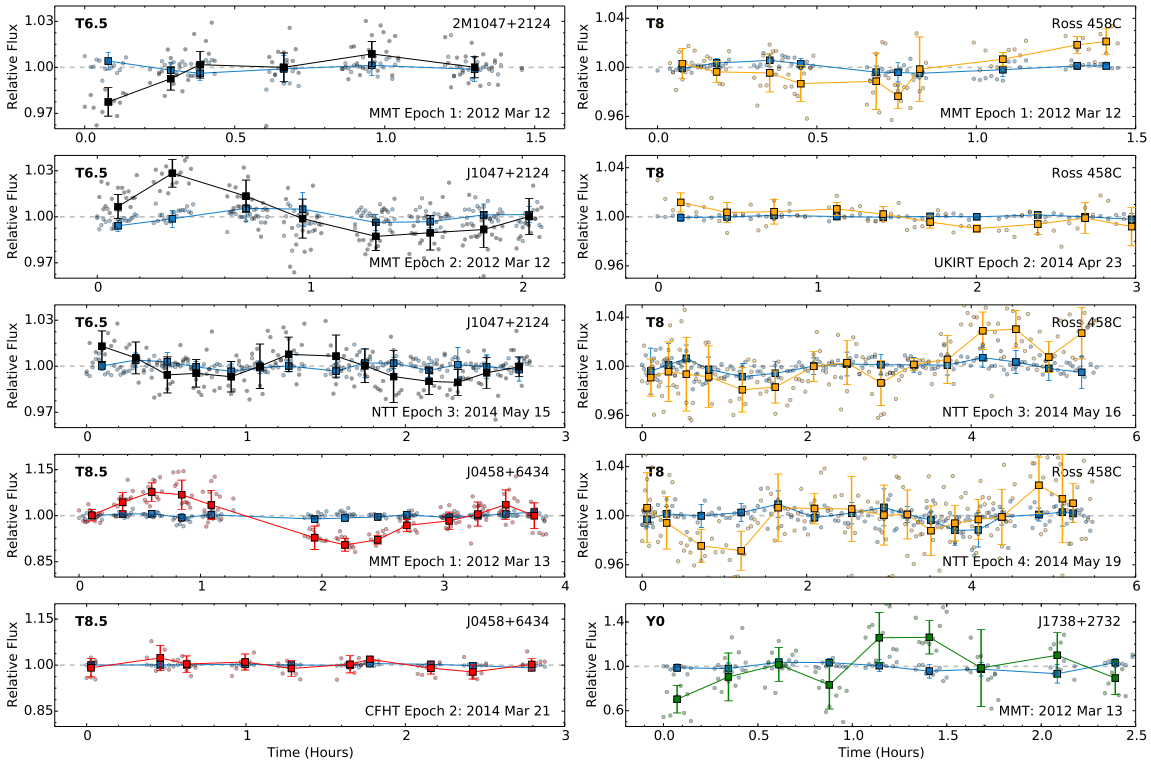

Figure 11. Detrended multi-epoch light curves for each of the targets with the master reference light curve (light blue). Top-left three panels are the different epochs for 2M1047 (black), with the date of observation and telescope noted in the panel. Bottom-left two panels are the same for W0458 (red). Top-right four panels are the multi-epoch observations for Ross 458C (orange). The bottom-right panel is the single epoch obtained for the Y0 brown dwarf WISE1738 (green).

The final target light curves were generated by the photometric pipeline developed as part of the BAM-I survey (Wilson *et al.*, 2014), modified to measure the photometry on each individual image. Measuring the photometry on individual images and taking the median value or forming a median image and measuring photometry on the median combined image did not result in significantly different light curves. The determination of whether the observed flux variation in the target light curve was due to an astrophysical process, required that the objects have a p-value $\leq$ 5 per cent. The p-value is defined as the probability that the final target light curve is the same

(p-value $> 10\%$) or different (p-value $\leq 5\%$) from the master reference light curve i.e. the median combination of all the reference light curves. Calculation of the p-value statistics for each of the light curves was carried out on weighted-mean combined data points where the errors are the 1 σ scatter in each bin, rather than on the light curves composed of the individual photometry points. This was done to ensure that the statistics were not biased by outlier data points with small errors.

2.5 Results

The J-band light curves for each target generated using the observations at each epoch are shown in Figure 11, plotted alongside the master reference light curve used to determine whether variations were observed. The master reference light curve is generated by median combining all the reference star light curves and shows any residual trends common to all light curves. A summary of the results of the light curve analysis, including the peak-to-peak amplitude of any variation and the associated p-value, is given in Table 5. Each light curve is normalised, and variability is only investigated over the time scale of an individual epoch; no attempt to distinguish photometry variations between the individual epochs was made.

2.5.1 2M1047

The time-series photometric measurements for the T6.5 dwarf 2M1047 are shown in the three top-left panels of Figure 11. The first two epochs are separated by $\sim$3.5 h and the final epoch of data was taken 2.2 yr later. None of the three light curves for this target show statistically significant variability, and these results are similar

Table 5. Summary of BAM-II variability study

Object	Spectral Type	Telescope	Duration (h)	Binned Images[a]	References	ν	χ^2_ν	p-value (%)	Amplitude/ Limit[b] (%)
2M1047	T6.5	MMT	0.95	12	7	6	3	20	< 0.8
		MMT	1.88	19	7	10	1.92	10	< 1.1
		NTT	2.75	10	5	15	0.79	98	< 1.0
Ross 458C	T8	MMT	1.78	7	6	11	0.58	10	< 1.1
		UKIRT	2.53	5	7	8	0.36	10	< 0.8
		NTT	5.29	10	9	13	0.41	94	< 1.8
		NTT	5.11	10	7	13	1.12	93	< 2.1
WISE0458	T8.5	MMT	3.68	11	8	12	11.37	0	13 ± 3
		CFHT	2.74	5	14	9	0.21	84	< 2.6
WISE1738	Y0	MMT	2.39	8	10	5	0.9	15	< 20.3

[a]The average number of individual images used to generate the weighted-mean light curves.

[b]For the constant light curves the limit is the 1-σ photometric error of the target light curve. For the variable epoch of W0458, the amplitude is the peak-to-trough value of the best fit sine curve to the data.

to a previous J-band monitoring with the 1.6 m telescope of the L'observatoire du Mont-Mégantic by Artigau *et al.* (2003b). Although there were no contemporaneous radio observations at the time of our J-band imaging, previous measurements of 2M1047 has shown variability at radio frequencies (e.g. Route and Wolszczan, 2012). The radio bursts occurred over a time period of ∼100 s which is less than a single binned data point in the light curves. Radio bursts were recorded three times out of the fifteen observations (2 h each) made with Arecibo, but the current near-infrared data show no intensive brightening over comparable 1–3 h time intervals. In addition to the intense radio bursts, quasi-quiescent fluctuations in the radio emission with a timescale of ∼45 min have been reported (Williams *et al.*, 2013), however these variations were a factor of a hundred fainter than the large bursts described in Route and Wolszczan (2012). Contemporaneous radio and near-IR observations are required to search for any correlation between radio bursts and variations in photospheric flux.

2.5.2 Ross 458C

The four light curves for Ross 458C are given in the top-right panels of Figure 11. The time spans between observations ranged from days to yr, with 2.1 yr from the first to second epoch, 23.7 days between the second and third epoch, and 3.2 days between the third and fourth epoch. No statistically significant variations were detected at any of the four epochs, and the limits on detectable amplitudes ranged from 0.8 to 2.1 per cent. The results suggest that there are no large and persistent storm features that would induce rotationally modulated brightness changes, or that the system is viewed pole-on. The Ross 458C data form the most comprehensive monitoring of the atmosphere of a brown dwarf that serves as an exoplanet analogue.

Ross 458C represents the later stage of atmosphere evolution compared to the younger imaged exoplanets such as HR8799 d and β Pic b that may have similar masses but are substantially warmer due to their younger ages. Ross 458C also occupies an intermediate location in the colour-magnitude diagram between the youngest directly imaged planets and the older, cooler GJ504 b exoplanet (Kuzuhara *et al.*, 2013), but is far less technically challenging to monitor because of the wider angular separation between Ross 458AB and Ross 458C.

2.5.3 WISE0458

The bottom left two light curves in Figure 11 show the dramatic difference between the two epochs of observations for the binary brown dwarf WISE0458. In the first epoch, the target is highly variable compared to the master reference, with a min-to-max amplitude of $\sim$ 17 per cent. The measured variability of WISE0458 is the second highest amplitude brown dwarf observed to date in a brown dwarf, with only 2M2139 exhibiting greater variability (Radigan *et al.*, 2012b). The first epoch of WISE0458 data exhibits a periodic pattern and we fit a series of pure sine waves of different amplitudes and periods to the light curve. The best fit periodic signal with an amplitude of 13.2 per cent and a period of 3 h is shown in Figure 12. The second epoch data on WISE0458 taken after a gap of $\sim$2 yr lacks any detectable variations. Further monitoring of WISE0458 will determine if the large amplitude variations recur.

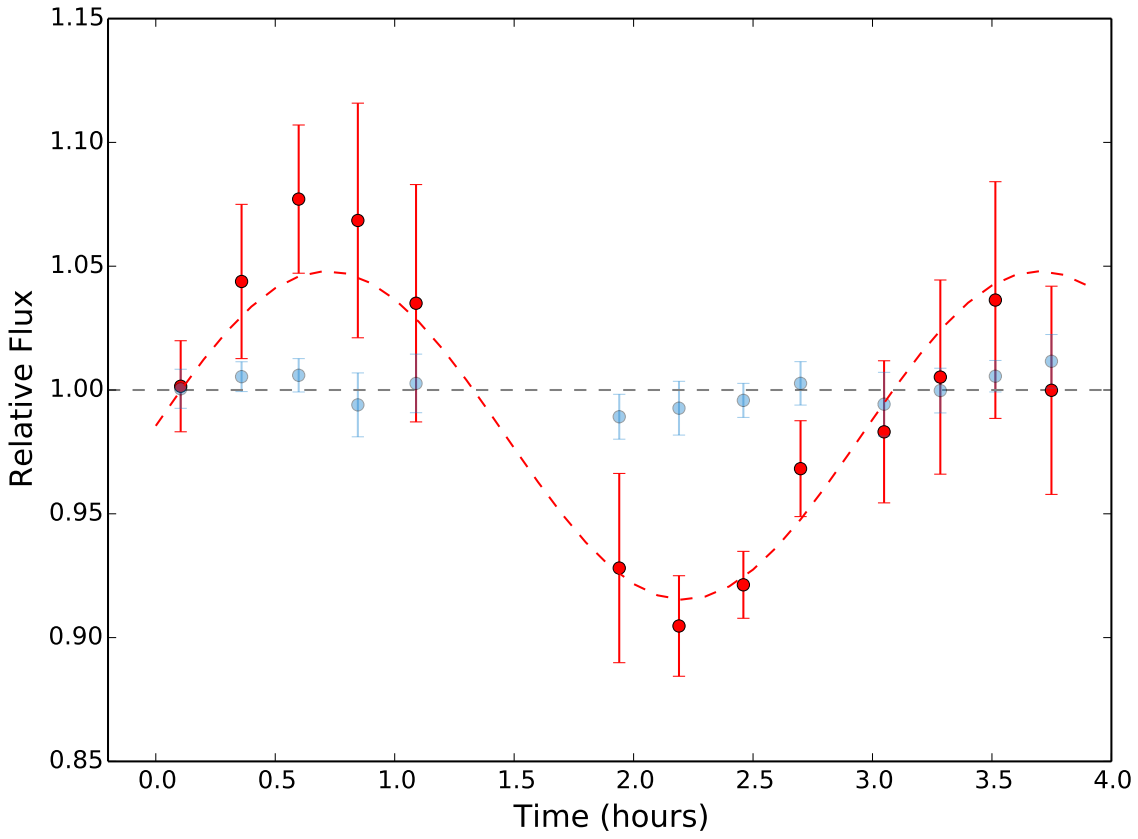

Figure 12. WISE0458 light curve (red circles) for the variable MMT epoch obtained on the 13th March 2012. Also plotted is the best fit sine wave (red dashed line) to the W0458 light curve resulting in a period of ∼3 h with a variable min-to-max amplitude of 13 per cent. The master reference light curve is plotted with the light blue points.

2.5.4 WISE1738

The light curve for the Y0 target WISE1738, shown on the bottom right of Figure 11, is impacted by the large uncertainties and the limited number of data points. During initial planning of the observing run at the MMT, WISE1738 was not expected to be the faintest target in our sample, however, as noted in Section 2, the photometry of this target was re-estimated to be 0.5 magnitudes fainter than originally measured (Leggett *et al.*, 2013). This intrinsic faintness combined with

variable seeing during the observation resulted in low signal-to-noise ratio detections of the target and, consequently, an extremely noisy light curve. The light curve does not show any statistically significant variations, but the limitations in the photometric precision restrict the interpretation of the source as a constant with a large limit on possible variations of < 20 per cent.

2.6 Discussion

The BAM-II study was designed as a pilot program to investigate the coolest brown dwarf atmospheres using multi-epoch photometric monitoring as a probe of the dynamics and surface brightness variations. To place the BAM-II results in the broader context of the brown dwarf population, Figure 14 combines the targets in both this study, and the previous BAM-I survey spanning the full L0-T8 sequence (Wilson *et al.*, 2014). Single epoch BAM-I variables are also included in the comparison. Additional epochs beyond the BAM-I measurements were provided by measurements from a recent large survey of L3-T9 brown dwarfs (Radigan *et al.*, 2014b) and from the more focused studies compiled in the BAM-I paper (Artigau *et al.*, 2009b; Buenzli *et al.*, 2012; Clarke *et al.*, 2008b; Girardin *et al.*, 2013; Khandrika *et al.*, 2013; Koen, 2013b; Metchev *et al.*, 2013; Radigan *et al.*, 2012b).

Nearly all of the amplitudes or limits shown in Figure 14 were measured in the J-band, however five objects include results from different filters, since this was the only way to include more than one epoch for those targets. Both the significant number of objects that switch between variable and constant states and the substantial range

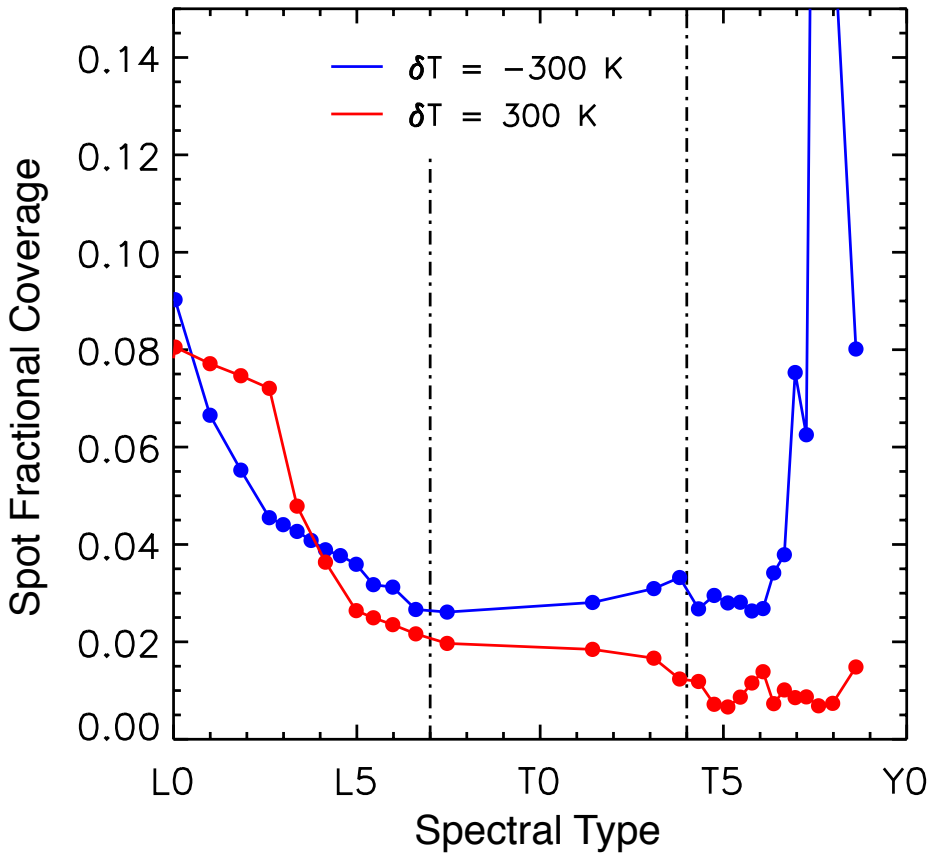

Figure 13. Spot fractional coverage required for a 2 per cent amplitude J-band light curve, plotted as a function of spectral type. The fractional coverage was estimated using the solar metallicity, log (g)=5.0 synthetic spectra within the BT-Settl model grid (Allard *et al.*, 2011). For each $T_{\rm eff}$ within the grid, the fractional projected surface area at a higher/lower temperature ($\Delta T_{\rm eff} = \pm 300$) required to increase/decrease the J-band flux by 2 per cent was estimated. This first-order approximation is analogous to the variability induced by a region of higher or lower temperature rotating in and out of view.

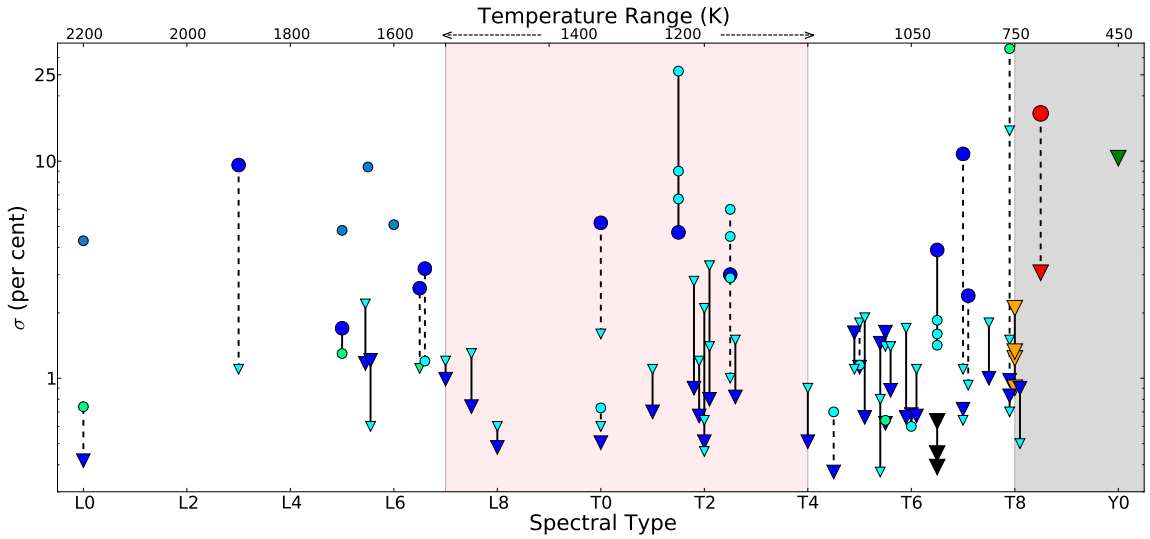

Figure 14. Plot summarizing literature multi-epoch variables and constants. Only objects with multiple epochs are plotted in the figure, with targets coming from (Artigau *et al.*, 2009b; Buenzli *et al.*, 2012; Clarke *et al.*, 2008b; Girardin *et al.*, 2013; Khandrika *et al.*, 2013; Koen, 2013b; Metchev *et al.*, 2013; Radigan *et al.*, 2014b; Wilson *et al.*, 2014). The BAM-II targets are indicated with black symbols for 2M1047, orange symbols for Ross 458C, red symbols for WISE0458 and green symbols for WISE1738. Each vertical line corresponds to a unique object, and solid lines indicate brown dwarfs that remained consistently variable or constant at more than one epoch, while the dashed lines identify the objects that switched between variable and constant states. The shaded regions indicate the L/T transition (pink) and T/Y boundary (gray) regions.

of amplitudes for the multi-epoch variables highlight the dynamic and evolving nature of substellar atmospheres, as well as the need for multi-epoch monitoring. Currently, the best studied case is that of SIMP0136 with monitoring from 2008 to 2012 revealing a remarkable evolution in both the amplitude (from > 5 per cent to undetectable) and the shape (from sinusoidal to multi-component) of the light curve measured over several hours per epoch (Metchev *et al.*, 2013). The BAM-I and BAM-II surveys have identified a set of targets spanning the full L-T sequence that warrant further monitoring.

The variable and constant brown dwarfs with spectral types of T5 and later that

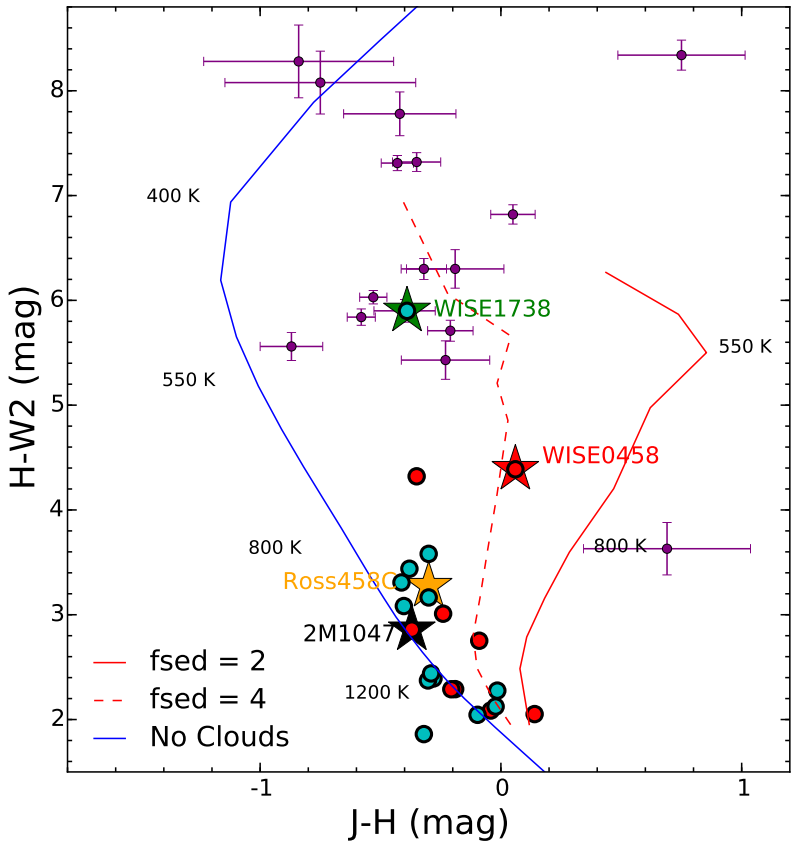

Figure 15. Colour-colour diagram showing the sample (large filled stars) and the Y dwarfs (purple) along with variable (red) and constant (blue) brown dwarfs with spectral type greater than T5 from Figure 14. Figure 10 shows the full sample. The blue line is the theoretical track for clear atmosphere from Saumon *et al.* (2012) and the red lines indicating cloudy atmospheres are from Morley *et al.* (2012). All of the models assume a surface gravity of log(g) = 5.

are included in Figure 14 are plotted on an $(H-W2)$ vs. $(J-H)$ colour-colour plot in Figure 15 to compare with a set of theoretical models (Saumon et al. 2012, Morley et al. 2012). A lack of *WISE* photometry for some targets in Figure 14 limits the number of brown dwarfs from this study that can be plotted in Figure 15. The distribution of the late-T and Y dwarf population in this colour-colour diagram (larger sample in Figure 10) cannot be reconciled with models of cloud-free atmospheres (see Figure 15), and a proposed explanation for the dispersion involves varying amounts of opacity parametrised in the value of $f_{\rm sed}$ (Morley *et al.*, 2012). The redder $J-H$ colour of WISE0458 places the target close to the $f_{\rm sed} = 4$ model with intermediate level of cloudiness as indicated in the colour-colour diagram of Figure 15. The constant targets (blue circles) amongst the late-T objects with multi-epoch measurements presented in Figure 15, appear concentrated near the cloud-free model, and the variables (red circles) appear to have redder and thus cloudier atmospheres. Changes in the $f_{\rm sed}$ values may be linked not only to the colour, but also to the presence or absence of variability. Determining whether or not there is a link between the variability and location in the colour-colour diagram requires a larger set of late-T monitoring observations.

Recent work on synthetic atmosphere models extending to the temperatures of late-T and Y dwarfs ($900-400$ K) has indicated that these brown dwarfs may have sulfide and alkali salt clouds in their photospheres (Morley et al. 2012). Such clouds peak in optical depth for objects with $T_{\rm eff} \sim 600$ K (T9) but persist in objects from 900 K to under 400 K. Three-dimensional models that include radiative transfer and cloud formation have not yet been developed for these cool objects. Idealised 3D-circulation simulations by Showman and Kaspi (2013) suggests that brown dwarfs may have complex circulation patterns on regional and global scales,

generated by the interaction of convective layers with the overlying stably stratified radiative atmosphere, potentially leading to patchy cloud structure. As stated in the introduction, atmospheric circulation models including atmospheric turbulence predict a range of variability amplitudes over multiple epochs for the emitted flux Zhang and Showman (2014). If cool brown dwarfs do have weather patterns causing heterogeneous cloud cover, the Morley *et al.* (2012) models predict that they would show photometric variability in the near-infrared, predominantly in Y and J-bands. Based on the initial results from this study, there is an indication that the variables have redder colours and are concentrated in the region of the colour-colour diagram associated with the atmosphere models more likely to have weather patterns. This suggestive link between theory and observations will be investigated further with larger surveys for multi-epoch variability among the coolest brown dwarfs.

Motivated by recent studies by Robinson and Marley (2014); Morley *et al.* (2014), we investigated what variability of different per cent amplitudes mean in terms of actual hot/cold spot fractional coverage on the brown dwarf photosphere. We ran a simple simulation using the BT-Settl model grid from Allard *et al.* (2011), similar to what was done in Kostov and Apai (2013) but for a larger temperature range. In the simulation we estimated the spot coverage required to produce a particular amplitude of variability as a function of the spectral type, where the spectral types are defined by their temperature. Figure 13 shows the results of a simulated 2 per cent variable, for which the patches have a $\Delta T_{\rm eff}$ of $\pm$300K. The figure indicates that for different spectral types, the spot fractional coverage required to produce the same amplitude of variation can differ by several percent. And amplitude cutoffs to indicate "strong" or "weak" variations might not necessarily indicate higher and lower spot fractional coverage.

Chapter 3

CHARACTERIZING THE ATMOSPHERES OF THE HR8799 PLANETS WITH HST/WFC3

3.1 Introduction

Within the past decade, direct imaging of exoplanets has advanced from initial discoveries of favorable low contrast, planetary mass companions like 2M1207b (Chauvin *et al.*, 2005a) and AB Pic b (Chauvin *et al.*, 2005b) to high-contrast exoplanets around bright young stars like the HR8799 planetary system (Marois *et al.*, 2008, 2010b), β Pic b (Lagrange *et al.*, 2010), and HD 95086b (Rameau *et al.*, 2013a), and GJ 504b (Kuzuhara *et al.*, 2013). Directly imaged exoplanets form a critical subset of the exoplanet population for which it is possible to characterize atmospheric properties from thermal emission. Given the steep, monotonic decline in planet brightness with time (e.g. Burrows *et al.*, 2001), the currently known directly imaged exoplanets (companions to young stars), enable investigations into the early evolution of exoplanets. Imaged young atmospheres also present a valuable comparison to the transmission(e.g. Deming *et al.*, 2005; Sing *et al.*, 2008) and emission (e.g. Charbonneau *et al.*, 2005; Knutson *et al.*, 2007) spectra of intensely irradiated planets orbiting older stars.

HST has been employed successfully in characterizing exoplanet systems for over a decade (Charbonneau *et al.*, 2002; Soummer *et al.*, 2012). We present Wide Field Camera 3 imaging of the multiple planet system, HR8799. The system has four young, massive planets ($\sim$4–7 M_{Jup}) orbiting a $\sim$30 Myr (Zuckerman *et al.*, 2011) A5 star, amenable to both photometric and spectroscopic follow-up. This is the first time

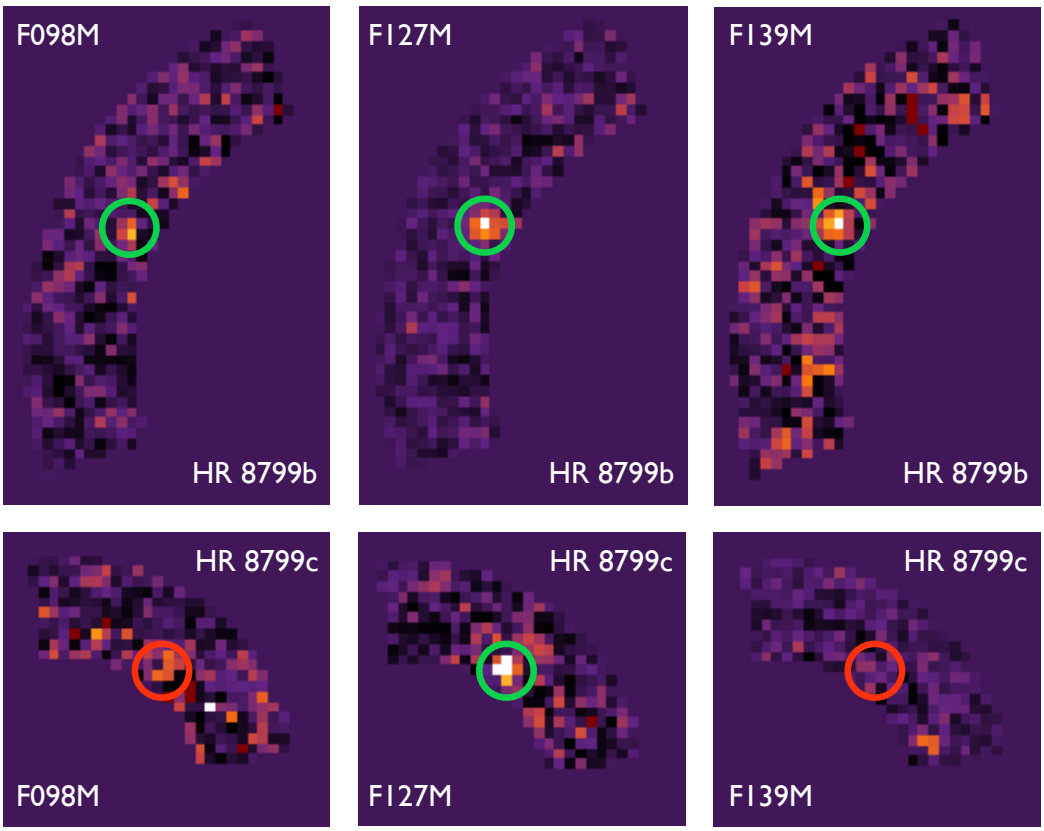

Figure 16. Multi-wavelength *HST* HR8799 data. Top: Image zones with locally optimized KLIP detections of HR8799b in all three filters - F098M, F127M and F139M, respectively. Bottom: Same as above, for HR8799c. HR8799c is only detected in the F127M filter, with upper limits in F098M and F139M.

that planets with high contrasts have been successfully imaged with WFC3/IR, a camera without a coronagraph and undersampled point spread function (PSF). The techniques described in the paper should enable future studies of planetary systems with *HST*. In this paper, we characterize the outer two planets, HR8799 *b* and *c*, by combining the new space-based near-infrared photometric data to the existing suite of ground-based data available for the two planets and discuss the implications of the new photometry.

3.2 Observations

Observations for this study[2] were taken from Nov 2011 to Dec 2012 with the near-IR channel of WFC3 on the *HST*. Due to the brightness of the primary star (J=5.3 mag), all combinations of sub-array and detector readout time results in saturated zeroth read. In the absence of a coronagraph we designed the observations to saturate the central $\sim 0.''5$ of the stellar PSF using 2.2s long observations, focusing the program on the b and c planets.

The HR8799 system was observed in three medium-band filters, F098M, F127M, and F139M over 15 orbits. The orbits were grouped contiguously in sets of three to increase PSF correlation. The observing sequence was designed to maximize the total roll angle and minimize variations in the PSF of the observations over the duration of the program. To maximize the rotation, the star was observed over two different roll angles in each orbit, resulting in observations taken over 30 separate roll angles covering ∼270 degrees (not uniformly sampled) to enable Angular Differential Imaging (ADI) reduction (Marois *et al.*, 2006a). Within each roll, the telescope was dithered using a customized nine-point spiral dither pattern covering a $0.''13 \times 0.''13$ region, with half-pixel dithers (∼64 mas), ensuring a well sampled PSF. This observing procedure enhanced stability, but resulted in reduced total exposure time on the object and a limited range of roll angles within each block of three orbits. At the conclusion of the observing program, the full dataset comprised 270 images in each of the three filters.

[2]GO Program #12511

3.3 Data Calibration

The WFC3/IR images are undersampled data at our wavelengths of interest. The `DRIZZLEPAC` software is the standard tool to improve the resolution of *HST* data, but it not optimal for high contrast imaging since it corrects the geometric distortion prior to improving the resolution of the images, the opposite being more appropriate here. We therefore modified the *ALICE* pipeline (Soummer *et al.*, 2014; Choquet *et al.*, 2014) to include the calibration of dithered WFC3 images.

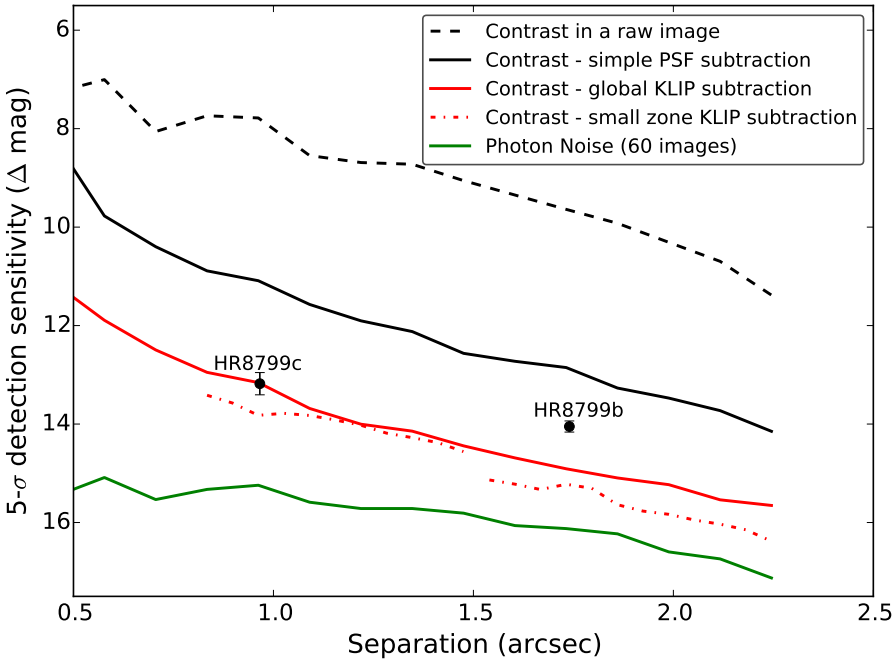

Figure 17. 5-σ HR8799 detection sensitivity with ΔF127M magnitudes as a function of angular separation from the star. The black circles are our photometry values for HR8799bc. The solid red line shows the contrast estimated from a global KLIP reduction and the red dashed segments are contrast levels obtained in the optimized zones. This figure is intended to help preparation of future observations at high-contrast with *HST/WFC3* with the green line indicating the photon noise floor for the full dataset.

The program used a 9-pt spiral dither pattern with 0.5 pixel dither steps. *HST*

pointing stability within a single orbit for small dithers is ∼2–5 mas. Using the WCS information and the "interleave method" (Lauer, 1999), the dithered frames were combined to improve the resolution by a factor of 2 (∼64 mas/pixel). The selected dither pattern does not permit reconstruction of two fully independent images using interleaving and one dithered frame has to be shared between them. The additional time-sampling provided by generating two images per 9-pt dither meant a deeper contrast and was thus preferred over the one image per 9-pt dither case. The upsampled images are then corrected from the detector distorted frame to an undistorted frame using correction maps (J. Anderson, private comm). Finally, the images were aligned by cross-correlating on the diffraction spikes in the data, resulting in 60 aligned and upsampled images.

The data were reduced by the Karhunen-Loéve Image Projection (KLIP) algorithm based on principal component analysis (PCA, Soummer *et al.*, 2012) used in the ALICE pipeline. For each of the 60 upsampled images, the reference PSF library is assembled imposing a minimum rotation of 2×FWHM at planet location to reduce self-subtraction.

We assumed knowledge of the location of the planets and reduced data in local zones around the expected positions for planets b and c, similar to what was done in Soummer *et al.* (2011a). The reduction was performed in annular sections, over a parameter space exploring two radial sizes and three azimuthal widths. With ∼25 KLIP reductions per image our parameter space includes ∼150 images, giving ∼9000 images for each reduction of a given planet/filter combination. We explored a number of geometries and in particular the location of the planet with respect to the zone with best results when the planet is close to the inner edge of the zone.

Each reduced image is corrected for the KLIP throughput loss using forward

modeling, estimated by projecting a *TinyTim* model PSF (Krist *et al.*, 2011a) onto the KL modes, as described in Soummer *et al.* (2012); Pueyo *et al.* (2015). We then compute a data quality criterion as the ratio of the algorithm throughput to a noise estimate with matched-filtering in a local region around the planet. This criterion is therefore proportional to the true SNR, but without introducing any of the planet signal in the calculation so that it does not bias the results by amplifying speckles. The reduced data are ordered according to this criterion and cumulatively-combined using a median. The data quality criterion is then recalculated to determine the optimal number of images in the final image, shown in Fig. 16. This approach permits exploration of any algorithm parameter space to produce a single final image automatically by identifying the best combination of algorithm throughput and speckle suppression.

Photometry was obtained using matched-filtering with a truncated model PSF (5 pix) to reduce potential contamination from local speckles. This matched filter combined with partial truncation of the planet PSF by the reduction zone leads to an incomplete fraction of the planet flux ($\sim 80\%$). All these effects were carefully calibrated using aperture photometry on archival WFC3 data of white dwarfs (GD153, G191B2B) from *HST* calibration programs, and of similar spectral type isolated brown dwarfs. The overall photometric correction precision is of the order of 3-4%, significantly smaller than the final photometric error bars on the planets.

The PSF library is not rigorously free of companion contribution, however the contribution of the companion at other roll angles is limited, since the data is not a true ADI sequence (the orients span the 270 degrees over multiple epochs) and the planets are very faint compared to the PSF wings. In addition, the noise is zero-mean within the reduction zone from KLIP but is not necessarily zero-mean within the

matched-filter equivalent aperture, and small biases may remain. The validity of the forward modeling approach for this particular dataset was investigated by injecting *TinyTim* PSFs in the data at the planets' radial separation over a range of azimuthal angles (25 PSFs for b and 20 PSFs for c). The injected PSF flux was iteratively adjusted to result in the same SNR as each true planet after reduction. The mean photometric error on the synthetic planets was used as a bias correction to account for the two effects discussed above and the error on the photometry was estimated from the standard deviation in the measured signal for each of the fakes. Upper limit detections for HR 8799 c in F098M and F139M were obtained by adjusting the injected PSFs to detect almost all of them.

To ensure the absence of speckle amplification we injected "zero-flux synthetic planets" using the exact same pipeline. No significant detection could be noticed at the location of these injected zero-flux PSFs. Various combinations of reduced images were tested for the presence of flux at given positions as a function of telescope roll angle and reduction parameters, see Soummer *et al.* (2011a) for a detailed description. We estimated the False Positive Fraction (FPF) of 7.6×10^{-22} (SNR $\sim$10) and 3.8×10^{-7} (SNR$\sim$5.3) for b and c in the F127M filter assuming Gaussian statistics. We also calculated an FPF of 2.7×10^{-11} (SNR$\sim$7) and 1.3×10^{-4} (SNR$\sim$4) for b and c in F127M filter assuming a small number of resolution elements using the Student's t-test relation presented in Mawet *et al.* (2014).

3.4 Results

Contrast curves for the data in the F127M filter are shown in Fig. 17, the figure indicates the contrast achieved using different analysis techniques and the contrast in

the global-KLIP and small-zone KLIP reductions. The global-KLIP reduction is not used in our analysis, we present this contrast curve estimate to guide future possible studies at high-contrast with *HST/WFC3-IR*. The measured `VEGAMAG` photometry for the detections and 1σ limits is presented in Table 6 using revised zero-points[3]. The photometry of the planets is compared with brown dwarfs measured in the same *HST* filters in the color-magnitude diagram in Fig. 18. The positions of the planets in Fig. 18, verifies that the flux measurement for the planets do not deviate unrealistically from the brown dwarfs. The spectral type derived for each planet is dependent on the contrast between J and water band fluxes being similar to that measured for brown dwarfs. Using a relation converting *HST* photometric colors to a spectral type from Aberasturi *et al.* (2014)[4], we calculate a spectral type of L9.5 $\pm$ 0.5 for HR8799b and >L7 for HR8799c. The errors are the quadrature sum of the intrinsic scatter in the relation and the error in the photometric color. The larger role of clouds in giant planets with temperatures comparable to cloud-free brown dwarfs complicates the conversion of the color-magnitude position into spectral types. The following two subsections model the combined *HST* photometry with measurements from the literature at different wavelengths to determine the atmospheric properties.

3.4.1 HR8799b

The *HST* data in F139M provide the first detection of the planet b in the water absorption region at 1.4μm. Additionally, the photometric points in F098M and

[3]Revised ZP: F098M = 24.2209 mag, F127M = 23.7503 mag, F139M = 23.7679 mag

[4]SpT=1.56-6.25*(F127M-F139M)

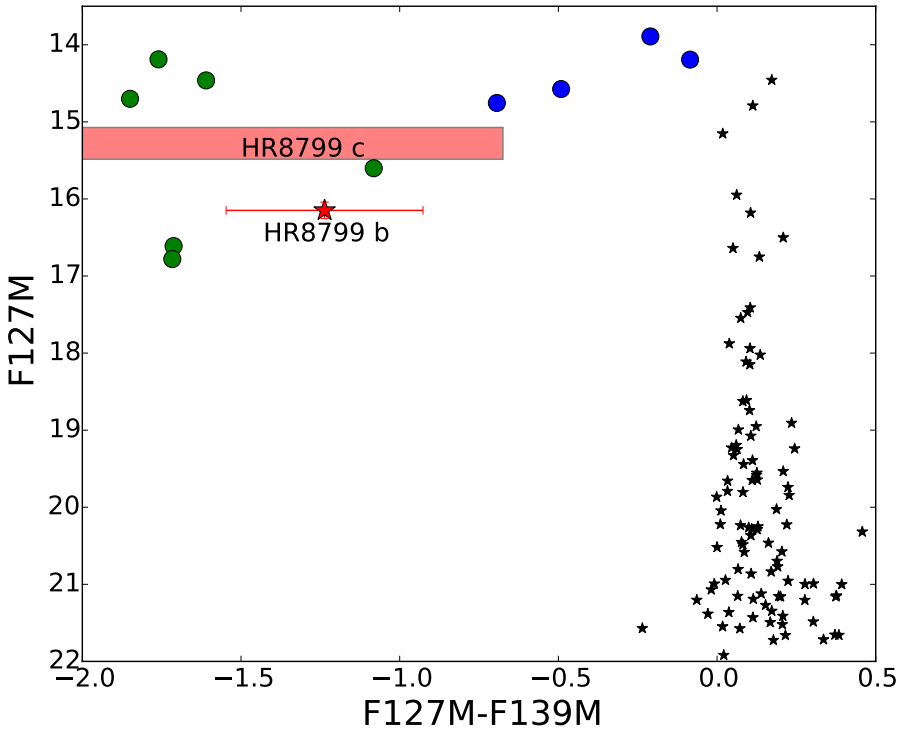

Figure 18. *HST* near-infrared color-magnitude diagram. The HR8799bc planets (red star, shaded region) are plotted with field L (blue circles) and T (green circles) brown dwarfs from recent *HST* studies (Aberasturi *et al.*, 2014; Apai *et al.*, 2013; Yang *et al.*, 2014). The black points are background field targets. The red rectangle for *c* represents our upper-limit estimate.

the peak of the *J* band (F127M) are consistent with measurements taken across similar wavelengths with ground based instruments (Currie *et al.*, 2011a; Marois *et al.*, 2008; Oppenheimer *et al.*, 2013). We combine the new *HST* data with photometric data available in the literature and fit the fluxes to synthetic model spectra from Barman *et al.* (2011, 2015) (cited as B15 in the rest of the paper). The models include clouds located at the intersection of the pressure-temperature profile and the chemical equilibrium condensation curve with a parameterized thickness but a homogeneous distribution in latitude and longitude across the planet. The models also include non-equilibrium chemistry for all important C, N and O bearing molecules, as well as

updated line lists for CH4 and NH3 (see B15 for details). The particle size-distribution is centered on 5μm following a log-normal distribution.

Figure 19 (top) shows two fits for the HR8799b photometry, the best fitting model to the F139M (black line), and the best fit to the [4.05] point (Currie *et al.*, 2014b, green line). No individual model was able to fit the pair of neighboring fluxes at either F127M and F139M or L' and [4.05]. The discrepancy may indicate missing physical processes in the model and the data is complicated by the non-contemporaneous measurements. Although the [4.05] band covers the Br-α line, accretion is unlikely due to the lack of Br-γ emission in the K-band spectrum (Barman *et al.*, 2011). The ratio of F139M flux to F127M flux may be useful for estimating the combined effects of cloud size distribution, cloud thickness and coverage. However, effective temperature, gravity and composition will need to be better constrained to avoid degeneracies in the model fitting and better agreement with evolutionary models.

Fitting a combination of near-IR spectroscopy and IR photometry, B15 found a best matching model with T_{eff} = 1000K and log(g) = 3.5, with potentially subsolar water abundance and enhanced C/O, however, the uncertain surface gravity results in a wide spread of values including solar metallicity. In this paper, the cooler best-fit model has solar abundances and we find T_{eff} = 1000–1100 K and log(g) = 3.0–4.5, indicating consistency between photometry-based fits and those including spectroscopy. Our measured water band flux, relative to J-band, however, is brighter than predicted by all of the non-solar models explored by B15, suggesting that perhaps clouds play an important role.

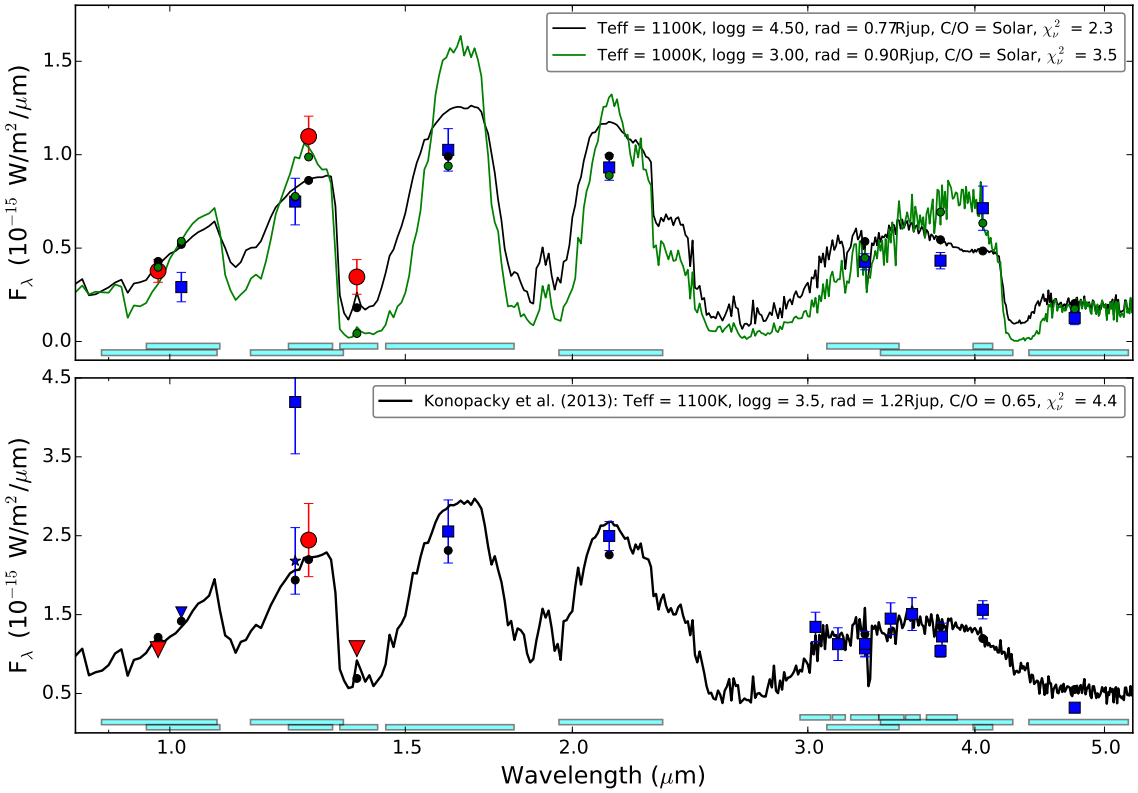

Figure 19. Top: Model fits to HR8799b data. In the figure the red circles are *HST* photometry, and the blue squares are ground-based photometry, with the filter width shown as cyan bars at the bottom of the plot. The black and green lines (and corresponding circles) are the model spectra fitted to the full dataset. Bottom: The black line is the Konopacky *et al.* (2013) HR8799c model. The ground-based photometry in this paper comes from Marois *et al.* (2008); Currie *et al.* (2011a); Oppenheimer *et al.* (2013); Currie *et al.* (2014b); Skemer *et al.* (2012, 2014); Galicher *et al.* (2011). The blue star for HR8799c is the *J*-band photometry from Oppenheimer *et al.* (2013).

3.4.2 HR8799c

For HR8799c we measured the photometry in the F127M band and upper limits were determined for the F098M and F139M filters. The F127M flux is consistent with values obtained by integrating the spectrum from P1640 over the same wavelength range (Oppenheimer *et al.*, 2013), but substantially lower than the reported J-band photometry (Marois *et al.*, 2008). The new *HST* data were combined with similar and longer wavelength fluxes from the literature to construct the spectral energy distribution given in Fig. 19 (bottom). Plotted with the data is a model with T_{eff} = 1100K, log(g) = 3.5 and elevated C/O that fit the K-band spectrum from Konopacky *et al.* (2013). The fits agree well with the *HST* photometry and the longer wavelength data with the exception of a significant difference with the earliest measurement of the J-band photometry and an $\sim 2.5\sigma$ difference with the [4.05] data point. Our models for HR8799c with homogeneous cloud model agree, within the uncertainties, with the *HST* photometry and longer wavelength data out to $\sim 3.5\mu$m with the exception of the first epoch of J-band photometry[5]. The difficulty in fitting all available photometry with reported uncertainties persists even when using patchy cloud models formed by combining clouds at different temperatures (Skemer *et al.*, 2014) or opacity (Currie *et al.*, 2014b) and the *HST* F127M measurement is more consistent with the patchy cloud models. Our attempts with a linear combination of models did not provide a better fit than the homogeneous cloud model with higher C/O ratio presented in Fig. 19 (bottom).

[5]Improved analysis techniques and stellar variability cannot account for the factor of two difference in flux

Table 6. HR8799bc absolute photometry

Planet	HST Photometry		
	F098M	F127M[a]	F139M
HR8799b	16.90 ± 0.18	16.20 ± 0.12	17.36 ± 0.26
HR8799c	>15.72	15.38 ± 0.17	>16.16

a: P1640 spectrum through the F127M filter gives, HR8799b = 16.16 ± 0.27 and HR8799c = 15.17 ± 0.08.

3.5 Discussion

Among the *HST* filters, the F127M is the most analogous to a ground-based filter and can be directly compared to previous results reported in the J-band. The HR8799b F127M photometry is consistent with previous results (Marois *et al.*, 2008). There are two prior reported values for HR8799c - a P1640 spectrum (Oppenheimer *et al.*, 2013) and a Keck J-band flux (Marois *et al.*, 2008). The ground-based J-band photometry for HR8799c is approximately twice as bright as the measured *HST* flux. Integrating the HR8799c flux calibrated P1640 spectrum through the F127M filter matches the *HST* photometry to within 2-σ. A potential solution for this discrepancy might be intrinsic photometric variability caused by heterogeneous cloud layers, which we find is not required in our model fits. The early groundbased photometry might also have suffered from calibration issues which combined by the intrinsic variability of the star might explain some of the difference in flux measurement.

Efforts to match synthetic spectra to the ensemble of photometric data for HR8799b result in high effective temperatures and corresponding radii that are smaller by ∼50% (0.69 - 0.92 R_{Jup}), than predicted by theoretical brown dwarf and giant planet cooling tracks (see Marley *et al.*, 2012, for a summary). Difficulty finding a model spectrum that simultaneously matches the near and mid-IR photometry could be due to the non-contemporaneous nature of the observations or perhaps the model-observation

inconsistencies at multiple bands are an indication of large-scale flux variations. Large variability would bias such model comparisons. For example, the bright J-band flux from Marois *et al.* (2008) is more consistent with higher effective temperatures than our *HST* F127M flux. The deep water absorption demonstrates that the atmospheres of both b and c are not enshrouded in high altitude hazes or clouds many pressure scale heights thick, important for many transiting exoplanets (Kreidberg *et al.*, 2014). Nonetheless, clouds are important in shaping the overall SED of the planets. Both best-matching models plotted in Fig. 19 (top panel) have clouds composed primarily of Iron and Magnesium-Silcate grains, located in the near-infrared photosphere. The cooler model has a cloud located at Pgas $\sim$ 1 bar and extending upward 1 pressure scale-height. The warmer (and higher gravity) model has a cloud base near 10 bar, extending upward 2 pressure scale heights. Using single models to reproduce the observations assumes global cloud coverage which is probably an overestimation.

With spectral energy distributions well sampled observationally and with model spectra that match reasonably well, the bolometric luminosities of both planets can be estimated, and we determine L_{bol} values of -5.1$\pm$0.1 for b and -4.7$\pm$0.1 for c consistent with Marois *et al.* (2008).

3.6 Conclusions

In this study, we have demonstrated that WFC3 is capable of investigating the atmospheres of planets requiring high contrast at wavelengths either inaccessible from the ground or at which the extreme adaptive optics systems perform poorly. With its photometric stability, *HST* provides a valuable resource to explore exoplanet atmospheres and will enable measurements such as the search for atmospheric variability.aw

The data from the current program can be used to build a PSF library for future high contrast imaging programs. Based on experience from the current program future studies would benefit from obtaining more exposures rather than performing the time-consuming in-orbit roll.

In this study, we were able to detect HR8799b in three WFC3 filters. In this work and in other studies, matching all of the data simultaneously has not been possible. In particular, some of the shortest wavelength data favor warmer conditions while some of the longer wavelength IR data favor cooler conditions, possibly caused by clouds. For HR8799c, we find very good agreement between the model fit with the F127M, resolving the long standing difficulty of fitting the previously reported J-band photometry. A possible explanation for the F127M and J-band flux difference is variability. Future spectrophotometric monitoring of HR8799b and HR8799c in the near and mid-IR might resolve whether the planets are variable over the duration of a single rotation period.

Chapter 4

THE GPIES CAMPAIGN AND SEARCHING FOR A CIRCUMPLANETARY DISK AROUND HD 106906B

The Gemini Planet Imager (Macintosh *et al.*, 2014) is a facility instrument on the Gemini South telescope designed to image exoplanets at separtions of 5–30 AU, inaccessible for most stars with the previous generation adaptive optics instruments. One of the largest concerns for directly imaging exoplanets, is suppressing the flux from the star. A young ($\sim$10 Myr), 2–4 M_{Jup} planet has a contrast of 10^{-6} compared to the star. When imaging a star with a ground based telescope, a few things that need to be corrected for are the atmospheric turbulence which induces large wavefront error and scattering of the light once it enters the telescope. The Gemini Planet Imager (GPI) is one of the first of the next-generation coronagraphic instruments that are designed to maximize the suppression of stellar flux and "quasi-static" speckles through a multi-pronged approach with the goal of directly imaging planets. The adaptive optics (AO) system on GPI provides significant improvements when compared to the previous generation Keck AO system, for e.g. GPI regularly achieves 90 – 120 nm of wavefront error compared to $\sim$250 nm on Keck (van Dam *et al.*, 2004). The GPI AO system employs a "woofer-tweeter" system of deformable mirrors (DM) in combination with a Shack-Hartmann wavefront sensor in order to correct the optical wavefront. Here the woofer is a piezoelectric DM designed to correct low-order wavefront aberrations and the tweeter is a high-order 4096 actuator MEMS DM. GPI uses an Apodized Pupil Lyot Coronagraph (APLC) that was designed to maximize the achromaticity over the bandpass of interest while still providing $> 10^{-7}$ contrast at separations greater than

$5\lambda_0$/D (Soummer *et al.*, 2011b). A significant source of uncertainty with traditional coronagraph systems is the location and brightness of the star behind the mask. To circumvent this issue, GPI has a square grid of narrowly spaced lines printed on the apodizer, these act as a diffraction grating that generate copies of the stellar point spread function at controlled locations, referred to as "satellite spots", in the science image (Sivaramakrishnan and Oppenheimer, 2006). Where the location of the satellite spots is determined by the periodicity of the grating relative to the full pupil diameter, and the brightness depends on the line width relative to the line spacing. The science camera on the Gemini Planet Imager is a near-IR Integral Field Spectrograph with 2.8×2.8 arcsecond field of view, producing spectral cubes across the $YJHK$ bands with spectral resolutions of $\Delta\lambda/\lambda$=30–70.

The Gemini Planet Imager Exoplanet Survey (PI: Macintosh; Macintosh *et al.*, 2014), is a 890 hour campaign that makes use of the improved stellar suppression of the Gemini Planet Imager to find exoplanets. The campaign is designed to observe ∼600 young, nearby stars, at high sensitivity, optimized to detect and characterize 1–10 M_{Jup} planets. The primary goal of the survey is to measure the abundance of young Jovian planets at separations of 5–50 au from the parent star as a function of stellar mass, age and infrared excess. Further, for the planets (and sub-stellar companions) detected, measure the astrometry to estimate the orbital motion and $YJHK$ spectroscopy to characterize the atmospheric properties. The GPIES campaign is currently ∼2 years in, with over 300 stars out of the 600 star survey observed, see Figure 20. The initial search is conducted in the H-band with typical sequences being ∼1 hour long centered on meridian passage to maximize the field of view rotation. Each hour long sequence has 36–40 individual exposure taken with 60 sec exposure time. Follow-up of potential planet-mass candidates is conducted separately, typically the follow-up observations

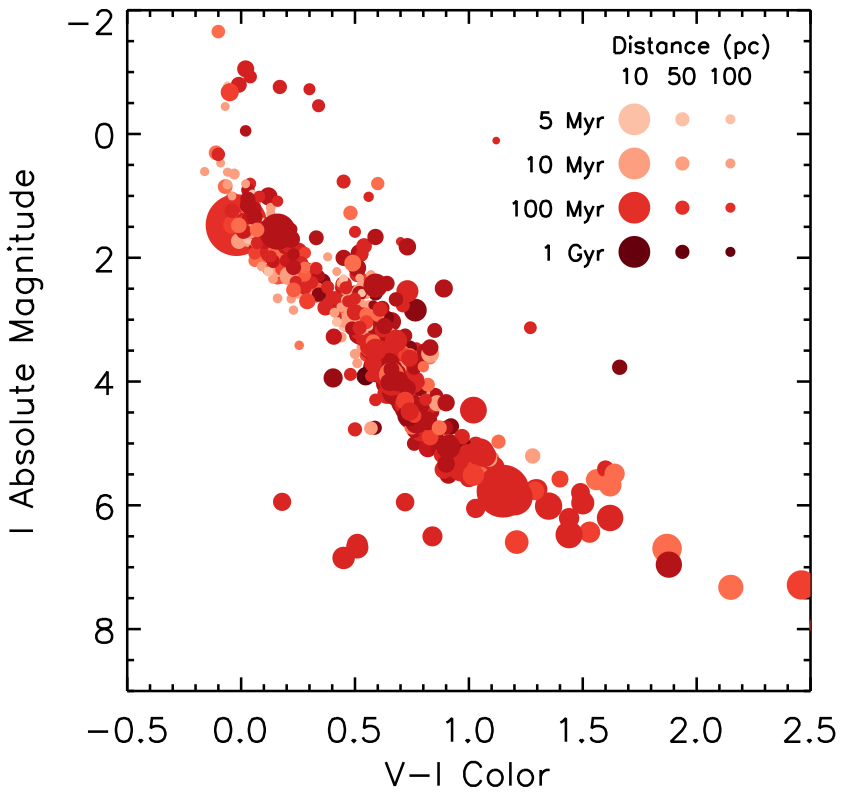

Figure 20. HR diagram for the stars included in the GPIES campaign. The circles are color coded to indicate youth, with lighter shades for the youngest stars and darker shades for the oldest stars. The circle sizes show the distance to the star, with the closest stars having the largest circles and vice versa. Permission to reproduce figure granted by R. De Rosa.

are conducted with sufficient gap from the initial epoch to confirm that the companion is co-moving. When merited multi-wavelength observations are taken to classify the spectral type of the detected companion.

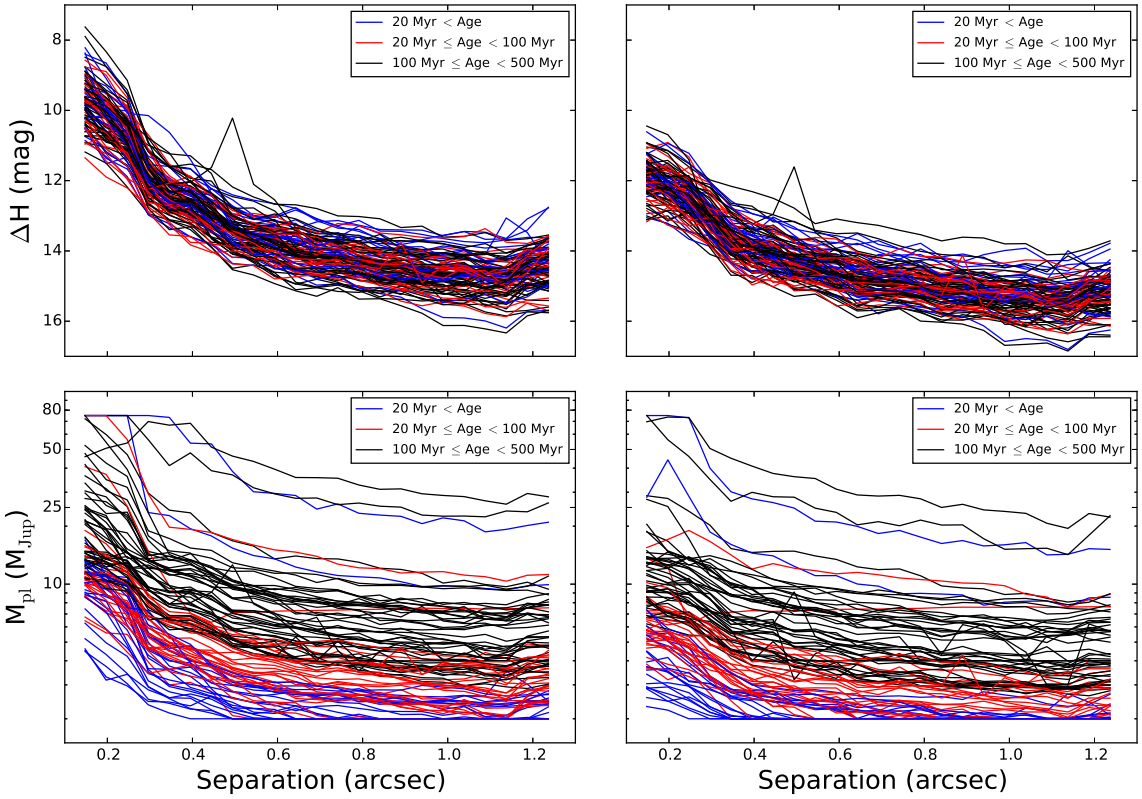

Figure 21. 5σ contrast curves for a subset (95 stars) of the observed GPIES stars and planet sensitivity of the same data. GPIES datacubes are combined with a weighted average, assuming an early L-type and mid T-type spectral shape for the weight. **Top-Left:** Contrast curves where the data was combined assuming the flatter early L-type brown dwarf spectral template. **Top-Right:** Assuming the mid T-type spectral template. **Bottom:** Planet detection sensitivity of the survey computed by taking the contrasts shown above and converting to mass estimates using the BT-Settl grid (Allard *et al.*, 2012a).

4.1 Understanding the GPIES contrast budget

During the original survey design of GPIES, the expected 1σ contrast for an hour of data was between 10^{-8}–10^{-7} at $\sim$0.4″ for stars between 4 to 8 mag in I-band (Graham *et al.*, 2007). Plotted in Figure 21 are the final post processed contrast curves for a

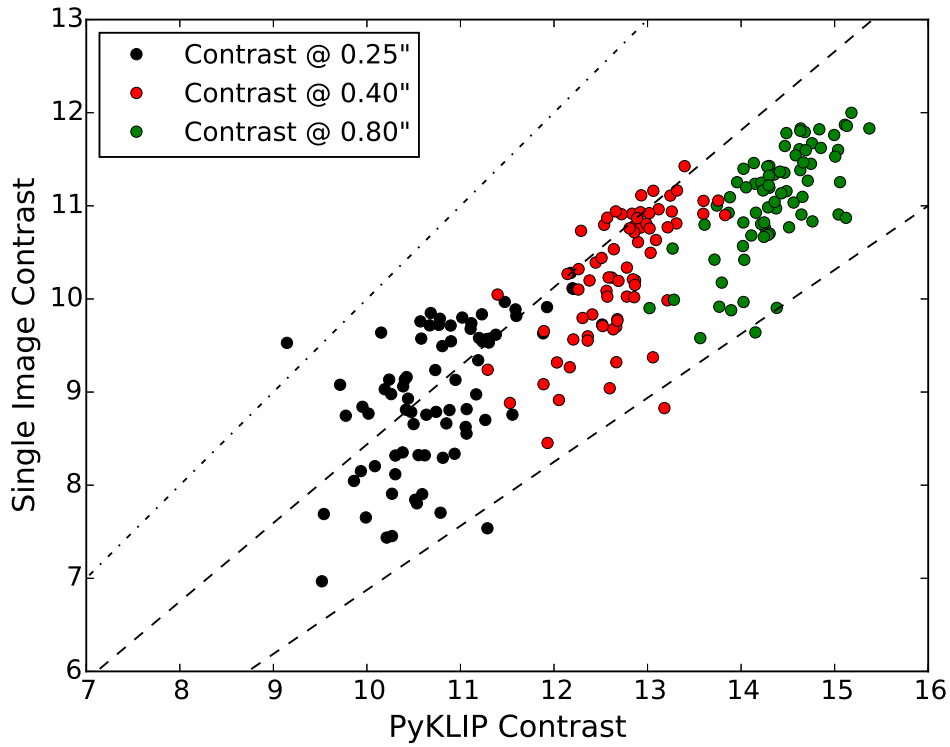

Figure 22. Comparing the median 5σ raw contrast for all the data taken in a sequence against the final post-processed 5σ contrast, assuming the L-type spectral template, at the same separations. The lines plotted in the figure indicate the 1:1, 1:10, and 1:100 factors of improvement. The roughly linear trend suggests that the mean raw contrast can be used to approximate the final post-processed contrast.

subset of the GPIES stars observed thus far. Each individual contrast curve indicates a single, approximately hour long sequence of a star observed in campaign mode i.e. 20 – 40 images, where each image has an exposure time of 60s. The data is reduced using the `pyKLIP` implementation of the Karhunen-Loève Image Projection algorithm (Soummer *et al.*, 2012; Wang *et al.*, 2015). In both top panels, the final reduced IFS datacubes are collapsed using a weighted average, using either the spectrum of an L-type brown dwarf (left) or a T-type brown dwarf (right) to weight the H-band spectrum. The L-type spectrum shape is flatter when compared to the T-type which is why the contrast improves at close separations. The two panels in the bottom show

how the contrast curves affect the campaign sensitivity to detecting different planetary mass companions. The 5σ contrasts shown in the top two plots are converted to mass estimates using the BT-Settl model grid (Allard *et al.*, 2012a). For the L-type spectral template: 72% of the data is sensitive to companions with masses < 20 M_{Jup} across the full GPI field of view and 19% are sensitive to planets < 10 M_{Jup}. For the T-type spectrum: 92% of the targets are sensitive to companions with masses < 20 M_{Jup} across the full GPI field of view and 68% are sensitive to planets < 10 M_{Jup}. Two things are obvious from Figure 21, first the spread in contrast between the best curve and the worst curve is quite large, $\sim$2 mag, and second the on-sky performance of the Gemini Planet Imager does not match the original predictions by greater than an order of magnitude.

As part of campaign operations to improve the instrument contrast, the team initiated investigations into understanding the largest contributing factors affecting the contrast and exploring methods of either remedying the issue or modifying the conditions under which the campaign is observed. The survey infrastructure is setup so that as data is collected at the telescope, it is immediately archived on Dropbox and the header information along with other diagnostic information including the contrast at different separations are ingested into an SQL database. The Gemini Observatories operate primarily on a queue-based mode. However, GPIES is observed in "priority-visitor" mode; where the team has access to the instrument in stretches of 5–6 days only observing when conditions are suitable. This has several consequences for the campaign, the main one being to understand the effect of atmosphere and telescope conditions on the final sensitivity to planet detection. Aside from that, understanding when to observe and when to hand the telescope back to the queue to save campaign hour are also of great importance. In the following section we show

how the realtime science data processing permits analysis of the data and making these decisions.

4.1.1 Raw and Final Contrast

Plotted in Figure 23 are histograms for the 5σ contrast in single, 60 second GPIES exposures taken over the course of the survey. The raw contrast values are estimated at three separations, $0.25''$, $0.40''$, and $0.80''$ respectively. The 60s IFS cube is median combined to generate a single image for estimation of the contrast. The contrast is then, the ratio of the standard deviation in an annulus centered on the star at the three separations of interest relative to the satellite spot flux measured in the same image. The raw contrasts are separated in magnitude bins and show a clear trend of worsening contrasts as the stars get fainter. Also plotted is the median value for each separation and each magnitude bin with a colored dashed line. An obvious trend in the contrast histogram is the worsening of the instrument performance in the last two magnitude bins, $I > 8$mag. This is caused by the AO system switching from 1 KHz readout to 500 Hz to enable faint star operation, which results in lower AO performance for stars fainter than 8th mag. The second is that at $0.25''$, the contrast is roughly independent of stellar brightness, a consequence of the data being dominated by the "quasi-static" speckle noise. At $0.80''$, the data is mostly background-limited and contrast varies almost linearly with star brightness.

As shown in Figure 21, the sensitivity/ability of the survey to detect companions can be directly tied to the final post processed contrast. However, the final contrast curve for each dataset is only available after completing a sequence on a target and is thus unavailable to inform the observers while the data is being taken. Plotted in

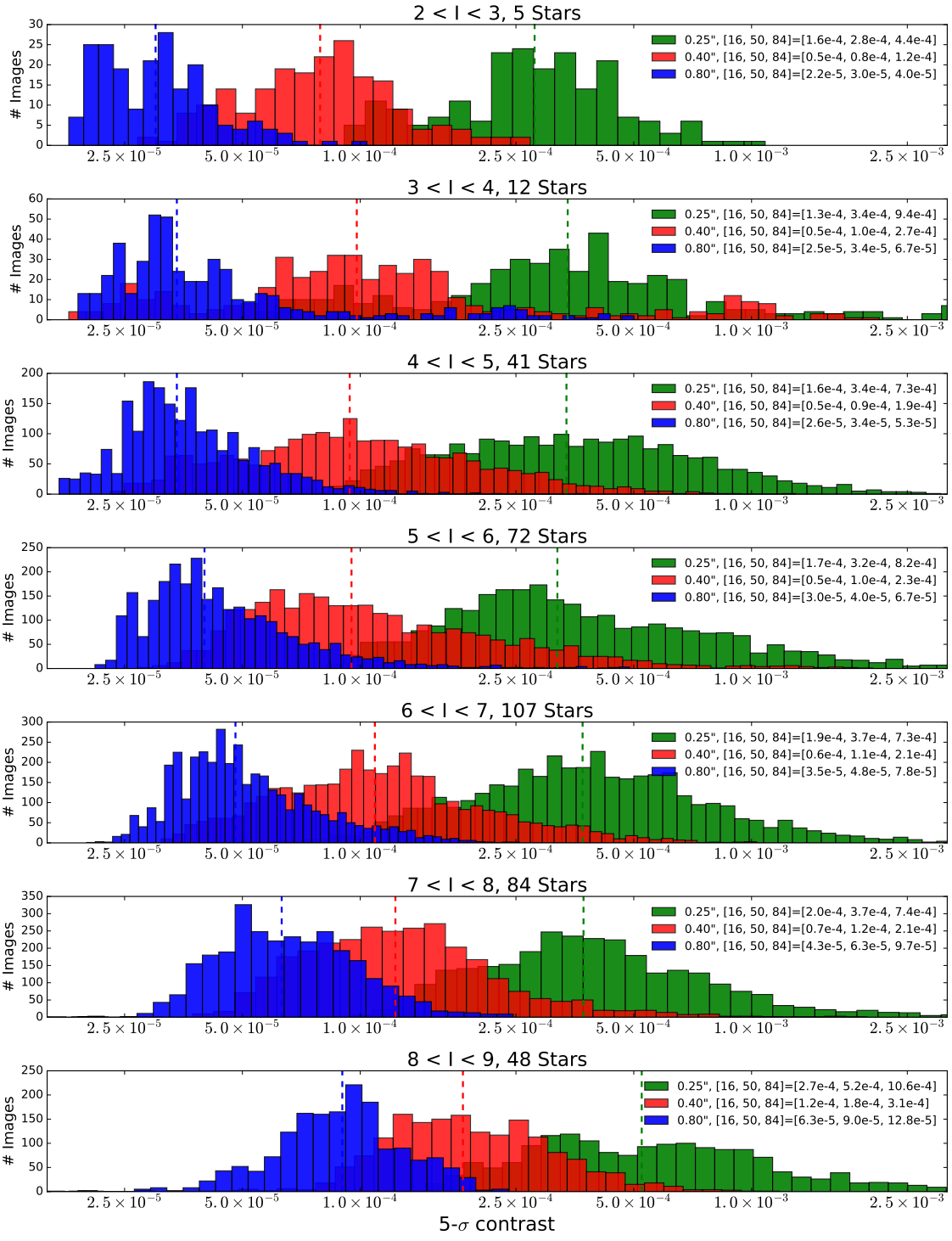

Figure 23. Histogram of the estimated 5σ contrast in each single 60s image as a function of the stars I-band magnitude. The contrast values are estimated at three separations in the raw images, $0.25''$, $0.40''$, and $0.80''$ respectively. The stars are separated into magnitude bins and for each bin the 16, 50 and 84th percentile values are indicated in the legend.

Figure 22 is a comparison of the final contrast obtained in each hour long H-band campaign sequence against the median of the raw contrasts for 20–40 exposures that are part of the sequence. The final contrasts are on average at least $10\times$ better than the average raw contrasts. The encouraging aspect, is that despite the advanced image processing applied to the final images, there appears to be an approximately linear trend between the raw and final contrasts. Thus trends noticed in the final post processed contrast curves can be compared against environmental parameters measured during the observations to derive correlations that can be applied to the raw data and contrasts estimated in the raw data to make informed decisions while observing.

4.1.2 Comparing contrast to header values

The Gemini South telescope populates every science image header with range of atmospheric and environment parameters that are typically measured in real time. In this study we investigated correlations between the final post processed contrast and a subset of these header values. The parameters studied include the brightness of the source, total integration time at the end of the sequence, airmass of the target, RMS wavefront error, total field of view of rotation, seeing estimates from the Differential Image Motion Monitor (DIMM; Sarazin and Roddier, 1990) and Multi-Aperture Scintillation Sensor (MASS; Kornilov *et al.*, 2003), coherence time (τ_0), which is defined as the time it takes a turbulent cell to move a third its length, and the wind speed measured on the secondary mirror of the telescope.

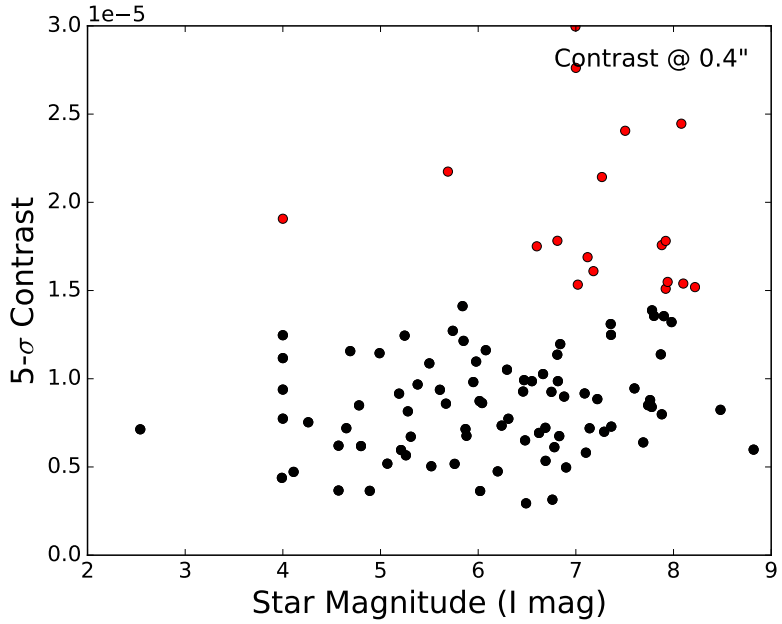

Figure 24. Plotted in the figure are the 5σ final contrast at $0.4''$ as a function of the star I-magnitude. Points with contrast $>1.5\times10^{-5}$ are colored with red circles. Typically, these low contrast values tend to occur for the faintest stars.

Plotted in Figure 24 is the 5σ contrast as a function of the I-band magnitude at $0.4''$ separation. As stated earlier, the raw contrast shows a trend of poorer contrast as the star gets fainter. As expected this trend is also seen in the final post processed contrast values seen on this figure. To understand correlations arising from parameters aside from star brightness for the remaining analysis we mark all stars with contrast greater than 1.5×10^{-5} with red circles and look for potential second-order correlation that are unrelated to stellar brightness. The comparisons are shown in Figure 25, and 26. Similar to the comparison against the magnitude of the star, in these figures we plot the contrast as a function of the environmental parameters mentioned above. For typical observations the atmospheric seeing is expected to drive the quality of the data, however as can be seen the GPI observations show no obvious correlation when compared to either the DIMM seeing which represents the ground layer turbulence or the MASS seeing which accounts seeing variations at higher atmospheric layers.

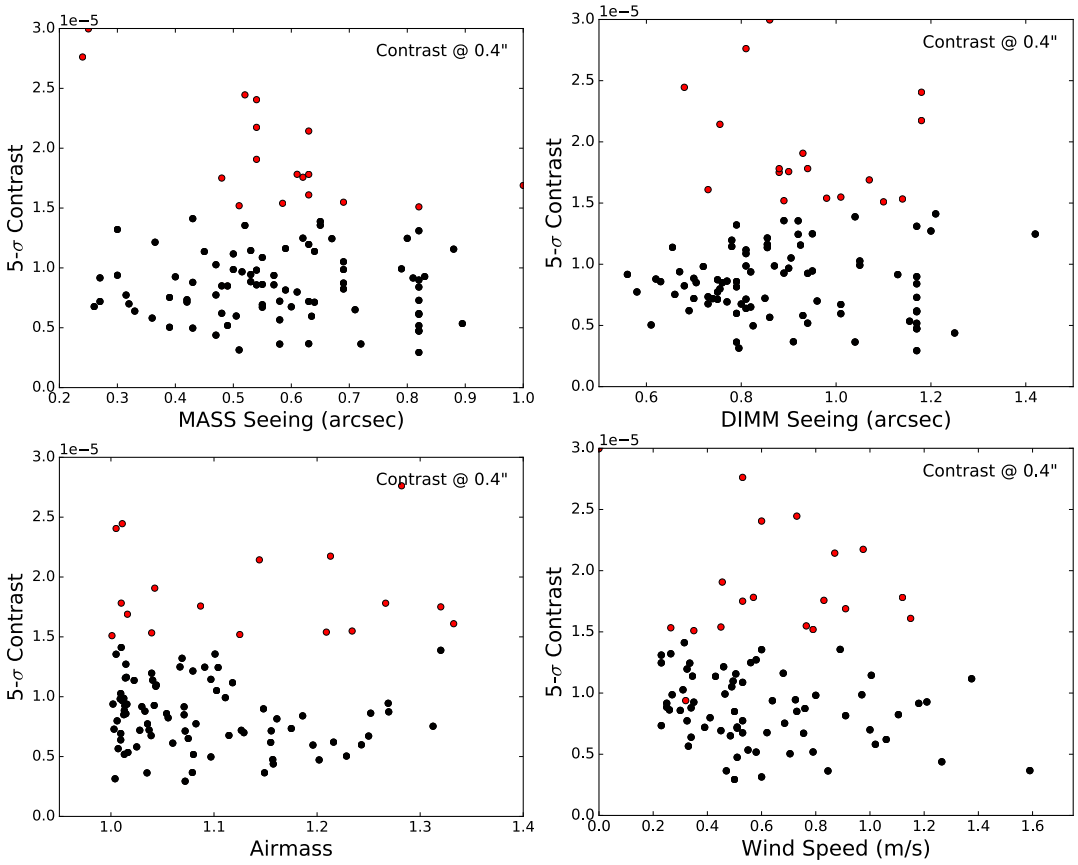

Figure 25. Plotted in the figure are the 5σ contrast at $0.4''$ as a function of a) MASS seeing, b) DIMM seeing, c) airmass, d) wind speed on the secondary. No correlations are visible in any of the parameters tested. Points with contrast $>1.5\times10^{-5}$ are colored with red circles.

Typical GPIES observations are taken when the star is close to zenith, so the lack of correlation with airmass is expected. We also chose to compare against the wind hitting the secondary mirror since it is fairly susceptible to high winds and can require the observatory to be closed due to gusts. However, there appears to be no correlation with the wind velocity. The field of view rotation and total integration time can positively affect contrast, however the spectral information available in GPIES data means that once a target achieves >20 deg of rotation there is no apparent gain in contrast due to rotation or integration time.

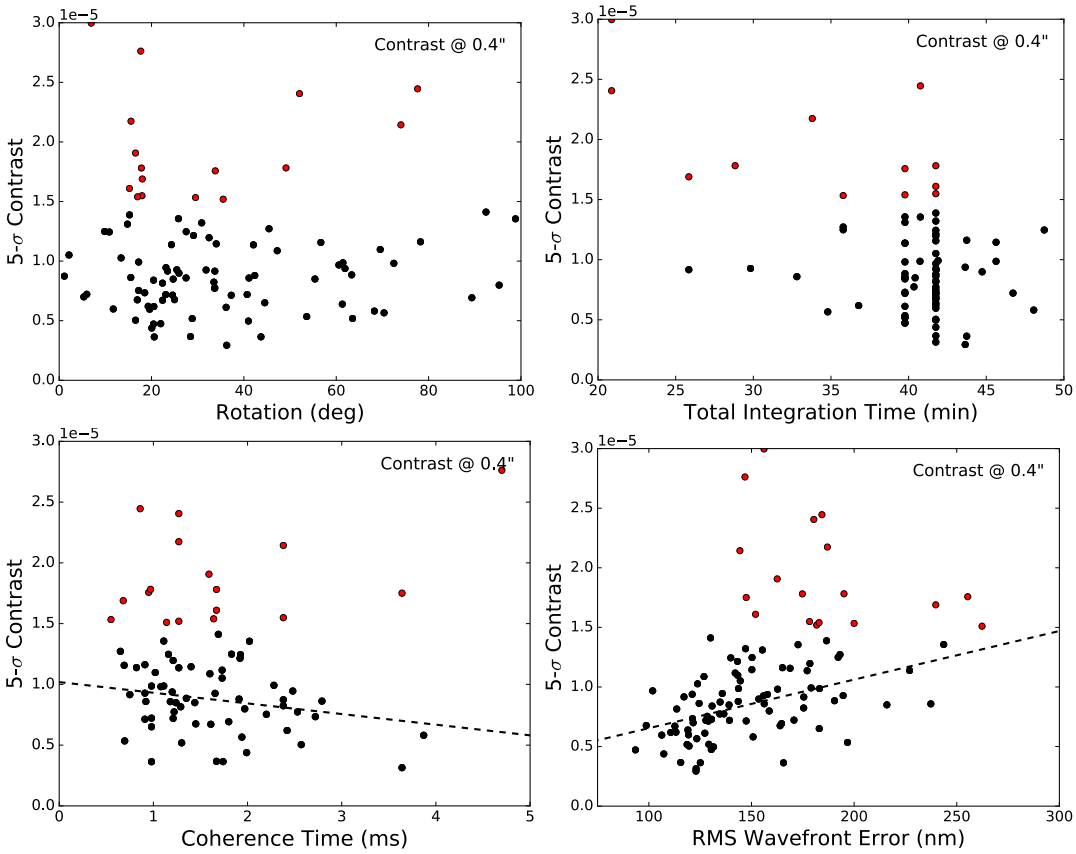

Figure 26. Plotted in the figure are the 5σ contrast at $0.4''$ as a function of a) rotation, b) total exposure of sequence, c) coherence time, d) RMS wavefront error. There appear to be trends with the rotation, coherence time and RMS wavefront error. Points with contrast $>1.5\times10^{-5}$ are colored with red circles.

The parameters plotted in the bottom two panels of Figure 26 are the only ones that show clear correlations against contrast, aside from the guide star magnitude. The RMS wavefront error is highly dependent on the brightness of the AO guide star magnitude and thus the star brightness, so the correlation is expected. Since fainter stars have larger wavefront error and poorer contrast. The correlation against coherence time (τ_0) is interesting and provides a clear observable that can be used to make decisions regarding observing strategy. A linear fit to the data indicates that as τ_0 increases the contrast correspondingly improves. Interesting, GPI was designed to

operate in median $\tau_0 \gtrsim 5$ms which is clearly not the prevalent conditions at Gemini South.

The preliminary analysis presented in this text presented a clear path forward for the GPIES team to understand the complete contrast budget. Further studies into understanding both the raw and final contrast when compared to AO telemetry data are presented in Bailey *et al.* (2016).

4.2 Direct imaging of an asymmetric debris disk in the HD 106906 planetary system

HD 106906, a young star in Lower Centaurus Crux (de Zeeuw *et al.*, 1999), was observed as part of the 600 star Gemini Planet Imager Exoplanet Survey. This star was previously identified to host a co-moving, substellar companion (11 ± 2 $M_{\rm Jup}$) at a projected separation of 654 AU (Bailey *et al.*, 2014). Kalas *et al.* (2015b) presented an analysis of the GPIES data where the authors examined several questions regarding the system including a) the morphology of the debris disk with both GPIES and archival *HST* data, b) search for planets closer in to the star, c) exploring whether the planet interacted with the debris disk at any point in its evolution, d) examine the near-IR spectral energy distribution of the planet to constrain the presence of circumplanetary material around the planet. In this thesis, we present the latter three points of investigation in greater detail. It is worth mentioning that the GPIES data was used to confirm the presence of a two-component edge on debris disk for HD 106906, with the inner debris disk visible in the GPIES imaging and the outer disk in the HST/ACS data. The *HST* data shows an edge on disk extending to $\sim$550 AU to the west, in the direction of the planet while the corresponding feature is missing on the east. Figures 27, 29, and 30, Tables 7, and 8 and Sections 4.2.1 and 4.2.3.3 were

primarily produced by me, while Figure 28, and Sections 4.2.2, 4.2.3., 4.2.3.1, 4.2.3.2 and 4.2.4 are written by Kalas *et al.* (2015b) and are reproduced here to provide context. For greater details on the examination of the debris disk I would like to refer the readers to Kalas *et al.* (2015b).

4.2.1 Search for Additional Planets with GPI

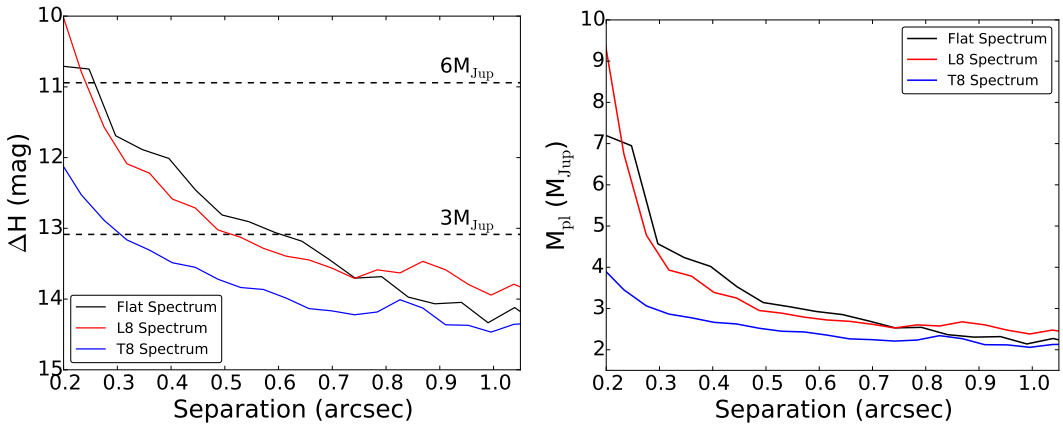

Figure 27. Left: 5-σ contrast in the H-band as a function of angular separation from the star. Three contrast curves are shown for different companion spectral shapes: flat (black), L8 (red), and T8 (blue). Over-plotted is the detection threshold for a $3M_{Jup}$ and $6M_{Jup}$ planet calculated using a 13 Myr BT-Settl model (Allard *et al.*, 2012a). Right: Minimum detectable planet mass (5-σ limit) as a function of angular separation.

Figure 27 translates our point source detection limits with GPI to planet mass detectability under a variety of model assumptions. The important point is that no planet as massive as HD 106906b (11 M_J) is detected in the GPI field, with an inner working radius of 0″2 (18.4 AU). This is relevant because if HD 106906b formed in a circumstellar disk around the primary and was subsequently ejected to large radii by planet-planet scattering, a perturber with comparable or greater mass might still reside in the system. Unfortunately, our search with an 18.4 AU projected inner radius

is not exhaustive; for example, a β Pic b analog with a $\sim$ 9 AU semimajor axis and low eccentricity would remain hidden around HD 106906b with the current GPI data (though planned non-redundant aperture masking with GPI can probe closer to the star).

4.2.2 Optical Photometry of HD 106906b with HST

Our recovery of HD 106906b with HST/ACS validates the Bailey *et al.* (2014) discovery in these data. Overall, we confirm their astrometric measurements, but can refine their F606W photometry, which they give as "[F606W] = 24.27 $\pm$ 0.03 mag". In our version we restrict our measurement to the first 1250-second exposure (`j917711lkq_drz.fits`) because there are no cosmic ray hits within the boundary of the first Airy ring. We use the same PSF subtraction as displayed for Fig. 3, but the data are not rotated to north to avoid interpolation artifacts. We measure photometry within $0''.2$ radius and our estimate for the sky background value is the median value of pixels contained in an annulus between $0''.200$ and $0''.375$ radius. The photometry within $0''.2$ gives 1.934 electrons/second. We use the information provided by Chiaberge *et al.* (2009) to adopt a 0.009 mag charge-transfer efficiency (CTE) correction.

For the aperture correction, Sirianni *et al.* (2005) give 0.180 mag at 0.600 μm to correct from an $0''.20$ aperture to a $5''.5$ radius aperture. However,they recommend that the encircled energy profiles of stars in the observations at hand are used due to various effects such as differences in focus. For the five brightest field stars we empirically determined the aperture correction from $0.2''$ to $0.5''$. This gives a median value of 0.212$\pm$0.005 mag. Then we used Sirianni *et al.* (2005) to add the published aperture correction from $0.5''$ to $5.5''$ radius, which is 0.089 mag. Thus the average

aperture correction is 0.301 mag. We arrive at the final photometric measurements for HD 106906b, which are CTE and aperture corrected: VEGAMAG = 24.07 mag, STMAG = 24.31 mag, ABMAG = 24.15 mag (or 0.800 μJy, assuming a F606W zeropoint of 3630 Jy). The 1-σ uncertainty in deriving an aperture correction is 0.005 mag. However, PSF subtracted images have residual background fluctuations that dominate the photometric noise. To empirically estimate the photometric measurement uncertainty for a source this faint, we inserted 13 copies of a TinyTim PSF (appropriately scaled to the flux of HD 106906b) into the regions free of cosmic-ray hits within 2″ of the location of HD 106906b. We then performed aperture photometry using exactly the same technique as for HD 106906b, and determined a 1-σ photometric uncertainty of 0.14 mag.

4.2.3 Testing for a circumplanetary disk

To search for evidence of a circumplanetary disk, we conducted three experiments: (1) measure the radial profile of HD 106906b in the HST image to determine if the object is extended, (2) test whether or not scattered light could account for the optical flux, and (3) compare the colors of HD 106906b to both model predictions and an empirical sample of other bound, substellar objects with similar ages and spectral types.

4.2.3.1 Radial profile of HD 106906b

With the stable PSF delivered by HST and the presence of numerous additional point sources in the ACS image, the HD 106906b radial profile can be tested for

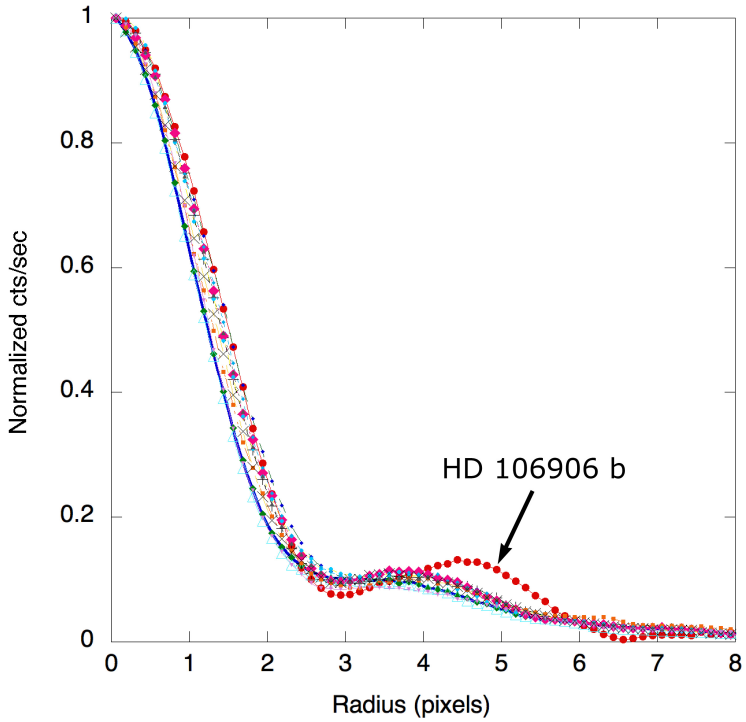

Figure 28. Radial intensity profiles (the median value in concentric rings centered on each star) of HD 106906b and 11 other point sources in the HST/HRC F606W field, normalized to unity. The HRC pixel scale is 25 mas/pixel and the measurements are made with IDP3 (Lytle *et al.*, 1999), resampling the image by a factor of eight using bicubic sinc interpolation. For HD 106906b, the azimuthal morphology of the first Airy ring is similar to the other stars, but there is a distinct outward radial offset in the peak of the first Airy ring, which also contains more flux than the 11 comparison stars.

extended nebulosity. If HD 106906b is an 11 M_J object 650 AU from a 1.5 $M_\odot$ star, the Hill sphere has radius 86 AU (0.93″).

If the dust was captured when HD 106906b was located closer to the star, the Hill radius would be smaller (e.g. the planet at 100 AU has a Hill radius of 13 AU or 0.14″). Therefore, a debris cloud surrounding HD 106906b could be resolved.

To test for extended nebulosity in the F606W data, we measured the radial profiles of HD 106906b and 11 other point sources in the field. Figure 5 demonstrates that the PSF core of HD 106906b is consistent with the other 11 sources, but the PSF

wing is anomalously bright between 0.10″ and 0.15″ radius (9–14 AU). Specifically, in this radial region the HD 106906b PSF has 26% more summed light than the summed light of the average PSF from field stars (all PSF peaks are normalized to unity). Or, including the cores of the PSF, the summed light from 0″ to 0.15″ is 1.6% greater. Therefore, the extra PSF halo brightens the optical magnitude of HD 106906b by 0.017 mag.

The PSFs are also distinguished by the radius at which the first Airy ring peaks. For HD 106906b the peak is at 4.44 pixels radius (111 mas or 10.2 AU), whereas for the 11 field stars the Airy ring peaks at a median value of 3.69±0.23 pixels. To estimate the uncertainty for the value of the HD 106906b Airy ring maximum, we turn to the 13 artificial point sources that were inserted into the data for the purpose of determining the photometric uncertainty (Section 3.3). As discussed below, the TinyTim PSF does not exactly represent the astrophysical PSF of HD 106906b, but we can nevertheless use it to quantify how the measurements of the Airy ring peaks are influenced by noise at the 13 different insertion points near HD 106906b. This experiment shows that the Airy peak measurement on a source as faint as HD 106906b has $\sigma = 0.14$ pixel. Adding the two uncertainties in quadrature, the difference between the planet and the field star Airy ring peaks is 0.71±0.27 pixels.

To test whether or not the PSF shape is due to the extreme red color of HD 106906b, we examined the TinyTim (Krist *et al.*, 2011b) calculations of PSF structure for HST/ACS/HRC coronagraphic observations in F606W. We find that the first Airy ring for an A0V star, an M3V star, and a 1000 K blackbody peaks at 3.52 pixels (0.088″), 3.68 pixels, and 3.68 pixels radius, respectively. The maximum flux level of the 1000 K Airy ring is 5% lower than the A0V Airy ring. HD 106906b, on the other hand, has significantly more flux in the first Airy ring compared to the

comparison objects in the field, and the ring peaks at a greater radius, as shown above. The TinyTim models for PSF structure therefore do not account for the extended HD 106906b PSF size.

The experiments above give tentative evidence for a slightly resolved structure surrounding HD 106906b. What we were identifying as the peak of an Airy ring around HD 106906b should instead be termed a shoulder on top of the intrinsic Airy ring. Nevertheless, it is critically important to observe HD 106906b to greater depth and with different instrumentation to understand if spurious noise and/or a distant background object could account for the shoulder detected in the ACS data.

4.2.3.2 Origin of optical flux for HD 106906b

We also examined whether or not the measured F606W flux is higher than expected from the calculated in-band integrated flux of model atmospheres, matching the published effective temperature, age and mass of the companion from Bailey *et al.* (2014). A similar exercise was conducted with the HST optical discovery of Fomalhaut b, which was found to have flux two orders of magnitude greater than that predicted by models (Kalas *et al.*, 2008). For HD 106906b, the BT-Dusty and BT-Settl models (scaled to the J-band data) predict F606W apparent VEGAMAG magnitudes 24.64 ($5.71 \cdot 10^{-7}$ Jy) and 25.68 ($2.23 \cdot 10^{-7}$ Jy), respectively. Our measured F606W value of 24.07 mag is 0.57 mag and 1.61 mag brighter, respectively. The combined uncertainty of the F606W flux (0.14 mag) and the J-band data (0.3 mag) is σ =0.33 mag, which means that the observed optical flux is 1.7 σ and 4.9 σ greater than the respective theoretical predictions. This is certainly not as large a discrepancy as in the case of Fomalhaut b, but it is consistent with the hypothesis that captured material would

add reflected light to the intrinsic flux from the planet. The two important caveats, as noted in Section 4.1, are that the atmosphere models are uncertain, and there is an intrinsic astrophysical diversity in the colors of low-mass objects.

Hypothetically, we find that all of the optical light from HD 106906b could in fact arise from scattered starlight. The stellar flux received at Earth (assuming D=92 pc, $L_\star = 2.143 \cdot 10^{27}$ W) is $f_\star = 2.116 \cdot 10^{-11}$ W m^{-2}. For a star-planet separation of d=1000 AU, the stellar flux received at the planet is $7.58 \cdot 10^{-3}$ W m^{-2} (Fomalhaut b was 1.7 W m^{-2}). The reflected light will depend on several factors such as the geometry of the system, the total scattering surface (Σ) from the planet and its dust cloud or ring, and a scattering efficiency, Q_s, such as the product of the geometric albedo and phase function at a given phase. For a circumplanetary ring such as Saturn's main rings, the scattering geometry is important, but for more radially extended dust distributions we can reasonably assume an optically thin and roughly spherical dust cloud. Therefore all the grains are illuminated and it does not matter how the planet is oriented relative to the incident light and the observer. We can write the flux received at earth as:

$$\begin{aligned} f_p &= 7.58 \cdot 10^{-3}\ \Sigma\ Q_s \tfrac{4}{-}\pi\ D^2 \\ &= 7.48 \cdot 10^{-41}\ \Sigma\ Q_s\ [\text{W m}^{-2}] \end{aligned}$$

We can rewrite this as a contrast in apparent magnitude between the planet's reflected light and the star:

$$\begin{aligned} m_p - m_\star &= m_p - 7.81\ \text{mag} = -2.5\ \log\ (f_p/f_\star) \\ m_p &= -2.5\ \log(\Sigma \cdot Q_s) + 81.44\ \text{mag} \end{aligned}$$

For the sake of argument, we assume the albedo and phase function average to

$Q_s = 0.1$ and then ask how large does Σ have to be in order to satisfy our F606W magnitude of $m_p = 24.07$ mag? In this case $\Sigma = 10^{24}$ m^2 which in the geometry of a large circular disk projected onto the sky has radius r = $1.669{\cdot}10^{12}$ m = 11 AU = 0.12″. Observationally, this value is similar to the radial extent of the anomalous PSF shown in Figure 5 and the possible range of Hill radii given in Section 4.2.1. If this projected surface area is due to dust grains with radius 5 μm and density 2000 kg m^3, then the total mass is $\sim 10^{22}$ kg (i.e. similar to Pluto). Therefore the hypothetical size and mass of the dust cloud do not violate any observational or theoretical constraint. Some or all of the optical light could arise from a circumplanetary dust cloud scattering stellar light.

4.2.3.3 Infrared Colors of HD 106906b

A circumplanetary dust disk or cloud would be very cold due to the relatively low luminosity of the planet and the large distance from the host star. We studied the 2MASS, Spitzer, Herschel and ALMA data and do not detect a source at the location of HD 106906b, which is expected given its extremely low luminosity ($2.3{\times}10^{-4}$ L$_\odot$; Bailey et al. 2014). For example, given the noise properties of the Sco-Cen Spitzer observations in aggregate, uncontaminated observations place a 3-σ limit on the 24 μm emission of $\sim$0.3 mJy (this is a best-case limit because of source confusion.) If we assume that the peak for the emergent thermal emission arises at 24 μm, then we can approximate $L_{IR} < 9.7 \times 10^{-6}$ L$_\odot$ assuming the same heliocentric distance as the primary (92 pc). Given the instrument configuration and the integration time, we can only place an upper limit on $L_{IR}/L_{planet} < 0.042$.

We also investigated whether or not the NIR photometry for HD 106906b published

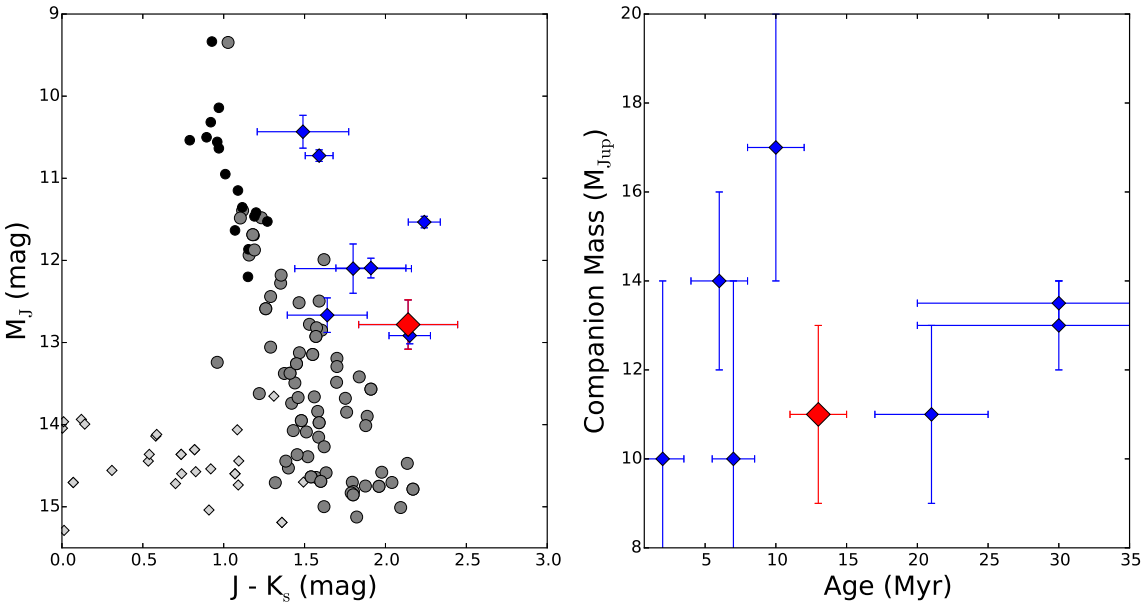

Figure 29. Left: Near-infrared color-magnitude diagram for M dwarfs (black circles), L dwarfs (gray circles), and T dwarfs (gray diamonds) along with a sample of known, young, low-mass companions with ages between 2 and 30 Myr and spectral types from L0 - L4 (blue diamonds). HD 106906b is marked with a large red diamond. The M, L, and T dwarf photometry is taken from Dupuy and Liu (2012b). Right: Companion mass as a function of age for the companion sample from the left panel. The sample, presented in Table 7 and 8, includes targets with ages spanning both younger and older than HD106906 with masses comparable to the HD 106906b.

in Bailey *et al.* (2014) is anomalous empirically (relative to several comparison objects), and theoretically (when compared against two different atmospheric model predictions). The infrared photometry is compiled in Table 7 along with the photometry for a set of seven low mass companions with similar masses and ages (Kraus *et al.*, 2014, 2015; Bailey *et al.*, 2013; Lagrange *et al.*, 2009; Patience *et al.*, 2012; Delorme *et al.*, 2013). The comparison sample is plotted on a color-magnitude diagram in Figure 29 (left) and all the young (2 – 30 Myr) imaged companions with spectral types of L0 to L4, similar to HD 106906b. The young, planetary mass companions to 2M1207 and HR8799 are not included due to their considerably cooler temperatures and later spectral types. The distribution of the comparison, young low mass companions in

estimated mass and age is given in Figure 29 (right) and shows that the sample can serve as an analogous comparison sample.

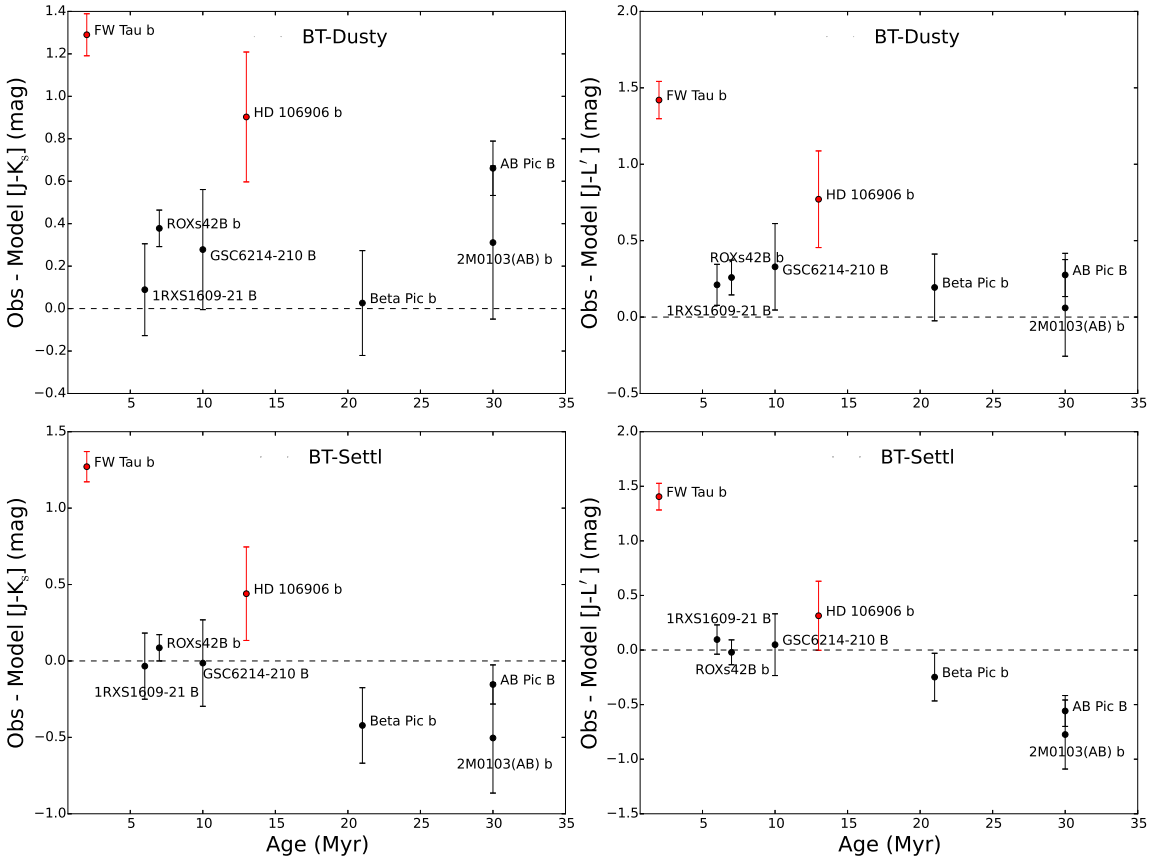

Figure 30. The difference between observed and model colors as a function of age for the young companion sample in Table 7. The dashed line indicates a color difference of zero. The plot illustrates that only two objects, HD 106906b and FW Tau b, consistently show observed colors redder than the models.

Two evolutionary models - BT-Dusty (Allard *et al.*, 2001b) and BT-Settl (Allard *et al.*, 2012a) - were used to estimate the photospheric colors; both grids provide photometry values for objects that span the full range of ages and masses covered by the low mass companions. The grid points were interpolated with a power law to estimate magnitudes at the specific ages of the target using a model mass consistent with each target. The model photospheric colors for each target and each model

Table 7. Literature photometry for the imaged companions

Companion Name	Mass (M_{Jup})	Age (Myr)	Apparent Magnitude J (mag)	Ks (mag)	L' (mag)	Evidence for disk	References
HD 106906b	11 ± 2	13 ± 2	17.6 ± 0.3	15.46 ± 0.06	14.6 ± 0.1	*HST* extended PSF, optical and NIR excess	[1], [2]
FW Taub	10 ± 4	2 ± 1.5	17.34 ± 0.07	15.1 ± 0.1	14.3 ± 0.1	Acretion signatures & ALMA disk detection	[3], [4], [5]
ROXs 42Bb	10 ± 4	7 ± 1.5	16.12 ± 0.07	14.53 ± 0.05	13.7 ± 0.1	no evidence of disk	[5], [6]
GSC 6214-210B	17 ± 3	10 ± 2	16.2 ± 0.2	14.8 ± 0.2	13.8 ± 0.2	Hα, Paβ, NIR excess	[3], [4], [7], [8]
1RXS 1609-2105B	14 ± 2	6 ± 2	17.9 ± 0.1	15.99 ± 0.18	14.8 ± 0.1	Optical and NIR excess	[7], [9], [10]
Beta Picb	11 ± 2	21 ± 4	14.11 ± 0.21	12.47 ± 0.13	11.17 ± 0.06	none reported	[11], [12], [13], [14]
AB PicB	13.5 ± 0.5	30 ± 10	16.3 ± 0.1	14.14 ± 0.08	13.01 ± 0.09	none reported	[15], [16], [17]
2M0103(AB)b	13 ± 1	30 ± 10	15.5 ± 0.3	13.7 ± 0.2	12.7 ± 0.1	none reported	[17]

References: [1] Bailey *et al.* (2014), [2] this paper, [3] Kraus *et al.* (2014), [4] Bowler *et al.* (2014), [5] Kraus *et al.* (2015), [6] Currie *et al.* (2014a), [7] Bailey *et al.* (2013), [8] Zhou *et al.* (2014), [9] Lafrenière *et al.* (2008), [10] Wu *et al.* (2015), [11] Lagrange *et al.* (2009), [12] Bonnefoy *et al.* (2011), [13] Binks and Jeffries (2014), [14] Currie *et al.* (2011b), [15] Bonnefoy *et al.* (2010), [16] Patience *et al.* (2012), [17] Delorme *et al.* (2013)

are listed in Table 8 with the measured colors for HD 106906b and the comparison sample. This approach to inferring the presence of a disk from photometry is similar to previous studies (e.g. Bailey *et al.*, 2013).

Several of the comparison objects have previously reported evidence for disks. The most substantial disk has been detected around FW Tau b with ALMA continuum emission (Kraus *et al.*, 2015) and accretion signatures (Bowler *et al.*, 2014). Both GSC 6214-210B and 1RXS 1609-2105B exhibit excess emission (Bailey *et al.*, 2013; Wu *et al.*, 2015), and GSC 6214-210B also shows both Hα and Paβ emission from accretion signatures (Bowler *et al.*, 2011; Zhou *et al.*, 2014; Bowler *et al.*, 2014). In Figure 30, the difference in observed and model colors is plotted as a function of age, which is also expected to correlate with surface gravity. FW Tau b,the object with the strongest evidence for a disk, stands out as the reddest object, HD 106906b has the second largest offset from the model photospheres. The HD 106906b color excess is larger than the two other comparison objects with reported evidence of disks - GSC 6214-210B and 1RXS 1609-2105B.

Due to the 0.3 mag uncertainty on the J-band photometry, the significance of the red excess is limited, but the results suggest the possibility of the presence of a circumplanetary dust around HD 106906b. Based on the combination of evidence from the IR color, *HST* optical radial profile, and the optical flux level, we conclude that there may be a disk of material that was either captured in an encounter with the primary star's disk, or retained from the time of formation of the planetary mass companion. Additional observations are required to clarify these tentative conclusions about the environment surrounding HD 106906b.

Table 8. Comparison of observed infrared colors vs. model colors for the imaged companions

Companion Name	Observed Color J-Ks (mag)	Model Color (J-Ks) BT-Settl	Model Color (J-Ks) BT-Dusty	Observed Color J-L′ (mag)	Model Color (J-L′) BT-Settl	Model Color (J-L′) BT-Dusty
HD 106906b	2.14 ± 0.3	1.7	1.24	3.0 ± 0.3	2.69	2.23
FW Taub	2.24 ± 0.1	0.97	0.95	3.09 ± 0.12	1.69	1.67
ROXs 42Bb	1.59 ± 0.09	1.50	1.21	2.42 ± 0.11	2.44	2.16
GSC 6214-210B	1.49 ± 0.28	1.50	1.21	2.49 ± 0.28	2.44	2.16
1RXS 1609-2105B	1.91 ± 0.22	1.94	1.82	3.1 ± 0.13	3.00	2.89
Beta Picb	1.64 ± 0.25	2.06	1.61	2.94 ± 0.22	3.19	2.75
AB PicB	2.15 ± 0.13	2.30	1.49	3.28 ± 0.13	3.57	2.74
2M0103(AB)b	1.8 ± 0.36	2.30	1.49	2.8 ± 0.32	3.57	2.74

4.2.4 Comparison to HD 15115 and Fomalhaut b

The HD 15115 debris disk was the first in what seems to be a class of debris disks that are so extreme in their disturbed morphology, they resemble a "needle" in the near edge-on view over 10^2 AU scales (Kalas *et al.*, 2007). On scales of $\sim$10 AU, Mazoyer *et al.* (2014) discovered that HD 15115 has a more symmetric inner hole, essentially representing the "eye of the needle." As with our GPI image of HD 106906b (Figure 1), the eye of HD 15115 has a northern edge that is significantly brighter due to preferential forward scattering and a $\sim 87^\circ$ line of sight inclination.

Kalas *et al.* (2007) suggested that a nearby M dwarf may have perturbed the HD 15115 disk, though this scenario was found unlikely by Debes *et al.* (2008), and therefore the origin of the extreme asymmetry for HD 15115 remains an open question. The discovery of a needle-like debris disk around HD 106906 represents a fresh opportunity to investigate the origin of such structure.

The question of how HD 106906b obtained an apparent position outside of the primary's debris disk invites comparisons to the Fomalhaut system. Fomalhaut b is currently located very near the inner edge of the debris disk, but its highly eccentric orbit will place it beyond the outer edge in the future (Kalas *et al.*, 2013). Its low mass ($\lesssim 1 M_J$; Janson *et al.* 2012) means that the prominent 140 AU dust belt may survive many planet crossings whereas the high mass of HD 106906b tends to argue that it did not recently encounter the inner disk of the system. In both cases, significant future work is necessary to answer the fundamental question of whether or not the planet is coplanar with the disk. However, in both cases the question is raised on whether or not the planet has acquired circumplanetary material due to the possible interactions with the debris disk. For Fomalhaut b the evidence for circumplanetary

material rests on the anomalously high optical flux, whereas for HD 106906b the evidence is based on the possible infrared excess, the brighter optical flux than the model predictions, and the extended shape of the optical PSF compared to all other field stars. Fomalhaut b may also be extended in the optical (Galicher *et al.*, 2013), but this result is also tentative given that the extended morphology is detected in only one bandpass (F814W).

Chapter 5

CHARACTERIZING 51 ERI B FROM 1–5 μM: A PATCHY-CLOUD EXOPLANET

Until recently, most of the imaged planetary mass companions detected were typically orbiting their parent star at large orbital separations, >30 au. However, new instrumentation with second generation adaptive optics such as the Gemini Planet Imager (GPI, Macintosh *et al.*, 2014) and Spectro-Polarimetric High-contrast Exoplanet REsearch (SPHERE, Beuzit *et al.*, 2008) are now routinely obtaining deep contrasts ($> 10^5 - 10^6$) in the inner arcsecond (5–30 au). The recent detection of new companions (Macintosh *et al.*, 2015; Konopacky *et al.*, 2016; Wagner *et al.*, 2016; Milli *et al.*, 2017) and debris disks (Currie *et al.*, 2015; Wahhaj *et al.*, 2016; Millar-Blanchaer *et al.*, 2016; Bonnefoy *et al.*, 2017) showcase the advances made by these next generation AO systems. Direct imaging, unlike non-direct methods such as radial velocity and transits, measures light from companion directly, which permits measuring the atmospheric spectrum, with the caveat that the final calibration is dependant on complete understanding of the stellar properties. These new AO instruments combine excellent image stability and high throuput with IFU spectrographs, enabling the measurement of a spectrum of the planet in the near infrared (IR) wavelength range. Combining the near-IR spectra with mid-IR photometry from instruments such as Keck/NIRC2, MagAO/Clio or LBT/LMIRCam, provides valuable constraints on the effective temperature and non-equilibrium chemistry when undertaking comprehensive modeling of the exoplanet spectral energy distribution.

In this study we focus on the planetary companions, 51 Eridani b (51 Eri b; Macintosh *et al.*, 2015). 51 Eri b is the first planet discovered by the Gemini Planet

Imager Exoplanet Survey (GPIES), a survey targeting 600 young and nearby stars using GPI to search for exoplanets. The planet orbits 51 Eri A, a young F0IV star with an age of 26 ± 3 Myr (Nielsen *et al.*, 2016), that is part of the β Pic moving group (Malo *et al.*, 2013). The primary is part of a hierarchical triple with two M-star companions, GJ 3305AB, separated from the primary by ∼2000 au (Feigelson *et al.*, 2006; Montet *et al.*, 2015). 51 Eri A is known to have an IR excess, and a debris disk was detected in *Herschel Space Observatory* 70 and 100 μm bands with very low IR luminosity of $L_{IR}/L_{\star} = 2 \times 10^{-6}$ and an a lower limit on the inner radius of 82 au (Riviere-Marichalar *et al.*, 2014) as well as a detection at 24 μm with the *Spitzer Space Telescope* (Rebull *et al.*, 2008). The debris disk was not detected in Macintosh *et al.* (2015), which, given the low fractional luminosity would be extremely challenging. The analysis of the atmosphere of 51 Eri b by Macintosh *et al.* (2015) was based on GPI JH spectra (1.1–1.8 μm) and Keck L_P photometry (3.76 μm), using two different model atmosphere grids to estimate planet properties. While the models agreed on the temperature and luminosity, they were highly discrepant in terms of best fitting surface gravity with one grid suggesting low surface gravity and youth while the other required a high surface gravity and an old planet. Similarly, one grid best fit the atmosphere when using a linear combination of cloudy and clear models while the other best fit the data with clear atmosphere. These discrepancies indicate that more data is required to fully constrain the planet parameters.

In this paper, we present new observations and revised data analysis that can be used to discriminate between some of the disagreements. In Section 5.1, we present the first $K1$ (1.90–2.19 μm) and $K2$ (2.10–2.40 μm) spectrum of the planet taken with GPI. We also present updated L_P photometry and new observations of the planet in the M_S-band (4.67 μm). In Section 5.2, we present new near-IR photometry of the

star and revise the stellar spectral energy distribution (SED) used in the rest of the analysis. In Section 5.3, we examine the near- and mid-IR photometry of 51 Eri b in relation to that of other field and young brown dwarfs through the brown dwarf color-magnitude diagram. We also compare the near-IR spectrum of 51 Eri b to field brown dwarfs, and planetary-mass companions to estimate the best fitting spectral type of the planet. Finally, in Section 5.4 we model the planet SED using two different grids spanning effective temperatures from 450K to 1000K with deep iron/silicate clouds or sulfide/salt clouds. The 1–5 μm spectral energy distribution in combination with these two model grids with help refine the planet properties and clarify whether the atmosphere is best fit by clouds, or not.

5.1 Observations and Data Reduction

5.1.1 GPI K1 and K2

51 Eri b was observed with the Integral Field Spectrograph (IFS) of GPI through the $K1$ filter on 2015 November 06 UT and 2016 January 26 and through the $K2$ filter on 2015 December 18 UT (see Table 9). Standard procedures, namely using an argon-arc lamp, were used to correct the data for instrumental flexure. To maximize the parallactic rotation for Angular Differential Imaging (ADI; Marois *et al.*, 2006a), the observations were centered on meridian passage. All the GPI datasets underwent the same initial data processing steps using the GPI Data Reduction Pipeline v1.3.0 (DRP; Perrin *et al.*, 2014). The processing steps included dark current subtraction, bad pixel identification and interpolation, this is followed by compensating for instrument flexure using the argon arc spectrum (Wolff *et al.*, 2014). Following this step, the

Table 9. Observations of 51 Eri b

Date	Instrument	Filter	Total Int. time (min)	Field Rot. (deg)	Averaged airmass	Averaged DIMM seeing (as)	Averaged MASS τ_0 (ms)
2015 Jan 30	GS/GPI	J	70	23.8	1.15	0.52	3.26
2014 Dec 18	GS/GPI	H	38	37.7	1.14	–	–
2015 Nov 06	GS/GPI	$K1$	55	30.46	1.17	0.38	1.56
2015 Dec 18	GS/GPI	$K1$	97	55.48	1.15	0.86	4.40
2016 Jan 26	GS/GPI	$K2$	103	71.72	1.22	0.69	0.94
2015 Oct 27	Keck/NIRC2	L_P	100	74.2	1.10	–	–
2016 Jan 02	Keck/NIRC2	M_S	139	115.7	1.18	–	–
2016 Jan 21	Keck/NIRC2	M_S	174	116.0	1.21	–	–
2016 Feb 04	Keck/NIRC2	M_S	148	101.4	1.21	–	–
2016 Feb 05	Keck/NIRC2	M_S	142	102.1	1.21	–	–

microspectra are extracted to generate the IFS datacubes (Maire *et al.*, 2014). During the process of generating the 3D (x, y, λ) cubes, the microspectra data are resampled to $\lambda/\delta\lambda = 65$, and 75 at $K1$ and $K2$, respectively, after which they are interpolated to a common wavelength scale and correction for geometric distortion Konopacky *et al.* (2014). The datacubes are then aligned to a common center calculated using the four satellite spots (Wang *et al.*, 2014). The satellite spots are copies of the occulted central star, generated by the use of a regular square grid printed on the apodizer in the pupil plane (Sivaramakrishnan and Oppenheimer, 2006; Marois *et al.*, 2006b; Macintosh *et al.*, 2014). The satellite spots also help convert the photometry from contrast units to flux units. No background subtraction was performed since the following steps of high-pass filtering and PSF subtraction efficiently remove this low frequency component.

Further steps to remove quasi-static speckles and large scale structures were executed outside the DRP. Each datacube was filtered using an unsharp mask with a box width of 11 pixels. The four satellite spots were then extracted from each wavelength slice, and averaged over time to obtain templates of star point spread function (PSF). The Linear Optimized Combination of Images algorithm (LOCI, Lafrenière *et al.*, 2007) was used to suppress the speckle field in each frame using a combination of aggressive parameters: $dr = 5$ px, N_A=200 PSF full width at half maximum (FWHM), $g = 0.5$, and $N_\delta = 0.5 - 0.75$ FWHM for the three datasets. Where dr is the radial width of the optimization zone, N_A is the number of PSF FWHM that can be included in the zone, g is the ratio of the azimuthal and radial widths of the optimization zone, and N_δ defines the maximum separation of a potential astrophysical source in FWHM between the target and the reference PSF. The residual

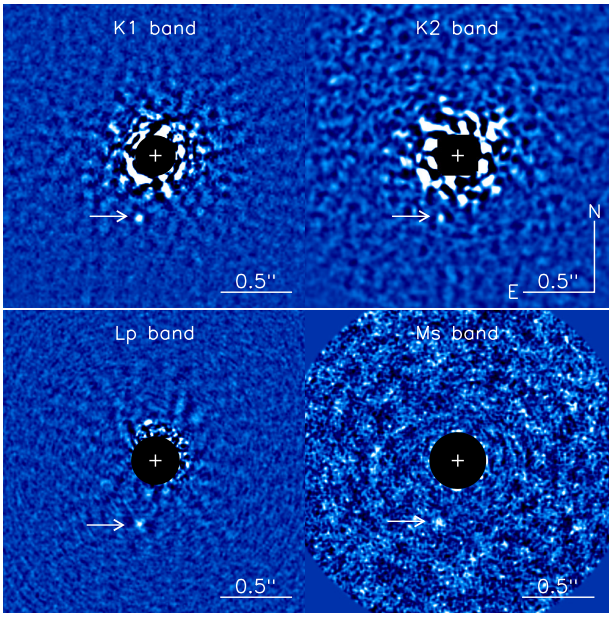

Figure 31. Final PSF subtracted images of 51 Eri b. (Top) LOCI-reduced GPIES images at $K1$ (2016 Jan 28, left) and $K2$ band (2015 Dec 18, right). (Bottom) `pyKLIP`-reduced NIRC2 images, smoothed with a box of width of 2 pixels, at L_P (2015 Oct 27, left), and a combined image of all four M_S datasets (right). The images are scaled linearly, but are different in each panel in order to saturate the core of the planet PSF.

image of each wavelength slice was built from a trimmed (10%) temporal average of the sequence.

Final $K1$ and $K2$ broad-band images were created using a weighted-mean of the residual wavelength frames according to the spectrum of the planet, examples of which can be found in Figure 31. These broad-band images were used to extract the astrometry of the planet in each dataset thanks to higher signal-to-noise ratio (SNR) than in individual frames. To do so, a negative template PSF was injected into the raw data at the estimated position and flux of the planet before applying LOCI and reduced using the same matrix coefficients as the original reduction (Marois *et al.*, 2010a). The process was iterated over these three parameters (x position, y

position, flux) with the amoeba-simplex optimization (Nelder and Mead, 1965) until the integration squared pixel noise in a wedge of 2×2 FWHM was minimized. The best fit position was then used to extract the contrast of the planet in each dataset. The same procedure was executed in the non-collapsed wavelength residual images but varying only the flux of the negative template PSF and keeping the position fixed to prevent the algorithm from catching nearby brighter residual speckles in the lower SNR spectral slices. To measure uncertainties, we injected the template PSF with the measured planet contrast into each datacube at the same separation and 20 different position angles. We measured the fake signal with the same extraction procedure. The contrasts measured in the 2015 Nov 06 and 2016 Jan 28 $K1$ datasets agreed within the uncertainties, the latter having significantly better SNR, and were combined with weighted mean to provide the final planet contrasts.

5.1.1.1 Spectral covariances

Estimation of a directly imaged planets properties from its measured spectrum is complicated by the fact that spectral covariances are present within the extracted spectra. In the GPI data these are caused by the residual speckle noise in the final PSF-subtracted image, and the oversampling of the individual microspectra during the initial data reduction process. Atmosphere modeling without properly accounting for these covariances can lead to biased results. We present the derivation of the correlation using the parameterization of Greco and Brandt (2016) in the Appendix C.

We use the spectral covariance when carrying out comparison of the planet spectrophotometry against other field and young dwarfs as well as during model fitting. The covariance helps correctly account for the correlation in the spectra while also

increasing the importance of the photometry, and thus the use of the covariance tends to move the best fits towards cooler temperatures when compared to using the variance directly.

5.1.2 Keck L_P

We observed the 51 Eri system on 2015 Oct 27 in the L_P filter with the NIRC2 camera (McLean and Sprayberry, 2003) at the Keck-II observatory (Program ID - U055N2). The observations were taken in ADI mode, starting $\sim$1 hour prior to meridian crossing to maximize the field of view rotation. The target was observed for $\sim$3 hours total, with 100 min of on-source integration. To calibrate the planet brightness unsaturated observations of the star were taken at the end of the observing sequence. The images were dark and flat field corrected. We used twilight sky images to build the flatfield and masked hot and bad pixels. As these observations were taken after the April 2015 servicing of NIRC2, the geometric distortion was corrected using the solution presented in Service *et al.* (2016) (updating the original Yelda *et al.* (2010) solution), with a plate scale of 9.971 $\pm$ 0.004 mas pixel^{-1}. Post-processing of the data was carried out using the Python version of the Karhunen—Loève Image Projection algorithm (KLIP, Soummer *et al.*, 2012; Amara and Quanz, 2012), `pyKLIP` (Wang *et al.*, 2015). As part of this study, we included a NIRC2 module in the `pyKLIP` codebase that is publicly available for users. [6] The algorithm accepts aligned images and performs PSF subtraction using KLIP where the image can be divided into sections both radially and azimuthally. Aside from the choice of zones, there are two main parameters that were adjusted, the number of modes used in the Karhunen—Loève

[6] https://bitbucket.org/pyKLIP/pyklip

(KL) transform and an exclusion criterion for reference PSFs, similar to N_δ mentioned above, that determines the number of pixels an astrophysical source would move due to the rotation of the reference stack. We carried out a parameter search where the four parameters mentioned were varied to optimize the signal to noise in the planet signal. The planet photometry was estimated using the method described above for the $K1$ and $K2$ filters, using a negative template PSF. The L_P magnitude contrast for the star-planet is 11.58 $\pm$ 0.15 mag which agrees very well with the photometry in the original epoch, 11.62 $\pm$ 0.17 mag. The weighted mean of both measurements is used in the rest of the analysis.

5.1.3 Keck M_S

Observations of 51 Eri b were taken in the M_S-band filter over four separate half nights on 2016 Jan 02, 21 and 2016 Feb 04, 05 with Keck/NIRC2 Narrow camera. The details of the observations are presented in Table 9. Each night the target was observed for a period of $\sim$6 hours, as part of two separate NASA and UC Keck observing programs (Program ID - N179N2, U117N2). The data were obtained in ADI mode, with the field of view rotating at the sidereal rate. To reduce the effects of persistence and enable accurate thermal background correction, the star was nodded across the detector in four large dithers centered in each quadrant of the detector. Furthermore to prevent saturation of the detector by the thermal background, the exposures were limited to 0.3s with 200 co-adds, without using an occulting spot. The images were dark and flat field corrected with twilight sky flats, followed by hot and bad pixel correction. As with the L_P data, the solution provided by Service *et al.* (2016) was used to correct the NIRC2 Narrow camera geometric distortion. Finally, all

the images were rotated to put north up. An additional step required for the M_S-band data that is not as critical for the other datasets is the background subtraction. Since the thermal background at 5μm is large and highly time variable, rather than median combine, or high pass filter to remove the background we adopted the least-squares sky subtraction algorithm proposed in Galicher *et al.* (2011). For each point in the dither pattern, the algorithm uses the images where the star is in one of the other three positions to construct a reference library. We used a ring centered on the star to estimate the thermal background in each image, with an inner annulus of 24 pixels and an outer annulus of 240 pixels. The final calibration step involved aligning the background corrected PSFs. Since the core of the PSF is saturated in the data, we aligned the data using two different methods, a) fitting a 2D Gaussian to the wings of the stellar PSF to estimate the center of the star and then shifting the PSF to a pre-determined pixel value to align all the images and b) using the rotation symmetry of the PSF using the method described in Morzinski *et al.* (2015). To compare the two methods, we calculated the residuals between images aligned using the methods and compared the noise in the residuals and found them to be similar and chose to go with the 2D Gaussian which is computationally faster.

The procedure used for the PSF subtraction for the M_S data was similar to the L_P data. The planet is not detected in each of the individual half-night datasets, requiring a combination of all four half-nights to increase the signal to noise ratio to detect the planet flux. To correctly combine the planet flux across the multiple epochs, we adjusted the PA to account for the astrophysical motion of the planet around the star, for which we used the best fitting orbit presented in De Rosa *et al.* (2015). In the month between the first and last dataset, the planet rotated $\sim$0.48 degrees or $\sim$0.4 pixel, which is a sufficiently large correction that it must be included

in the data reduction. Each nights data was reduced individually to generate 603 PSF subtracted images. These images were then combined by dividing each image into 13 annuli which were combined using a weighted mean, where the weights are the inverse variance in each annulus. As seen in Figure 31, we detect the planet signal at ∼2–3 sigma. To confirm that we are detecting the planet, we rotated the data to match the PA value of the L_P epoch to find that the flux peak in the M_S-band matches the location of the planet in L_P. We measured a star to planet contrast of 11.5 mag using the same procedure as described for the L_P data. We injected 25 fake PSFs that were scaled to match the contrast measured for the planet and detected the fakes at the same contrast as the planet. The final magnitude of the planet-star contrast in the M_S is 11.5 ± 0.5 mag.

5.2 Results

To estimate stellar parameters of 51 Eri A, Macintosh *et al.* (2015) made use of Two Micron All-Sky Survey photometry (2MASS; Cutri *et al.*, 2003; Skrutskie *et al.*, 2006b). However, the J and H-band photometry for the star are flagged as 'E', indicating that the photometry is of the poorest quality and potentially unreliable (as compared to an 'A' flag for the the K-band photometry). Further, the study used photometry taken with the *Wide-field Infrared Survey Explorer* (WISE; Wright *et al.*, 2010b) in the $W1$ filter ($\lambda_{\rm eff}$=3.35 μm, $\Delta\lambda$=1.11 μm) as an approximation for the L_P-band magnitude of the primary star. The photometry for 51 Eri A in $W1$, from the AllWISE catalog (Cutri and et al., 2013)), has large errors and contributes to more than half the error budget of the final planet photometry. In this study, we thus

chose to re-observe the star in the JHK_S filters and fit all the available photometry to estimate the photometry in filters where no calibrated stellar data exists.

5.2.1 Revised Stellar Photometry at J,H,K_S

The 2MASS near-IR colors of 51 Eri A were compared to empirical colors for young F0 stars taken from Kenyon and Hartmann (1995), where an F0IV star should have a $J - H = 0.13$ mag and $H - K = 0.03$ mag. The colors of 51 Eri A estimated using the 2MASS photometry are however discrepant, with $J - H = -0.03 \pm 0.08$, and $H - K = 0.23 \pm 0.08$ mag. The discrepant near-IR colors combined with poor quality flags suggest that the published photometry is potentially incorrect.

We observed the star 51 Eri A using the 6.5-m MMT on Mt. Hopkins with the ARIES instrument (McCarthy *et al.*, 1998) on 2016 Feb 28 UT under photometric conditions. We obtained data in the MKO JHK_S broadband filters (Tokunaga *et al.*, 2002), for a total of 3.4 minutes in each filter. To flux calibrate these observations, we observed a photometric standard star at a similar airmass as 51 Eri A, HR 1552 (Carter, 1990). The raw images for both targets were processed through a standard near-IR reduction pipeline, performing dark current subtraction, flat field calibration, and bad pixels correction. Aperture photometry was performed on both targets, with the curve of growth used to select an aperture which minimized the error on the measured flux. The measured brightness of 51 Eri A is presented in Table 10.

Converting the MKO K_S-band measurement into the 2MASS system using the empirical relations[7] yields $K_{S,\mathrm{2MASS}} = 4.551 \pm 0.032$, which is within 1-$\sigma$ of the published 2MASS photometry. Furthermore, the $J - H$ and $H - K$ colors estimated

[7]http://www.astro.caltech.edu/~jmc/2mass/v3/transformations/

from the revised photometry are 0.128 ± 0.037 and 0.016 ± 0.039 mag which are consistent with the empirical expectations.

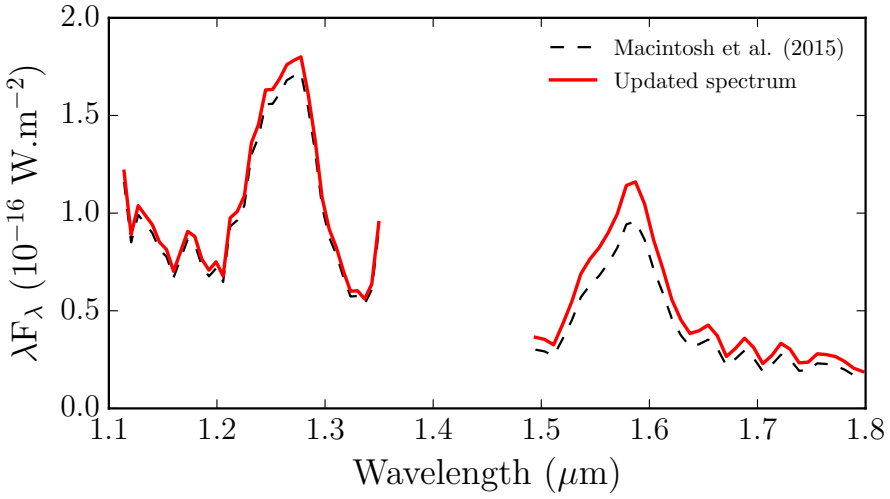

Figure 32. A comparison of the JH spectra of 51 Eri b using the literature 2MASS values against the new photometry measured in this study. The updated photometry increases the planet flux by ∼10% in J and ∼15% in the H-band. The updated stellar photometry is used in the remainder of this study. However the final stellar spectrum used to correct the planet spectrum does not depend on individual filter photometry, as in Macintosh *et al.* (2015) and shown in this plot, but is generated by modeling the full stellar SED prior to converting the planet spectra from contrast to flux units.

The published 51 Eri b spectrum in Macintosh *et al.* (2015) was calibrated using the Pickles stellar models (Pickles, 1998) to estimate the spectrum of the primary, where each band was scaled using the published 2MASS photometry. In Figure 32 we present a comparison between the published spectrum and one scaled using the new MKO photometry, using the same stellar models. The revised photometry scales the planet spectrum higher by ∼10% in the J-band and ∼15% in the H-band, which is significant given the high SNR of the H-band data.

5.2.2 Fitting the Spectral Energy Distribution of 51 Eri A

To mitigate the effects of incorrect photometry, rather than scale the spectrum in pieces using the relevant broadband photometry, we decided to fit the full SED of 51 Eri A using literature photometry and colors, including Geneva $U, B_1, B, B_2, V_1, V, G$ (Rufener and Nicolet, 1988), *Tycho2* B_T, V_T / *Hipparcos* H_P (Høg *et al.*, 2000; ESA, 1997), MKO JHK_S (this work), and *WISE* $W1, W2$ (Cutri and et al., 2013) measurements. We made use of the Geneva color relations as constraints to the full SED fit since the published Geneva V magnitude, which anchors the colors to estimate the remaining photometry, appears to be offset by ∼5% when compared to the *Tycho2* photometry. The *WISE* $W2$ photometry was corrected using the Cotten and Song (2016) relation for bright stars. We combine the photometry with model stellar atmospheres from the BT-NextGen grid[8] (Allard *et al.*, 2012b), we estimated the stellar spectrum using a five parameter MCMC grid search. The best fit atmosphere was found with $T_{\rm eff} = 7331 \pm 30$ K, $\log g = 3.95 \pm 0.04$, $[M/H] = -0.12 \pm 0.06$, and a stellar radius, $R = 1.45 \pm 0.02\ R_\odot$ (assuming a parallax of 33.98 ± 0.34 mas; van Leeuwen, 2007). No correction for extinction is performed as the extinction in the direction of 51 Eri is negligible ($A_V = 0.00$; Guarinos, 1992). These values are consistent with previous literature estimates (e.g. Koleva and Vazdekis, 2012). The final SED of 51 Eri A is shown in Figure 33, which highlights the significantly discrepant 2MASS JH-band photometry that was used previously to calibrate the spectrum of 51 Eri b. We extracted MKO K, NIRC2 L_P and M_S photometry from the SED fit using the filter response functions presented in Tokunaga *et al.* (2002), see Table 10.

[8] https://phoenix.ens-lyon.fr/Grids/BT-NextGen/SPECTRA/

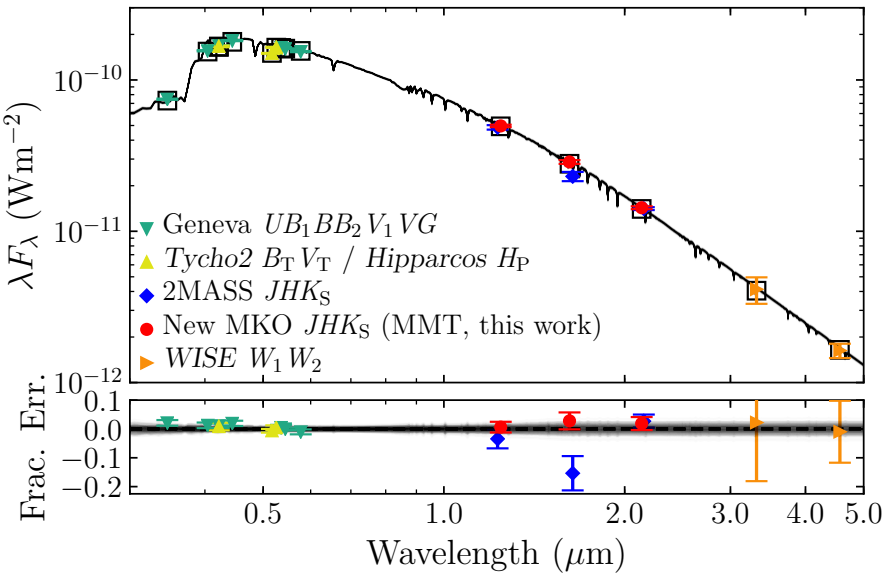

Figure 33. (top panel): Photometry of 51 Eri A from the literature, and from the results presented in this study (filled symbols). One hundred models were randomly selected from the MCMC search, and are plotted (translucent black curves). For each model, the synthetic magnitude was calculated for each filter. The median value for each filter is shown as an open square. The 2MASS photometry points are plotted to illustrate the offset relative to the new MKO measurements, and are not included in the fit. For the plotted Geneva photometry, we computed the Geneva V-band photometry using the best fit spectrum and then used the color relations to calculate the photometry in the remaining filters. (bottom panel): The fractional residuals relative to the median model.

5.2.2.1 Confirming the stellar L_P photometry

51 Eri b emits a substantial amount of flux in the mid-IR and L_P photometry in Macintosh *et al.* (2015) was used to constrain the effective temperature of the planet. There exists no L_P flux measurement for the star and thus they used the $W1$ magnitude reported in the AllWISE catalog ($W1 = 4.543 \pm 0.210$; Cutri and et al., 2013), and assumed a color of $W1 - L_P = 0$ based on the F0IV spectral type of 51 Eri (Abt and Morrell, 1995). The L_P photometry we estimated via the SED fits for 51 Eri

is $L_P = 4.562 \pm 0.014$ mag, which is consistent with the value reported in Macintosh *et al.* (2015) (4.52±0.21 mag) but with significantly smaller uncertainties.

As a final check for consistency, the 2MASS K_S magnitude of 51 Eri ($K_{\mathrm{S,\ 2MASS}} = 4.537 \pm 0.024$) was used instead as a starting point. The $K_S - L_P$ color for early F-type dwarfs and subgiants was estimated by folding model stellar spectra ($7200 \leq T_{\mathrm{eff}}/\mathrm{K} \leq 7400$, $4.0 \leq \log g \leq 4.5$, $[M/H] = 0$) from the BT-Settl model grid through the relative spectral response of the 2MASS K_S (Cohen *et al.*, 2003) and NIRC2 L_P filters. Over this range of temperatures and surface gravities, the color was calculated as $K_S - L_P = -0.001 \pm 0.001$. In order to realistically assess the uncertainties on this color, the near to thermal-IR spectra of F-type dwarfs and subgiants within the IRTF library (Rayner *et al.*, 2009) were processed in the same fashion, resulting in a $K_S - L_P = 0.014 \pm 0.055$. A color of $K_S - L_P = -0.001 \pm 0.055$ was adopted based on the color calculated from the model grid, and the uncertainty calculated from the empirical IRTF spectra. This color, combined with the $K_{S,\mathrm{2MASS}}$ magnitude of 51 Eri, gives an L_P apparent magnitude of 4.538 ± 0.060. Each estimate for the stellar L_P magnitude are within 1-σ of each other, and thus we adopt the value derived from the SED fit i.e. $L_P = 4.562 \pm 0.014$ mag.

5.2.3 51 Eri b Spectral Energy Distribution

We present the final spectral energy distribution of the planet 51 Eri b in Figure 34 and use it to analyze the system properties in the following sections. Using the stellar SED estimated earlier, we have updated the J and H spectra that were published in Macintosh *et al.* (2015). In Table 10, we present the properties of the system,

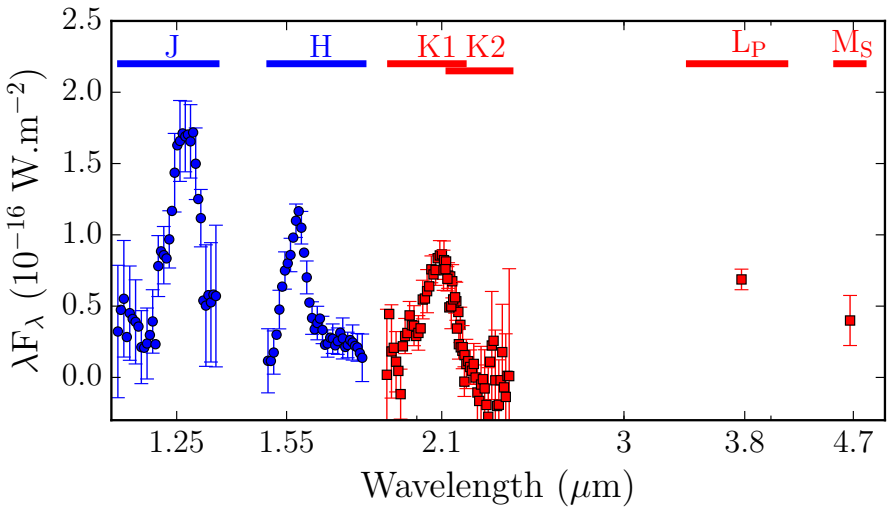

Figure 34. Final spectral energy distribution of the directly imaged exoplanet 51 Eri b. The new $K1$ and $K2$ GPI spectra along with the updated L_P and new M_S photometry are shown with red squares. The GPI J and H spectra, updated to account for the revised stellar flux, from the discovery paper (Macintosh *et al.*, 2015) are plotted with blue circles. The filter extent is shown with the horizontal line over each band. To reduce crowding in the spectra, the errors for one out of every two data points are plotted.

including the updated photometry for both the star and the planet. A future study will refine the orbital solution presented in De Rosa *et al.* (2015).

5.3 Analysis

5.3.1 Comparison against field brown dwarfs

We plot a set of brown dwarf Color Magnitude Diagrams (CMD) in Figure 35, and compare the photometry of field M, L, and T dwarfs and young brown dwarfs and imaged companions to that of 51 Eri b (red star). The colors of 51 Eri b seems to

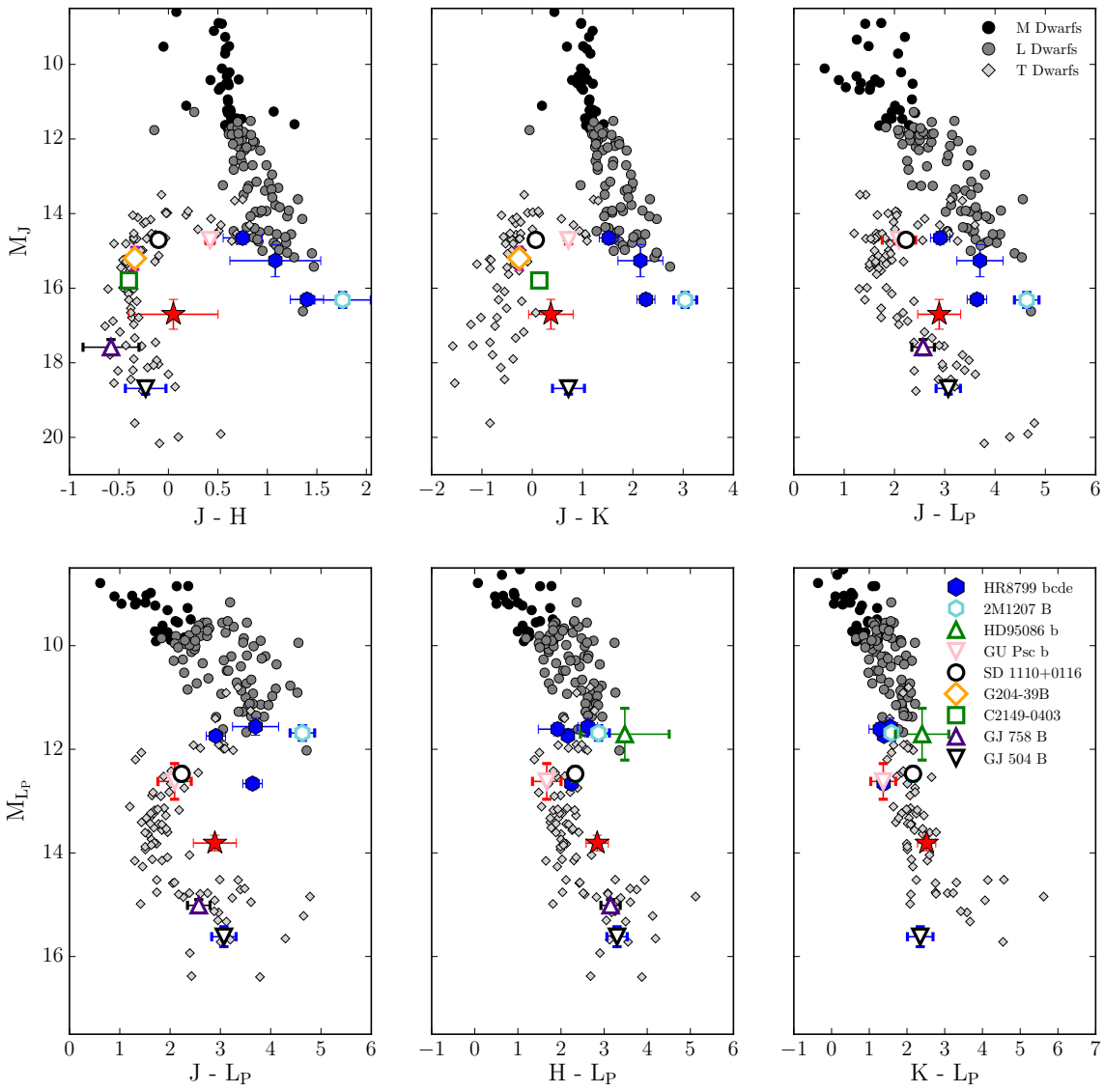

Figure 35. The brown dwarf and imaged exoplanet color magnitude diagram. 51 Eri b is shown with the red star. The colors of 51 Eri b place it among late T-dwarfs, where it is redder than most comparable temperature brown dwarfs likely indicative of greater cloud opacity in the atmosphere. The photometry for the field M-dwarfs (black circles), L-dwarfs (dark gray circles) and T-dwarfs (light gray diamonds) is taken from the compilation of Dupuy and Liu (2012a); Liu *et al.* (2016). We used a linear fit to convert *WISE* $W1$ photometry to L_P, similar to what was done in Macintosh *et al.* (2015). The photometry for the directly imaged planets and young brown dwarfs were taken from Marois *et al.* (2010b); Chauvin *et al.* (2005a); Rameau *et al.* (2013a); Naud *et al.* (2014); Leggett *et al.* (2007); Delorme *et al.* (2017); Janson *et al.* (2011b); Kuzuhara *et al.* (2013).

Table 10. System properties.

Property	51 Eri A	51 Eri b
Distance (pc)	29.4 ± 0.3^{a}	
Age (Myr)	26 ± 3^{b}	
Spectral type	F0IV	T6.5±1.5
$\log(L/L_{\odot})$	$0.85^{+0.06}_{-0.07}$ [c]	-5.75 to -5.88 [d]
$T_{\rm eff}$	7331±30 K [e]	600–700 K [d]
$\log g$	3.95±0.04 [e]	3.5–4.0 [d]
Mass	1.75 ± 0.05 $M_{\odot}$ [c]	2 $M_{\rm Jup}$ [c]
J	4.690 ± 0.020 [d]	16.70 ± 0.40 [d]
H	4.562 ± 0.031 [d]	16.65 ± 0.21 [d]
K_S	4.546 ± 0.024 [d]	16.15 ± 0.19 [d]
K	4.546 ± 0.024 [e]	16.33 ± 0.19 [d]
L_P	4.569 ± 0.014 [e]	13.81 ± 0.15 [d]
M_S	4.566 ± 0.014 [e]	13.7 ± 1.1 [d]

a: *Hipparcos* catalog (van Leeuwen, 2007)

b: Nielsen *et al.* (2016)

c: Macintosh *et al.* (2015) using hot-start predictions.

d: This work

e: Stellar photometry estimated using SED fit

match the phase space of the late-T dwarfs. To classify the spectral type of 51 Eri b, we do a chi-square comparison of the GPI $JHK1K2$ spectrum of 51 Eri b to a library of brown dwarf spectra compiled from the IRTF (Cushing *et al.*, 2005), SpeX (Burgasser, 2014), and Montreal (e.g. Gagné *et al.*, 2015b; Robert *et al.*, 2016) Spectral Libraries. Only a small sub-sample of the brown dwarfs have corresponding mid-IR photometry and thus we choose to restrict our comparison to the near-IR. The spectra within the library were convolved with a Gaussian kernel to match the spectral resolution of GPI.

To compute the chi-square between the spectrum of 51 Eri b and the objects within the library, we use two different equations. The first method permits each

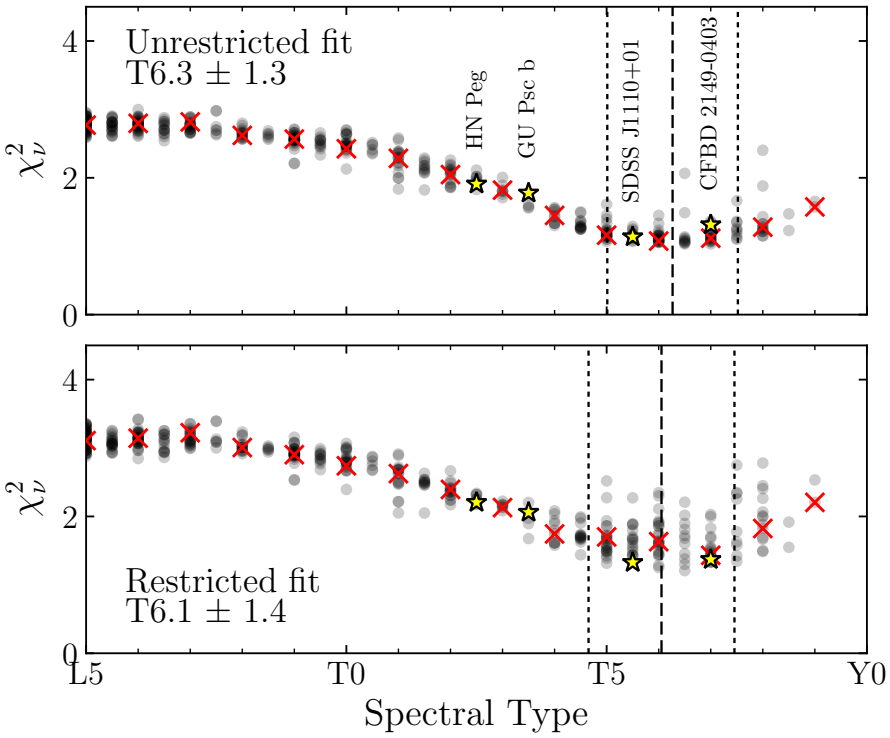

Figure 36. Comparison of L5 to T9 field (gray circles) and young (yellow stars) brown dwarf JHK spectra to 51 Eri b using the reduced χ^2. The standard brown dwarf for each spectral bin is plotted with a red cross (Kirkpatrick *et al.*, 2010; Burgasser *et al.*, 2006b; Cushing *et al.*, 2011). The dashed and dotted vertical lines give the best fitting spectral type, and corresponding uncertainty. (Top) Each spectral band of the comparison was allowed to float to find the lowest chi-square while fitting the planet spectrum. (Bottom) The spectrum was allowed to float up/down in flux, but was penalized by the spot ratio uncertainty in each respective band.

individual filter spectrum to vary freely (unrestricted fit). In the unrestricted fit, we compute the χ^2 statistic for the j^{th} object within the library as

$$\chi^2_j = \sum_{i=1}^{4} \left(\boldsymbol{S}_i - \alpha_{i,j}\boldsymbol{F}_{i,j}\right)^T \boldsymbol{C}_i^{-1} \left(\boldsymbol{S}_i - \alpha_{i,j}\boldsymbol{F}_{i,j}\right), \tag{5.1}$$

where $\boldsymbol{S}_i$ is the spectrum of the planet, $\boldsymbol{C}_i$ is the covariance matrix calculated in Section 5.1.1.1, and $\boldsymbol{F}_{i,j}$ is the spectrum of the j^{th} comparison brown dwarf, all for the i^{th} filter. For each object, the scale factor $\alpha_{i,j}$ that minimizes χ^2 is found using a

downhill simplex minimization algorithm. In this method the scale factor for each object, $\alpha_{i,j}$, is allowed to vary between the four filters ($JHK1K2$). This is equivalent to allowing the near-IR colors to vary freely up and down in order to better fit the object (e.g. Burningham *et al.*, 2011).

In the second method the individual filter spectra are still allowed to vary, only within the satellite spot brightness ratio uncertainty (restricted fit), thereby restricting the scale factor for each filter. For the restricted fit the scale factor is split into two components. The first, α_j, is independent of filter, and accounts for the bulk of the difference in flux between 51 Eri b and the comparison object due to differing distances and radii. The second, $\beta_{i,j}$, is a filter-dependent factor that accounts for uncertainties in the satellite spot ratios given in Maire *et al.* (2014). Equation 5.1 is modified to include an additional cost term restricting the possible values of $\beta_{i,j}$,

$$\chi^2_j = \sum_{i=1}^{4} \left[\left(\boldsymbol{S}_i - \alpha_j \beta_{i,j} \boldsymbol{F}_{i,j}\right)^T \boldsymbol{C}_i^{-1} \left(\boldsymbol{S}_i - \alpha_j \beta_{i,j} \boldsymbol{F}_{i,j}\right) \; + \; N_i \left(\frac{\beta_{i,j} - 1}{\sigma_i} \right)^2 \right] \tag{5.2}$$

where N_i is the number of spectral channels in the 51 Eri b spectrum for the i^{th} filter, and σ_i is the uncertainty on the satellite spot flux ratio given in Maire *et al.* (2014) for the same filter. The second term in Equation 5.2 penalizes values of the scale factor, $\beta_{i,j}$, that are very different from the satellite spot uncertainty and thus increases the chi-square for objects significantly different from 51 Eri b.

The spectral type of 51 Eri b was estimated for both fits from the χ^2 of the L5–T9 near-IR spectral standards (Kirkpatrick *et al.*, 2010; Burgasser *et al.*, 2006b; Cushing *et al.*, 2011). To compute the weighted mean and standard deviation of 51 Eri b, we converted the spectral type to a numerical value for the standard brown dwarfs, i.e. L5 = 75, T5 = 85. Each numerical spectral type when compared to 51 Eri b, is weighted according to the ratio of its χ^2 to the minimum χ^2 for all standards (e.g., Burgasser

et al., 2010), and the lowest value was adopted as the spectral type of 51 Eri b. A systematic uncertainty of one half subtype was assumed for the standards. We find that the two estimates are consistent with one another i.e. T6.3 ± 1.3 and 6.1 ± 1.4 for unrestricted and restricted fits, see Figure 36. We adopt a spectral type for 51 Eri b of T6.5 ± 1.5 from the unrestricted fit, rounded to the nearest half subtype.

The best-fit object for both the unrestricted and restricted fits was G 204-39 B (SDSS J175805.46+463311.9; $\chi^2_\nu = 1.033$ and 1.209), a T6.5 brown dwarf common proper motion companion to the nearby M3 star G 204-39 A (Faherty *et al.*, 2010). G 204-39 B has marginally low surface gravity based on photometric ($\log g \approx 4.5$; Knapp *et al.*, 2004) and spectroscopic measurements ($\log g = 4.7$–4.9; Burgasser *et al.*, 2006a), indicative of it being younger than the field population. While the binary system is not thought to be a member of any known young moving group (Gagné *et al.*, 2014), the stellar primary can be used to provide a constraint on the age of the system. Combining the X-ray and chromospheric activity indicators for the M dwarf primary, and a comparison of the luminosity of the secondary with evolutionary models, Faherty *et al.* (2010) adopt an age of 0.5–1.5 Gyr for the system. 51 Eri b is redder than the spectrum of G 204-39 B (Figure 37), especially in terms of the $H - K$ color, which is a photometric diagnostic of low surface gravity among T-dwarfs (e.g., Knapp *et al.*, 2004). This is consistent with the younger age of 51 Eri b, and the most likely cause for this is that it has lower surface gravity than that of G 204-39 B.

Additional good matches to the 51 Eri b spectrum include 2MASS J22282889–4310262 (2M 2228–43, $\chi^2_\nu = 1.07$ and 1.26 for the two fits) and 2MASS J10073369–4555147 (2M 1007–45, $\chi^2_\nu = 1.07$ and 1.33). 2M 2228–43 a well-studied T6 brown dwarf that exhibits spectrophotometric variability in multiple wavelengths indicative of patchy clouds in the photosphere (Buenzli *et al.*, 2012; Yang *et al.*, 2016). 2M 1007–45

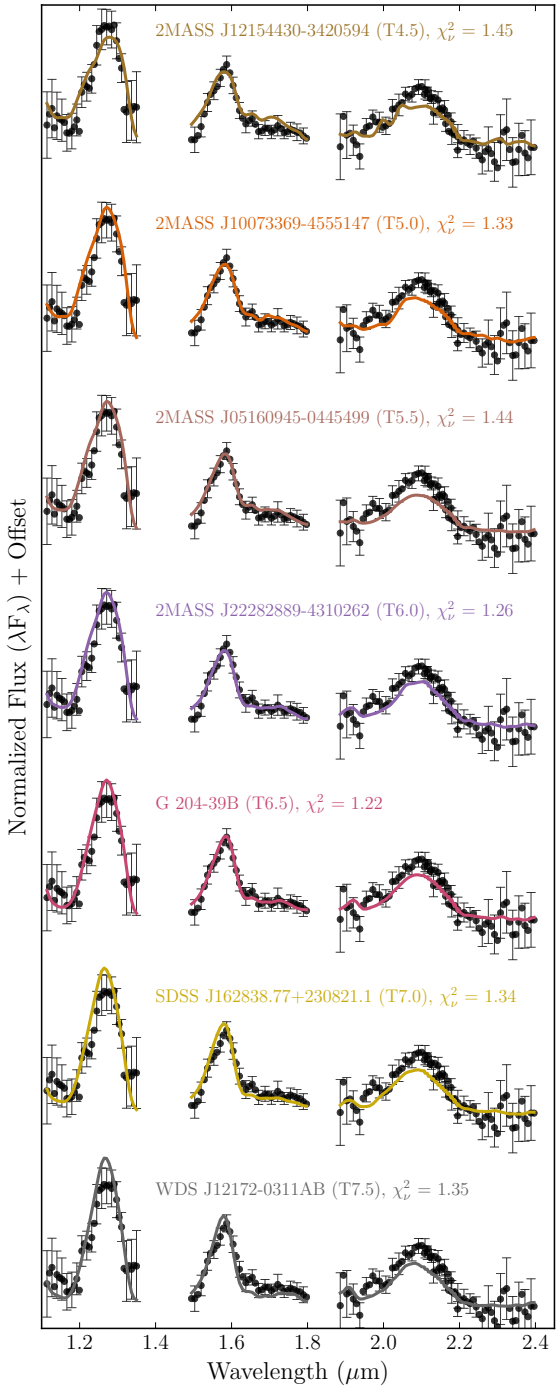

Figure 37. Comparing the spectra, using the restricted fit, of the best fitting T4.5 to T7.5 field brown dwarfs to 51 Eri b. The spectra fit in this figure are a subset of the data plotted in Figure 36, using the restricted chi-square equations presented in Equation 5.2. The T4.5 and T5.0 spectra are from Looper *et al.* (2007), the T5.5 is from Burgasser *et al.* (2008), the T6.0 is from Burgasser *et al.* (2004), the T6.5 and T7.5 are from Burgasser *et al.* (2006a), and the T7.0 is from Dupuy and Liu (2012a).

is a T5 brown dwarf at a distance of 17 ± 2 pc (Smart *et al.*, 2013). It was identified by Looper *et al.* (2007) as a low surface gravity object based on its $H_2O{-}J$ vs K/H spectral ratios defined in Burgasser *et al.* (2006a); comparisons against solar-metallicity models imply an age of between 200 and 400 Myrs (Looper *et al.*, 2007).

The best fit object for each spectral type between spectral types T4.5 and T7.5 using the restricted fit are plotted in Figure 37. While the quality of the fits were generally good, none of the objects were able to provide a good match across all of the bands simultaneously, being too luminous in either the J or K-bands. Differences in surface gravity, effective temperature, and/or metallicity could be the cause (e.g., Knapp *et al.*, 2004). The poor fit to the color of 51 Eri b is especially apparent in the CMDs plotted in Figure 35, with 51 Eri b having unusually red near-IR colors relative to similar spectral type objects.

5.3.2 Comparison against young brown dwarfs

Searches for young companions and moving group objects have resulted in detections of several tens to hundred of million year old L-type brown dwarf and planetary mass companions as well as the identification of L-dwarf sub-classes based on youth (e.g. Allers and Liu, 2013; Filippazzo *et al.*, 2015; Faherty *et al.*, 2016; Liu *et al.*, 2016). In comparison, there exist relatively few known (or suspected) young T-dwarf brown dwarfs. In Figure 38, we plot the known young T-dwarfs and compare them in a similar manner to what was done above for field brown dwarfs. The chi-square for the fits is not much better than what is seen for the field dwarfs which is likely due to the absence of young T-dwarfs of similar spectral type to 51 Eri b.

The brown dwarf SDSS J1110+0116 with a spectral type of T5/T5.5 is the best

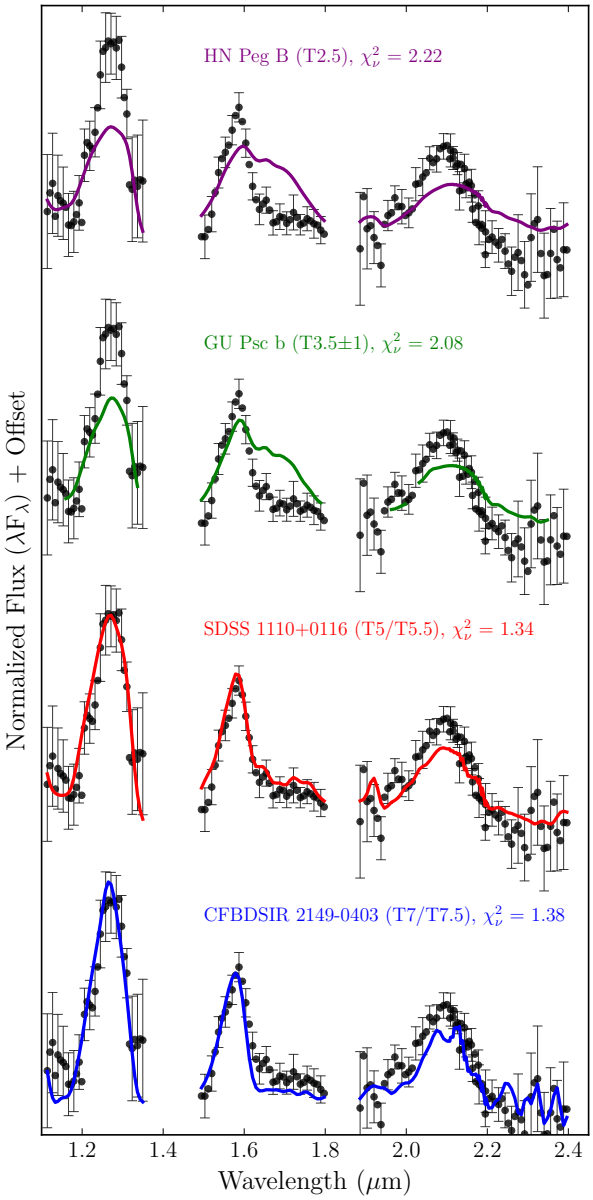

Figure 38. Comparing the spectra of known young T-dwarfs to that of 51 Eri b. Similar to the field sequence, the fits presented here were computed using the restricted chi-square. From top to bottom, the four spectra were sourced from Luhman *et al.* (2007), Naud *et al.* (2014), Burgasser *et al.* (2006a), and Delorme *et al.* (2012).

fitting young comparison object. It has been identified as a *bona fide* member of the AB Doradus moving group and is thus young (110–130 Myr) and low mass (10–12 M_{Jup}) (Gagné *et al.*, 2015a). The other young field object that closely matches the near-IR spectrum of 51 Eri b is the T7 brown dwarf CFBDSIR J2149-0403 (Delorme *et al.*, 2012). Similar to SDSS J1110+0116, CFBDSIR J2149-0403 has a high probability of being a member of the AB Doradus moving group, and is most likely a low temperature (700 K), low mass (4–7 M_{Jup}, $\log g \approx 4$) free-floating planetary mass object. CFBDSIR J2149-0403 shows stronger methane absorption features in the red end of the H-band spectrum as compared to 51 Eri b. However, it is worth pointing out that while both young objects, SDSS J1110+0116 and CFBDSIR J2149-0403, are reasonable matches across the J and H spectra of 51 Eri b, they appear to be under-luminous in the K-band. A likely reason for this is that 51 Eri b is much younger than both the comparison companions and thus has the lowest surface gravity amongst the three objects (Burgasser *et al.*, 2006a).

5.3.3 A very red T6 or an L-T transition planet?

Based on the position of 51 Eri b in Figure 35, it appears that the trend of planetary mass objects having redder colors compared to the field, seen in young L-type brown dwarfs and planetary mass companions (Faherty *et al.*, 2016; Liu *et al.*, 2016), possibly continues for the T-type companions. Note that the $K - L_P$ CMD shows little reddening, which is natural if clouds are causing the effect. The effect of clouds is negligible in the K and L_P bands. Across both the near and mid-IR CMDs, 51 Eri b is one of the reddest T type objects and within its spectral classification it has the reddest colors. This trend in the 51 Eri b colors was originally noted in

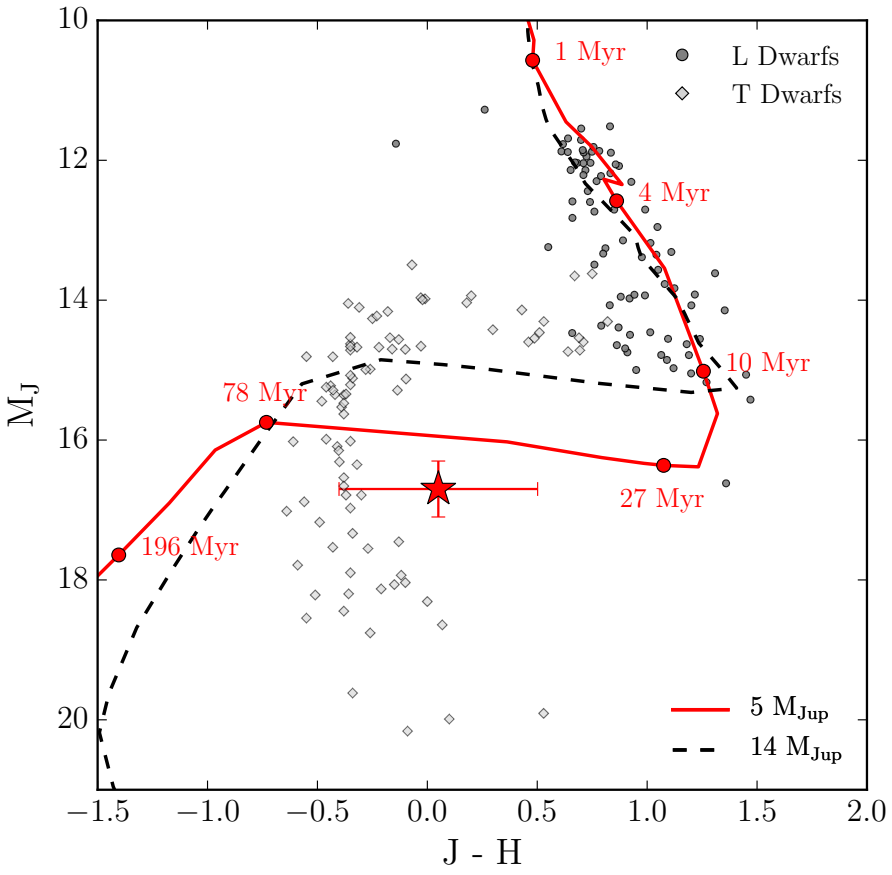

Figure 39. The J vs $J-H$ brown dwarf and imaged exoplanet color magnitude diagram reproduced from Figure 35. The photometry for 51 Eri b is shown with the red star. Also plotted on the CMD are the evolutionary tracks for 5 and 14 M_{Jup} object (Marley *et al.*, 2012), with the solid red line and dashed black line respectively. The models assume a simple gravity dependence for the initiation of the transition. A few ages for the 5 M_{Jup} track have been over plotted. The L-T transition for the 5 M_{Jup} planet starts at approximately 900 K and 20 Myr, but for a lower mass planet such as 51 Eri b will occur at younger ages.

Macintosh *et al.* (2015) where they compared the L_P vs $H - L_P$ color for the planet and noted that it was clearly redder than the field. Rather than simply being redder than the field T-dwarfs due to the presence of clouds, we present a second possible interpretation for the red colors of 51 Eri b. Where the planet is still in the process of completing its transition from L-type to T-type, where the evolutionary track followed is gravity dependant as shown in Figure 39. In this scenario, 51 Eri b transitions at fainter magnitudes than that seen for field L-T transition brown dwarfs and it has not yet completed its evolutionary transition to reach the blue colors typical of field, mid-T dwarfs.

In Figure 39, we re-plot the J vs $J - H$ panel from the series of CMDs shown in Figure 35. In addition to the photometry of 51 Eri b and the field and young brown dwarfs we also over-plot two low mass, 5 and 14 M_{Jup}, evolutionary model tracks (assuming hot-start conditions) from Saumon and Marley (2008); Marley *et al.* (2012). If the L-T transition is gravity dependent, as multiple lines of evidence now suggest (Leggett *et al.*, 2008; Dupuy *et al.*, 2009; Stephens and Leggett, 2004), then lower mass objects may turn blue at fainter absolute magnitudes than field objects. In Figure 39, we show a simple model in which the L to T transition begins at 900 K at $\log g = 4$ (solid red line) instead of 1200 K at $\log g = 5.3$ (dashed black line). In the case of a $5M_{Jup}$ planet the L to T transition begins and ends about 1 magnitude fainter in J band than observed for the field population. Furthermore the congruence of the spectrum of SDSS J1110+0116 with 51 Eri b (Figure 38) is interesting as SDSS J1110+0116 lies just short of the blue end of the field L to T transition, although it does so at an absolute magnitude just slightly fainter than the field transition magnitude. Clearly more sophisticated modeling of evolution through the L to T transition, accounting for inhomogeneous cloud cover and a gravity

dependent transition mechanism as well as a range of initial conditions is required to properly evaluate this hypothesis. Testing this hypothesis is difficult and would require knowledge of the true mass of the companion as well as the formation mechnism. If this hypothesis is true, then the only objects that are brighter on the CMD should be higher mass objects. There should not be any lower mass objects above and to the left of 51 Eri b on the J vs $J - H$ CMD shown in Figure 39.

5.4 Modeling the atmosphere of 51 Eri b

For the purpose of modeling the complete SED of 51 Eri b we made use of two updated atmospheric model grids from the same group, focusing on different parameter space (see Table 11). The first grid, described in Marley *et al.* (1996, 2002, 2010) focused on the higher effective temperature atmospheres (L-dwarfs) and includes iron and silicates clouds in the atmosphere. While the second grid, described in Morley *et al.* (2012, 2014) and Skemer *et al.* (2016), covers lower effective temperatures (T and Y dwarfs) and molecules expected to condense at these temperatures specifically salt and sulfide clouds.

The methodology used to fit the models to the data is the same for both model grids. To fit the models to the data, we bin the model spectra to match the spectral resolution of the GPIES spectra across each of the $JHK1K2$ filters. For the photometry we integrated the model flux through the Keck/NIRC2 L_P and M_S filter profiles respectively. The estimation of the best fitting model is done by computing the chi-square value for each model in the grid compared to the data using Equation 5.2. We made use of the covariance matrices estimated for the four spectral channels described in the appendix and also included the variance for each of the two photometric data

Table 11. Model grid parameters

Model Name	Effective Temperature (K)	Surface Gravity ($\log g$)	Metallicity [M/H]	Cloud Parameter (f_{sed})	Cloud Hole Fraction (%)
Iron/Silicate Cloud Grid	600–1000	3.25	0.0	2	0–75
Sulfide/Salt Cloud Grid	450–900	3.5–5.0	0.0, 0.5, 1.0	1, 2, 3, 5	–
Cloudless Grid	450–900	3.5–5.0	0.0, 0.5, 1.0	no cloud	–

points to compute the chi-square statistic. Note that we use the restricted fit equation in the computation of the best fitting model. This equation permits each of individual filters to scale within the 1-σ error of the satellite spot ratios. We also did the fitting without the scaling factor and found that the results are similar.

As stated earlier in section 5.1.1.1, the use of the covariance affects the model fitting where the peak of the posterior distribution occurs at slightly cooler effective temperatures, consistent within the errors. Due to the high spectral correlation in the J-band (see Figure 55), when using the covariance the best fitting models are not models that pass through the data but rather models that have lower flux in the J-band than the data. We present the specific modeling details in the following text.

5.4.1 Iron and Silicates Cloud Models

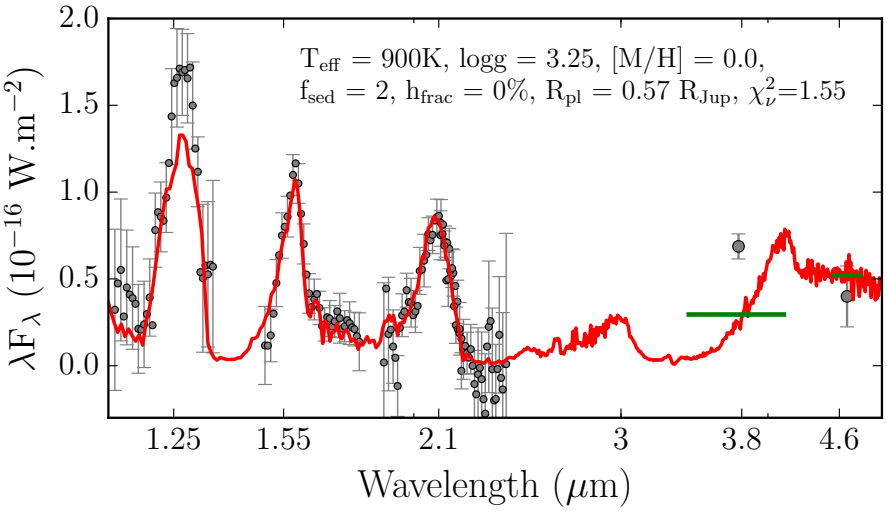

Figure 40. Spectral Energy Distribution of 51 Eri b with the best fitting iron and silicates cloudy model.

In sec. 5.3.3, we suggested that 51 Eri b, rather than having completely evolved to

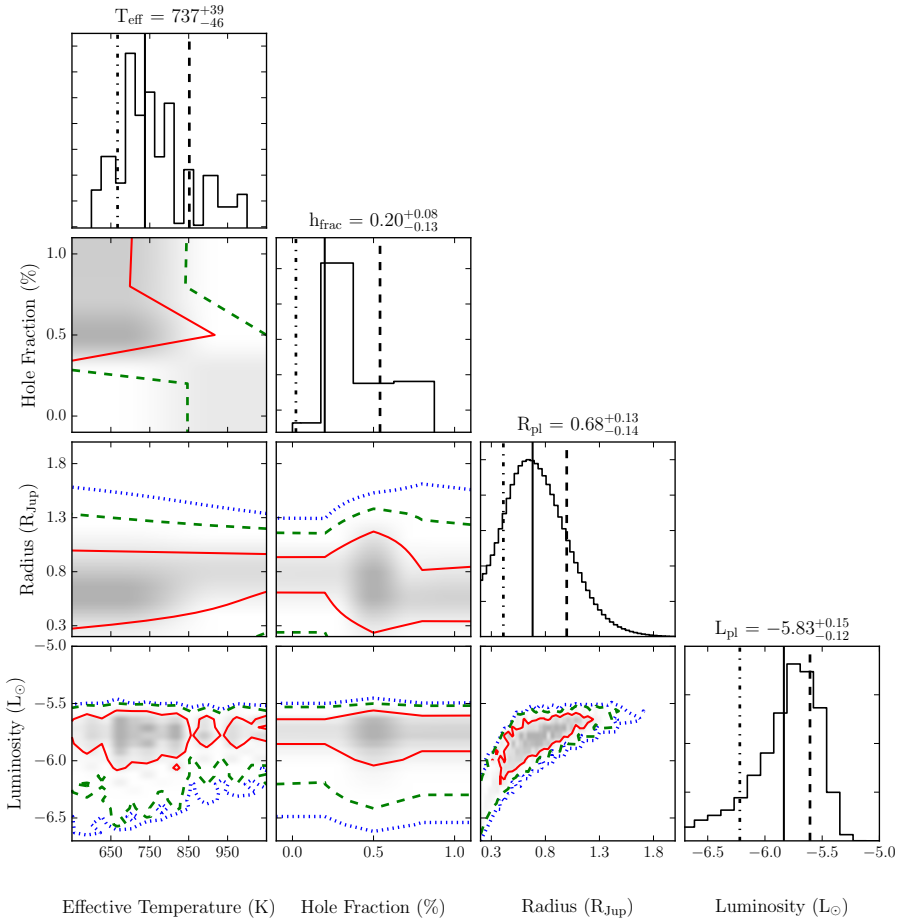

Figure 41. Normalized posterior distributions for the iron and silicates model grid. The PDFs are for the parameters varied in our fit along with the inferred distribution of the luminosity of 51 Eri b. The lines on the 1D histogram indicate the 16th, 50th, and 84th percentile values while those on the 2D histogram are the 1σ (solid red), 2σ (dashed green) and 3σ (dotted blue) values of the distribution. The values printed above each histogram are the median value along with the 1-σ error on it.

T-type, could be transitioning from L-to-T. In this scenario the cloud composition of the planetary atmosphere might still be influenced by the deep iron and silicates condensate grains and patchy cloud atmosphere. Therefore, we compared the planet SED to a grid of models with a fixed low surface gravity fixed and solar metallicity, where the key variable is cloud hole fraction and the unique aspect of this grid is the presence of iron/silicate clouds in an atmosphere with clear indications of methane

absorption. The clouds are modelled using the prescription presented in Ackerman and Marley (2001b), where cloud thickness is parameterized via an efficiency factor (f_{sed}). Where small values of f_{sed} indicate atmospheres with thick clouds while large values of f_{sed} are for atmospheres with large particles that rain out of the atmosphere leaving optically thinner clouds. As mentioned early the primary condensate species in this grid are iron, silicate, and corundum clouds, molecules that are expected to dominate clouds in L-dwarfs (Saumon and Marley, 2008; Stephens and Leggett, 2004). At the L-T transition clouds are expected to be patchy, thus for each T_{eff}, the models went from fully cloudy i.e. $f_{sed} = 2$ and 0% holes to an atmosphere with $f_{sed} = 2$ and 75% holes (patchy clouds). The methodology used to calculated the flux emitted from the patchy cloud atmosphere include both cloud and cloud-free regions simultaneously in the atmosphere using a single, global temperature-pressure profile and are not created via a linear combination of two models as is sometimes done in the literature Marley *et al.* (2010). The iron and silicates cloud grid models use solar metallicity (Lodders, 2003). The opacity database used for the absorbers are described in Freedman *et al.* (2008), including updated molecular line lists for ammonia and methane (Yurchenko *et al.*, 2011; Yurchenko and Tennyson, 2014). The models span effective temperatures from 600K to 1000K for solar metallicity ([M/H] = 0.0) and low surface gravity ($\log g$ = 3.25, 3.50) (see Table 11).

Presented in Figure 40 is the best fitting model to the SED of 51 Eri b. Stated in the figure are the model parameters along with the radius of the planet required to scale the model spectrum to match the planet SED. This scaling factor is required since the model spectra are typically computed to be the emission at the photosphere or at 10pc from the object. One of the free parameters in most model fitting codes is the term R^2/d^2 to scale the model flux to match the SED, where R is the radius of the

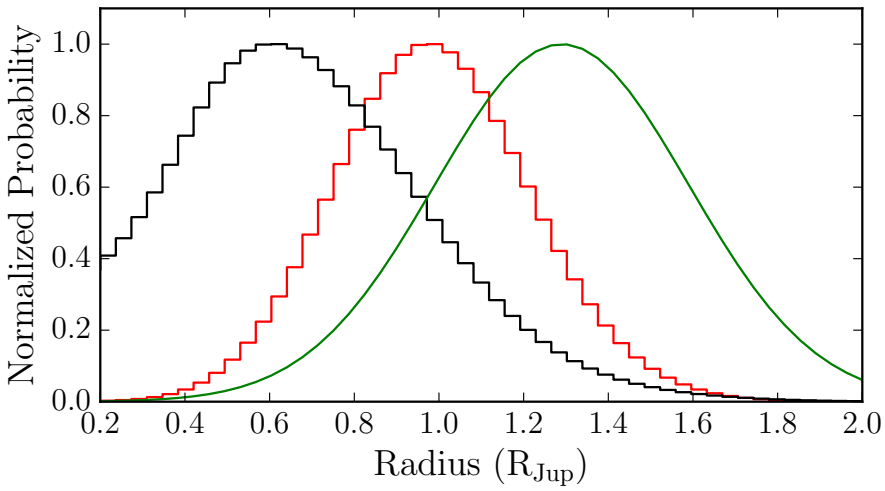

Figure 42. The figure shows the effect of applying a Gaussian radius prior when modeling with the iron/silicates grid. The prior shown by the green line is centered on the radius given by evolutionary models i.e. 1.29 R_{Jup} (Marley *et al.*, 2007; Fortney *et al.*, 2008). Also plotted are the likelihood (black) and posterior distribution (red).

planet and d is the distance to the object. For 51 Eri, the distance is known to better than 2% (see Table 10) and thus we only fit the radius term. Shown in Figure 41 is the posterior distribution for the radius where we find that the best fitting radii is significantly smaller than that predicted by evolutionary models, e.g. 1.33–1.14 R_{Jup} for a 2–10 M_{Jup} hot/cold start planet at the age of 51 Eri (Marley *et al.*, 2007; Fortney *et al.*, 2008). This discrepancy has been noted previously as well for the HR8799 planets (Marois *et al.*, 2008; Currie *et al.*, 2011a; Marley *et al.*, 2012), β Pic b (Morzinski *et al.*, 2015) and for 51 Eri b itself in the discovery paper (Macintosh *et al.*, 2015). In an attempt to circumvent this issue, while modeling the SED we adopted a Bayesian prior probability density function for the radius in the form of a Gaussian centered on the expected radius from evolutionary models (green line in Figure 42), with the width chosen to include the radius of Jupiter. Without the prior (i.e. using a uniform prior), the median radius is 0.68 R_{Jup} and $T_{eff} \sim 740$K, with the prior the median radius value is forced closer to the predictions of evolutionary models (red

line in Figure 42) at 0.98 R_{Jup}, and $T_{eff} \sim 690$K, biasing the luminosity of the planet to larger values. When fitting the SED, the term that is conserved is the luminosity rather than the effective temperature or the radius. Adopting the evolutionary radius and marginalizing over the uncertainty in radius raises the luminosity ($\log L/L_{\odot}$) from -5.83 to -5.65. Since observational constraints on the radius for young planets are unavailable, we chose to use an uninformative prior.

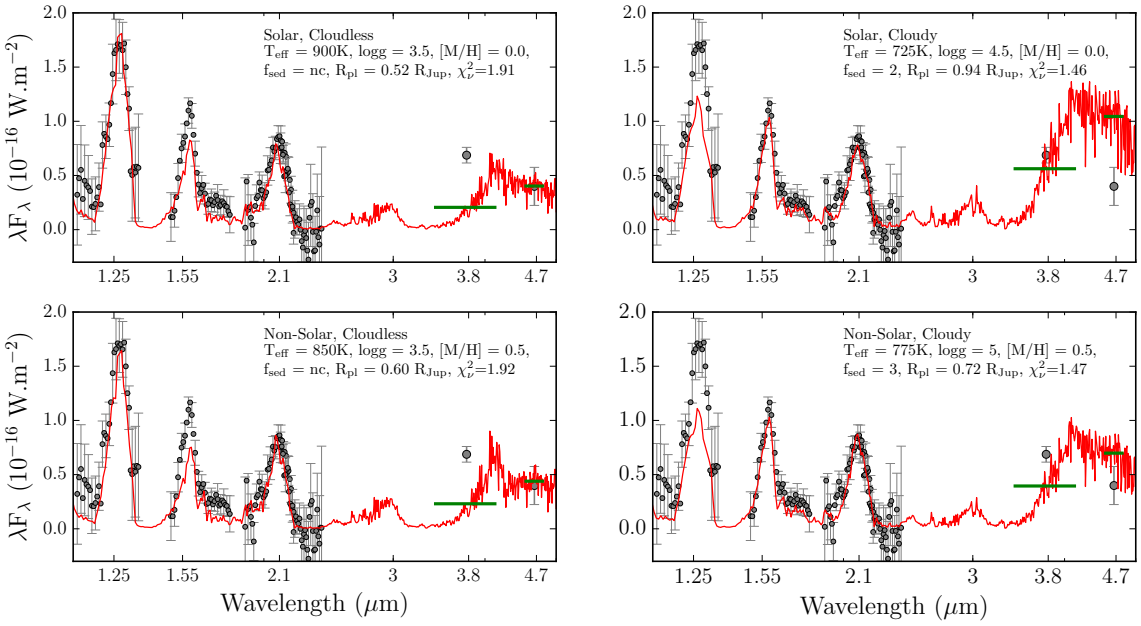

Figure 43. Spectral Energy Distribution of 51 Eri b with the best fitting salt and sulfide cloud models. Each panel shows the best fitting model under the specific conditions: top two panels show the best fitting *solar* metallicity models with cloudless atmosphere on the left and cloudy atmospheres on the right. Bottom two panels show the best fitting *non-solar* models with cloudless atmosphere on the left and cloudy atmospheres on the right.

Plotted in Figure 41 are the normalized posterior distributions for each of the model parameters varied in the model fit, along with the covariances to show how each of the parameters are affected. Since the grid only had a few models with $\log g$ = 3.5, with the majority being 3.25, we marginalized over the the surface gravity.

The irregular shape of the effective temperature posterior is caused by the missing models in the grid. The median effective temperature, 737 K, estimated from the grid falls right in between the range of best fitting temperatures from the models in the Macintosh *et al.* (2015) paper (700–750K). However, based on the shape of the posterior and the covariances, the peak of the effective temperature distribution extends to cooler temperatures. Since the L to T transition has been suggested to arise from holes or low opacity patches appearing in an initially more uniform cloud deck (Ackerman and Marley, 2001b; Burgasser *et al.*, 2002; Marley *et al.*, 2010), our finding here that partly cloudy models best fit the 51 Eri b spectrum is consistent with this interpretation. In general, however the models struggled to fit the entire planet SED, typically being able to fit either the near or mid IR portions of the SED. The inability to fit mid-IR photometry suggests that chemical equilibrium models are not appropriate. Disequilibrium chemistry predicts less CH_4 in the atmosphere and could explain higher flux at 1.6μm and in the L_P band. It would also introduce CO, accounting for lower flux in the M_S band.

5.4.2 Sulfide and Salt Cloud Models

In Section 5.3.1, we showed that the best fitting spectral type of 51 Eri b is a mid-to-late T-dwarf. At the effective temperatures of mid to late T-dwarfs, Cr, MnS, Na_2S, ZnS, and KCl are expected to condense and form clouds high in the photosphere. The second grid we tested the planet SED against made use of a model grid which includes salt and sulfide clouds to test additional parameters such as the surface gravity and metallicity (which were varied, unlike the iron/silicates grid) and the properties of clouds typically associated with T-dwarfs. The grid was designed

specifically for lower temperature objects (450 $\sim$ 900 K Morley *et al.*, 2012, 2014) and has been successfully to reproduce the SED of GJ 504 b (Skemer *et al.*, 2016), a cool planetary mass companion with a similar spectral type (late-T) which is comparable to 51 Eri b (Kuzuhara *et al.*, 2013). Note that the use of this cloud grid does not preclude the possibility of the planet transitioning from L-to-T.

Also included as part of this grid are the clear atmosphere models from Saumon and Marley (2008), the ranges for which are presented in Table 11. The range of parameters varied are presented in Table 11, including temperatures, surface gravities, metallicities, and sedimentation factor (f_{sed}) ranging from cloudy ($f_{sed} = 1$) to cloud free. The cloud model used in the sulfide/salt grid is the same as the one described above. In addition to the opacity updates mentioned above, opacity effects due to alkali metals (Li, Na, K) have been included using the results from Allard *et al.* (2005). Between effective temperatures of 450–775 K, the grid is complete with models available for every step of the varied parameters. For effective temperatures between 800–900K, the temperature steps switch from increments of 25K to 50K and there are no models with f_{sed} values of 1 and 2. This grid does not include opacity effect due to iron and silicates condensates. A future series of paper describing an extended atmosphere model grid will describe the updates, however the present grid extends the models to greater than solar metallicites.

In Figure 43, we present the four best fitting model atmospheres for 51 Eri b. Presented in each panel are the atmosphere with the lowest reduced chi-square in one of four cases, namely, solar and cloudless (top-left), solar and cloudy (top-right), non-solar and cloudless (bottom-left), non-solar and cloudy (bottom-right). Both cloudless model atmospheres are warmer and thus fit the near-IR spectrum of the planet while completely missing the L_P photometry. The cloudy atmosphere model

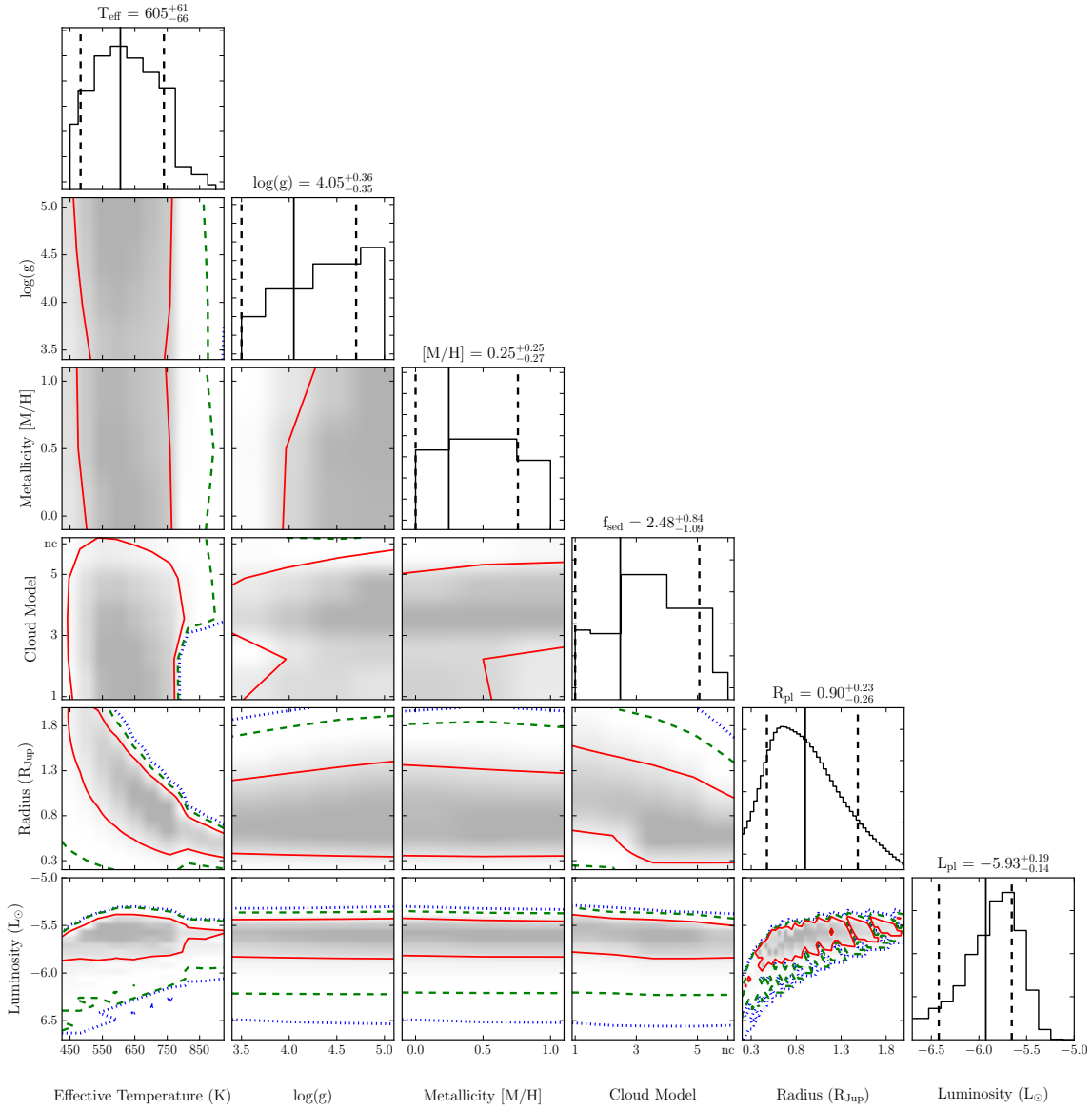

Figure 44. Normalized posterior distributions for the sulfide and salt model grid. Same as Figure 41.

fits are cooler and do a much better job of fitting the overall SED of the 51 Eri b and the best fitting atmosphere for both solar and non-solar metallicity have very similar reduced chi-square values.

The normalized posterior distributions for the different parameters varied as part

of the model fitting are shown in Figure 44. The best fitting $T_{\rm eff}$ (605^{+61}_{-66} K) is much cooler in comparison to the iron/silicates grid, but the values are within 2-σ of each other. We also note out that the median might not be the best estimate for the effective temperature PDF in the iron/silicates grid where the peak extended to cooler temperatures. For the surface gravity and metallicity posterior distributions, we present the median values and error bar assuming a Gaussian distribution, though they may not be Gaussian. The surface gravity PDF suggests that the planet has high surface gravity. However 51 Eri b is clearly a low mass companion indicating that the data does not constrain the gravity. A prior might help constrain the distribution, but there are currently no physically motivated priors available for the surface gravity of young planets. Similarly, the PDF for the metallicity is also unconstrained and higher resolution spectra in the K-band might help provide greater constraints on the metallicity of 51 Eri b (Konopacky *et al.*, 2013).

A difference between the iron/silicate and salt/sulfide atmosphere grids is in the planet radius, where the best fit radii for the cloudy models and the median radius of the PDF for the salt/sulfide models are much closer to evolutionary model predictions. A possible explanation for this discrepancy is that fitting the lower effective temperatures while still matching the bolometric luminosity, requires a larger radius. If the iron/silicates models extended to lower temperatures, assuming the continued presence of these clouds at these colder temperatures, it is likely that the radius discrepancy would not be as apparent. The sedimentation factor was fixed (at $f_{\rm sed}$=2) in the iron/silicates grids, but had varying hole fractions ($h_{\rm frac}$). In the sulfide/salt grid, $f_{\rm sed}$ was varied and the median value for the distribution is $f_{\rm sed}$=2.48. If we equate the $h_{\rm frac}$ from the iron/silicates model with the $f_{\rm sed}$ as the physics controlling the emission of flux from the photosphere then for both model

grids the best fitting models tend to be favoring the presence of clouds over cloud free atmospheres. Furthermore, in both cases the best fitting models were not the fully cloudy atmospheres, with the smallest h_{frac}/f_{sed}. While the cloud compositions in both models are different, fitting either grid require cloud opacity. This can be achieved in one of two ways: either make the deep iron/silicates clouds be very vertically extended (small f_{sed}) or introduce a new cloud layer in the form of the sulfide/salt clouds.

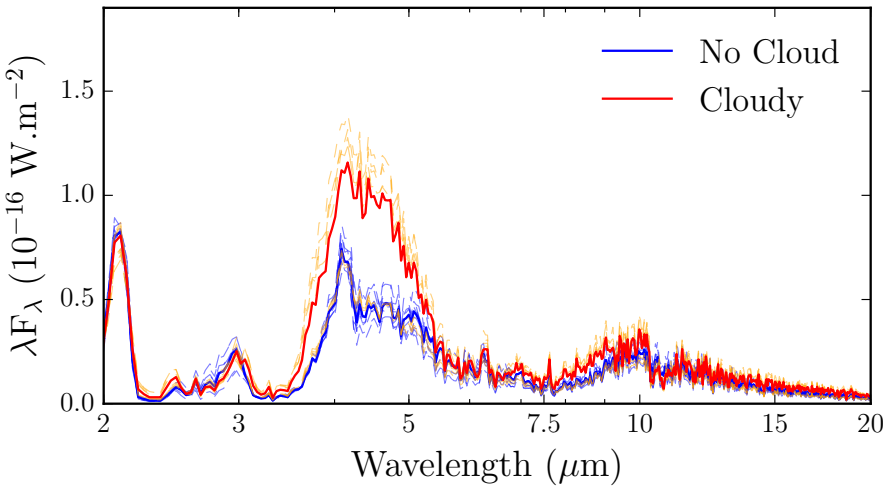

Figure 45. The ten best fitting cloudy (red) and cloudless (blue) atmospheres over the wavelength range of the *James Webb Space Telescope*. The median of the models is plotted with a thicker line. The models indicate the divergence between the model fits over the wavelength covered by *JWST*.

The cloudy model atmosphere fits presented in Figure 43 match the H through K spectrum while being slightly under luminous in the J and over luminous M_S bands. Given the large photometric errors in the M_S data, the model photometry lies within 2-σ of the data. *JWST* and other future low background mid-IR instruments will better constrain the 3–24 μm SED, a further test of current models. In Figure 45, we show ten of the best fitting models assuming cloudy (sulfide/salt clouds) or cloudless atmospheres extended out to 20μm. It is clear from these models that observations

with the coronagraph on Near InfraRed Camera (NIRCam), spanning the 3–5 μm wavelength will add significant constraints on the atmosphere of the planet. If the planet can be studied with the Mid Infrared Instrument (MIRI), it could be used to apply constraints on chemical disequilibrium in the atmosphere through observations NH_3 in the 10–11μm range.

5.4.3 Luminosity of the planet

The two different grids used in this study have produced similar luminosity predictions for the planet despite the different cloud compositions. From the iron/silicates grid we infer a bolometric luminosity of $\log L/L_{\odot} = -5.83^{+0.15}_{-0.12}$, and $\log L/L_{\odot} = -5.93^{+0.19}_{-0.14}$ from the sulfide/salt model atmospheres. We compare these luminosity estimates to predictions of evolutionary models to infer the planet mass and discuss its initial formation conditions.

5.4.3.1 Standard cold- and hot-start models

In Figure 46 we compare the bolometric luminosity to evolutionary models for planets formed via the two extreme scenarios namely, hot-start and cold-start models (Burrows *et al.*, 1997; Marley *et al.*, 2007). In the hot-start scenario, planets are formed with high initial-entropy and are very luminous at birth. This scenario is usually associated with rapid formation in the circumstellar disk through disk instabilities. Alternatively, in the cold-start scenario, which is often associated with current 1D models of the core-accretion mechanism, planets start with a solid core that accretes

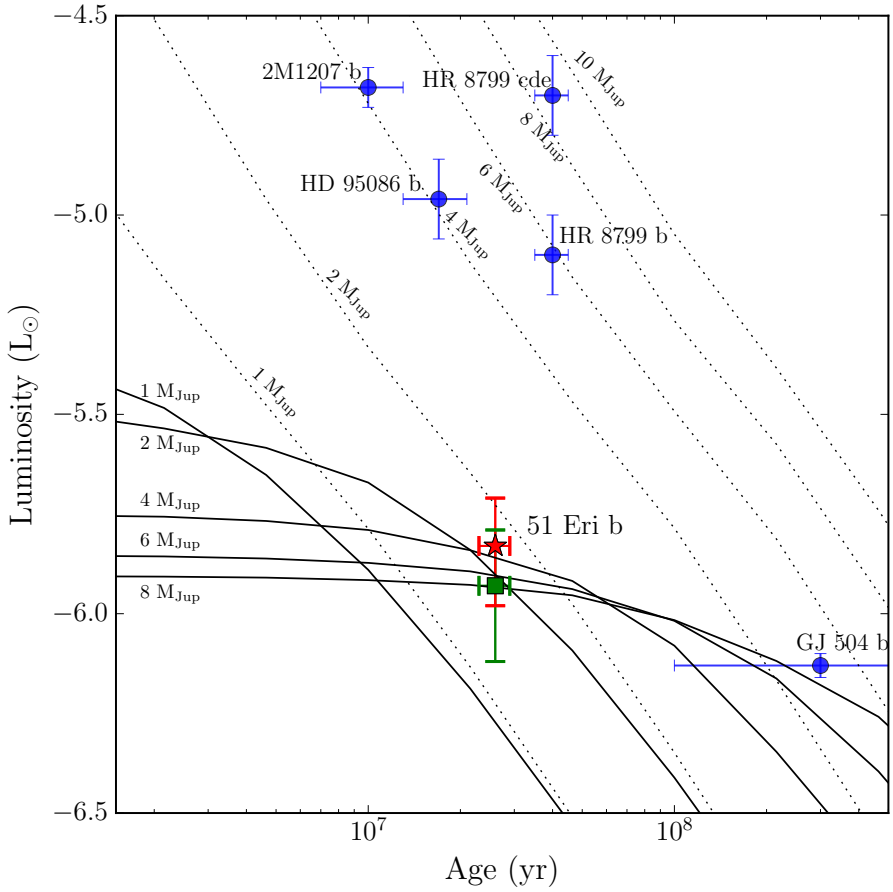

Figure 46. Luminosity of imaged planetary mass companions as a function of age. For 51 Eri b, the red star is the inferred luminosity from the Iron/Silicates model grid while the green square is the inferred luminosity from the Sulfide/Salt model grid. Also plotted are evolutionary tracks assuming different starting conditions i.e. the "hot-start" (dotted lines) and "cold-start" (solid lines) models of Marley *et al.* (2007); Fortney *et al.* (2008). 51 Eri b is consistent with both hot- and cold-start formation models. A subset of known directly imaged companions are plotted in figure illustrating the difference between 51 Eri b and other imaged planets. Data for the companions, 2M1207 b, HR8799 bcde, HD 95086 b, GJ 504 b were taken from Patience *et al.* (2010); Rajan *et al.* (2015); Zurlo *et al.* (2016); De Rosa *et al.* (2016); Skemer *et al.* (2016) respectively.

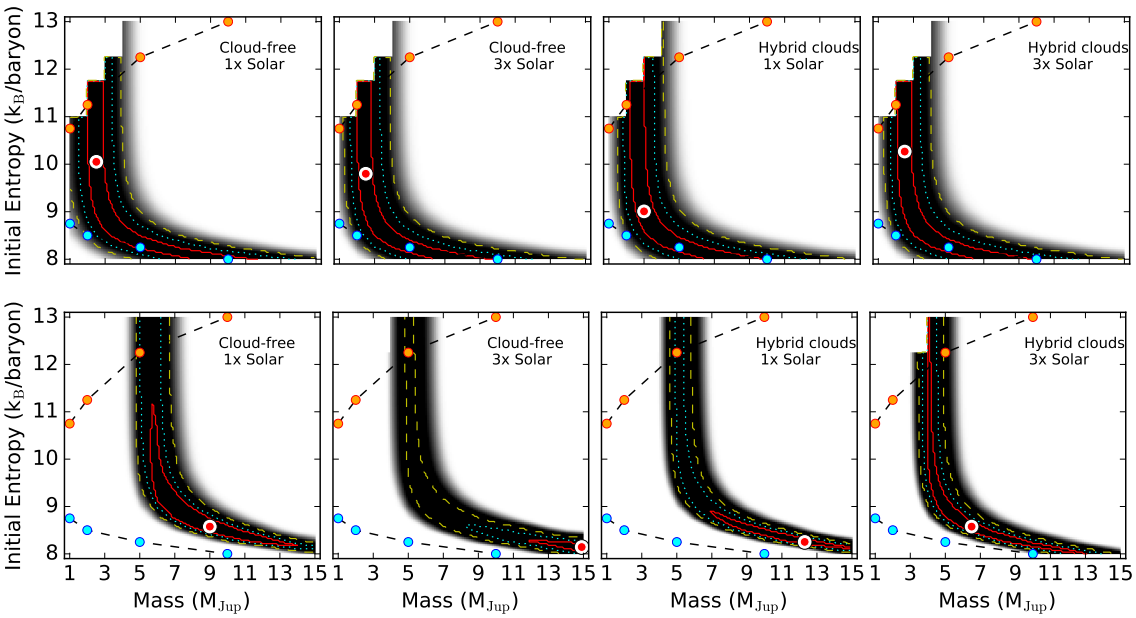

Figure 47. Comparing the planet spectrum and luminosity to a combination of initial entropy (k_B/baryon) and planet mass (M_{Jup}) from the warm-start evolutionary models of Spiegel and Burrows (2012). The four different atmospheres tested include cloud-free and hybrid cloud models, with both solar and super-solar metallicity. The red contour indicates the 50th percentile region. The entropy plotted in the figure and used in the modeling, is not the entropy for the evolved object but rather the entropy at formation. The best fitting model fit is indicated by the large circle (white and red circle). The orange filled circles show the hot-start model limits, while the blue filled circles show cold-start, which are presented as the boundary cases in Spiegel and Burrows (2012). The top row is comparing the model luminosity to the inferred luminosity for 51 Eri b, and the bottom row compares directly the SED to the evolutionary model spectra.

gas from the stellar disk. The accreting gas loses energy via a radiatively efficient accretion shock and form with low initial-entropy and thereby lower post-formation luminosity.

The other directly imaged companions plotted in Figure 46 can all be considered as having formed via the hot-start scenario. Despite the older age assessment for the companion in this study 26±3 Myr (Nielsen *et al.*, 2016) compared to 20±6 Myr (Macintosh *et al.*, 2015), the revised luminosity when compared to the system age

places 51 Eri b in a location where either cold or hot initial conditions are possible. Based on the hot-start tracks, it would have an inferred mass between 1–2 M_{Jup}. However, for the cold-start case the planet mass could lie anywhere between 2–12 M_{Jup}, since the model luminosity is largely independent of mass at the age of 51 Eri b. Dynamical mass estimates for the planet could help clarify the formation mechanism especially if the planet mass $> 2M_{Jup}$.

5.4.3.2 Warm-start models

Spiegel and Burrows (2012) proposed a complete family of solutions existing between the hot- and cold-start extreme cases. Warm-start models[9] explore a wide range of initial entropies aimed at covering the possible range of initial parameters that govern the formation of planets. In Figure 47, we compare the inferred bolometric luminosity and the planet SED to models from Spiegel and Burrows (2012). The Spiegel and Burrows (2012) models are evolutionary tracks calculated assuming different initial entropies for the planet, between 8 and 13 k_B/baryon, where k_B is Boltzmann's constant, with steps of 0.25 k_B/baryon and masses between 1 and 15 M_{Jup} with steps of 1 M_{Jup}. Four different model atmospheres are considered in combination with the evolutionary model: cloud-free and solar metallicity to fully cloudy with 3× solar metallicity (Burrows *et al.*, 2011). The bolometric luminosity of each point in the grid for each of the four atmosphere scenario was computed by integrating the SED over the wavelength range. Because of the sparse sampling of the grid, we linearly interpolate the evolutionary tracks with steps of 0.06 k_B/baryon and 0.2 M_{Jup}.

In the top row of Figure 47, we plot the probabilities for each grid point measured

[9]http://www.astro.princeton.edu/~burrows/

by comparing the average of the inferred bolometric luminosities from the SED fit ($\log L/L_{\odot} = -5.87 \pm 0.15$) to the predictions of the Spiegel and Burrows (2012) models with the four atmosphere conditions. For the bottom row in Figure 47, the surface is calculated by fitting the planet SED to the Spiegel and Burrows (2012) model atmosphere grid, using Equation 5.2. For both comparisons, luminosity and SED, we chose the age of the evolutionary grid best matching the age of 51 Eri (25 Myr), to minimize the number of interpolations, and only varied the mass of the planet and initial entropy for the models.

Mordasini (2013) find that the luminosity of a planet that underwent accretion through a super-critical shock (the standard cold-start core accretion hypothesis), is highly dependent on the mass of the core, $M_{\rm core}^{2-3}$. Therefore, the continuum of warm-start models can also be explained by similar bulk mass planets with increasing core mass. These models suggest that the entropy of 51 Eri b can be explained via core-accretion, with a core mass ranging between 15 and 127 $M_{\oplus}$, which can reproduce the planet luminosity with various initial entropies.

The four panels generated by fitting the inferred luminosity (upper four panels) appear highly consistent and in agreement with the results from Figure 46. The 1σ contour encompasses the entire available entropy space, where for intermediate and high entropies the most likely mass for the planet is between 2 and 3 $M_{\rm Jup}$ and for low initial entropy the most likely mass for the planet increases, making distinguishing between cold-, warm- and hot-start difficult.

When we compare the model spectra directly to the planet SED, the surface is qualitatively similar to that made with the luminosity but shifted to higher mass and with the 1σ contours and best fit models favoring lower entropy. According to the

Mordasini (2013) models, the fits presented here would be consistent with a planet having core masses ranging from 15–127 $M_{\oplus}$.

Conversely to other directly imaged companions (see figures in Marleau and Cumming, 2014), 51 Eri b is the only planet compatible with very low initial entropy and the cold-start case. Tighter constraints on the bolometric luminosity and/or higher signal to noise data will help to reduce the width of the two branches and independent mass constraints, from dynamical measurements, will enable to infer the initial entropy and possible formation route. Atmospheric retrievals and/or higher resolution spectra aimed at exploring and characterizing the planets chemical composition might also help understand whether the planet has higher C/O ratios compared to the star, since planetary C/O can be used to understand planet formation (Öberg *et al.*, 2011; Konopacky *et al.*, 2013).

5.5 Conclusion

In this paper, we have presented the first spectrum of 51 Eridani b in the K-band obtained with the Gemini Planet Imager (K1 and K2 bands) as well as the first photometric measurement of the planet at M_S obtained with the NIRC2 Narrow camera. We also obtained an additional L_P photometric point that agrees very well with the L_P measurement taken in the discovery paper (Macintosh *et al.*, 2015). In addition, we revised the stellar photometry by observing the star in the near IR and estimating its photometry in the mid IR through an SED fit. The new data are combined with the published J, and H spectra and the L_P photometry to present the spectral energy distribution spanning 1–5 μm for the planet.

As part of the data analysis, we calculated the covariance for each of the spectral

datasets i.e. $J, H, K1$, and $K2$ using the formalism presented in Greco and Brandt (2016). The spectral covariance was used in all the chi-squared minimization performed as part of this study, in combination with the photometric variance. Using the covariance ensured that the photometric points were weighted in a suitable manner and resulted in cooler effective temperatures for the best fits.

We compared the planet photometry to field and young brown dwarfs by fitting their near-IR spectra to 51 Eri b to estimate a spectral type of T6.5 $\pm$ 1.5. Due the relative paucity of known young T-dwarfs, our comparison of the planet spectrum to young T-dwarfs only included a handful of objects, and amongst the sample 51 Eri b appears to have the lowest surface gravity based on a comparison of their spectral shape and amplitude.

In a comparison of the near and mid IR photometry for the planet to the field and young brown dwarf population via a range of color magnitude diagrams we note that 51 Eri b is redder than brown dwarfs of similar spectral types. This was also noted in the discovery paper, and it was proposed that this might be due to presence of clouds, similar to young L-type planetary mass companions. In this study, we extended this idea to suggest that a possible reason for the presence of clouds (compared to the field), is that the planet is still transitioning from the L-type to the T-type. This would occur at a lower J magnitude than field brown dwarfs due to its lower mass when including a gravity-dependent transition in the evolution (Saumon and Marley, 2008).

We also fit the planet SED with two different model atmosphere grids that varied in the composition of molecules that could condense in the atmosphere. The best fitting models in both cases, were those that contained large amount of condensates in the atmosphere as compared to cloud free atmospheres. Through the iron/silicates

grid, we estimate that the planet has a patchy atmosphere with 10–25 % hole fraction in the surface cloud cover, which is consistent with the f_{sed} values of 2–3 resulting from the sulfide/salt grid. The median effective temperature from the two grids is 737^{+39}_{-46} K and 605^{+61}_{-66} K for iron/silicates and sulfide/salt respectively. This value is slightly cooler, compared to Macintosh *et al.* (2015), where the best fit models had temperatures of 700K and 750K respectively. The surface gravity and metallicity both appear to be unconstrained by the data, but empirical fits to young T-dwarfs suggest that the planet has lower surface gravity.

The two atmosphere grids provide similar luminosity estimates which were compared to hot-, warm- and cold-start models. 51 Eri b appears to be one of the only directly imaged planet that is consistent with the cold-start scenario and a comparison of the planet SED to a range of initial entropy models indicates that cloudy atmospheres with low initial entropies provide the best fit to the planet SED.

With future space missions such as the *James Webb Space Telescope*, the 3–24 μm SED of this planet could be observed at higher SNR, providing tests of current atmospheric models. The best fitting atmosphere models further indicate that the planet might have a cloudy atmosphere with patchy clouds, making 51 Eri b a prime candidate for atmospheric variability studies that might be possible with future instrumentation. Further analysis of this data using methods such as atmosphere retrievals could permit an exploration of other planet parameters that were not considered in this study such as chemical composition of the atmosphere and the thermal structure.

Chapter 6

CONCLUSIONS & FUTURE WORK

6.1 Brown dwarf variability

Isolated brown dwarfs are high signal-to-noise laboratories to build and test new models and increase our understanding of the physics of cool atmospheres. The field has continued to discover young new brown dwarfs and free floating planetary mass objects (e.g. PSO 318, SDSS 1110; Liu *et al.*, 2013; Gagné *et al.*, 2015a). These newly discovered young brown dwarfs appear to have near infrared colors similar to those of imaged exoplanets suggesting similar effective temperatures and mass. Studies of these young brown dwarfs can provide insights into the observables of imaged planets. The field has also been pushing to cooler brown dwarfs, such as WISE 0855 that have effective temperatures approaching that of solar system giant planets (Faherty *et al.*, 2014; Skemer *et al.*, 2016).

As part of the first BAM study, we detected a new sample of variable brown dwarfs and found that the frequency of variable brown dwarfs depends on different factors such as the observed wavelength and the variability amplitude. BAM-I was at the time the largest and most uniform ground-based search for variability. In our second BAM study, we noted a correlation between the near infrared color of the coolest T-dwarfs and the likelihood of them showing photometric variability. Here infrared colors represented cloud opacity, with redder colors being higher opacity clouds. We also suggested that only brown dwarfs that had intermediate opacity seemed to show variability matching the hypothesis that patchy clouds lead to variability.

Space based surveys using *HST* and *Spitzer* have been extremely effective in demonstrating the variable nature of brown dwarfs (Metchev *et al.*, 2015) as well as indicating that the variations measured across different wavelengths might be originating from different cloud layers (Yang *et al.*, 2016). A potential avenue to explore the long time baseline evolution of brown dwarf atmospheres is to use the *Kepler K2* mission which can monitor brown dwarfs for multiple months while providing high precision photometry (Gizis *et al.*, 2015). Continuous monitoring by $K2$ can distinguish between variations arising from rotational modulation and evolution of the atmosphere over timescales longer than a single to few rotations (Showman and Kaspi, 2013; Zhang and Showman, 2014). Multi-wavelength monitoring by the *James Webb Space Telescope* permits exploration of different atmospheric scale heights to probe deeper into the atmosphere. Through a combination of NIRSpec/NIRISS and MIRI spectroscopic observations, the full near to mid IR spectrum of these cool brown dwarfs can be studied for atmospheric variations. Differential spectra can be forward modeled to extract composition information that can be studied to look for correlation between the variability signatures and physical/features that might causing them.

6.2 Directly imaged planets

The field of comparative exoplanetology is still in its nascent stages. As part of this thesis, I studied the atmosphere of three different planetary systems against atmosphere/evolutionary model grids. The first study, conducted with *HST* demonstrated the potential of the Wide Field Camera 3 infrared channel to be used for high contrast imaging. The data was compared against a range of atmospheric models where we pointed out the inability to fit the near IR, the water band and the mid IR consistently

for the outermost planet, HR8799b. While no such inconsistency was seen in HR8799c, potentially suggesting that non-equilibrium chemistry might be required to explain the spectrum of the outer planet. The Gemini Planet Imager is one of the most advanced adaptive optics instruments and as part of the GPIES survey, I demonstrated some of the work being done to improve the camera by understanding its performance against a range of environmental data. As part of the investigation of the HD106906 planetary system, we searched archival and published data for evidence of circumplanetary material around the planetary mass companion. We found that the optical PSF of HD 106906b was radially extended compared to 11 comparison point sources in the HST data. Analysis of the near-infrared photometry and models showed that HD 106906b is redder than a comparison sample of sub-stellar companions, except for FW Tau b, which has strong evidence for a circumplanetary disk from ALMA (Kraus *et al.*, 2015). In our modeling of 51 Eri b, we noted that the luminosity of the planet is consistent with both cold and warm start models. Additionally, the planet requires patchy cloud atmospheres to fit the spectral energy distribution making an excellent candidate for variability studies with *JWST*.

The atmospheric characterization studies I did as part of my dissertation made use of pre-computed grid models with a few free parameters such as the effective temperature, surface gravity and some form of cloud. These models also tend to make assumptions such as thermochemical equilibrium, radiative convective equilibrium, and solar elemental abundances, thus making it difficult to reconcile differences between the data and model when they arise. Due to these reasons, recent studies in the field of transiting exoplanets (Kreidberg *et al.*, 2014) and brown dwarfs (Line *et al.*, 2014, 2015) have applied atmospheric retrievals using a Bayesian framework. Unlike model grids, retrieval-based algorithms do permit an exhaustive exploration of the

brown dwarf/exoplanet parameters including the abundance of a range of expected molecules, viz. H2O, CH4, CO2, CO, etc. as well as cloud opacity, surface gravity, thermal structure, etc. The power of retrievals comes from the fact that the results are motivated directly by the data and free of many of the model assumptions that are required when generating the grids. With future missions such as the *JWST* and the *Wide Field Infrared Survey Telescope* (*WFIRST*) atmospheric retrievals with be one of the key tools for exoplanet characterization.

Compared to current extreme AO systems, future space telescopes including *JWST* and *WFIRST* will be able to measure spectra spanning the optical or mid-infrared spectral ranges with single snapshots. For some of the more favorable targets such as HR8799 bcd, Beta Pic b, GJ 504 b, these telescopes will be capable of obtaining multiple high signal-to-noise spectra over short durations thus enabling spectrophotometric monitoring studies as well. Current high contrast imaging algorithms such LOCI and KLIP tend to focus on recovering the planet signal often at great cost to the photometric integrity. Future analysis will include forward modeling of the PSF (Pueyo, 2016) to extract the most accurate photometry. Additionally, unlike current pipelines the framework will be designed to permit the estimation of the posterior distribution directly from the data, thereby removing the need to calculate the covariance from the final reduced cube as demonstrated in (Greco and Brandt, 2016). This will ensure that any correlations in the spectrophotometric data are propagated directly into the retrieved atmospheric parameters.

For directly imaged planets, one of the most interesting science cases in the next decade will be the observation of atmospheric variability. In brown dwarfs, the most plausible explanation of temporal spectrophotometric variability detected in brown dwarfs is atmospheric heterogeneity. Observing the planets over multiple hours with

high SNR spectra and analyzing them using retrieval based algorithms will permit not just the estimation of the bulk planet properties but also the variations in pressure-temperature profile (Robinson and Marley, 2014), and atmospheric composition as a function of time. These results can also be compared against brown dwarfs of similar temperatures that will be studied concurrently to understand whether variability in brown dwarfs and imaged planets arise from similar causes. Combining many such programs will permit building the first 3D time-variable weather and composition map of an exoplanet.

Aberasturi, M., A. J. Burgasser, A. Mora, E. Solano, E. L. Martín, I. N. Reid and D. Looper, "Constraints on the binary Properties of mid to late T dwarfs from Hubble Space Telescope WFC3 Observations", ArXiv e-prints (2014).

Abt, H. A. and N. I. Morrell, "The Relation between Rotational Velocities and Spectral Peculiarities among A-Type Stars", ApJS, **99**, 135 (1995).

Ackerman, A. S. and M. S. Marley, "Precipitating Condensation Clouds in Substellar Atmospheres", ApJ, **556**, 872–884 (2001a).

Ackerman, A. S. and M. S. Marley, "Precipitating Condensation Clouds in Substellar Atmospheres", ApJ, **556**, 872–884 (2001b).

Allard, F., P. H. Hauschildt, D. R. Alexander, A. Tamanai and A. Schweitzer, "The Limiting Effects of Dust in Brown Dwarf Model Atmospheres", ApJ, **556**, 357–372 (2001a).

Allard, F., P. H. Hauschildt, D. R. Alexander, A. Tamanai and A. Schweitzer, "The Limiting Effects of Dust in Brown Dwarf Model Atmospheres", ApJ, **556**, 357–372 (2001b).

Allard, F., D. Homeier and B. Freytag, "Model Atmospheres From Very Low Mass Stars to Brown Dwarfs", in "16th Cambridge Workshop on Cool Stars, Stellar Systems, and the Sun", edited by C. Johns-Krull, M. K. Browning and A. A. West, vol. 448 of *Astronomical Society of the Pacific Conference Series*, p. 91 (2011).

Allard, F., D. Homeier and B. Freytag, "Models of very-low-mass stars, brown dwarfs and exoplanets", Philosophical Transactions of the Royal Society of London Series A **370**, 2765–2777 (2012a).

Allard, F., D. Homeier and B. Freytag, "Models of very-low-mass stars, brown dwarfs and exoplanets", Philosophical Transactions of the Royal Society of London Series A **370**, 2765–2777 (2012b).

Allard, N. F., F. Allard and J. F. Kielkopf, "Theoretical profiles of light alkali resonance lines for brown dwarf atmosphere conditions", A&A, **440**, 1195–1201 (2005).

Allers, K. N. and M. C. Liu, "A Near-infrared Spectroscopic Study of Young Field Ultracool Dwarfs", ApJ, **772**, 79 (2013).

Amara, A. and S. P. Quanz, "PYNPOINT: an image processing package for finding exoplanets", MNRAS, **427**, 948–955 (2012).

Apai, D., M. Janson, A. Moro-Martín, M. R. Meyer, E. E. Mamajek, E. Masciadri, T. Henning, I. Pascucci, J. S. Kim, L. A. Hillenbrand, M. Kasper and B. Biller, "A Survey for Massive Giant Planets in Debris Disks with Evacuated Inner Cavities", ApJ, **672**, 1196–1201 (2008).

Apai, D., M. Kasper, A. Skemer, J. R. Hanson, A.-M. Lagrange, B. A. Biller, M. Bonnefoy, E. Buenzli and A. Vigan, "High-cadence, High-contrast Imaging for Exoplanet Mapping: Observations of the HR 8799 Planets with VLT/SPHERE Satellite-spot-corrected Relative Photometry", ApJ, **820**, 40 (2016).

Apai, D., J. Radigan, E. Buenzli, A. Burrows, I. N. Reid and R. Jayawardhana, "HST Spectral Mapping of L/T Transition Brown Dwarfs Reveals Cloud Thickness Variations", ApJ, **768**, 121 (2013).

Artigau, É., S. Bouchard, R. Doyon and D. Lafrenière, "Photometric Variability of the T2.5 Brown Dwarf SIMP J013656.5+093347: Evidence for Evolving Weather Patterns", ApJ, **701**, 1534–1539 (2009a).

Artigau, É., S. Bouchard, R. Doyon and D. Lafrenière, "Photometric Variability of the T2.5 Brown Dwarf SIMP J013656.5+093347: Evidence for Evolving Weather Patterns", ApJ, **701**, 1534–1539 (2009b).

Artigau, É., D. Nadeau and R. Doyon, "T Dwarf Photometric Variability", in "Brown Dwarfs", edited by E. Martín, vol. 211 of *IAU Symposium*, p. 451 (2003a).

Artigau, É., D. Nadeau and R. Doyon, "T Dwarf Photometric Variability", in "Brown Dwarfs", edited by E. Martín, vol. 211 of *IAU Symposium*, p. 451 (2003b).

Bailer-Jones, C. A. L. and M. Lamm, "Limits on the infrared photometric monitoring of brown dwarfs", MNRAS, **339**, 477–485 (2003).

Bailer-Jones, C. A. L. and R. Mundt, "A search for variability in brown dwarfs and L dwarfs", A&A, **348**, 800–804 (1999).

Bailer-Jones, C. A. L. and R. Mundt, "Variability in ultra cool dwarfs: Evidence for the evolution of surface features", A&A, **367**, 218–235 (2001).

Bailey, V., P. M. Hinz, T. Currie, K. Y. L. Su, S. Esposito, J. M. Hill, W. F. Hoffmann, T. Jones, J. Kim, J. Leisenring, M. Meyer, R. Murray-Clay, M. J. Nelson, E. Pinna, A. Puglisi, G. Rieke, T. Rodigas, A. Skemer, M. F. Skrutskie, V. Vaitheeswaran and J. C. Wilson, "A Thermal Infrared Imaging Study of Very Low Mass, Wide-separation Brown Dwarf Companions to Upper Scorpius Stars: Constraining Circumstellar Environments", ApJ, **767**, 31 (2013).

Bailey, V., T. Meshkat, M. Reiter, K. Morzinski, J. Males, K. Y. L. Su, P. M. Hinz, M. Kenworthy, D. Stark, E. Mamajek, R. Briguglio, L. M. Close, K. B. Follette, A. Puglisi, T. Rodigas, A. J. Weinberger and M. Xompero, "HD 106906 b: A Planetary-mass Companion Outside a Massive Debris Disk", ApJL, **780**, L4 (2014).

Bailey, V. P., P. M. Hinz, A. T. Puglisi, S. Esposito, V. Vaitheeswaran, A. J. Skemer, D. Defrère, A. Vaz and J. M. Leisenring, "Large binocular telescope interferometer adaptive optics: on-sky performance and lessons learned", Proceedings of SPIE **9148**, 914803, URL http://proceedings.spiedigitallibrary.org/proceeding.aspx?doi=10.1117/12.2057138 (2014).

Bailey, V. P., L. A. Poyneer, B. A. Macintosh, D. Savransky, J. J. Wang, R. J. De Rosa, K. B. Follette, S. M. Ammons, T. Hayward, P. Ingraham, J. Maire, D. W. Palmer, M. D. Perrin, A. Rajan, F. T. Rantakyrö, S. Thomas and J.-P. Véran, "Status and performance of the Gemini Planet Imager adaptive optics system", in "Society of Photo-Optical Instrumentation Engineers (SPIE) Conference Series", vol. 9909 of *Proc. SPIE,* , p. 99090V (2016).

Barman, T. S., Q. M. Konopacky, B. Macintosh and C. Marois, "Simultaneous Detection of Water, Methane and Carbon Monoxide in the Atmosphere of Exoplanet HR8799b", ArXiv e-prints (2015).

Barman, T. S., B. Macintosh, Q. M. Konopacky and C. Marois, "Clouds and Chemistry in the Atmosphere of Extrasolar Planet HR8799b", ApJ, **733**, 65 (2011).

Becklin, E. E. and B. Zuckerman, "A low-temperature companion to a white dwarf star", Nature, **336**, 656–658 (1988).

Beuzit, J.-L., M. Feldt, K. Dohlen, D. Mouillet, P. Puget, F. Wildi, L. Abe, J. Antichi, A. Baruffolo, P. Baudoz, A. Boccaletti, M. Carbillet, J. Charton, R. Claudi, M. Downing, C. Fabron, P. Feautrier, E. Fedrigo, T. Fusco, J.-L. Gach, R. Gratton, T. Henning, N. Hubin, F. Joos, M. Kasper, M. Langlois, R. Lenzen, C. Moutou, A. Pavlov, C. Petit, J. Pragt, P. Rabou, F. Rigal, R. Roelfsema, G. Rousset, M. Saisse, H.-M. Schmid, E. Stadler, C. Thalmann, M. Turatto, S. Udry, F. Vakili and R. Waters, "SPHERE: a 'Planet Finder' instrument for the VLT", in "Ground-based and Airborne Instrumentation for Astronomy II", vol. 7014 of *Proc. SPIE,* , p. 701418 (2008).

Biller, B. A., L. M. Close, E. Masciadri, E. Nielsen, R. Lenzen, W. Brandner, D. McCarthy, M. Hartung, S. Kellner, E. Mamajek, T. Henning, D. Miller, M. Kenworthy and C. Kulesa, "An Imaging Survey for Extrasolar Planets around 45 Close, Young Stars with the Simultaneous Differential Imager at the Very Large Telescope and MMT", ApJS, **173**, 143–165 (2007).

Biller, B. A., M. C. Liu, Z. Wahhaj, E. L. Nielsen, T. L. Hayward, J. R. Males, A. Skemer, L. M. Close, M. Chun, C. Ftaclas, F. Clarke, N. Thatte, E. L. Shkolnik, I. N. Reid, M. Hartung, A. Boss, D. Lin, S. H. P. Alencar, E. de Gouveia Dal Pino, J. Gregorio-Hetem and D. Toomey, "The Gemini/NICI Planet-Finding Campaign: The Frequency of Planets around Young Moving Group Stars", ApJ, **777**, 160 (2013).

Binks, A. S. and R. D. Jeffries, "A lithium depletion boundary age of 21 Myr for the Beta Pictoris moving group", MNRAS, **438**, L11–L15 (2014).

Boley, A. C., "The two modes of gas giant planet formation", The Astrophysical Journal Letters **695**, 1, L53, URL http://stacks.iop.org/1538-4357/695/i=1/a=L53 (2009).

Bonnefoy, M., G. Chauvin, P. Rojo, F. Allard, A.-M. Lagrange, D. Homeier, C. Dumas and J.-L. Beuzit, "Near-infrared integral-field spectra of the planet/brown dwarf companion AB Pictoris b", A&A, **512**, A52 (2010).

Bonnefoy, M., A.-M. Lagrange, A. Boccaletti, G. Chauvin, D. Apai, F. Allard, D. Ehrenreich, J. H. V. Girard, D. Mouillet, D. Rouan, D. Gratadour and M. Kasper, "High angular resolution detection of β Pictoris b at 2.18 μm", A&A, **528**, L15 (2011).

Bonnefoy, M., J. Milli, F. Ménard, A. Vigan, A.-M. Lagrange, P. Delorme, A. Boccaletti, C. Lazzoni, R. Galicher, S. Desidera, G. Chauvin, J. C. Augereau, D. Mouillet, C. Pinte, G. van der Plas, R. Gratton, H. Beust and J. L. Beuzit, "Belt(s) of debris resolved around the Sco-Cen star HIP 67497", A&A, **597**, L7 (2017).

Borucki, W. J., "KEPLER Mission: development and overview", Reports on Progress in Physics **79**, 3, 036901 (2016).

Boss, A. P., "Giant planet formation by gravitational instability.", Science **276**, 1836–1839 (1997).

Boss, A. P., "Formation of Giant Planets by Disk Instability on Wide Orbits Around Protostars with Varied Masses", ApJ, **731**, 74 (2011).

Bowler, B. P., "Imaging Extrasolar Giant Planets", PASP, **128**, 10, 102001 (2016).

Bowler, B. P., M. C. Liu, A. L. Kraus and A. W. Mann, "Spectroscopic Confirmation of Young Planetary-mass Companions on Wide Orbits", ApJ, **784**, 65 (2014).

Bowler, B. P., M. C. Liu, A. L. Kraus, A. W. Mann and M. J. Ireland, "A Disk around the Planetary-mass Companion GSC 06214-00210 b: Clues about the Formation of Gas Giants on Wide Orbits", ApJ, **743**, 148 (2011).

Bowler, B. P., M. C. Liu, E. L. Shkolnik and M. Tamura, "Planets around Low-mass Stars (PALMS). IV. The Outer Architecture of M Dwarf Planetary Systems", ApJS, **216**, 7 (2015).

Brandner, W., H. Zinnecker, J. M. Alcalá, F. Allard, E. Covino, S. Frink, R. Köhler, M. Kunkel, A. Moneti and A. Schweitzer, "Timescales of Disk Evolution and Planet Formation: HST, Adaptive Optics, and ISO Observations of Weak-Line and Post-T Tauri Stars", AJ, **120**, 950–962 (2000).

Brandt, T. D., M. Kuzuhara, M. W. McElwain, J. E. Schlieder, J. P. Wisniewski, E. L. Turner, J. Carson, T. Matsuo, B. Biller, M. Bonnefoy, C. Dressing, M. Janson, G. R. Knapp, A. Moro-Martín, C. Thalmann, T. Kudo, N. Kusakabe, J. Hashimoto, L. Abe, W. Brandner, T. Currie, S. Egner, M. Feldt, T. Golota, M. Goto, C. A. Grady, O. Guyon, Y. Hayano, M. Hayashi, S. Hayashi, T. Henning, K. W. Hodapp, M. Ishii, M. Iye, R. Kandori, J. Kwon, K. Mede, S. Miyama, J.-I. Morino, T. Nishimura, T.-S. Pyo, E. Serabyn, T. Suenaga, H. Suto, R. Suzuki, M. Takami, Y. Takahashi, N. Takato, H. Terada, D. Tomono, M. Watanabe, T. Yamada, H. Takami, T. Usuda and M. Tamura, "The Moving Group Targets of the SEEDS High-contrast Imaging Survey of Exoplanets and Disks: Results and Observations from the First Three Years", ApJ, **786**, 1 (2014).

Brown, W. R., B. A. McLeod, J. C. Geary and E. C. Bowsher, "Smithsonian Widefield Infrared Camera", vol. 7014 of *SPIE Conference Series* (2008).

Buenzli, E., D. Apai, C. V. Morley, D. Flateau, A. P. Showman, A. Burrows, M. S. Marley, N. K. Lewis and I. N. Reid, "Vertical Atmospheric Structure in a Variable Brown Dwarf: Pressure-dependent Phase Shifts in Simultaneous Hubble Space Telescope-Spitzer Light Curves", ApJL, **760**, L31 (2012).

Buenzli, E., D. Apai, J. Radigan, I. N. Reid and D. Flateau, "Brown Dwarf Photospheres are Patchy: A Hubble Space Telescope Near-infrared Spectroscopic Survey Finds Frequent Low-level Variability", ApJ, **782**, 77 (2014a).

Buenzli, E., D. Apai, J. Radigan, I. N. Reid and D. Flateau, "Brown Dwarf Photospheres are Patchy: A Hubble Space Telescope Near-infrared Spectroscopic Survey Finds Frequent Low-level Variability", ApJ, **782**, 77 (2014b).

Burgasser, A. J., "The SpeX Prism Library: 1000+ low-resolution, near-infrared spectra of ultracool M, L, T and Y dwarfs", in "Astronomical Society of India Conference Series", vol. 11 of *Astronomical Society of India Conference Series* (2014).

Burgasser, A. J., A. Burrows and J. D. Kirkpatrick, "A Method for Determining the Physical Properties of the Coldest Known Brown Dwarfs", ApJ, **639**, 1095–1113 (2006a).

Burgasser, A. J., K. L. Cruz, M. Cushing, C. R. Gelino, D. L. Looper, J. K. Faherty, J. D. Kirkpatrick and I. N. Reid, "SpeX Spectroscopy of Unresolved Very Low Mass Binaries. I. Identification of 17 Candidate Binaries Straddling the L Dwarf/T Dwarf Transition", ApJ, **710**, 1142–1169 (2010).

Burgasser, A. J., T. R. Geballe, S. K. Leggett, J. D. Kirkpatrick and D. A. Golimowski, "A Unified Near-Infrared Spectral Classification Scheme for T Dwarfs", ApJ, **637**, 1067–1093 (2006b).

Burgasser, A. J., C. R. Gelino, M. C. Cushing and J. D. Kirkpatrick, "Resolved Spectroscopy of a Brown Dwarf Binary at the T Dwarf/Y Dwarf Transition", ApJ, **745**, 26 (2012).

Burgasser, A. J., J. D. Kirkpatrick, M. E. Brown, I. N. Reid, A. Burrows, J. Liebert, K. Matthews, J. E. Gizis, C. C. Dahn, D. G. Monet, R. M. Cutri and M. F. Skrutskie, "The Spectra of T Dwarfs. I. Near-Infrared Data and Spectral Classification", ApJ, **564**, 421–451 (2002).

Burgasser, A. J., J. D. Kirkpatrick, M. E. Brown, I. N. Reid, J. E. Gizis, C. C. Dahn, D. G. Monet, C. A. Beichman, J. Liebert, R. M. Cutri and M. F. Skrutskie, "Discovery of Four Field Methane (T-Type) Dwarfs with the Two Micron All-Sky Survey", ApJL, **522**, L65–L68 (1999).

Burgasser, A. J., J. D. Kirkpatrick, I. N. Reid, M. E. Brown, C. L. Miskey and J. E. Gizis, "Binarity in Brown Dwarfs: T Dwarf Binaries Discovered with the Hubble Space Telescope Wide Field Planetary Camera 2", ApJ, **586**, 512–526 (2003).

Burgasser, A. J., M. C. Liu, M. J. Ireland, K. L. Cruz and T. J. Dupuy, "Subtle Signatures of Multiplicity in Late-type Dwarf Spectra: The Unresolved M8.5 + T5 Binary 2MASS J03202839-0446358", ApJ, **681**, 579–593 (2008).

Burgasser, A. J., M. W. McElwain, J. D. Kirkpatrick, K. L. Cruz, C. G. Tinney and I. N. Reid, "The 2MASS Wide-Field T Dwarf Search. III. Seven New T Dwarfs and Other Cool Dwarf Discoveries", AJ, **127**, 2856–2870 (2004).

Burningham, B., S. K. Leggett, D. Homeier, D. Saumon, P. W. Lucas, D. J. Pinfield, C. G. Tinney, F. Allard, M. S. Marley, H. R. A. Jones, D. N. Murray, M. Ishii, A. Day-Jones, J. Gomes and Z. H. Zhang, "The properties of the T8.5p dwarf Ross 458C", MNRAS, **414**, 3590–3598 (2011).

Burrows, A., K. Heng and T. Nampaisarn, "The Dependence of Brown Dwarf Radii on Atmospheric Metallicity and Clouds: Theory and Comparison with Observations", ApJ, **736**, 47 (2011).

Burrows, A., W. B. Hubbard, J. I. Lunine and J. Liebert, "The theory of brown dwarfs and extrasolar giant planets", Reviews of Modern Physics **73**, 719–765 (2001).

Burrows, A., M. Marley, W. B. Hubbard, J. I. Lunine, T. Guillot, D. Saumon, R. Freedman, D. Sudarsky and C. Sharp, "A Nongray Theory of Extrasolar Giant Planets and Brown Dwarfs", ApJ, **491**, 856–875 (1997).

Burrows, A., D. Sudarsky and I. Hubeny, "L and T Dwarf Models and the L to T Transition", ApJ, **640**, 1063–1077 (2006).

Burrows, A., D. Sudarsky and J. I. Lunine, "Beyond the T Dwarfs: Theoretical Spectra, Colors, and Detectability of the Coolest Brown Dwarfs", ApJ, **596**, 587–596 (2003).

Cameron, A. G. W., "Physics of the primitive solar accretion disk", Moon and Planets **18**, 5–40 (1978).

Carson, J. C., S. S. Eikenberry, B. R. Brandl, J. C. Wilson and T. L. Hayward, "The Cornell High-Order Adaptive Optics Survey for Brown Dwarfs in Stellar Systems. I. Observations, Data Reduction, and Detection Analyses", AJ, **130**, 1212–1220 (2005).

Carter, B. S., "Southern JHKL standards", MNRAS, **242**, 1–5 (1990).

Casali, M., A. Adamson, C. Alves de Oliveira, O. Almaini, K. Burch, T. Chuter, J. Elliot, M. Folger, S. Foucaud, N. Hambly, M. Hastie, D. Henry, P. Hirst, M. Irwin, D. Ives, A. Lawrence, K. Laidlaw, D. Lee, J. Lewis, D. Lunney, S. McLay, D. Montgomery, A. Pickup, M. Read, N. Rees, I. Robson, K. Sekiguchi, A. Vick, S. Warren and B. Woodward, "The UKIRT wide-field camera", A&A, **467**, 777–784 (2007).

Chabrier, G., I. Baraffe, F. Allard and P. Hauschildt, "Evolutionary Models for Very Low-Mass Stars and Brown Dwarfs with Dusty Atmospheres", ApJ, **542**, 464–472 (2000).

Chabrier, G., A. Johansen, M. Janson and R. Rafikov, "Giant Planet and Brown Dwarf Formation", Protostars and Planets VI pp. 619–642 (2014).

Charbonneau, D., L. E. Allen, S. T. Megeath, G. Torres, R. Alonso, T. M. Brown, R. L. Gilliland, D. W. Latham, G. Mandushev, F. T. O'Donovan and A. Sozzetti, "Detection of Thermal Emission from an Extrasolar Planet", ApJ, **626**, 523–529 (2005).

Charbonneau, D., T. M. Brown, D. W. Latham and M. Mayor, "Detection of Planetary Transits Across a Sun-like Star", ApJL, **529**, L45–L48 (2000).

Charbonneau, D., T. M. Brown, R. W. Noyes and R. L. Gilliland, "Detection of an Extrasolar Planet Atmosphere", ApJ, **568**, 377–384 (2002).

Charbonneau, D., H. A. Knutson, T. Barman, L. E. Allen, M. Mayor, S. T. Megeath, D. Queloz and S. Udry, "The Broadband Infrared Emission Spectrum of the Exoplanet HD 189733b", ApJ, **686**, 1341–1348 (2008).

Chauvin, G., A.-M. Lagrange, M. Bonavita, B. Zuckerman, C. Dumas, M. S. Bessell, J.-L. Beuzit, M. Bonnefoy, S. Desidera, J. Farihi, P. Lowrance, D. Mouillet and I. Song, "Deep imaging survey of young, nearby austral stars . VLT/NACO near-infrared Lyot-coronographic observations", A&A, **509**, A52 (2010).

Chauvin, G., A.-M. Lagrange, C. Dumas, B. Zuckerman, D. Mouillet, I. Song, J.-L. Beuzit and P. Lowrance, "A giant planet candidate near a young brown dwarf. Direct VLT/NACO observations using IR wavefront sensing", A&A, **425**, L29–L32 (2004).

Chauvin, G., A.-M. Lagrange, C. Dumas, B. Zuckerman, D. Mouillet, I. Song, J.-L. Beuzit and P. Lowrance, "Giant planet companion to 2MASSW J1207334-393254", A&A, **438**, L25–L28 (2005a).

Chauvin, G., A.-M. Lagrange, B. Zuckerman, C. Dumas, D. Mouillet, I. Song, J.-L. Beuzit, P. Lowrance and M. S. Bessell, "A companion to AB Pic at the planet/brown dwarf boundary", A&A, **438**, L29–L32 (2005b).

Chauvin, G., M. Thomson, C. Dumas, J.-L. Beuzit, P. Lowrance, T. Fusco, A.-M. Lagrange, B. Zuckerman and D. Mouillet, "Adaptive optics imaging survey of the Tucana-Horologium association", A&A, **404**, 157–162 (2003).

Chauvin, G., A. Vigan, M. Bonnefoy, S. Desidera, M. Bonavita, D. Mesa, A. Boccaletti, E. Buenzli, J. Carson, P. Delorme, J. Hagelberg, G. Montagnier, C. Mordasini, S. P. Quanz, D. Segransan, C. Thalmann, J.-L. Beuzit, B. Biller, E. Covino, M. Feldt, J. Girard, R. Gratton, T. Henning, M. Kasper, A.-M. Lagrange, S. Messina, M. Meyer, D. Mouillet, C. Moutou, M. Reggiani, J. E. Schlieder and A. Zurlo, "The VLT/NaCo large program to probe the occurrence of exoplanets and brown dwarfs at wide orbits. II. Survey description, results, and performances", A&A, **573**, A127 (2015).

Chiaberge, M., P. L. Lim, V. Kozhurina-Platais, M. Sirianni and J. Mack, "Updated CTE photometric correction for WFC and HRC", Tech. rep. (2009).

Choquet, É., L. Pueyo, J. B. Hagan, E. Gofas-Salas, A. Rajan, C. Chen, M. D. Perrin, J. Debes, D. Golimowski, D. C. Hines, M. N'Diaye, G. Schneider, D. Mawet, C. Marois and R. Soummer, "Archival legacy investigations of circumstellar environments: overview and first results", in "Society of Photo-Optical Instrumentation Engineers (SPIE) Conference Series", vol. 9143 of *Society of Photo-Optical Instrumentation Engineers (SPIE) Conference Series*, p. 57 (2014).

Clarke, F. J., S. T. Hodgkin, B. R. Oppenheimer, J. Robertson and X. Haubois, "A search for J-band variability from late-L and T brown dwarfs", MNRAS, **386**, 2009–2014 (2008a).

Clarke, F. J., S. T. Hodgkin, B. R. Oppenheimer, J. Robertson and X. Haubois, "A search for J-band variability from late-L and T brown dwarfs", MNRAS, **386**, 2009–2014 (2008b).

Clarke, F. J., B. R. Oppenheimer and C. G. Tinney, "A mini-survey for variability in early L dwarfs", MNRAS, **335**, 1158–1162 (2002a).

Clarke, F. J., C. G. Tinney and K. R. Covey, "Periodic photometric variability of the brown dwarf Kelu-1", MNRAS, **332**, 361–366 (2002b).

Cohen, M., W. A. Wheaton and S. T. Megeath, "Spectral Irradiance Calibration in the Infrared. XIV. The Absolute Calibration of 2MASS", AJ, **126**, 1090–1096 (2003).

Cotten, T. H. and I. Song, "A Comprehensive Census of Nearby Infrared Excess Stars", ApJS, **225**, 15 (2016).

Crossfield, I. J. M., "Doppler imaging of exoplanets and brown dwarfs", A&A, **566**, A130 (2014).

Currie, T., A. Burrows and S. Daemgen, "A First-look Atmospheric Modeling Study of the Young Directly Imaged Planet-mass Companion, ROXs 42Bb", ApJ, **787**, 104 (2014a).

Currie, T., A. Burrows, J. H. Girard, R. Cloutier, M. Fukagawa, S. Sorahana, M. Kuchner, S. J. Kenyon, N. Madhusudhan, Y. Itoh, R. Jayawardhana, S. Matsumura and T.-S. Pyo, "Deep Thermal Infrared Imaging of HR 8799 bcde: New Atmospheric Constraints and Limits on a Fifth Planet", ArXiv e-prints (2014b).

Currie, T., A. Burrows, Y. Itoh, S. Matsumura, M. Fukagawa, D. Apai, N. Madhusudhan, P. M. Hinz, T. J. Rodigas, M. Kasper, T.-S. Pyo and S. Ogino, "A Combined Subaru/VLT/MMT 1-5 micron Study of Planets Orbiting HR 8799: Implications for Atmospheric Properties, Masses, and Formation", ApJ, **729**, 128 (2011a).

Currie, T., C. M. Lisse, M. Kuchner, N. Madhusudhan, S. J. Kenyon, C. Thalmann, J. Carson and J. Debes, "Direct Imaging and Spectroscopy of a Young Extrasolar Kuiper Belt in the Nearest OB Association", ApJL, **807**, L7 (2015).

Currie, T., C. Thalmann, S. Matsumura, N. Madhusudhan, A. Burrows and M. Kuchner, "A 5 μm Image of β Pictoris b at a Sub-Jupiter Projected Separation: Evidence for a Misalignment Between the Planet and the Inner, Warped Disk", ApJL, **736**, L33 (2011b).

Cushing, M. C., J. D. Kirkpatrick, C. R. Gelino, R. L. Griffith, M. F. Skrutskie, A. Mainzer, K. A. Marsh, C. A. Beichman, A. J. Burgasser, L. A. Prato, R. A. Simcoe, M. S. Marley, D. Saumon, R. S. Freedman, P. R. Eisenhardt and E. L. Wright, "The Discovery of Y Dwarfs using Data from the Wide-field Infrared Survey Explorer (WISE)", ApJ, **743**, 50 (2011).

Cushing, M. C., J. T. Rayner and W. D. Vacca, "An Infrared Spectroscopic Sequence of M, L, and T Dwarfs", ApJ, **623**, 1115–1140 (2005).

Cutri, R. M. and et al., "VizieR Online Data Catalog: AllWISE Data Release (Cutri+ 2013)", VizieR Online Data Catalog **2328** (2013).

Cutri, R. M., M. F. Skrutskie, S. van Dyk, C. A. Beichman, J. M. Carpenter, T. Chester, L. Cambresy, T. Evans, J. Fowler, J. Gizis, E. Howard, J. Huchra, T. Jarrett, E. L. Kopan, J. D. Kirkpatrick, R. M. Light, K. A. Marsh, H. McCallon, S. Schneider, R. Stiening, M. Sykes, M. Weinberg, W. A. Wheaton, S. Wheelock and N. Zacarias, "VizieR Online Data Catalog: 2MASS All-Sky Catalog of Point Sources (Cutri+ 2003)", VizieR Online Data Catalog **2246** (2003).

De Rosa, R. J., E. L. Nielsen, S. C. Blunt, J. R. Graham, Q. M. Konopacky, C. Marois, L. Pueyo, J. Rameau, D. M. Ryan, J. J. Wang, V. Bailey, A. Chontos, D. C. Fabrycky, K. B. Follette, B. Macintosh, F. Marchis, S. M. Ammons, P. Arriaga, J. K. Chilcote, T. H. Cotten, R. Doyon, G. Duchêne, T. M. Esposito, M. P. Fitzgerald, B. Gerard, S. J. Goodsell, A. Z. Greenbaum, P. Hibon, P. Ingraham, M. Johnson-Groh, P. G. Kalas, D. Lafrenière, J. Maire, S. Metchev, M. A. Millar-Blanchaer, K. M. Morzinski, R. Oppenheimer, R. I. Patel, J. L. Patience, M. D. Perrin, A. Rajan, F. T. Rantakyrö, J.-B. Ruffio, A. C. Schneider, A. Sivaramakrishnan, I. Song, D. Tran, G. Vasisht, K. Ward-Duong and S. G. Wolff, "Astrometric Confirmation and Preliminary Orbital Parameters of the Young Exoplanet 51 Eridani b with the Gemini Planet Imager", ApJL, **814**, L3 (2015).

De Rosa, R. J., J. Rameau, J. Patience, J. R. Graham, R. Doyon, D. Lafrenière, B. Macintosh, L. Pueyo, A. Rajan, J. J. Wang, K. Ward-Duong, L.-W. Hung, J. Maire, E. L. Nielsen, S. M. Ammons, J. Bulger, A. Cardwell, J. K. Chilcote, R. L. Galvez, B. L. Gerard, S. Goodsell, M. Hartung, P. Hibon, P. Ingraham, M. Johnson-Groh, P. Kalas, Q. M. Konopacky, F. Marchis, C. Marois, S. Metchev, K. M. Morzinski, R. Oppenheimer, M. D. Perrin, F. T. Rantakyrö, D. Savransky and S. Thomas, "Spectroscopic Characterization of HD 95086 b with the Gemini Planet Imager", ApJ, **824**, 121 (2016).

de Zeeuw, P. T., R. Hoogerwerf, J. H. J. de Bruijne, A. G. A. Brown and A. Blaauw, "A HIPPARCOS Census of the Nearby OB Associations", AJ, **117**, 354–399 (1999).

Debes, J. H., A. J. Weinberger and I. Song, "Color Gradients Detected in the HD 15115 Circumstellar Disk", ApJL, **684**, L41 (2008).

Delfosse, X., C. G. Tinney, T. Forveille, N. Epchtein, E. Bertin, J. Borsenberger, E. Copet, B. de Batz, P. Fouque, S. Kimeswenger, T. Le Bertre, F. Lacombe, D. Rouan and D. Tiphene, "Field brown dwarfs found by DENIS", A&A, **327**, L25–L28 (1997).

Delorme, P., L. Albert, T. Forveille, E. Artigau, X. Delfosse, C. Reylé, C. J. Willott, E. Bertin, S. M. Wilkins, F. Allard and D. Arzoumanian, "Extending the Canada-France brown dwarfs survey to the near-infrared: first ultracool brown dwarfs from CFBDSIR", A&A, **518**, A39 (2010).

Delorme, P., T. Dupuy, J. Gagné, C. Reylé, T. Forveille, M. C. Liu, E. Artigau, L. Albert, X. Delfosse, F. Allard, D. Homeier, L. Malo, C. Morley, M. E. Naud and M. Bonnefoy, "CFBDSIR 2149-0403: young isolated planetary-mass object or high-metallicity low-mass brown dwarf??", ArXiv e-prints (2017).

Delorme, P., J. Gagné, J. H. Girard, A. M. Lagrange, G. Chauvin, M.-E. Naud, D. Lafrenière, R. Doyon, A. Riedel, M. Bonnefoy and L. Malo, "Direct-imaging discovery of a 12-14 Jupiter-mass object orbiting a young binary system of very low-mass stars", A&A, **553**, L5 (2013).

Delorme, P., J. Gagné, L. Malo, C. Reylé, E. Artigau, L. Albert, T. Forveille, X. Delfosse, F. Allard and D. Homeier, "CFBDSIR2149-0403: a 4-7 Jupiter-mass free-floating planet in the young moving group AB Doradus?", A&A, **548**, A26 (2012).

Deming, D., T. M. Brown, D. Charbonneau, J. Harrington and L. J. Richardson, "A New Search for Carbon Monoxide Absorption in the Transmission Spectrum of the Extrasolar Planet HD 209458b", ApJ, **622**, 1149–1159 (2005).

Dupuy, T. J. and A. L. Kraus, "Distances, Luminosities, and Temperatures of the Coldest Known Substellar Objects", Science **341**, 1492–1495 (2013).

Dupuy, T. J. and M. C. Liu, "The Hawaii Infrared Parallax Program. I. Ultracool Binaries and the L/T Transition", ApJS, **201**, 19 (2012a).

Dupuy, T. J. and M. C. Liu, "The Hawaii Infrared Parallax Program. I. Ultracool Binaries and the L/T Transition", ApJS, **201**, 19 (2012b).

Dupuy, T. J. and M. C. Liu, "Individual Dynamical Masses of Ultracool Dwarfs", ArXiv e-prints (2017).

Dupuy, T. J., M. C. Liu and M. J. Ireland, "Keck Laser Guide Star Adaptive Optics Monitoring of the M8+L7 Binary LHS 2397aAB: First Dynamical Mass Benchmark at the L/T Transition", ApJ, **699**, 168–185 (2009).

Enoch, M. L., M. E. Brown and A. J. Burgasser, "Photometric Variability at the L/T Dwarf Boundary", AJ, **126**, 1006–1016 (2003).

Epchtein, N., E. Deul, S. Derriere, J. Borsenberger, D. Egret, G. Simon, C. Alard, L. G. Balázs, B. de Batz, M.-R. Cioni, E. Copet, M. Dennefeld, T. Forveille, P. Fouqué, F. Garzón, H. J. Habing, A. Holl, J. Hron, S. Kimeswenger, F. Lacombe, T. Le Bertre, C. Loup, G. A. Mamon, A. Omont, G. Paturel, P. Persi, A. C. Robin, D. Rouan, D. Tiphène, I. Vauglin and S. J. Wagner, "A preliminary database of DENIS point sources", A&A, **349**, 236–242 (1999).

ESA, ed., *The HIPPARCOS and TYCHO catalogues. Astrometric and photometric star catalogues derived from the ESA HIPPARCOS Space Astrometry Mission*, vol. 1200 of *ESA Special Publication* (1997).

Esposito, S., A. Riccardi, E. Pinna, A. Puglisi, F. Quirós-Pacheco, C. Arcidiacono, M. Xompero, R. Briguglio, G. Agapito, L. Busoni, L. Fini, J. Argomedo, A. Gherardi, G. Brusa, D. Miller, J. C. Guerra, P. Stefanini and P. Salinari, "Large Binocular Telescope Adaptive Optics System: new achievements and perspectives in adaptive optics", in "Astronomical Adaptive Optics Systems and Applications IV", vol. 8149 of *Proc. SPIE,* , p. 814902 (2011).

Faherty, J. K., A. J. Burgasser, A. A. West, J. J. Bochanski, K. L. Cruz, M. M. Shara and F. M. Walter, "The Brown Dwarf Kinematics Project. II. Details on Nine Wide Common Proper Motion Very Low Mass Companions to Nearby Stars", AJ, **139**, 176–194 (2010).

Faherty, J. K., A. R. Riedel, K. L. Cruz, J. Gagne, J. C. Filippazzo, E. Lambrides, H. Fica, A. Weinberger, J. R. Thorstensen, C. G. Tinney, V. Baldassare, E. Lemonier and E. L. Rice, "Population Properties of Brown Dwarf Analogs to Exoplanets", ApJS, **225**, 10 (2016).

Faherty, J. K., C. G. Tinney, A. Skemer and A. J. Monson, "Indications of Water Clouds in the Coldest Known Brown Dwarf", ApJL, **793**, L16 (2014).

Feigelson, E. D., W. A. Lawson, M. Stark, L. Townsley and G. P. Garmire, "51 Eridani and GJ 3305: A 10-15 Myr old Binary Star System at 30 Parsecs", AJ, **131**, 1730–1739 (2006).

Filippazzo, J. C., E. L. Rice, J. Faherty, K. L. Cruz, M. M. Van Gordon and D. L. Looper, "Fundamental Parameters and Spectral Energy Distributions of Young and Field Age Objects with Masses Spanning the Stellar to Planetary Regime", ApJ, **810**, 158 (2015).

Foreman-Mackey, D., D. W. Hogg, D. Lang and J. Goodman, "emcee: The MCMC Hammer", PASP, **125**, 306 (2013).

Fortney, J. J., M. S. Marley, D. Saumon and K. Lodders, "Synthetic Spectra and Colors of Young Giant Planet Atmospheres: Effects of Initial Conditions and Atmospheric Metallicity", ApJ, **683**, 1104–1116 (2008).

Freedman, R. S., M. S. Marley and K. Lodders, "Line and Mean Opacities for Ultracool Dwarfs and Extrasolar Planets", ApJS, **174**, 504–513 (2008).

Gagné, J., A. J. Burgasser, J. K. Faherty, D. Lafreniére, R. Doyon, J. C. Filippazzo, E. Bowsher and C. P. Nicholls, "SDSS J111010.01+011613.1: A New Planetary-mass T Dwarf Member of the AB Doradus Moving Group", ApJL, **808**, L20 (2015a).

Gagné, J., J. K. Faherty, K. L. Cruz, D. Lafreniére, R. Doyon, L. Malo, A. J. Burgasser, M.-E. Naud, É. Artigau, S. Bouchard, J. E. Gizis and L. Albert, "BANYAN. VII. A New Population of Young Substellar Candidate Members of Nearby Moving Groups from the BASS Survey", ApJS, **219**, 33 (2015b).

Gagné, J., D. Lafrenière, R. Doyon, L. Malo and É. Artigau, "BANYAN. II. Very Low Mass and Substellar Candidate Members to Nearby, Young Kinematic Groups with Previously Known Signs of Youth", ApJ, **783**, 121 (2014).

Galicher, R., C. Marois, B. Macintosh, T. Barman and Q. Konopacky, "M-band Imaging of the HR 8799 Planetary System Using an Innovative LOCI-based Background Subtraction Technique", ApJL, **739**, L41 (2011).

Galicher, R., C. Marois, B. Macintosh, B. Zuckerman, T. Barman, Q. Konopacky, I. Song, J. Patience, D. Lafrenière, R. Doyon and E. L. Nielsen, "The International Deep Planet Survey. II. The frequency of directly imaged giant exoplanets with stellar mass", A&A, **594**, A63 (2016).

Galicher, R., C. Marois, B. Zuckerman and B. Macintosh, "Fomalhaut b: Independent Analysis of the Hubble Space Telescope Public Archive Data", ApJ, **769**, 42 (2013).

Gaudi, B. S., "Microlensing Surveys for Exoplanets", ARA&A, **50**, 411–453 (2012).

Geballe, T. R., G. R. Knapp, S. K. Leggett, X. Fan, D. A. Golimowski, S. Anderson, J. Brinkmann, I. Csabai, J. E. Gunn, S. L. Hawley, G. Hennessy, T. J. Henry, G. J. Hill, R. B. Hindsley, Ž. Ivezić, R. H. Lupton, A. McDaniel, J. A. Munn, V. K. Narayanan, E. Peng, J. R. Pier, C. M. Rockosi, D. P. Schneider, J. A. Smith, M. A. Strauss, Z. I. Tsvetanov, A. Uomoto, D. G. York and W. Zheng, "Toward Spectral Classification of L and T Dwarfs: Infrared and Optical Spectroscopy and Analysis", ApJ, **564**, 466–481 (2002).

Gelino, C. R., J. D. Kirkpatrick, M. C. Cushing, P. R. Eisenhardt, R. L. Griffith, A. K. Mainzer, K. A. Marsh, M. F. Skrutskie and E. L. Wright, "WISE Brown Dwarf Binaries: The Discovery of a T5+T5 and a T8.5+T9 System", AJ, **142**, 57 (2011).

Gelino, C. R., M. S. Marley, J. A. Holtzman, A. S. Ackerman and K. Lodders, "L Dwarf Variability: I-Band Observations", ApJ, **577**, 433–446 (2002).

Gillon, M., A. H. M. J. Triaud, B.-O. Demory, E. Jehin, E. Agol, K. M. Deck, S. M. Lederer, J. de Wit, A. Burdanov, J. G. Ingalls, E. Bolmont, J. Leconte, S. N. Raymond, F. Selsis, M. Turbet, K. Barkaoui, A. Burgasser, M. R. Burleigh, S. J. Carey, A. Chaushev, C. M. Copperwheat, L. Delrez, C. S. Fernandes, D. L. Holdsworth, E. J. Kotze, V. Van Grootel, Y. Almleaky, Z. Benkhaldoun, P. Magain and D. Queloz, "Seven temperate terrestrial planets around the nearby ultracool dwarf star TRAPPIST-1", Nature, **542**, 456–460 (2017).

Girardin, F., É. Artigau and R. Doyon, "In Search of Dust Clouds: Photometric Monitoring of a Sample of Late L and T Dwarfs", ApJ, **767**, 61 (2013).

Gizis, J. E., K. G. Dettman, A. J. Burgasser, S. Camnasio, M. Alam, J. C. Filippazzo, K. L. Cruz, S. Metchev, E. Berger and P. K. G. Williams, "Kepler Monitoring of an L Dwarf. II. Clouds with Multi-year Lifetimes", ApJ, **813**, 104 (2015).

Goldman, B., S. Marsat, T. Henning, C. Clemens and J. Greiner, "A new benchmark T8-9 brown dwarf and a couple of new mid-T dwarfs from the UKIDSS DR5+ LAS", MNRAS, **405**, 1140–1152 (2010).

Golimowski, D. A., S. K. Leggett, M. S. Marley, X. Fan, T. R. Geballe, G. R. Knapp, F. J. Vrba, A. A. Henden, C. B. Luginbuhl, H. H. Guetter, J. A. Munn, B. Canzian, W. Zheng, Z. I. Tsvetanov, K. Chiu, K. Glazebrook, E. A. Hoversten, D. P. Schneider and J. Brinkmann, "L' and M' Photometry of Ultracool Dwarfs", AJ, **127**, 3516–3536 (2004).

Graham, J. R., B. Macintosh, R. Doyon, D. Gavel, J. Larkin, M. Levine, B. Oppenheimer, D. Palmer, L. Saddlemyer, A. Sivaramakrishnan, J.-P. Veran and K. Wallace, "Ground-Based Direct Detection of Exoplanets with the Gemini Planet Imager (GPI)", ArXiv e-prints (2007).

Greco, J. P. and T. D. Brandt, "The Measurement, Treatment, and Impact of Spectral Covariance and Bayesian Priors in Integral-field Spectroscopy of Exoplanets", ApJ, **833**, 134 (2016).

Guarinos, J., "The Interstellar Medium as Shown by the UBV Data Archive", in "European Southern Observatory Conference and Workshop Proceedings", edited by A. Heck and F. Murtagh, vol. 43 of *European Southern Observatory Conference and Workshop Proceedings*, p. 301 (1992).

Hayashi, C. and T. Nakano, "Evolution of Stars of Small Masses in the Pre-Main-Sequence Stages", Progress of Theoretical Physics **30**, 460–474 (1963).

Heintz, W. D., "Photographic astrometry of binar and proper-motion stars: 8.", AJ, **108**, 2338–2347 (1994).

Heinze, A. N., P. M. Hinz, M. Kenworthy, M. Meyer, S. Sivanandam and D. Miller, "Constraints on Long-period Planets from an L'- and M-band Survey of Nearby Sun-like Stars: Modeling Results", ApJ, **714**, 1570–1581 (2010).

Heinze, A. N., S. Metchev and K. Kellogg, "Weather on Other Worlds. III. A Survey for T Dwarfs with High-amplitude Optical Variability", ApJ, **801**, 104 (2015).

Helling, C. and S. Casewell, "Atmospheres of brown dwarfs", A&A Rv, **22**, 80 (2014).

Helling, C. and P. Woitke, "Dust in brown dwarfs. V. Growth and evaporation of dirty dust grains", A&A, **455**, 325–338 (2006).

Henry, T. J. and D. W. McCarthy, Jr., "A systematic search for brown dwarfs orbiting nearby stars", ApJ, **350**, 334–347 (1990).

Hinkley, S., B. R. Oppenheimer, N. Zimmerman, D. Brenner, I. R. Parry, J. R. Crepp, G. Vasisht, E. Ligon, D. King, R. Soummer, A. Sivaramakrishnan, C. Beichman, M. Shao, L. C. Roberts, Jr., A. Bouchez, R. Dekany, L. Pueyo, J. E. Roberts, T. Lockhart, C. Zhai, C. Shelton and R. Burruss, "A New High Contrast Imaging Program at Palomar Observatory", PASP, **123**, 74 (2011).

Høg, E., C. Fabricius, V. V. Makarov, S. Urban, T. Corbin, G. Wycoff, U. Bastian, P. Schwekendiek and A. Wicenec, "The Tycho-2 catalogue of the 2.5 million brightest stars", A&A, **355**, L27–L30 (2000).

Hubickyj, O., P. Bodenheimer and J. J. Lissauer, "Accretion of the gaseous envelope of Jupiter around a 5 10 Earth-mass core", Icarus, **179**, 415–431 (2005).

Irwin, M. J., "Processing Wide Field Imaging Data", in "2007 ESO Instrument Calibration Workshop", edited by A. Kaufer and F. Kerber, p. 541 (2008).

Janson, M., M. Bonavita, H. Klahr, D. Lafrenière, R. Jayawardhana and H. Zinnecker, "High-contrast Imaging Search for Planets and Brown Dwarfs around the Most Massive Stars in the Solar Neighborhood", ApJ, **736**, 89 (2011a).

Janson, M., T. D. Brandt, A. Moro-Martín, T. Usuda, C. Thalmann, J. C. Carson, M. Goto, T. Currie, M. W. McElwain, Y. Itoh, M. Fukagawa, J. Crepp, M. Kuzuhara, J. Hashimoto, T. Kudo, N. Kusakabe, L. Abe, W. Brandner, S. Egner, M. Feldt, C. A. Grady, O. Guyon, Y. Hayano, M. Hayashi, S. Hayashi, T. Henning, K. W. Hodapp, M. Ishii, M. Iye, R. Kandori, G. R. Knapp, J. Kwon, T. Matsuo, S. Miyama, J.-I. Morino, T. Nishimura, T.-S. Pyo, E. Serabyn, T. Suenaga, H. Suto, R. Suzuki, Y. Takahashi, M. Takami, N. Takato, H. Terada, D. Tomono, E. L. Turner, M. Watanabe, J. Wisniewski, T. Yamada, H. Takami and M. Tamura, "The SEEDS Direct

Imaging Survey for Planets and Scattered Dust Emission in Debris Disk Systems", ApJ, **773**, 73 (2013).

Janson, M., J. Carson, C. Thalmann, M. W. McElwain, M. Goto, J. Crepp, J. Wisniewski, L. Abe, W. Brandner, A. Burrows, S. Egner, M. Feldt, C. A. Grady, T. Golota, O. Guyon, J. Hashimoto, Y. Hayano, M. Hayashi, S. Hayashi, T. Henning, K. W. Hodapp, M. Ishii, M. Iye, R. Kandori, G. R. Knapp, T. Kudo, N. Kusakabe, M. Kuzuhara, T. Matsuo, S. Mayama, S. Miyama, J.-I. Morino, A. Moro-Martín, T. Nishimura, T.-S. Pyo, E. Serabyn, H. Suto, R. Suzuki, M. Takami, N. Takato, H. Terada, B. Tofflemire, D. Tomono, E. L. Turner, M. Watanabe, T. Yamada, H. Takami, T. Usuda and M. Tamura, "Near-infrared Multi-band Photometry of the Substellar Companion GJ 758 B", ApJ, **728**, 85 (2011b).

Janson, M., J. C. Carson, D. Lafrenière, D. S. Spiegel, J. R. Bent and P. Wong, "Infrared Non-detection of Fomalhaut b: Implications for the Planet Interpretation", ApJ, **747**, 116 (2012).

Jensen-Clem, R., M. Millar-Blanchaer, D. Mawet, J. R. Graham, J. K. Wallace, B. Macintosh, S. Hinkley, S. J. Wiktorowicz, M. D. Perrin, M. S. Marley, M. P. Fitzgerald, R. Oppenheimer, S. M. Ammons, F. T. Rantakyrö and F. Marchis, "Point Source Polarimetry with the Gemini Planet Imager: Sensitivity Characterization with T5.5 Dwarf Companion HD 19467 B", ApJ, **820**, 111 (2016).

Johansen, A. and A. Youdin, "Protoplanetary Disk Turbulence Driven by the Streaming Instability: Nonlinear Saturation and Particle Concentration", ApJ, **662**, 627–641 (2007).

Kalas, P., M. P. Fitzgerald and J. R. Graham, "Discovery of Extreme Asymmetry in the Debris Disk Surrounding HD 15115", ApJL, **661**, L85–L88 (2007).

Kalas, P., J. R. Graham, E. Chiang, M. P. Fitzgerald, M. Clampin, E. S. Kite, K. Stapelfeldt, C. Marois and J. Krist, "Optical Images of an Exosolar Planet 25 Light-Years from Earth", Science **322**, 1345 (2008).

Kalas, P., J. R. Graham, M. P. Fitzgerald and M. Clampin, "STIS Coronagraphic Imaging of Fomalhaut: Main Belt Structure and the Orbit of Fomalhaut b", ApJ, **775**, 56 (2013).

Kalas, P. G., A. Rajan, J. J. Wang, M. A. Millar-Blanchaer, G. Duchene, C. Chen, M. P. Fitzgerald, R. Dong, J. R. Graham, J. Patience, B. Macintosh, R. Murray-Clay, B. Matthews, J. Rameau, C. Marois, J. Chilcote, R. J. De Rosa, R. Doyon, Z. H. Draper, S. Lawler, S. M. Ammons, P. Arriaga, J. Bulger, T. Cotten, K. B. Follette, S. Goodsell, A. Greenbaum, P. Hibon, S. Hinkley, L.-W. Hung, P. Ingraham, Q. Konapacky, D. Lafreniere, J. E. Larkin, D. Long, J. Maire, F. Marchis, S. Metchev, K. M.

Morzinski, E. L. Nielsen, R. Oppenheimer, M. D. Perrin, L. Pueyo, F. T. Rantakyrö, J.-B. Ruffio, L. Saddlemyer, D. Savransky, A. C. Schneider, A. Sivaramakrishnan, R. Soummer, I. Song, S. Thomas, G. Vasisht, K. Ward-Duong, S. J. Wiktorowicz and S. G. Wolff, "Direct Imaging of an Asymmetric Debris Disk in the HD 106906 Planetary System", ApJ, **814**, 32 (2015a).

Kalas, P. G., A. Rajan, J. J. Wang, M. A. Millar-Blanchaer, G. Duchene, C. Chen, M. P. Fitzgerald, R. Dong, J. R. Graham, J. Patience, B. Macintosh, R. Murray-Clay, B. Matthews, J. Rameau, C. Marois, J. Chilcote, R. J. De Rosa, R. Doyon, Z. H. Draper, S. Lawler, S. M. Ammons, P. Arriaga, J. Bulger, T. Cotten, K. B. Follette, S. Goodsell, A. Greenbaum, P. Hibon, S. Hinkley, L.-W. Hung, P. Ingraham, Q. Konapacky, D. Lafreniere, J. E. Larkin, D. Long, J. Maire, F. Marchis, S. Metchev, K. M. Morzinski, E. L. Nielsen, R. Oppenheimer, M. D. Perrin, L. Pueyo, F. T. Rantakyrö, J.-B. Ruffio, L. Saddlemyer, D. Savransky, A. C. Schneider, A. Sivaramakrishnan, R. Soummer, I. Song, S. Thomas, G. Vasisht, K. Ward-Duong, S. J. Wiktorowicz and S. G. Wolff, "Direct Imaging of an Asymmetric Debris Disk in the HD 106906 Planetary System", ApJ, **814**, 32 (2015b).

Kenyon, S. J. and L. Hartmann, "Pre-Main-Sequence Evolution in the Taurus-Auriga Molecular Cloud", ApJS, **101**, 117 (1995).

Khandrika, H., A. J. Burgasser, C. Melis, C. Luk, E. Bowsher and B. Swift, "A Search for Photometric Variability in L- and T-type Brown Dwarf Atmospheres", AJ, **145**, 71 (2013).

Kirkpatrick, J. D., C. A. Beichman and M. F. Skrutskie, "The coolest isolated m dwarf and other 2mass discoveries", The Astrophysical Journal **476**, 1, 311, URL http://stacks.iop.org/0004-637X/476/i=1/a=311 (1997).

Kirkpatrick, J. D., C. R. Gelino, M. C. Cushing, G. N. Mace, R. L. Griffith, M. F. Skrutskie, K. A. Marsh, E. L. Wright, P. R. Eisenhardt, I. S. McLean, A. K. Mainzer, A. J. Burgasser, C. G. Tinney, S. Parker and G. Salter, "Further Defining Spectral Type "Y" and Exploring the Low-mass End of the Field Brown Dwarf Mass Function", ApJ, **753**, 156 (2012).

Kirkpatrick, J. D., D. L. Looper, A. J. Burgasser, S. D. Schurr, R. M. Cutri, M. C. Cushing, K. L. Cruz, A. C. Sweet, G. R. Knapp, T. S. Barman, J. J. Bochanski, T. L. Roellig, I. S. McLean, M. R. McGovern and E. L. Rice, "Discoveries from a Near-infrared Proper Motion Survey Using Multi-epoch Two Micron All-Sky Survey Data", ApJS, **190**, 100–146 (2010).

Kirkpatrick, J. D., I. N. Reid, J. Liebert, R. M. Cutri, B. Nelson, C. A. Beichman, C. C. Dahn, D. G. Monet, J. E. Gizis and M. F. Skrutskie, "Dwarfs Cooler than "M": The Definition of Spectral Type "L" Using Discoveries from the 2 Micron All-Sky Survey (2MASS)", ApJ, **519**, 802–833 (1999).

Knapp, G. R., S. K. Leggett, X. Fan, M. S. Marley, T. R. Geballe, D. A. Golimowski, D. Finkbeiner, J. E. Gunn, J. Hennawi, Z. Ivezić, R. H. Lupton, D. J. Schlegel, M. A. Strauss, Z. I. Tsvetanov, K. Chiu, E. A. Hoversten, K. Glazebrook, W. Zheng, M. Hendrickson, C. C. Williams, A. Uomoto, F. J. Vrba, A. A. Henden, C. B. Luginbuhl, H. H. Guetter, J. A. Munn, B. Canzian, D. P. Schneider and J. Brinkmann, "Near-Infrared Photometry and Spectroscopy of L and T Dwarfs: The Effects of Temperature, Clouds, and Gravity", AJ, **127**, 3553–3578 (2004).

Knutson, H. A., D. Charbonneau, L. E. Allen, J. J. Fortney, E. Agol, N. B. Cowan, A. P. Showman, C. S. Cooper and S. T. Megeath, "A map of the day-night contrast of the extrasolar planet HD 189733b", Nature, **447**, 183–186 (2007).

Koen, C., "A search for short time-scale I-band variability in ultracool dwarfs", MNRAS, **346**, 473–482 (2003).

Koen, C., "I-band time-series observations of five bright ultracool dwarfs", MNRAS, **354**, 378–386 (2004).

Koen, C., "I_C and R_C band time-series observations of some bright ultracool dwarfs", MNRAS, **360**, 1132–1142 (2005).

Koen, C., "An extensive search for rapid optical variability in ultracool dwarfs", MNRAS, **428**, 2824–2839 (2013a).

Koen, C., "An extensive search for rapid optical variability in ultracool dwarfs", MNRAS, **428**, 2824–2839 (2013b).

Koen, C., N. Matsunaga and J. Menzies, "A search for short time-scale JHK variability in ultracool dwarfs", MNRAS, **354**, 466–476 (2004).

Koen, C., T. Tanabé, M. Tamura and N. Kusakabe, "JHK_s time-series observations of a few ultracool dwarfs", MNRAS, **362**, 727–736 (2005a).

Koen, C., T. Tanabé, M. Tamura and N. Kusakabe, "JHK_s time-series observations of a few ultracool dwarfs", MNRAS, **362**, 727–736 (2005b).

Koleva, M. and A. Vazdekis, "Stellar population models in the UV. I. Characterisation of the New Generation Stellar Library", A&A, **538**, A143 (2012).

Konopacky, Q. M., T. S. Barman, B. A. Macintosh and C. Marois, "Detection of Carbon Monoxide and Water Absorption Lines in an Exoplanet Atmosphere", Science **339**, 1398–1401 (2013).

Konopacky, Q. M., J. Rameau, G. Duchêne, J. C. Filippazzo, P. A. Giorla Godfrey, C. Marois, E. L. Nielsen, L. Pueyo, R. R. Rafikov, E. L. Rice, J. J. Wang, S. M. Ammons, V. P. Bailey, T. S. Barman, J. Bulger, S. Bruzzone, J. K. Chilcote,

T. Cotten, R. I. Dawson, R. J. De Rosa, R. Doyon, T. M. Esposito, M. P. Fitzgerald, K. B. Follette, S. Goodsell, J. R. Graham, A. Z. Greenbaum, P. Hibon, L.-W. Hung, P. Ingraham, P. Kalas, D. Lafrenière, J. E. Larkin, B. A. Macintosh, J. Maire, F. Marchis, M. S. Marley, B. C. Matthews, S. Metchev, M. A. Millar-Blanchaer, R. Oppenheimer, D. W. Palmer, J. Patience, M. D. Perrin, L. A. Poyneer, A. Rajan, F. T. Rantakyrö, D. Savransky, A. C. Schneider, A. Sivaramakrishnan, I. Song, R. Soummer, S. Thomas, J. K. Wallace, K. Ward-Duong, S. J. Wiktorowicz and S. G. Wolff, "Discovery of a Substellar Companion to the Nearby Debris Disk Host HR 2562", ApJL, **829**, L4 (2016).

Konopacky, Q. M., S. J. Thomas, B. A. Macintosh, D. Dillon, N. Sadakuni, J. Maire, M. Fitzgerald, S. Hinkley, P. Kalas, T. Esposito, C. Marois, P. J. Ingraham, F. Marchis, M. D. Perrin, J. R. Graham, J. J. Wang, R. J. De Rosa, K. Morzinski, L. Pueyo, J. K. Chilcote, J. E. Larkin, D. Fabrycky, S. J. Goodsell, B. R. Oppenheimer, J. Patience, L. Saddlemyer and A. Sivaramakrishnan, "Gemini planet imager observational calibrations V: astrometry and distortion", in "Ground-based and Airborne Instrumentation for Astronomy V", vol. 9147 of *Proc. SPIE,* , p. 914784 (2014).

Kornilov, V., A. A. Tokovinin, O. Vozyakova, A. Zaitsev, N. Shatsky, S. F. Potanin and M. S. Sarazin, "MASS: a monitor of the vertical turbulence distribution", in "Adaptive Optical System Technologies II", edited by P. L. Wizinowich and D. Bonaccini, vol. 4839 of *Proc. SPIE,* , pp. 837–845 (2003).

Kostov, V. and D. Apai, "Mapping Directly Imaged Giant Exoplanets", ApJ, **762**, 47 (2013).

Kraus, A. L., S. M. Andrews, B. P. Bowler, G. Herczeg, M. J. Ireland, M. C. Liu, S. Metchev and K. L. Cruz, "An ALMA Disk Mass for the Candidate Protoplanetary Companion to FW Tau", ApJL, **798**, L23 (2015).

Kraus, A. L., M. J. Ireland, L. A. Cieza, S. Hinkley, T. J. Dupuy, B. P. Bowler and M. C. Liu, "Three Wide Planetary-mass Companions to FW Tau, ROXs 12, and ROXs 42B", ApJ, **781**, 20 (2014).

Kreidberg, L., J. L. Bean, J.-M. Désert, B. Benneke, D. Deming, K. B. Stevenson, S. Seager, Z. Berta-Thompson, A. Seifahrt and D. Homeier, "Clouds in the atmosphere of the super-Earth exoplanet GJ1214b", Nature, **505**, 69–72 (2014).

Krist, J. E., R. N. Hook and F. Stoehr, "20 years of Hubble Space Telescope optical modeling using Tiny Tim", in "Society of Photo-Optical Instrumentation Engineers (SPIE) Conference Series", vol. 8127 of *Society of Photo-Optical Instrumentation Engineers (SPIE) Conference Series*, p. 0 (2011a).

Krist, J. E., R. N. Hook and F. Stoehr, "20 years of Hubble Space Telescope optical modeling using Tiny Tim", in "Optical Modeling and Performance Predictions V", vol. 8127 of *Proc. SPIE,* , p. 81270J (2011b).

Kumar, S. S., "The Helmholtz-Kelvin Time Scale for Stars of Very Low Mass.", ApJ, **137**, 1126 (1963a).

Kumar, S. S., "The Structure of Stars of Very Low Mass.", ApJ, **137**, 1121 (1963b).

Kuzuhara, M., M. Tamura, T. Kudo, M. Janson, R. Kandori, T. D. Brandt, C. Thalmann, D. Spiegel, B. Biller, J. Carson, Y. Hori, R. Suzuki, A. Burrows, T. Henning, E. L. Turner, M. W. McElwain, A. Moro-Martín, T. Suenaga, Y. H. Takahashi, J. Kwon, P. Lucas, L. Abe, W. Brandner, S. Egner, M. Feldt, H. Fujiwara, M. Goto, C. A. Grady, O. Guyon, J. Hashimoto, Y. Hayano, M. Hayashi, S. S. Hayashi, K. W. Hodapp, M. Ishii, M. Iye, G. R. Knapp, T. Matsuo, S. Mayama, S. Miyama, J.-I. Morino, J. Nishikawa, T. Nishimura, T. Kotani, N. Kusakabe, T.-S. Pyo, E. Serabyn, H. Suto, M. Takami, N. Takato, H. Terada, D. Tomono, M. Watanabe, J. P. Wisniewski, T. Yamada, H. Takami and T. Usuda, "Direct Imaging of a Cold Jovian Exoplanet in Orbit around the Sun-like Star GJ 504", ApJ, **774**, 11 (2013).

Lafrenière, D., R. Jayawardhana and M. H. van Kerkwijk, "Direct Imaging and Spectroscopy of a Planetary-Mass Candidate Companion to a Young Solar Analog", ApJL, **689**, L153 (2008).

Lafrenière, D., C. Marois, R. Doyon, D. Nadeau and É. Artigau, "A New Algorithm for Point-Spread Function Subtraction in High-Contrast Imaging: A Demonstration with Angular Differential Imaging", ApJ, **660**, 770–780 (2007).

Lagrange, A.-M., M. Bonnefoy, G. Chauvin, D. Apai, D. Ehrenreich, A. Boccaletti, D. Gratadour, D. Rouan, D. Mouillet, S. Lacour and M. Kasper, "A Giant Planet Imaged in the Disk of the Young Star β Pictoris", Science **329**, 57– (2010).

Lagrange, A.-M., D. Gratadour, G. Chauvin, T. Fusco, D. Ehrenreich, D. Mouillet, G. Rousset, D. Rouan, F. Allard, É. Gendron, J. Charton, L. Mugnier, P. Rabou, J. Montri and F. Lacombe, "A probable giant planet imaged in the β Pictoris disk. VLT/NaCo deep L'-band imaging", A&A, **493**, L21–L25 (2009).

Lambrechts, M. and A. Johansen, "Rapid growth of gas-giant cores by pebble accretion", A&A, **544**, A32 (2012).

Lauer, T. R., "The Photometry of Undersampled Point-Spread Functions", PASP, **111**, 1434–1443 (1999).

Lawrence, A., S. J. Warren, O. Almaini, A. C. Edge, N. C. Hambly, R. F. Jameson, P. Lucas, M. Casali, A. Adamson, S. Dye, J. P. Emerson, S. Foucaud, P. Hewett,

P. Hirst, S. T. Hodgkin, M. J. Irwin, N. Lodieu, R. G. McMahon, C. Simpson, I. Smail, D. Mortlock and M. Folger, "The UKIRT Infrared Deep Sky Survey (UKIDSS)", MNRAS, **379**, 1599–1617 (2007).

Leggett, S. K., T. R. Geballe, X. Fan, D. P. Schneider, J. E. Gunn, R. H. Lupton, G. R. Knapp, M. A. Strauss, A. McDaniel, D. A. Golimowski, T. J. Henry, E. Peng, Z. I. Tsvetanov, A. Uomoto, W. Zheng, G. J. Hill, L. W. Ramsey, S. F. Anderson, J. A. Annis, N. A. Bahcall, J. Brinkmann, B. Chen, I. Csabai, M. Fukugita, G. S. Hennessy, R. B. Hindsley, Ž. Ivezić, D. Q. Lamb, J. A. Munn, J. R. Pier, D. J. Schlegel, J. A. Smith, C. Stoughton, A. R. Thakar and D. G. York, "The Missing Link: Early Methane ("T") Dwarfs in the Sloan Digital Sky Survey", ApJL, **536**, L35–L38 (2000).

Leggett, S. K., C. V. Morley, M. S. Marley and D. Saumon, "Near-infrared Photometry of Y Dwarfs: Low Ammonia Abundance and the Onset of Water Clouds", ApJ, **799**, 37 (2015).

Leggett, S. K., C. V. Morley, M. S. Marley, D. Saumon, J. J. Fortney and C. Visscher, "A Comparison of Near-infrared Photometry and Spectra for Y Dwarfs with a New Generation of Cool Cloudy Models", ApJ, **763**, 130 (2013).

Leggett, S. K., D. Saumon, L. Albert, M. C. Cushing, M. C. Liu, K. L. Luhman, M. S. Marley, J. D. Kirkpatrick, T. L. Roellig and K. N. Allers, "HN Peg B: A Test of Models of the L to T Dwarf Transition", ApJ, **682**, 1256–1263 (2008).

Leggett, S. K., D. Saumon, M. S. Marley, T. R. Geballe, D. A. Golimowski, D. Stephens and X. Fan, "3.6-7.9 μm Photometry of L and T Dwarfs and the Prevalence of Vertical Mixing in their Atmospheres", ApJ, **655**, 1079–1094 (2007).

Line, M. R., J. J. Fortney, M. S. Marley and S. Sorahana, "A Data-driven Approach for Retrieving Temperatures and Abundances in Brown Dwarf Atmospheres", ApJ, **793**, 33 (2014).

Line, M. R., J. Teske, B. Burningham, J. J. Fortney and M. S. Marley, "Uniform Atmospheric Retrieval Analysis of Ultracool Dwarfs. I. Characterizing Benchmarks, Gl 570D and HD 3651B", ApJ, **807**, 183 (2015).

Liu, M. C., P. Delorme, T. J. Dupuy, B. P. Bowler, L. Albert, E. Artigau, C. Reylé, T. Forveille and X. Delfosse, "CFBDSIR J1458+1013B: A Very Cold (T10) Brown Dwarf in a Binary System", ApJ, **740**, 108 (2011).

Liu, M. C., T. J. Dupuy and K. N. Allers, "The Hawaii Infrared Parallax Program. II. Young Ultracool Field Dwarfs", ApJ, **833**, 96 (2016).

Liu, M. C., E. A. Magnier, N. R. Deacon, K. N. Allers, T. J. Dupuy, M. C. Kotson, K. M. Aller, W. S. Burgett, K. C. Chambers, P. W. Draper, K. W. Hodapp, R. Jedicke, N. Kaiser, R.-P. Kudritzki, N. Metcalfe, J. S. Morgan, P. A. Price, J. L. Tonry and R. J. Wainscoat, "The Extremely Red, Young L Dwarf PSO J318.5338-22.8603: A Free-floating Planetary-mass Analog to Directly Imaged Young Gas-giant Planets", ApJL, **777**, L20 (2013).

Lodders, K., "Solar System Abundances and Condensation Temperatures of the Elements", ApJ, **591**, 1220–1247 (2003).

Lodders, K. and B. Fegley, Jr., *Chemistry of Low Mass Substellar Objects*, p. 1 (2006).

Looper, D. L., J. D. Kirkpatrick and A. J. Burgasser, "Discovery of 11 New T Dwarfs in the Two Micron All Sky Survey, Including a Possible L/T Transition Binary", AJ, **134**, 1162–1182 (2007).

Lowrance, P. J., E. E. Becklin, G. Schneider, J. D. Kirkpatrick, A. J. Weinberger, B. Zuckerman, C. Dumas, J.-L. Beuzit, P. Plait, E. Malumuth, S. Heap, R. J. Terrile and D. C. Hines, "An Infrared Coronagraphic Survey for Substellar Companions", AJ, **130**, 1845–1861 (2005).

Luhman, K. L., K. K. McLeod and N. Goldenson, "A Hubble Space Telescope Search for Substellar Companions in the Young Cluster IC 348", ApJ, **623**, 1141–1156 (2005).

Luhman, K. L., B. M. Patten, M. Marengo, M. T. Schuster, J. L. Hora, R. G. Ellis, J. R. Stauffer, S. M. Sonnett, E. Winston, R. A. Gutermuth, S. T. Megeath, D. E. Backman, T. J. Henry, M. W. Werner and G. G. Fazio, "Discovery of Two T Dwarf Companions with the Spitzer Space Telescope", ApJ, **654**, 570–579 (2007).

Lunine, J. I., W. B. Hubbard, A. Burrows, Y.-P. Wang and K. Garlow, "The effect of gas and grain opacity on the cooling of brown dwarfs", ApJ, **338**, 314–337 (1989).

Lyot, B., "The study of the solar corona and prominences without eclipses (George Darwin Lecture, 1939)", MNRAS, **99**, 580 (1939).

Lytle, D., E. Stobie, A. Ferro and I. Barg, "Image Display Paradigm #3", in "Astronomical Data Analysis Software and Systems VIII", edited by D. M. Mehringer, R. L. Plante and D. A. Roberts, vol. 172 of *Astronomical Society of the Pacific Conference Series*, p. 445 (1999).

Macintosh, B., J. R. Graham, T. Barman, R. J. De Rosa, Q. Konopacky, M. S. Marley, C. Marois, E. L. Nielsen, L. Pueyo, A. Rajan, J. Rameau, D. Saumon, J. J. Wang, J. Patience, M. Ammons, P. Arriaga, E. Artigau, S. Beckwith, J. Brewster, S. Bruzzone, J. Bulger, B. Burningham, A. S. Burrows, C. Chen, E. Chiang, J. K.

Chilcote, R. I. Dawson, R. Dong, R. Doyon, Z. H. Draper, G. Duchêne, T. M. Esposito, D. Fabrycky, M. P. Fitzgerald, K. B. Follette, J. J. Fortney, B. Gerard, S. Goodsell, A. Z. Greenbaum, P. Hibon, S. Hinkley, T. H. Cotten, L.-W. Hung, P. Ingraham, M. Johnson-Groh, P. Kalas, D. Lafreniere, J. E. Larkin, J. Lee, M. Line, D. Long, J. Maire, F. Marchis, B. C. Matthews, C. E. Max, S. Metchev, M. A. Millar-Blanchaer, T. Mittal, C. V. Morley, K. M. Morzinski, R. Murray-Clay, R. Oppenheimer, D. W. Palmer, R. Patel, M. D. Perrin, L. A. Poyneer, R. R. Rafikov, F. T. Rantakyrö, E. L. Rice, P. Rojo, A. R. Rudy, J.-B. Ruffio, M. T. Ruiz, N. Sadakuni, L. Saddlemyer, M. Salama, D. Savransky, A. C. Schneider, A. Sivaramakrishnan, I. Song, R. Soummer, S. Thomas, G. Vasisht, J. K. Wallace, K. Ward-Duong, S. J. Wiktorowicz, S. G. Wolff and B. Zuckerman, "Discovery and spectroscopy of the young jovian planet 51 Eri b with the Gemini Planet Imager", Science **350**, 64–67 (2015).

Macintosh, B., J. R. Graham, P. Ingraham, Q. Konopacky, C. Marois, M. Perrin, L. Poyneer, B. Bauman, T. Barman, A. S. Burrows, A. Cardwell, J. Chilcote, R. J. De Rosa, D. Dillon, R. Doyon, J. Dunn, D. Erikson, M. P. Fitzgerald, D. Gavel, S. Goodsell, M. Hartung, P. Hibon, P. Kalas, J. Larkin, J. Maire, F. Marchis, M. S. Marley, J. McBride, M. Millar-Blanchaer, K. Morzinski, A. Norton, B. R. Oppenheimer, D. Palmer, J. Patience, L. Pueyo, F. Rantakyro, N. Sadakuni, L. Saddlemyer, D. Savransky, A. Serio, R. Soummer, A. Sivaramakrishnan, I. Song, S. Thomas, J. K. Wallace, S. Wiktorowicz and S. Wolff, "First light of the Gemini Planet Imager", Proceedings of the National Academy of Science **111**, 12661–12666 (2014).

Macintosh, B., C. Max, B. Zuckerman, E. E. Becklin, D. Kaisler, P. Lowrance, A. Weinberger, J. Christou, G. Schneider and S. Acton, "Keck Adaptive Optics Observations of TW Hydrae Association Members", in "Young Stars Near Earth: Progress and Prospects", edited by R. Jayawardhana and T. Greene, vol. 244 of *Astronomical Society of the Pacific Conference Series*, p. 309 (2001).

Madhusudhan, N., H. Knutson, J. J. Fortney and T. Barman, "Exoplanetary Atmospheres", Protostars and Planets VI pp. 739–762 (2014).

Mainzer, A., M. C. Cushing, M. Skrutskie, C. R. Gelino, J. D. Kirkpatrick, T. Jarrett, F. Masci, M. S. Marley, D. Saumon, E. Wright, R. Beaton, M. Dietrich, P. Eisenhardt, P. Garnavich, O. Kuhn, D. Leisawitz, K. Marsh, I. McLean, D. Padgett and K. Rueff, "The First Ultra-cool Brown Dwarf Discovered by the Wide-field Infrared Survey Explorer", ApJ, **726**, 30 (2011).

Maire, J., P. J. Ingraham, R. J. De Rosa, M. D. Perrin, A. Rajan, D. Savransky, J. J. Wang, J.-B. Ruffio, S. G. Wolff, J. K. Chilcote, R. Doyon, J. R. Graham, A. Z. Greenbaum, Q. M. Konopacky, J. E. Larkin, B. A. Macintosh, C. Marois,

M. Millar-Blanchaer, J. Patience, L. A. Pueyo, A. Sivaramakrishnan, S. J. Thomas and J. L. Weiss, "Gemini planet imager observational calibrations VI: photometric and spectroscopic calibration for the integral field spectrograph", in "Ground-based and Airborne Instrumentation for Astronomy V", vol. 9147 of *Proc. SPIE,* , p. 914785 (2014).

Maiti, M., "Observational Evidence of Optical Variability in L Dwarfs", AJ, **133**, 1633–1644 (2007).

Maiti, M., S. Sengupta, P. S. Parihar and G. C. Anupama, "Observation of R-Band Variability of L Dwarfs", ApJL, **619**, L183–L186 (2005).

Malo, L., R. Doyon, D. Lafrenière, É. Artigau, J. Gagné, F. Baron and A. Riedel, "Bayesian Analysis to Identify New Star Candidates in Nearby Young Stellar Kinematic Groups", ApJ, **762**, 88 (2013).

Marleau, G.-D. and A. Cumming, "Constraining the initial entropy of directly detected exoplanets", MNRAS, **437**, 1378–1399 (2014).

Marley, M. S., J. J. Fortney, O. Hubickyj, P. Bodenheimer and J. J. Lissauer, "On the Luminosity of Young Jupiters", ApJ, **655**, 541–549 (2007).

Marley, M. S., D. Saumon, M. Cushing, A. S. Ackerman, J. J. Fortney and R. Freedman, "Masses, Radii, and Cloud Properties of the HR 8799 Planets", ApJ, **754**, 135 (2012).

Marley, M. S., D. Saumon and C. Goldblatt, "A Patchy Cloud Model for the L to T Dwarf Transition", ApJL, **723**, L117–L121 (2010).

Marley, M. S., D. Saumon, T. Guillot, R. S. Freedman, W. B. Hubbard, A. Burrows and J. I. Lunine, "Atmospheric, Evolutionary, and Spectral Models of the Brown Dwarf Gliese 229 B", Science **272**, 1919–1921 (1996).

Marley, M. S., S. Seager, D. Saumon, K. Lodders, A. S. Ackerman, R. S. Freedman and X. Fan, "Clouds and Chemistry: Ultracool Dwarf Atmospheric Properties from Optical and Infrared Colors", ApJ, **568**, 335–342 (2002).

Marois, C., D. Lafrenière, R. Doyon, B. Macintosh and D. Nadeau, "Angular Differential Imaging: A Powerful High-Contrast Imaging Technique", ApJ, **641**, 556–564 (2006a).

Marois, C., D. Lafrenière, B. Macintosh and R. Doyon, "Accurate Astrometry and Photometry of Saturated and Coronagraphic Point Spread Functions", ApJ, **647**, 612–619 (2006b).

Marois, C., B. Macintosh, T. Barman, B. Zuckerman, I. Song, J. Patience, D. Lafrenière and R. Doyon, "Direct Imaging of Multiple Planets Orbiting the Star HR 8799", Science **322**, 1348– (2008).

Marois, C., B. Macintosh and J.-P. Véran, "Exoplanet imaging with LOCI processing: photometry and astrometry with the new SOSIE pipeline", in "Society of Photo-Optical Instrumentation Engineers (SPIE) Conference Series", vol. 7736 of *Society of Photo-Optical Instrumentation Engineers (SPIE) Conference Series* (2010a).

Marois, C., B. Zuckerman, Q. M. Konopacky, B. Macintosh and T. Barman, "Images of a fourth planet orbiting HR 8799", Nature, **468**, 1080–1083 (2010b).

Martín, E. L., M. R. Zapatero Osorio and H. J. Lehto, "Photometric Variability in the Ultracool Dwarf BRI 0021-0214: Possible Evidence for Dust Clouds", ApJ, **557**, 822–830 (2001).

Mawet, D., J. Milli, Z. Wahhaj, D. Pelat, O. Absil, C. Delacroix, A. Boccaletti, M. Kasper, M. Kenworthy, C. Marois, B. Mennesson and L. Pueyo, "Fundamental Limitations of High Contrast Imaging Set by Small Sample Statistics", ApJ, **792**, 97 (2014).

Mayor, M. and D. Queloz, "A Jupiter-mass companion to a solar-type star", Nature, **378**, 355–359 (1995).

Mazoyer, J., A. Boccaletti, J.-C. Augereau, A.-M. Lagrange, R. Galicher and P. Baudoz, "Is the HD 15115 inner disk really asymmetrical?", A&A, **569**, A29 (2014).

McCarthy, C. and B. Zuckerman, "The Brown Dwarf Desert at 75-1200 AU", AJ, **127**, 2871–2884 (2004).

McCarthy, D. W., J. H. Burge, J. R. P. Angel, J. Ge, R. J. Sarlot, B. C. Fitz-Patrick and J. L. Hinz, "ARIES: Arizona infrared imager and echelle spectrograph", in "Infrared Astronomical Instrumentation", edited by A. M. Fowler, vol. 3354 of *Proc. SPIE,* , pp. 750–754 (1998).

McLean, I. S. and D. Sprayberry, "Instrumentation at the Keck observatory", in "Instrument Design and Performance for Optical/Infrared Ground-based Telescopes", edited by M. Iye and A. F. M. Moorwood, vol. 4841 of *Proc. SPIE,* , pp. 1–6 (2003).

Meshkat, T., M. A. Kenworthy, M. Reggiani, S. P. Quanz, E. E. Mamajek and M. R. Meyer, "Searching for gas giant planets on Solar system scales - a NACO/APP L'-band survey of A- and F-type main-sequence stars", MNRAS, **453**, 2533–2539 (2015).

Metchev, S., D. Apai, J. Radigan, É. Artigau, A. Heinze, C. Helling, D. Homeier, S. Littlefair, C. Morley, A. Skemer and C. Stark, "Clouds in brown dwarfs and giant planets", Astronomische Nachrichten **334**, 40–43 (2013).

Metchev, S. A., A. Heinze, D. Apai, D. Flateau, J. Radigan, A. Burgasser, M. S. Marley, É. Artigau, P. Plavchan and B. Goldman, "Weather on Other Worlds. II. Survey Results: Spots are Ubiquitous on L and T Dwarfs", ApJ, **799**, 154 (2015).

Millar-Blanchaer, M. A., J. J. Wang, P. Kalas, J. R. Graham, G. Duchêne, E. L. Nielsen, M. Perrin, D.-S. Moon, D. Padgett, S. Metchev, S. M. Ammons, V. P. Bailey, T. Barman, S. Bruzzone, J. Bulger, C. H. Chen, J. Chilcote, T. Cotten, R. J. De Rosa, R. Doyon, Z. H. Draper, T. M. Esposito, M. P. Fitzgerald, K. B. Follette, B. L. Gerard, A. Z. Greenbaum, P. Hibon, S. Hinkley, L.-W. Hung, P. Ingraham, M. Johnson-Groh, Q. Konopacky, J. E. Larkin, B. Macintosh, J. Maire, F. Marchis, M. S. Marley, C. Marois, B. C. Matthews, R. Oppenheimer, D. Palmer, J. Patience, L. Poyneer, L. Pueyo, A. Rajan, J. Rameau, F. T. Rantakyrö, D. Savransky, A. C. Schneider, A. Sivaramakrishnan, I. Song, R. Soummer, S. Thomas, D. Vega, J. K. Wallace, K. Ward-Duong, S. Wiktorowicz and S. Wolff, "Imaging an 80 au Radius Dust Ring around the F5V Star HD 157587", AJ, **152**, 128 (2016).

Milli, J., P. Hibon, V. Christiaens, É. Choquet, M. Bonnefoy, G. M. Kennedy, M. C. Wyatt, O. Absil, C. A. Gómez González, C. del Burgo, L. Matrà, J.-C. Augereau, A. Boccaletti, C. Delacroix, S. Ertel, W. R. F. Dent, P. Forsberg, T. Fusco, J. H. Girard, S. Habraken, E. Huby, M. Karlsson, A.-M. Lagrange, D. Mawet, D. Mouillet, M. Perrin, C. Pinte, L. Pueyo, C. Reyes, R. Soummer, J. Surdej, Y. Tarricq and Z. Wahhaj, "Discovery of a low-mass companion inside the debris ring surrounding the F5V star HD 206893", A&A, **597**, L2 (2017).

Mizuno, H., "Formation of the Giant Planets", Progress of Theoretical Physics **64**, 544–557 (1980).

Montes, D., J. López-Santiago, M. C. Gálvez, M. J. Fernández-Figueroa, E. De Castro and M. Cornide, "Late-type members of young stellar kinematic groups - I. Single stars", MNRAS, **328**, 45–63 (2001).

Montet, B. T., B. P. Bowler, E. L. Shkolnik, K. M. Deck, J. Wang, E. P. Horch, M. C. Liu, L. A. Hillenbrand, A. L. Kraus and D. Charbonneau, "Dynamical Masses of Young M Dwarfs: Masses and Orbital Parameters of GJ 3305 AB, the Wide Binary Companion to the Imaged Exoplanet Host 51 Eri", ApJL, **813**, L11 (2015).

Moorwood, A., J.-G. Cuby and C. Lidman, "SOFI sees first light at the NTT.", The Messenger **91**, 9–13 (1998).

Morales-Calderón, M., J. R. Stauffer, J. D. Kirkpatrick, S. Carey, C. R. Gelino, D. Barrado y Navascués, L. Rebull, P. Lowrance, M. S. Marley, D. Charbonneau, B. M. Patten, S. T. Megeath and D. Buzasi, "A Sensitive Search for Variability in Late L Dwarfs: The Quest for Weather", ApJ, **653**, 1454–1463 (2006).

Mordasini, C., "Luminosity of young Jupiters revisited. Massive cores make hot planets", A&A, **558**, A113 (2013).

Morley, C. V., J. J. Fortney, M. S. Marley, C. Visscher, D. Saumon and S. K. Leggett, "Neglected Clouds in T and Y Dwarf Atmospheres", ApJ, **756**, 172 (2012).

Morley, C. V., M. S. Marley, J. J. Fortney and R. Lupu, "Spectral Variability from the Patchy Atmospheres of T and Y Dwarfs", ApJL, **789**, L14 (2014).

Morzinski, K. M., J. R. Males, A. J. Skemer, L. M. Close, P. M. Hinz, T. J. Rodigas, A. Puglisi, S. Esposito, A. Riccardi, E. Pinna, M. Xompero, R. Briguglio, V. P. Bailey, K. B. Follette, D. Kopon, A. J. Weinberger and Y.-L. Wu, "Magellan Adaptive Optics First-light Observations of the Exoplanet β Pic b. II. 3-5 μm Direct Imaging with MagAO+Clio, and the Empirical Bolometric Luminosity of a Self-luminous Giant Planet", ApJ, **815**, 108 (2015).

Nakajima, T., S. T. Durrance, D. A. Golimowski and S. R. Kulkarni, "A coronagraphic search for brown dwarfs around nearby stars", ApJ, **428**, 797–804 (1994).

Nakajima, T., J.-I. Morino, T. Tsuji, H. Suto, M. Ishii, M. Tamura, M. Fukagawa, K. Murakawa, S. Miyama, H. Takami, N. Takato, S. Oya, S. Hayashi, T. Kudo, Y. Itoh, Y. Oasa and B. R. Oppenheimer, "A coronagraphic search for brown dwarfs and planets around nearby stars", Astronomische Nachrichten **326**, 952–957 (2005).

Nakajima, T., B. R. Oppenheimer, S. R. Kulkarni, D. A. Golimowski, K. Matthews and S. T. Durrance, "Discovery of a cool brown dwarf", Nature, **378**, 463–465 (1995).

Naud, M.-E., É. Artigau, L. Malo, L. Albert, R. Doyon, D. Lafrenière, J. Gagné, D. Saumon, C. V. Morley, F. Allard, D. Homeier, C. A. Beichman, C. R. Gelino and A. Boucher, "Discovery of a Wide Planetary-mass Companion to the Young M3 Star GU Psc", ApJ, **787**, 5 (2014).

Nelder, J. A. and R. Mead, "A simplex method for function minimization", The computer journal **7**, 4, 308–313 (1965).

Neuhäuser, R., E. W. Guenther, J. Alves, N. Huélamo, T. Ott and A. Eckart, "An infrared imaging search for low-mass companions to members of the young nearby β Pic and Tucana/Horologium associations", Astronomische Nachrichten **324**, 535–542 (2003).

Nielsen, E. L., R. J. De Rosa, J. Wang, J. Rameau, I. Song, J. R. Graham, B. Macintosh, M. Ammons, V. P. Bailey, T. S. Barman, J. Bulger, J. K. Chilcote, T. Cotten, R. Doyon, G. Duchêne, M. P. Fitzgerald, K. B. Follette, A. Z. Greenbaum, P. Hibon, L.-W. Hung, P. Ingraham, P. Kalas, Q. M. Konopacky, J. E. Larkin, J. Maire,

F. Marchis, M. S. Marley, C. Marois, S. Metchev, M. A. Millar-Blanchaer, R. Oppenheimer, D. W. Palmer, J. Patience, M. D. Perrin, L. A. Poyneer, L. Pueyo, A. Rajan, F. T. Rantakyrö, D. Savransky, A. C. Schneider, A. Sivaramakrishnan, R. Soummer, S. Thomas, J. K. Wallace, K. Ward-Duong, S. J. Wiktorowicz and S. G. Wolff, "Dynamical Mass Measurement of the Young Spectroscopic Binary V343 Normae AaAb Resolved With the Gemini Planet Imager", AJ, **152**, 175 (2016).

Nielsen, E. L., M. C. Liu, Z. Wahhaj, B. A. Biller, T. L. Hayward, L. M. Close, J. R. Males, A. J. Skemer, M. Chun, C. Ftaclas, S. H. P. Alencar, P. Artymowicz, A. Boss, F. Clarke, E. de Gouveia Dal Pino, J. Gregorio-Hetem, M. Hartung, S. Ida, M. Kuchner, D. N. C. Lin, I. N. Reid, E. L. Shkolnik, M. Tecza, N. Thatte and D. W. Toomey, "The Gemini NICI Planet-Finding Campaign: The Frequency of Giant Planets around Young B and A Stars", ApJ, **776**, 4 (2013).

Nielsen, E. L., M. C. Liu, Z. Wahhaj, B. A. Biller, T. L. Hayward, J. R. Males, L. M. Close, K. M. Morzinski, A. J. Skemer, M. J. Kuchner, T. J. Rodigas, P. M. Hinz, M. Chun, C. Ftaclas and D. W. Toomey, "The Gemini NICI Planet-Finding Campaign: The Orbit of the Young Exoplanet β Pictoris b", ApJ, **794**, 158 (2014).

Öberg, K. I., R. Murray-Clay and E. A. Bergin, "The Effects of Snowlines on C/O in Planetary Atmospheres", ApJL, **743**, L16 (2011).

Oppenheimer, B. R., C. Baranec, C. Beichman, D. Brenner, R. Burruss, E. Cady, J. R. Crepp, R. Dekany, R. Fergus, D. Hale, L. Hillenbrand, S. Hinkley, D. W. Hogg, D. King, E. R. Ligon, T. Lockhart, R. Nilsson, I. R. Parry, L. Pueyo, E. Rice, J. E. Roberts, L. C. Roberts, Jr., M. Shao, A. Sivaramakrishnan, R. Soummer, T. Truong, G. Vasisht, A. Veicht, F. Vescelus, J. K. Wallace, C. Zhai and N. Zimmerman, "Reconnaissance of the HR 8799 Exosolar System. I. Near-infrared Spectroscopy", ApJ, **768**, 24 (2013).

Oppenheimer, B. R., D. A. Golimowski, S. R. Kulkarni, K. Matthews, T. Nakajima, M. Creech-Eakman and S. T. Durrance, "A Coronagraphic Survey for Companions of Stars within 8 Parsecs", AJ, **121**, 2189–2211 (2001).

Oppenheimer, B. R. and S. Hinkley, "High-Contrast Observations in Optical and Infrared Astronomy", ARA&A, **47**, 253–289 (2009).

Oppenheimer, B. R., S. R. Kulkarni, K. Matthews and T. Nakajima, "Infrared Spectrum of the Cool Brown Dwarf Gl 229B", Science **270**, 1478–1479 (1995).

Oppenheimer, B. R., S. R. Kulkarni and J. R. Stauffer, "Brown Dwarfs", Protostars and Planets IV p. 1313 (2000).

Patience, J., R. R. King, R. J. de Rosa and C. Marois, "The highest resolution near infrared spectrum of the imaged planetary mass companion 2M1207 b", A&A, **517**, A76 (2010).

Patience, J., R. R. King, R. J. De Rosa, A. Vigan, S. Witte, E. Rice, C. Helling and P. Hauschildt, "Spectroscopy across the brown dwarf/planetary mass boundary. I. Near-infrared JHK spectra", A&A, **540**, A85 (2012).

Perrin, M. D., J. Maire, P. Ingraham, D. Savransky, M. Millar-Blanchaer, S. G. Wolff, J.-B. Ruffio, J. J. Wang, Z. H. Draper, N. Sadakuni, C. Marois, A. Rajan, M. P. Fitzgerald, B. Macintosh, J. R. Graham, R. Doyon, J. E. Larkin, J. K. Chilcote, S. J. Goodsell, D. W. Palmer, K. Labrie, M. Beaulieu, R. J. De Rosa, A. Z. Greenbaum, M. Hartung, P. Hibon, Q. Konopacky, D. Lafreniere, J.-F. Lavigne, F. Marchis, J. Patience, L. Pueyo, F. T. Rantakyrö, R. Soummer, A. Sivaramakrishnan, S. Thomas, K. Ward-Duong and S. Wiktorowicz, "Gemini Planet Imager observational calibrations I: Overview of the GPI data reduction pipeline", in "Ground-based and Airborne Instrumentation for Astronomy V", vol. 9147 of *Proc. SPIE,* , p. 91473J (2014).

Pickles, A. J., "A Stellar Spectral Flux Library: 1150-25000 Å", PASP, **110**, 863–878 (1998).

Pollack, J. B., O. Hubickyj, P. Bodenheimer, J. J. Lissauer, M. Podolak and Y. Greenzweig, "Formation of the Giant Planets by Concurrent Accretion of Solids and Gas", Icarus, **124**, 62–85 (1996).

Pueyo, L., "Detection and Characterization of Exoplanets using Projections on Karhunen Loeve Eigenimages: Forward Modeling", ApJ, **824**, 117 (2016).

Pueyo, L., R. Soummer, J. Hoffmann, R. Oppenheimer, J. R. Graham, N. Zimmerman, C. Zhai, J. K. Wallace, F. Vescelus, A. Veicht, G. Vasisht, T. Truong, A. Sivaramakrishnan, M. Shao, L. C. Roberts, Jr., J. E. Roberts, E. Rice, I. R. Parry, R. Nilsson, T. Lockhart, E. R. Ligon, D. King, S. Hinkley, L. Hillenbrand, D. Hale, R. Dekany, J. R. Crepp, E. Cady, R. Burruss, D. Brenner, C. Beichman and C. Baranec, "Reconnaissance of the HR 8799 Exosolar System. II. Astrometry and Orbital Motion", ApJ, **803**, 31 (2015).

Puget, P., E. Stadler, R. Doyon, P. Gigan, S. Thibault, G. Luppino, G. Barrick, T. Benedict, T. Forveille, W. Rambold, J. Thomas, T. Vermeulen, J. Ward, J.-L. Beuzit, P. Feautrier, Y. Magnard, G. Mella, O. Preis, P. Vallee, S.-y. Wang, C.-J. Lin, D. N. Hall and K. W. Hodapp, "WIRCam: the infrared wide-field camera for the Canada-France-Hawaii Telescope", in "Ground-based Instrumentation for Astronomy", edited by A. F. M. Moorwood and M. Iye, vol. 5492 of *Society of Photo-Optical Instrumentation Engineers (SPIE) Conference Series*, pp. 978–987 (2004).

Radigan, J., R. Jayawardhana, D. Lafrenière, É. Artigau, M. Marley and D. Saumon, "Large-amplitude Variations of an L/T Transition Brown Dwarf: Multi-wavelength Observations of Patchy, High-contrast Cloud Features", ApJ, **750**, 105 (2012a).

Radigan, J., R. Jayawardhana, D. Lafrenière, É. Artigau, M. Marley and D. Saumon, "Large-amplitude Variations of an L/T Transition Brown Dwarf: Multi-wavelength Observations of Patchy, High-contrast Cloud Features", ApJ, **750**, 105 (2012b).

Radigan, J., D. Lafrenière, R. Jayawardhana and E. Artigau, "Strong Brightness Variations Signal Cloudy-to-Clear Transition of Brown Dwarfs", ArXiv e-prints: 1404.3247 (2014a).

Radigan, J., D. Lafrenière, R. Jayawardhana and E. Artigau, "Strong Brightness Variations Signal Cloudy-to-clear Transition of Brown Dwarfs", ApJ, **793**, 75 (2014b).

Rafikov, R. R., "Convective Cooling and Fragmentation of Gravitationally Unstable Disks", ApJ, **662**, 642–650 (2007).

Rafikov, R. R., "Constraint on the Giant Planet Production by Core Accretion", ApJ, **727**, 86 (2011).

Rajan, A., J. Patience, P. A. Wilson, J. Bulger, R. J. De Rosa, K. Ward-Duong, C. Morley, F. Pont and R. Windhorst, "The brown dwarf atmosphere monitoring (BAM) project - II. Multi-epoch monitoring of extremely cool brown dwarfs", MNRAS, **448**, 3775–3783 (2015).

Rameau, J., G. Chauvin, A.-M. Lagrange, A. Boccaletti, S. P. Quanz, M. Bonnefoy, J. H. Girard, P. Delorme, S. Desidera, H. Klahr, C. Mordasini, C. Dumas and M. Bonavita, "Discovery of a Probable 4-5 Jupiter-mass Exoplanet to HD 95086 by Direct Imaging", ApJL, **772**, L15 (2013a).

Rameau, J., G. Chauvin, A.-M. Lagrange, H. Klahr, M. Bonnefoy, C. Mordasini, M. Bonavita, S. Desidera, C. Dumas and J. H. Girard, "A survey of young, nearby, and dusty stars conducted to understand the formation of wide-orbit giant planets. VLT/NaCo adaptive optics thermal and angular differential imaging", A&A, **553**, A60 (2013b).

Rayner, J. T., M. C. Cushing and W. D. Vacca, "The Infrared Telescope Facility (IRTF) Spectral Library: Cool Stars", ApJS, **185**, 289–432 (2009).

Rebull, L. M., K. R. Stapelfeldt, M. W. Werner, V. G. Mannings, C. Chen, J. R. Stauffer, P. S. Smith, I. Song, D. Hines and F. J. Low, "Spitzer MIPS Observations of Stars in the β Pictoris Moving Group", ApJ, **681**, 1484–1504 (2008).

Rice, E. L., R. Oppenheimer, N. Zimmerman, L. C. Roberts and S. Hinkley, "A New Method for Characterizing Very Low-Mass Companions with Low-Resolution Near-Infrared Spectroscopy", PASP, **127**, 479 (2015).

Riviere-Marichalar, P., D. Barrado, B. Montesinos, G. Duchêne, H. Bouy, C. Pinte, F. Menard, J. Donaldson, C. Eiroa, A. V. Krivov, I. Kamp, I. Mendigutía, W. R. F. Dent and J. Lillo-Box, "Gas and dust in the beta Pictoris moving group as seen by the Herschel Space Observatory", A&A, **565**, A68 (2014).

Robert, J., J. Gagné, É. Artigau, D. Lafrenière, D. Nadeau, R. Doyon, L. Malo, L. Albert, C. Simard, D. C. Bardalez Gagliuffi and A. J. Burgasser, "A Brown Dwarf Census from the SIMP Survey", ApJ, **830**, 144 (2016).

Robinson, T. D. and M. S. Marley, "Temperature Fluctuations as a Source of Brown Dwarf Variability", ApJ, **785**, 158 (2014).

Rockenfeller, B., C. A. L. Bailer-Jones and R. Mundt, "Variability and periodicity of field M dwarfs revealed by multichannel monitoring", A&A, **448**, 1111–1124 (2006).

Route, M. and A. Wolszczan, "The Arecibo Detection of the Coolest Radio-flaring Brown Dwarf", ApJL, **747**, L22 (2012).

Rufener, F. and B. Nicolet, "A new determination of the Geneva photometric passbands and their absolute calibration", A&A, **206**, 357–374 (1988).

Sarazin, M. and F. Roddier, "The ESO differential image motion monitor", A&A, **227**, 294–300 (1990).

Sartoretti, P., R. A. Brown, D. W. Latham and G. Torres, "A search for substellar companions around nine weak-lined T-Tauri stars with the Planetary Camera 2 of the Hubble Space Telescope", A&A, **334**, 592–598 (1998).

Saumon, D. and M. S. Marley, "The Evolution of L and T Dwarfs in Color-Magnitude Diagrams", ApJ, **689**, 1327–1344 (2008).

Saumon, D., M. S. Marley, M. Abel, L. Frommhold and R. S. Freedman, "New H_2 Collision-induced Absorption and NH_3 Opacity and the Spectra of the Coolest Brown Dwarfs", ApJ, **750**, 74 (2012).

Schneider, G., K. Wood, M. D. Silverstone, D. C. Hines, D. W. Koerner, B. A. Whitney, J. E. Bjorkman and P. J. Lowrance, "NICMOS Coronagraphic Observations of the GM Aurigae Circumstellar Disk", AJ, **125**, 1467–1479 (2003).

Schroeder, D. J., D. A. Golimowski, R. A. Brukardt, C. J. Burrows, J. J. Caldwell, W. G. Fastie, H. C. Ford, B. Hesman, I. Kletskin, J. E. Krist, P. Royle and R. A. Zubrowski, "A Search for Faint Companions to Nearby Stars Using the Wide Field Planetary Camera 2", AJ, **119**, 906–922 (2000).

Service, M., J. R. Lu, R. Campbell, B. N. Sitarski, A. M. Ghez and J. Anderson, "A New Distortion Solution for NIRC2 on the Keck II Telescope", PASP, **128**, 9, 095004 (2016).

Showman, A. P. and Y. Kaspi, "Atmospheric Dynamics of Brown Dwarfs and Directly Imaged Giant Planets", ApJ, **776**, 85 (2013).

Sing, D. K., F. Pont, S. Aigrain, D. Charbonneau, J.-M. Désert, N. Gibson, R. Gilliland, W. Hayek, G. Henry, H. Knutson, A. Lecavelier Des Etangs, T. Mazeh and A. Shporer, "Hubble Space Telescope transmission spectroscopy of the exoplanet HD 189733b: high-altitude atmospheric haze in the optical and near-ultraviolet with STIS", MNRAS, **416**, 1443–1455 (2011).

Sing, D. K., A. Vidal-Madjar, J.-M. Désert, A. Lecavelier des Etangs and G. Ballester, "Hubble Space Telescope STIS Optical Transit Transmission Spectra of the Hot Jupiter HD 209458b", ApJ, **686**, 658–666 (2008).

Sirianni, M., M. J. Jee, N. Benítez, J. P. Blakeslee, A. R. Martel, G. Meurer, M. Clampin, G. De Marchi, H. C. Ford, R. Gilliland, G. F. Hartig, G. D. Illingworth, J. Mack and W. J. McCann, "The Photometric Performance and Calibration of the Hubble Space Telescope Advanced Camera for Surveys", PASP, **117**, 1049–1112 (2005).

Sivaramakrishnan, A., C. D. Koresko, R. B. Makidon, T. Berkefeld and M. J. Kuchner, "Ground-based Coronagraphy with High-order Adaptive Optics", ApJ, **552**, 397–408 (2001).

Sivaramakrishnan, A. and B. R. Oppenheimer, "Astrometry and Photometry with Coronagraphs", ApJ, **647**, 620–629 (2006).

Skemer, A. J., P. Hinz, M. Montoya, M. F. Skrutskie, J. Leisenring, O. Durney, C. E. Woodward, J. Wilson, M. Nelson, V. Bailey, D. Defrere and J. Stone, "First light with ALES: A 2-5 micron adaptive optics Integral Field Spectrograph for the LBT", in "Techniques and Instrumentation for Detection of Exoplanets VII", vol. 9605 of *Proc. SPIE,* , p. 96051D (2015).

Skemer, A. J., P. M. Hinz, S. Esposito, A. Burrows, J. Leisenring, M. Skrutskie, S. Desidera, D. Mesa, C. Arcidiacono, F. Mannucci, T. J. Rodigas, L. Close, D. McCarthy, C. Kulesa, G. Agapito, D. Apai, J. Argomedo, V. Bailey, K. Boutsia, R. Briguglio, G. Brusa, L. Busoni, R. Claudi, J. Eisner, L. Fini, K. B. Follette, P. Garnavich, R. Gratton, J. C. Guerra, J. M. Hill, W. F. Hoffmann, T. Jones, M. Krejny, J. Males, E. Masciadri, M. R. Meyer, D. L. Miller, K. Morzinski, M. Nelson, E. Pinna, A. Puglisi, S. P. Quanz, F. Quiros-Pacheco, A. Riccardi, P. Stefanini, V. Vaitheeswaran, J. C. Wilson and M. Xompero, "First Light LBT AO Images of HR 8799 bcde at 1.6 and 3.3 μm: New Discrepancies between Young Planets and Old Brown Dwarfs", ApJ, **753**, 14 (2012).

Skemer, A. J., M. S. Marley, P. M. Hinz, K. M. Morzinski, M. F. Skrutskie, J. M. Leisenring, L. M. Close, D. Saumon, V. P. Bailey, R. Briguglio, D. Defrere, S. Esposito, K. B. Follette, J. M. Hill, J. R. Males, A. Puglisi, T. J. Rodigas and M. Xompero, "Directly Imaged L-T Transition Exoplanets in the Mid-infrared", ApJ, **792**, 17 (2014).

Skemer, A. J., C. V. Morley, N. T. Zimmerman, M. F. Skrutskie, J. Leisenring, E. Buenzli, M. Bonnefoy, V. Bailey, P. Hinz, D. Defrére, S. Esposito, D. Apai, B. Biller, W. Brandner, L. Close, J. R. Crepp, R. J. De Rosa, S. Desidera, J. Eisner, J. Fortney, R. Freedman, T. Henning, K.-H. Hofmann, T. Kopytova, R. Lupu, A.-L. Maire, J. R. Males, M. Marley, K. Morzinski, A. Oza, J. Patience, A. Rajan, G. Rieke, D. Schertl, J. Schlieder, J. Stone, K. Su, A. Vaz, C. Visscher, K. Ward-Duong, G. Weigelt and C. E. Woodward, "The LEECH Exoplanet Imaging Survey: Characterization of the Coldest Directly Imaged Exoplanet, GJ 504 b, and Evidence for Superstellar Metallicity", ApJ, **817**, 166 (2016).

Skrutskie, M. F., R. M. Cutri, R. Stiening, M. D. Weinberg, S. Schneider, J. M. Carpenter, C. Beichman, R. Capps, T. Chester, J. Elias, J. Huchra, J. Liebert, C. Lonsdale, D. G. Monet, S. Price, P. Seitzer, T. Jarrett, J. D. Kirkpatrick, J. E. Gizis, E. Howard, T. Evans, J. Fowler, L. Fullmer, R. Hurt, R. Light, E. L. Kopan, K. A. Marsh, H. L. McCallon, R. Tam, S. Van Dyk and S. Wheelock, "The Two Micron All Sky Survey (2MASS)", AJ, **131**, 1163–1183 (2006a).

Skrutskie, M. F., R. M. Cutri, R. Stiening, M. D. Weinberg, S. Schneider, J. M. Carpenter, C. Beichman, R. Capps, T. Chester, J. Elias, J. Huchra, J. Liebert, C. Lonsdale, D. G. Monet, S. Price, P. Seitzer, T. Jarrett, J. D. Kirkpatrick, J. E. Gizis, E. Howard, T. Evans, J. Fowler, L. Fullmer, R. Hurt, R. Light, E. L. Kopan, K. A. Marsh, H. L. McCallon, R. Tam, S. Van Dyk and S. Wheelock, "The Two Micron All Sky Survey (2MASS)", AJ, **131**, 1163–1183 (2006b).

Skrutskie, M. F., W. J. Forrest and M. Shure, "An infrared search for low-mass companions of stars near the sun", AJ, **98**, 1409–1417 (1989).

Smart, R. L., C. G. Tinney, B. Bucciarelli, F. Marocco, U. Abbas, A. Andrei, G. Bernardi, B. Burningham, C. Cardoso, E. Costa, M. T. Crosta, M. Daprá, A. Day-Jones, B. Goldman, H. R. A. Jones, M. G. Lattanzi, S. K. Leggett, P. Lucas, R. Mendez, J. L. Penna, D. Pinfield, L. Smith, A. Sozzetti and A. Vecchiato, "NPARSEC: NTT Parallaxes of Southern Extremely Cool objects. Goals, targets, procedures and first results", MNRAS, **433**, 2054–2063 (2013).

Snellen, I., B. Brandl, R. de Kok, M. Brogi, J. Birkby and H. Schwarz, "The fast spin-rotation of a young extrasolar planet", ArXiv e-prints (2014).

Soummer, R., J. Brendan Hagan, L. Pueyo, A. Thormann, A. Rajan and C. Marois, "Orbital Motion of HR 8799 b, c, d Using Hubble Space Telescope Data from 1998: Constraints on Inclination, Eccentricity, and Stability", ApJ, **741**, 55 (2011a).

Soummer, R., A. Ferrari, C. Aime and L. Jolissaint, "Speckle Noise and Dynamic Range in Coronagraphic Images", ApJ, **669**, 642–656 (2007).

Soummer, R., M. D. Perrin, L. Pueyo, É. Choquet, C. Chen, D. A. Golimowski, J. Brendan Hagan, T. Mittal, M. Moerchen, M. N'Diaye, A. Rajan, S. Wolff, J. Debes, D. C. Hines and G. Schneider, "Five Debris Disks Newly Revealed in Scattered Light from the Hubble Space Telescope NICMOS Archive", ApJL, **786**, L23 (2014).

Soummer, R., L. Pueyo and J. Larkin, "Detection and Characterization of Exoplanets and Disks Using Projections on Karhunen-Loève Eigenimages", ApJL, **755**, L28 (2012).

Soummer, R., A. Sivaramakrishnan, L. Pueyo, B. Macintosh and B. R. Oppenheimer, "Apodized Pupil Lyot Coronagraphs for Arbitrary Apertures. III. Quasi-achromatic Solutions", ApJ, **729**, 144 (2011b).

Spiegel, D. S. and A. Burrows, "Spectral and Photometric Diagnostics of Giant Planet Formation Scenarios", ApJ, **745**, 174 (2012).

Stephens, D. C. and S. K. Leggett, "JHK Magnitudes for L and T Dwarfs and Infrared Photometric Systems", PASP, **116**, 9–21 (2004).

Stevenson, D. J., "Planetary origin, evolution, and structure", Tech. rep. (1991).

Strauss, M. A., X. Fan, J. E. Gunn, S. K. Leggett, T. R. Geballe, J. R. Pier, R. H. Lupton, G. R. Knapp, J. Annis, J. Brinkmann, J. H. Crocker, I. Csabai, M. Fukugita, D. A. Golimowski, F. H. Harris, G. S. Hennessy, R. B. Hindsley, Ž. Ivezić , S. Kent, D. Q. Lamb, J. A. Munn, H. J. Newberg, R. Rechenmacher, D. P. Schneider, J. A. Smith, C. Stoughton, D. L. Tucker, P. Waddell and D. G. York, "The Discovery of a Field Methane Dwarf from Sloan Digital Sky Survey Commissioning Data", ApJL, **522**, L61–L64 (1999).

Tanner, A., C. Beichman, R. Akeson, A. Ghez, K. N. Grankin, W. Herbst, L. Hillenbrand, M. Huerta, Q. Konopacky, S. Metchev, S. Mohanty, L. Prato and M. Simon, "SIM PlanetQuest Key Project Precursor Observations to Detect Gas Giant Planets around Young Stars", PASP, **119**, 747–767 (2007).

Tarter, J. C., *The interaction of gas and galaxies within galaxy clusters*, Ph.D. thesis, California Univ., Berkeley. (1975).

Tinney, C. G. and A. J. Tolley, "Searching for weather in brown dwarfs", MNRAS, **304**, 119–126 (1999).

Todorov, K. O., M. R. Line, J. E. Pineda, M. R. Meyer, S. P. Quanz, S. Hinkley and J. J. Fortney, "The Water Abundance of the Directly Imaged Substellar Companion {\kappa} And b Retrieved from a Near Infrared Spectrum", ArXiv e-prints (2015).

Tokunaga, A. T., D. A. Simons and W. D. Vacca, "The Mauna Kea Observatories Near-Infrared Filter Set. II. Specifications for a New JHKL'M' Filter Set for Infrared Astronomy", PASP, **114**, 180–186 (2002).

Tokunaga, A. T. and W. D. Vacca, "The Mauna Kea Observatories Near-Infrared Filter Set. III. Isophotal Wavelengths and Absolute Calibration", PASP, **117**, 421–426 (2005).

Toomre, A., "On the gravitational stability of a disk of stars", ApJ, **139**, 1217–1238 (1964).

Tremblin, P., D. S. Amundsen, G. Chabrier, I. Baraffe, B. Drummond, S. Hinkley, P. Mourier and O. Venot, "Cloudless Atmospheres for L/T Dwarfs and Extrasolar Giant Planets", ApJL, **817**, L19 (2016).

Tsuji, T., "Dust in the Photospheric Environment: Unified Cloudy Models of M, L, and T Dwarfs", ApJ, **575**, 264–290 (2002).

Tsvetanov, Z. I., D. A. Golimowski, W. Zheng, T. R. Geballe, S. K. Leggett, H. C. Ford, A. F. Davidsen, A. Uomoto, X. Fan, G. R. Knapp, M. A. Strauss, J. Brinkmann, D. Q. Lamb, H. J. Newberg, R. Rechenmacher, D. P. Schneider, D. G. York, R. H. Lupton, J. R. Pier, J. Annis, I. Csabai, R. B. Hindsley, Ž. Ivesić, J. A. Munn, A. R. Thakar and P. Waddell, "The Discovery of a Second Field Methane Brown Dwarf from Sloan Digital Sky Survey Commissioning Data", ApJL, **531**, L61–L65 (2000).

van Dam, M. A., D. Le Mignant and B. A. Macintosh, "Performance of the Keck Observatory Adaptive-Optics System", ApOpt, **43**, 5458–5467 (2004).

van Leeuwen, F., "Validation of the new Hipparcos reduction", A&A, **474**, 653–664 (2007).

Vigan, A., M. Bonavita, B. Biller, D. Forgan, K. Rice, G. Chauvin, S. Desidera, J.-C. Meunier, P. Delorme, J. E. Schlieder, M. Bonnefoy, J. Carson, E. Covino, J. Hagelberg, T. Henning, M. Janson, A.-M. Lagrange, S. P. Quanz, A. Zurlo, J.-L. Beuzit, A. Boccaletti, E. Buenzli, M. Feldt, J. H. V. Girard, R. Gratton, M. Kasper, H. Le Coroller, D. Mesa, S. Messina, M. Meyer, G. Montagnier, C. Mordasini, D. Mouillet, C. Moutou, M. Reggiani, D. Segransan and C. Thalmann, "The VLT/NaCo large program to probe the occurrence of exoplanets and brown dwarfs

at wide orbits. IV. Gravitational instability rarely forms wide, giant planets", ArXiv e-prints (2017).

Vigan, A., J. Patience, C. Marois, M. Bonavita, R. J. De Rosa, B. Macintosh, I. Song, R. Doyon, B. Zuckerman, D. Lafrenière and T. Barman, "The International Deep Planet Survey. I. The frequency of wide-orbit massive planets around A-stars", A&A, **544**, A9 (2012).

Visscher, C., K. Lodders and B. Fegley, Jr., "Atmospheric Chemistry in Giant Planets, Brown Dwarfs, and Low-Mass Dwarf Stars. II. Sulfur and Phosphorus", ApJ, **648**, 1181–1195 (2006).

Vrba, F. J., A. A. Henden, C. B. Luginbuhl, H. H. Guetter, J. A. Munn, B. Canzian, A. J. Burgasser, J. D. Kirkpatrick, X. Fan, T. R. Geballe, D. A. Golimowski, G. R. Knapp, S. K. Leggett, D. P. Schneider and J. Brinkmann, "Preliminary Parallaxes of 40 L and T Dwarfs from the US Naval Observatory Infrared Astrometry Program", AJ, **127**, 2948–2968 (2004).

Wagner, K., D. Apai, M. Kasper, K. Kratter, M. McClure, M. Robberto and J.-L. Beuzit, "Direct imaging discovery of a Jovian exoplanet within a triple-star system", Science **353**, 673–678 (2016).

Wahhaj, Z., M. C. Liu, E. L. Nielsen, B. A. Biller, T. L. Hayward, L. M. Close, J. R. Males, A. Skemer, C. Ftaclas, M. Chun, N. Thatte, M. Tecza, E. L. Shkolnik, M. Kuchner, I. N. Reid, E. M. de Gouveia Dal Pino, S. H. P. Alencar, J. Gregorio-Hetem, A. Boss, D. N. C. Lin and D. W. Toomey, "The Gemini Planet-finding Campaign: The Frequency Of Giant Planets around Debris Disk Stars", ApJ, **773**, 179 (2013).

Wahhaj, Z., J. Milli, G. Kennedy, S. Ertel, L. Matrà, A. Boccaletti, C. del Burgo, M. Wyatt, C. Pinte, A.-M. Lagrange, O. Absil, E. Choquet, C. A. Gómez González, H. Kobayashi, D. Mawet, D. Mouillet, L. Pueyo, W. R. F. Dent, J.-C. Augereau and J. Girard, "The SHARDDS survey: First resolved image of the HD 114082 debris disk in the Lower Centaurus Crux with SPHERE", A&A, **596**, L4 (2016).

Walter, M. and G. Weigelt, "Roll deconvolution of space telescope data", Advances in Space Research **5**, 169–171 (1985).

Wang, J. J., A. Rajan, J. R. Graham, D. Savransky, P. J. Ingraham, K. Ward-Duong, J. Patience, R. J. De Rosa, J. Bulger, A. Sivaramakrishnan, M. D. Perrin, S. J. Thomas, N. Sadakuni, A. Z. Greenbaum, L. Pueyo, C. Marois, B. R. Oppenheimer, P. Kalas, A. Cardwell, S. Goodsell, P. Hibon and F. T. Rantakyrö, "Gemini planet imager observational calibrations VIII: characterization and role of satellite spots", in "Ground-based and Airborne Instrumentation for Astronomy V", vol. 9147 of *Proc. SPIE,* , p. 914755 (2014).

Wang, J. J., J.-B. Ruffio, R. J. De Rosa, J. Aguilar, S. G. Wolff and L. Pueyo, "pyKLIP: PSF Subtraction for Exoplanets and Disks", Astrophysics Source Code Library (2015).

West, A. A., S. L. Hawley, J. J. Bochanski, K. R. Covey, I. N. Reid, S. Dhital, E. J. Hilton and M. Masuda, "Constraining the Age-Activity Relation for Cool Stars: The Sloan Digital Sky Survey Data Release 5 Low-Mass Star Spectroscopic Sample", AJ, **135**, 785–795 (2008).

Williams, P. K. G., E. Berger and B. A. Zauderer, "Quasi-quiescent Radio Emission from the First Radio-emitting T Dwarf", ApJL, **767**, L30 (2013).

Wilson, P. A., A. Rajan and J. Patience, "The brown dwarf atmosphere monitoring (BAM) project. I. The largest near-IR monitoring survey of L and T dwarfs", A&A, **566**, A111 (2014).

Wolff, S. G., M. D. Perrin, J. Maire, P. J. Ingraham, F. T. Rantakyrö and P. Hibon, "Gemini planet imager observational calibrations IV: wavelength calibration and flexure correction for the integral field spectograph", in "Ground-based and Airborne Instrumentation for Astronomy V", vol. 9147 of *Proc. SPIE,* , p. 91477H (2014).

Wright, E. L., P. R. M. Eisenhardt, A. K. Mainzer, M. E. Ressler, R. M. Cutri, T. Jarrett, J. D. Kirkpatrick, D. Padgett, R. S. McMillan, M. Skrutskie, S. A. Stanford, M. Cohen, R. G. Walker, J. C. Mather, D. Leisawitz, T. N. Gautier, III, I. McLean, D. Benford, C. J. Lonsdale, A. Blain, B. Mendez, W. R. Irace, V. Duval, F. Liu, D. Royer, I. Heinrichsen, J. Howard, M. Shannon, M. Kendall, A. L. Walsh, M. Larsen, J. G. Cardon, S. Schick, M. Schwalm, M. Abid, B. Fabinsky, L. Naes and C.-W. Tsai, "The Wide-field Infrared Survey Explorer (WISE): Mission Description and Initial On-orbit Performance", AJ, **140**, 1868–1881 (2010a).

Wright, E. L., P. R. M. Eisenhardt, A. K. Mainzer, M. E. Ressler, R. M. Cutri, T. Jarrett, J. D. Kirkpatrick, D. Padgett, R. S. McMillan, M. Skrutskie, S. A. Stanford, M. Cohen, R. G. Walker, J. C. Mather, D. Leisawitz, T. N. Gautier, III, I. McLean, D. Benford, C. J. Lonsdale, A. Blain, B. Mendez, W. R. Irace, V. Duval, F. Liu, D. Royer, I. Heinrichsen, J. Howard, M. Shannon, M. Kendall, A. L. Walsh, M. Larsen, J. G. Cardon, S. Schick, M. Schwalm, M. Abid, B. Fabinsky, L. Naes and C.-W. Tsai, "The Wide-field Infrared Survey Explorer (WISE): Mission Description and Initial On-orbit Performance", AJ, **140**, 1868–1881 (2010b).

Wu, Y.-L., L. M. Close, J. R. Males, T. S. Barman, K. M. Morzinski, K. B. Follette, V. P. Bailey, T. J. Rodigas, P. Hinz, A. Puglisi, M. Xompero and R. Briguglio, "New Extinction and Mass Estimates of the Low-mass Companion 1RXS 1609 B with the Magellan AO System: Evidence of an Inclined Dust Disk", ApJL, **807**, L13 (2015).

Yamamoto, K., T. Matsuo, H. Shibai, Y. Itoh, M. Konishi, J. Sudo, R. Tanii, M. Fukagawa, T. Sumi, T. Kudo, J. Hashimoto, N. Kusakabe, L. Abe, W. Brandner, T. D. Brandt, J. Carson, T. Currie, S. E. Egner, M. Feldt, M. Goto, C. Grady, O. Guyon, Y. Hayano, M. Hayashi, S. Hayashi, T. Henning, K. Hodapp, M. Ishii, M. Iye, M. Janson, R. Kandori, G. R. Knapp, M. Kuzuhara, J. Kwon, M. McElwain, S. Miyama, J.-I. Morino, A. Moro-Martin, J. Nishikawa, T. Nishimura, T.-S. Pyo, E. Serabyn, H. Suto, R. Suzuki, M. Takami, N. Takato, H. Terada, C. Thalmann, D. Tomono, E. L. Turner, J. Wisniewski, M. Watanabe, T. Yamada, H. Takami and T. Usuda, "Direct Imaging Search for Extrasolar Planets in the Pleiades", PASJ, **65**, 90 (2013).

Yang, H., D. Apai, M. S. Marley, T. Karalidi, D. Flateau, A. P. Showman, S. Metchev, E. Buenzli, J. Radigan, É. Artigau, P. J. Lowrance and A. J. Burgasser, "Extrasolar Storms: Pressure-dependent Changes in Light-curve Phase in Brown Dwarfs from Simultaneous HST and Spitzer Observations", ApJ, **826**, 8 (2016).

Yang, H., D. Apai, M. S. Marley, D. Saumon, C. V. Morley, E. Buenzli, E. Artigau, J. Radigan, S. Metchev, A. J. Burgasser, S. Mohanty, P. L. Lowrance, A. P. Showman, T. Karalidi, D. Flateau and A. N. Heinze, "HST Rotational Spectral Mapping of Two L-Type Brown Dwarfs: Variability In and Out of Water Bands Indicates High-Altitude Haze Layers", ArXiv e-prints (2014).

Yelda, S., J. R. Lu, A. M. Ghez, W. Clarkson, J. Anderson, T. Do and K. Matthews, "Improving Galactic Center Astrometry by Reducing the Effects of Geometric Distortion", ApJ, **725**, 331–352 (2010).

York, D. G., J. Adelman, J. E. Anderson, Jr., S. F. Anderson, J. Annis, N. A. Bahcall, J. A. Bakken, R. Barkhouser, S. Bastian, E. Berman, W. N. Boroski, S. Bracker, C. Briegel, J. W. Briggs, J. Brinkmann, R. Brunner, S. Burles, L. Carey, M. A. Carr, F. J. Castander, B. Chen, P. L. Colestock, A. J. Connolly, J. H. Crocker, I. Csabai, P. C. Czarapata, J. E. Davis, M. Doi, T. Dombeck, D. Eisenstein, N. Ellman, B. R. Elms, M. L. Evans, X. Fan, G. R. Federwitz, L. Fiscelli, S. Friedman, J. A. Frieman, M. Fukugita, B. Gillespie, J. E. Gunn, V. K. Gurbani, E. de Haas, M. Haldeman, F. H. Harris, J. Hayes, T. M. Heckman, G. S. Hennessy, R. B. Hindsley, S. Holm, D. J. Holmgren, C.-h. Huang, C. Hull, D. Husby, S.-I. Ichikawa, T. Ichikawa, Ž. Ivezić, S. Kent, R. S. J. Kim, E. Kinney, M. Klaene, A. N. Kleinman, S. Kleinman, G. R. Knapp, J. Korienek, R. G. Kron, P. Z. Kunszt, D. Q. Lamb, B. Lee, R. F. Leger, S. Limmongkol, C. Lindenmeyer, D. C. Long, C. Loomis, J. Loveday, R. Lucinio, R. H. Lupton, B. MacKinnon, E. J. Mannery, P. M. Mantsch, B. Margon, P. McGehee, T. A. McKay, A. Meiksin, A. Merelli, D. G. Monet, J. A. Munn, V. K. Narayanan, T. Nash, E. Neilsen, R. Neswold, H. J. Newberg, R. C. Nichol, T. Nicinski, M. Nonino, N. Okada, S. Okamura, J. P. Ostriker, R. Owen, A. G. Pauls, J. Peoples, R. L. Peterson, D. Petravick,

J. R. Pier, A. Pope, R. Pordes, A. Prosapio, R. Rechenmacher, T. R. Quinn, G. T. Richards, M. W. Richmond, C. H. Rivetta, C. M. Rockosi, K. Ruthmansdorfer, D. Sandford, D. J. Schlegel, D. P. Schneider, M. Sekiguchi, G. Sergey, K. Shimasaku, W. A. Siegmund, S. Smee, J. A. Smith, S. Snedden, R. Stone, C. Stoughton, M. A. Strauss, C. Stubbs, M. SubbaRao, A. S. Szalay, I. Szapudi, G. P. Szokoly, A. R. Thakar, C. Tremonti, D. L. Tucker, A. Uomoto, D. Vanden Berk, M. S. Vogeley, P. Waddell, S.-i. Wang, M. Watanabe, D. H. Weinberg, B. Yanny, N. Yasuda and SDSS Collaboration, "The Sloan Digital Sky Survey: Technical Summary", AJ, **120**, 1579–1587 (2000).

Youdin, A. N., "From Grains to Planetesimals", in "EAS Publications Series", edited by T. Montmerle, D. Ehrenreich and A.-M. Lagrange, vol. 41 of *EAS Publications Series*, pp. 187–207 (2010).

Youdin, A. N. and J. Goodman, "Streaming Instabilities in Protoplanetary Disks", ApJ, **620**, 459–469 (2005).

Yurchenko, S. N., R. J. Barber and J. Tennyson, "A variationally computed line list for hot NH_3", MNRAS, **413**, 1828–1834 (2011).

Yurchenko, S. N. and J. Tennyson, "ExoMol line lists - IV. The rotation-vibration spectrum of methane up to 1500 K", MNRAS, **440**, 1649–1661 (2014).

Zhang, X. and A. P. Showman, "Atmospheric Circulation of Brown Dwarfs: Jets, Vortices, and Time Variability", ApJL, **788**, L6 (2014).

Zhou, Y., G. J. Herczeg, A. L. Kraus, S. Metchev and K. L. Cruz, "Accretion onto Planetary Mass Companions of Low-mass Young Stars", ApJL, **783**, L17 (2014).

Zuckerman, B. and E. E. Becklin, "A search for brown dwarfs and late M dwarfs in the Hyades and the Pleiades", ApJL, **319**, L99–L102 (1987).

Zuckerman, B., J. H. Rhee, I. Song and M. S. Bessell, "The Tucana/Horologium, Columba, AB Doradus, and Argus Associations: New Members and Dusty Debris Disks", ApJ, **732**, 61 (2011).

Zurlo, A., A. Vigan, R. Galicher, A.-L. Maire, D. Mesa, R. Gratton, G. Chauvin, M. Kasper, C. Moutou, M. Bonnefoy, S. Desidera, L. Abe, D. Apai, A. Baruffolo, P. Baudoz, J. Baudrand, J.-L. Beuzit, P. Blancard, A. Boccaletti, F. Cantalloube, M. Carle, E. Cascone, J. Charton, R. U. Claudi, A. Costille, V. de Caprio, K. Dohlen, C. Dominik, D. Fantinel, P. Feautrier, M. Feldt, T. Fusco, P. Gigan, J. H. Girard, D. Gisler, L. Gluck, C. Gry, T. Henning, E. Hugot, M. Janson, M. Jaquet, A.-M. Lagrange, M. Langlois, M. Llored, F. Madec, Y. Magnard, P. Martinez, D. Maurel, D. Mawet, M. R. Meyer, J. Milli, O. Moeller-Nilsson, D. Mouillet, A. Origné, A. Pavlov, C. Petit, P. Puget, S. P. Quanz, P. Rabou, J. Ramos, G. Rousset,

A. Roux, B. Salasnich, G. Salter, J.-F. Sauvage, H. M. Schmid, C. Soenke, E. Stadler, M. Suarez, M. Turatto, S. Udry, F. Vakili, Z. Wahhaj, F. Wildi and J. Antichi, "First light of the VLT planet finder SPHERE. III. New spectrophotometry and astrometry of the HR 8799 exoplanetary system", A&A, **587**, A57 (2016).

APPENDIX A

MANUAL EXPLAINING THE BAM CODE

A.1 The Brown dwarf Atmosphere Monitoring Photometry Code

The Brown dwarf Atmosphere Monitoring Photometry Code or BAM-Phot was written for the first BAM paper by Paul A. Wilson to work with data taken from the NTT in Chile. The code was subsequently updated with some bug fixes and upgrades implemented by Abhijith Rajan for BAM-II. One of the major improvements from BAM-I to BAM-II is the ability to work with a range of telescopes and a revision in the manner of light curve generation, whereby lightcurves are generated using both a weighted mean and a median of the comparison stars. The user can then choose which of the two methods is preferred.

The code is publicly available via github[10] and is available for anyone to use in their research. If your research has benefited from the use of the BAM-Phot code please acknowledge both BAM papers (Wilson *et al.*, 2014; Rajan *et al.*, 2015). Note, this code makes use of the PyRAF, the python based IRAF programming language. If you do not have PyRAF installed on your machine, you can install it from here.

A.1.1 Setting up the code

The recommended way to download the code would be fork it on github. A fork is a copy of a repository (repo), within GitHub, that belongs to you. It is not necessary to fork the main course repo (you could clone it directly; see below), but by doing so the local copy is still tied to the original BAM repo and thus any bugs located in the code can be communicated back to the original code.

To get a repo onto your local system, you need to clone it with the command

```
git clone <address>
```

Here, `<address>` is the git url of the remote repo (either the original or your fork), available on the website. Once cloned to the local system, the code is now available to work on your data.

One of the first files that need to be modified to get the code working properly is file `param.py` in the src directory, see Figure 48. This file contains a list of variables

[10] https://github.com/abhijithrajan/bam

Figure 48. Screen shot of the param.py file.

needed by the code to analyze the data including `rootdir` which needs to be modified in order for the code to know the location of the source code. Change this variable to point to the directory where the repository has been downloaded.

Changing the address will immediately allow the user to run the BAM-Phot code, which can be run using the following command

```
./bam.py
```

However, before starting the code it is essential to set up the remaining variables in the param.py file, shown in Figure 48.

- The first six variables in the param.py file are related to the instrument, namely `pixel_scale`, `read_noise`, and `gain` which should be standard values available for the instrument. These keywords are used in the calculation of the photometry and error and should not be left empty or with incorrect values. The next two are header keywords, `JD_header`, and `airmass`. Both these keywords are typically

available in the header of data. The airmass keyword is what informs the correction of the images, and the `JD_header` keyword is the only way for the pipeline to know the time stamp for each image in the sequence.

- The next two header keywords are meant to point to the location of the code and by now the `rootdir` has already been set, the `datadir` keyword can be left to "data" or changed as needed. A directory labelled "data" needs to be created in the root directory, this directory is the repository of all the science data that will be operated upon by the photometry pipeline.
- The next keyword i.e. `binned_data`, requires a boolean value to indicates whether the code should bin the images in case they are unbinned. Or if they are already whether they are already combined then it should not further bin the images. False - tells the code that the data is unbinned and it should bin the images and vice versa.
- The pipeline expects the science data to be subdivided by targets i.e. at one time it reduces the data for one object before proceeding to the next. The order is simply to create directories in the data directory labelled OBJ01, OBJ02, etc. The `data_sub_dir` variable tells the code where the images are located within each OBJ directory. All science images should be copied to a directory with the name of this variable, which in the example param.py file is in a directory called "data_unbinned".

- The next variable labelled `ds9_name` is the first few letters and the last few letters of the name of the coordinate file used to point the pipeline to the location of the target and the reference stars to be used in the photometry. An example of a region file is shown in Figure 49 indicating the values required by the pipeline. For the BAM papers, these region files were typically created using

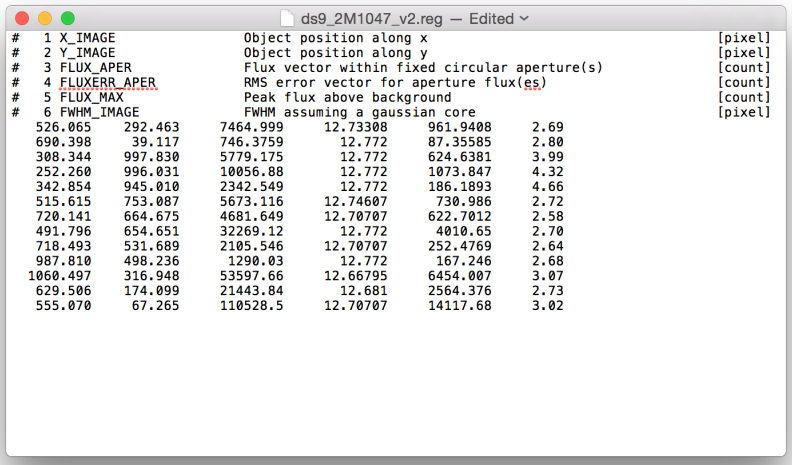

Figure 49. An example of the contents of a normal coordinate file. The different values are the x, y, position of an object, its flux along with error, the maximum flux of the target and the full width at half maximum of the star.

Source Extractor[11], which will output the files in the exact format required by the pipeline, the variable names for which are present in the example finder file. *Note, The coordinates of the target star or brown dwarf must be the first line in the finder. This is used by the pipeline to identify the target.*

- `image_name` is the variable that specifies which files in the directory are the science images on which to act. The format is similar as above, where the first and last few letters must be specified.
- `variable_aperture` is a keyword used decide during the process of computing the photometry whether to use a single aperture for all the photometry or whether to use variable aperture sizes determined by the median Full Width Half Maximum (FWHM) for each image. Note, this is not to suggest a variable aperture per target and reference star but rather different apertures based

[11] http://www.astromatic.net/software/sextractor

on varying seeing conditions. If the seeing remains consistent throughout the sequence, this will reduce to having a constant aperture throughout the data reduction. The assumption being made by the pipeline is that the data has been corrected for variations within the image itself.

- `airmass_detrend` is the keyword that determines whether the photometry is corrected for airmass changes across the entire sequence. The `airmass` keyword needs to be correctly set for this correction to be enabled. This correction is carried out by fitting a second order polynomial to the relative flux of the master reference as a function of airmass.
- In the next three keywords, `std_cutoff` determines the standard deviation above which a comparison star is rejected from being included as a comparison star. `cut_offs` is actually a list of values that determines different cut off values the first one is not used, the second applied a Mean Absolute Deviation cut off which is no longer used in the code. The next two are integer values indicating the maximum number of starting reference stars to use from the finder, and the minimum number of references required for the code. The final two are the required flux in the comparison stars which come from the photometry included in the finder file - the first is the minimum value required for an object to be accepted as a reference and the second is the maximum value, this will reject any stars above the cut off which could be the saturation value or the flux above which the star is no longer linear to within some percent value.

The start up screen for the code is shown in Figure 50. It lists the five different options that are available within the code, and they are each described in greater detail below.

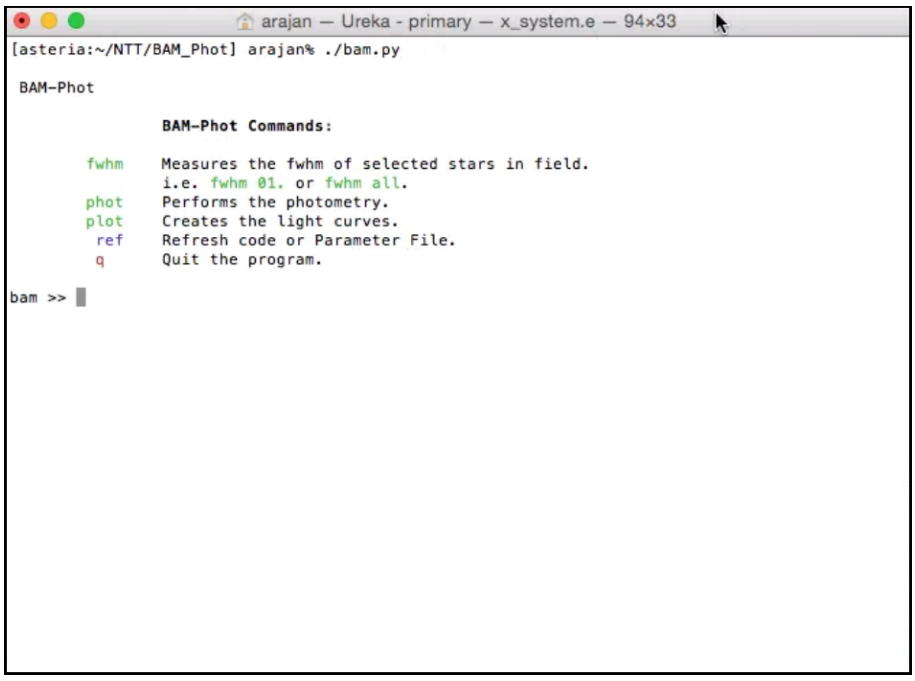

Figure 50. Start-up screen for the BAM-Phot code.

- fwhm: For a fresh dataset, the very first task to be carried out is the estimation of the FWHM for each brown dwarf/star identified in the finder chart specified earlier. Using the coordinates, a function using `IRAF` measures the FWHM for all the objects in an image and uses them to calculate the median value for the image and stores the output to a file called "fwhm.txt" for the full sequence in the `data_sub_dir`.

  `fwhm 01` - will measure the median FWHM for all the images of star 01.

  `fwhm all` - will measure the median FWHM for all the images of all the stars in the `datadir`.

- phot: After running the "fwhm" step, the next step in the pipeline is to estimate the photometry. *Note, the photometry step will not run without the presence of the "fwhm.txt" file in the directory.*

  `phot 01` or `phot all` - will run `IRAF/DAOPHOT` aperture photometry on each

target.

Depending on the choice above the data will be stored in either a variable aperture or constant aperture directory where the aperture size is 1.5×FWHM. If the choice is variable aperture, then the photometry uses an aperture of 1.5×FWHM where the FWHM varies for each image. If not, then the aperture is 1.5×FWHM – however the FWHM is now the median FWHM of the entire sequence. *From experience, constant aperture should only be chosen in excellent seeing conditions.* Modifying the aperture size is currently not supported out of the box, and requires the changes to be applied directly in the `phot.py` routine.

- plot: After running the "phot" step, the final step is to estimate the light curve. The description of how the references are chosen is described in detail in (Wilson *et al.*, 2014). To generate the light curves the user needs simply type either `plot 01` or `plot all` to run it for a single star or for all the stars.

  Unlike the other routines in this pipeline, the "plot" routine runs twice per target. the first time it generates a light curve using *all* the reference stars. The second time it applies the selection criteria and generates the final light curve. For each of these step the pipeline generates a figure (see Figure 51 and 52) which helps determine the quality of the reference stars chosen for the final light curve (the figures are saved to the "plots" directory located in the root directory). At this point the user can choose to increase or decrease the various cut offs that are being applied to make the pipeline reject fewer or more comparisons.

  In addition to these plot files, there are further text files with the values that go into generating the figures. These are located in "plots/data/(un)binned" the name is dependent on whether the user choose to bin the data points or not.

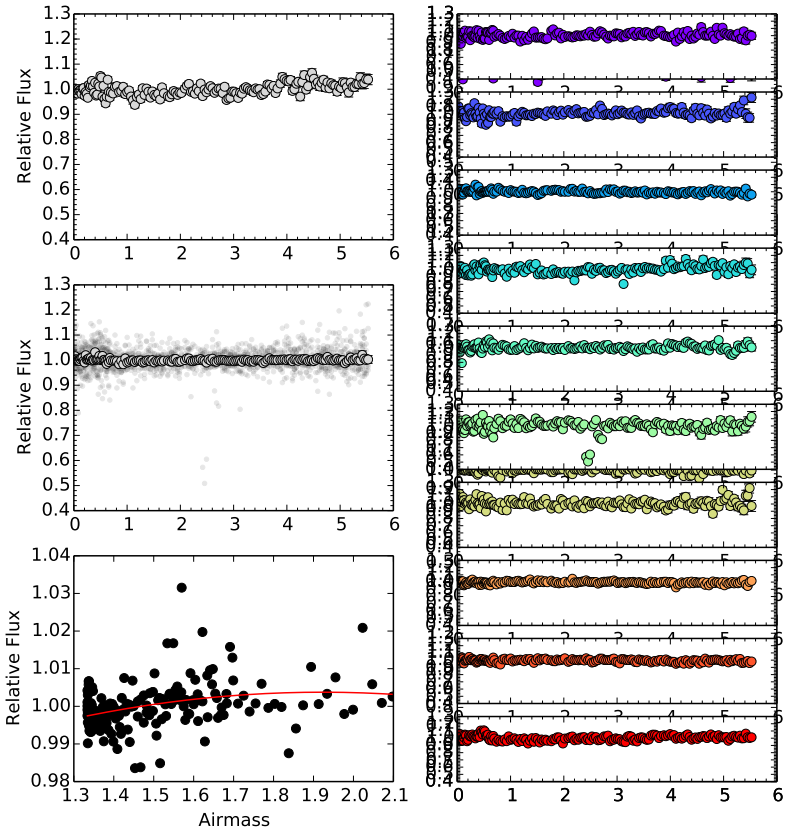

Figure 51. First step of light curve generation code. This step uses all the reference stars, light curves for which are shown on the right side. The target light curve is on the top left, middle left is the combined reference light curve and bottom left is the airmass for the sequence along with the polynomial fit used to correct it.

- ref: The refresh command allows users to update the code or the param.py file and re-run the pipeline without needing to exit the `bam` environment.
- q: By typing "q", the user can exit out of the code. This will cause all information stored in memory to be lost, and should only be done in cases where no further tasks need to be performed.

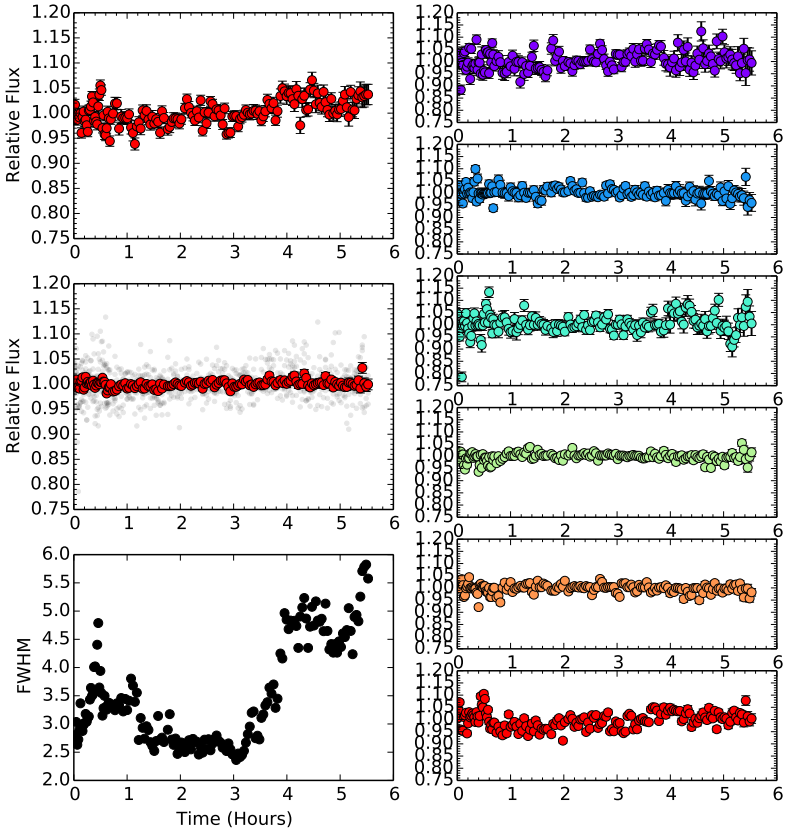

Figure 52. Second step of light curve generation code. This step uses only the best reference stars, light curves for which are shown on the right side. The target light curve is on the top left, middle left is the final reference light curve in red and all the reference star data points shown in gray and bottom left is the FWHM for the sequence.

APPENDIX B

STATISTICS CALCULATED TO CONFIRM THE PLANET DETECTIONS IN THE HST/WFC3 DATA

B.1 Quantifying a detection

The detections of the HR8799 b and c in the F098M and F139M data were of low signal to noise and to confirm that the detections were real and not artifacts from the data processing, we performed a test using "zero-flux" planets which is elaborated below.

The optimization method utilized in the analysis pipeline maximizes the ratio of the throughput to the residual noise, where the throughput is measured using an injected template PSF at a given location and the residual noise is measured from the standard deviation of pixels surrounding this location, the noise is measured by masking the location of the injected PSF. A concern with this technique is that rather than optimize the SNR, the code could be choosing parameters that breed speckles and thus result in spurious detections. To eliminate this concern, template PSFs with the signal zeroed out or "zero-flux" planets were injected into the data (at locations separated from the real planet) and processed in the exact same manner as the real planet. For the test, the throughput of "zero-flux" planet at a given location is calculated and used to derive the data quality criterion and since there is no signal, the test will determine whether the data quality criterion itself will cause speckles to be amplified such that a planet with a non-zero flux appears to exist. This process was used for pipeline verification purpose. The data was analyzed by injecting these zero-flux planets at 20 – 25 locations for each real planet and did not generate any spurious objects comparable to the reported planet detections.

B.2 Calculating the SNR

The planet photometry is calculated in each image using a matched filter, similar to the procedure adopted in Soummer *et al.* (2012). To ensure that we understand the throughput losses caused by the algorithm, we calculated an aperture correction validated by comparisons against HST calibration data on several white dwarfs that are standard photometric standards as well as field brown dwarfs of similar spectral type range.

The root mean square (RMS) noise level was estimated as the standard deviation in the optimized zone after masking the location of the planet. Additionally, we compared our results against the Student t-test suggested in the Mawet *et al.* (2014) paper. The zone radial boundaries range from 14.5 λ/D to 20 λ/D for planet b and from 8 λ/D to 11.5 λ/D for planet c in the three filters. Based on these separations we anticipate between $\sim$44-60 and $\sim$24-33 resolution elements for the planets in each of the small zones.

Also shown in Figure 53 is the probability distribution function of the signal for both HR8799 b and c in the F127M filter. We computed the Shapiro-Wilk test on these data and found that both PDF are best approximated with a normal distribution with a p-value of 0.2 and 0.7 for b and c respectively. Using equations 5 and 10 from Mawet *et al.* (2014), we estimated the false positive fraction (FPF) for the four detections (b in three filters and c in F127M) presented in the paper and the signal to noise ratio calculated assuming both a Gaussian and student-t distribution.

For HR8799 b (assuming the PDF is Gaussian):

- F098M - FPF = 3.46e-04, SNR = 3.8

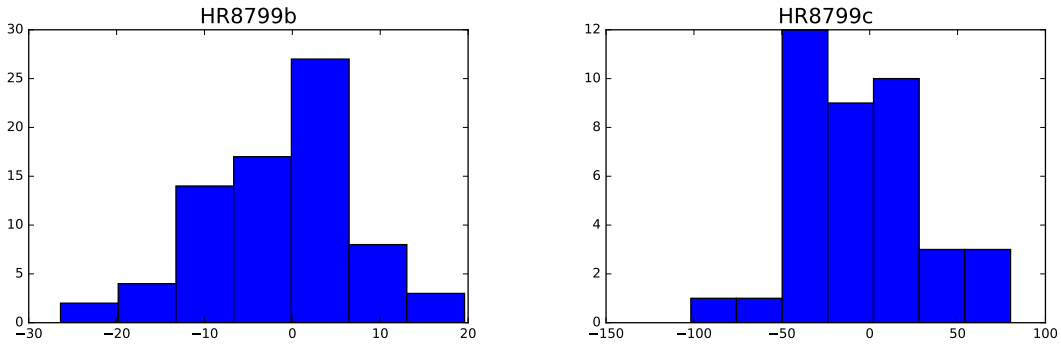

Figure 53. The probability distribution functions for HR8799 b and c in the F127M filter. Both point spread functions are best approximated by a normal function based on the results of a Shapiro-Wilk test.

- F127M - FPF = 7.57e-22, SNR = 9.8
- F139M - FPF = 1.30e-03, SNR = 3.4

Assuming small number statistics and a modified Rician distribution, where only the elements in the annulus radially surrounding the companion are used in the calculation:

Number of elements = 38

- F098M - FPF = 1.75e-03, SNR = 3.3
- F127M - FPF = 2.74e-11, SNR = 6.8
- F139M - FPF = 4.26e-03, SNR = 3.0

For HR8799 c (assuming the PDF is Gaussian):

- F127M - FPF = 3.79e-07, SNR = 5.3

Assuming small number statistics, and estimating the FPF estimated using the student-t distribution:

- F127M: Number of elements = 20, FPF = 1.27e-04, SNR = 4.0

We also computed the same statistics for the single bright speckle seen in the F139M data for HR8799 c. The SNR in the residual F139M speckle:
Assuming a Gaussian PDF: FPF = 4.62e-04, SNR = 3.7
Assuming a non-Gaussian PDF: Number of elements = 20, FPF = 2.65e-03, SNR = 2.23

An important caveat to the above exercise is to point out that the errors presented for the photometry in this study paper are not calculated from the SNR. Instead we measured them by injecting 25 fakes for 'b' and 20 for 'c' (fewer to avoid the location of the real planet) and calculating the standard deviation in the measured signal for each of the fakes. The detection SNR is not used to quantify the errors for the photometry, they are used to determine the criterion for selecting the best images to combine.

APPENDIX C

CALCULATING THE CORRELATION FOR THE 51 ERI IFU DATA

C.1 Derivation of Spectral Covariance

We follow the method described in Greco and Brandt (2016) to measure the inter-pixel correlation within the PSF-subtracted images, and convert these into a covariance matrix. For each image (J, H, $K1$, and $K2$), the correlation ψ_{ij} between pixel values at wavelengths λ_i and λ_j within a 1.5 λ/D annulus was estimated as

$$\psi_{ij} = \frac{\langle I_i I_j \rangle}{\sqrt{\langle I_i^2 \rangle \langle I_j^2 \rangle}} \tag{C.1}$$

where $\langle I_i \rangle$ is the average intensity within the annulus at wavelength λ_i. This was repeated for all wavelength pairs, and at five different separations: 350, 454 (the separation of 51 Eri b), 550, 650, and 750 mas. To avoid biasing the measurement, 51 Eri b was masked in the 454 mas annulus.

The measurements of the correlation ψ_{ij} at the eight different separations within the final image were used to fit the parametrized correlation model of Greco and Brandt (2016),

$$\psi_{ij} \approx A_\rho \exp\left[-\frac{1}{2}\left(\frac{\rho}{\sigma_\rho}\frac{\lambda_i - \lambda_j}{\lambda_c}\right)^2\right] + A_\lambda \exp\left[-\frac{1}{2}\left(\frac{1}{\sigma_\lambda}\frac{\lambda_i - \lambda_j}{\lambda_c}\right)^2\right] + A_\delta \delta_{ij} \tag{C.2}$$

where the symbols are as in Greco and Brandt (2016). This model is based on the assumption that the correlation consists of three components. The first two terms model the contribution of the speckle noise and the correlation induced by the interpolation within the reduction process. The third models uncorrelated noise, such as read noise, which do not contribute to the off-diagonal terms of the correlation matrix. The amplitude of the first two terms (A_ρ, A_λ) were allowed to vary with separation, while the two correlation lengths (σ_ρ, σ_λ) were fixed. As the sum of the

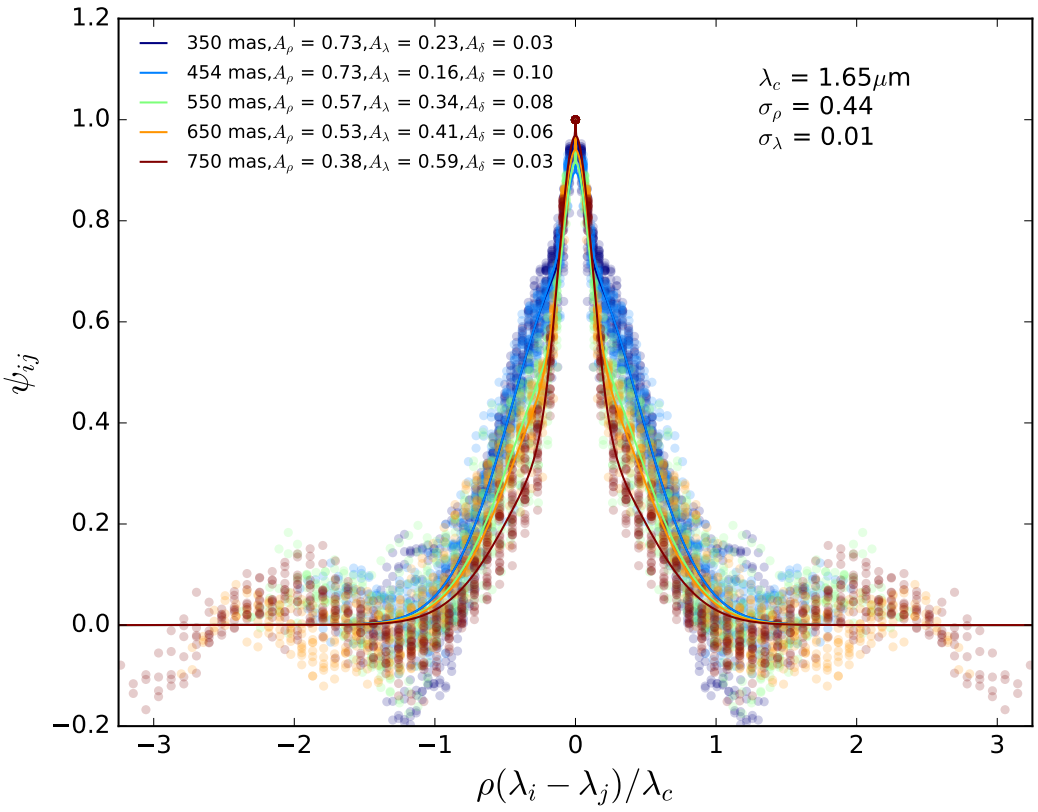

Figure 54. Example of the correlation function as a function of angular separation for H-band spectral cube. The figure shows the measured spectral correlation at the various angular separations included in the fit. The different colors correspond to the angular separations, with the circles being the value of the correlation for all the wavelength pairs and the lines of the same color indicate the best fit to Equation C.2.

amplitudes must equal unity, A_δ was derived from the other amplitudes. Figure 54 shows an example of the spectral correlation as a function of the angular separation for the H-band spectral cube, λ_c is the central wavelength of the spectrum (1.65 μm for H). The colored lines in the plot are the best fits to Equation C.2.

Due to the high dimensionality of the problem, we use a parallel-tempered Markov Chain Monte Carlo algorithm (Foreman-Mackey *et al.*, 2013) to find the global minimum. The best fit parameters at the separation of 51 Eri b within the PSF-subtracted image at each band is given in Table 12. Using these parameters, the

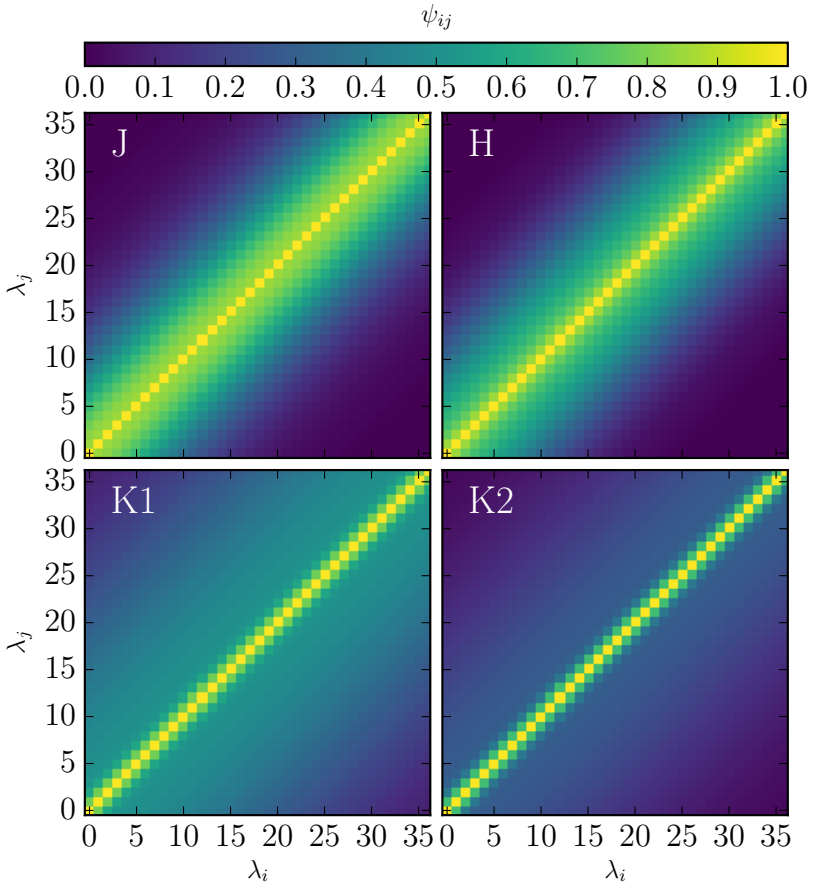

Figure 55. Presenting the correlation matrices calculated for each of the four $JHK1K2$ spectra. Going from J-band through $K2$ the correlation length can be seen to change as a function of speckle vs background noise. The spectra are highly correlated at J with up to 5 channels showing high correlation values, down to $\sim$3 at $K2$ which is a consequence of the spectral re-sampling.

Table 12. Correlation model parameters

Band	A_ρ	A_λ	A_δ	σ_ρ	σ_λ
J	0.43	0.43	0.14	0.44	0.05
H	0.73	0.16	0.10	0.44	0.01
$K1$	0.51	0.41	0.07	0.68	0.004
$K2$	0.30	0.62	0.08	0.43	0.004

covariance matrix, C, was constructed for each band. The diagonal elements contained the square of the uncertainties of the spectrum of the planet, and the off-diagonal elements were calculated using

$$\psi_{ij} \equiv \frac{C_{ij}}{\sqrt{C_{ii}C_{jj}}} \tag{C.3}$$

The fitted parameters in Table 12 demonstrate that the primary cause of correlation at the shorter wavelengths is speckle noise, with the correlation induced by interpolation becoming more significant in the $K1$ and $K2$ images. In each case the amplitude of the speckle noise term (A_ρ) is significantly higher than seen for HD 95086 b (De Rosa *et al.*, 2016). This can be attributed to the fact that 51 Eri A is approximately two magnitudes brighter at $K1$ (than HD 95086 A), leading to a significantly brighter speckle field. The typical correlation lengths in the PSF-subtracted image for each band are visualized in Figure 55, with the data being highly correlated at J band at wavelengths separated by up to five spectral channels.